



**HAL**  
open science

# Methods for improved brain PET quantification using super-resolution and non-negative matrix factorization

Yanis Chemli

► **To cite this version:**

Yanis Chemli. Methods for improved brain PET quantification using super-resolution and non-negative matrix factorization. Image Processing [eess.IV]. Institut Polytechnique de Paris, 2023. English. NNT : 2023IPPAT026 . tel-04367958

**HAL Id: tel-04367958**

**<https://theses.hal.science/tel-04367958v1>**

Submitted on 31 Dec 2023

**HAL** is a multi-disciplinary open access archive for the deposit and dissemination of scientific research documents, whether they are published or not. The documents may come from teaching and research institutions in France or abroad, or from public or private research centers.

L'archive ouverte pluridisciplinaire **HAL**, est destinée au dépôt et à la diffusion de documents scientifiques de niveau recherche, publiés ou non, émanant des établissements d'enseignement et de recherche français ou étrangers, des laboratoires publics ou privés.

# Methods for improved brain PET quantification using super-resolution and non-negative matrix factorization

Thèse de doctorat de l'Institut Polytechnique de Paris  
préparée à Télécom Paris

École doctorale n°626 Institut Polytechnique de Paris (ED IP Paris)  
Spécialité de doctorat : Signal, images, automatique et robotique

Thèse présentée et soutenue à Palaiseau, le 12 mai 2023, par  
**Yanis Chemli**

Composition du Jury :

Régine Trebossen Directrice de recherche, CEA (DRF)	Présidente / Examinatrice
Françoise Peyrin Directrice de recherche émérite, Insa Lyon (Creatis)	Rapporteuse
David Sarrut Directeur de recherche, Insa Lyon (Creatis)	Rapporteur
Hamid Sabet Assistant professor, Harvard Medical School (Radiology)	Examineur
Jinsong Ouyang Associate professor, Harvard Medical School (Radiology)	Examineur
Isabelle Bloch Professeure, Telecom Paris (LTCl) et Sorbonne Université (LIP6)	Directrice de thèse
Georges El Fakhri Professor, Harvard Medical School (Radiology)	Co-Directeur de thèse



# Acknowledgments

بِسْمِ اللَّهِ الرَّحْمَنِ الرَّحِيمِ

I want to take this moment to extend my profound appreciation to everyone who supported and guided me on this journey that was my Ph.D. thesis.

First and foremost, I extend my heartfelt gratitude to both my advisors, Dr. Isabelle Bloch at Telecom Paris in France, and Dr. Georges El Fakhri at the Gordon Center for Medical Imaging (GCMi) in Boston, who allowed this Ph.D. to concretize and flourish.

Naturally, I would like to thank my mentors, Dr. Jinsong Ouyang, Dr. Yoann Petibon, and Dr. Nicolas Guehl. Your consistent guidance, expertise, and unwavering support played an invaluable role in the development and completion of my work. I appreciate your dedication, patience, and the wisdom you shared with me in medical imaging.

To the esteemed jury members, thank you for your time and constructive feedback. Your valuable insights not only enriched this research but also my growth as a scientist. I am grateful for the opportunity to learn from your extensive knowledge and experience.

Most of my work was conducted in Boston, and to all the faculty and staff at the GCMi, I cannot express enough thanks for your unwavering support and camaraderie. This journey would not have been as fruitful or enjoyable without your contribution.

I am fortunate to have been part of such an enriching environment and I look forward to maintaining these connections in my future endeavors.

Finally, a big thank you to my family and friends. Your ongoing encouragement have been fundamental in my journey. Your support has been not just a source of strength during my PhD studies, but throughout my life.

This accomplishment is not just my own but a testament to the incredible support system I have been fortunate enough to be part of.

Thank you.



# Abstract

The advent of radiotracers binding to misfolded proteins, such as amyloid and neurofibrillary tangles (tau), has ushered in a new era of PET imaging for neurodegenerative diseases, bringing new requirements for image quantification and processing. In particular, imaging of tau pathology, especially in early disease stages, is fueling a need for improved PET quantification to allow for accurate imaging of more focal tracer uptake patterns and small brain structures, such as the entorhinal cortex. However, this task is usually affected by the poor spatial resolution inherent to PET imaging, noise, and the partial volume effect. To address these issues, this thesis explores different methods for improving quantification, such as super-resolution (SR) and non-negative matrix factorization (NMF).

Super-resolution (SR) is a methodology that seeks to improve image resolution by exploiting the increased spatial sampling information obtained from multiple acquisitions of the same target with accurately known sub-resolution shifts. The first contribution of this work aims to study, develop and evaluate an SR estimation framework for brain positron emission tomography (PET), taking advantage of a high-resolution infra-red tracking camera to measure shifts precisely and continuously. Moving phantoms and non-human primate (NHP) experiments were performed on a GE Discovery MI PET/CT scanner (GE Healthcare) using an NDI Polaris Vega (Northern Digital Inc), an external optical motion tracking device. To enable SR, a robust temporal and spatial calibration of the two devices was developed, as well as a list-mode Ordered Subset Expectation Maximization (OSEM) PET reconstruction algorithm, incorporating the high-resolution tracking data from the Polaris Vega to correct motion for a measured line of responses (LORs) on an event-by-event basis. For both phantoms and NHP studies, the SR reconstruction method yielded PET images with visibly increased spatial resolution compared to standard static acquisitions, allowing improved visualization of small structures. Quantitative analysis in terms of SSIM, CNR, and line profiles was conducted and validated our observations. The results demonstrate that SR can be achieved in brain PET by measuring target motion in real-time using a high-resolution infrared tracking camera.

The second objective of this thesis was to explore the use of non-negative matrix factorization (NMF) in dynamic PET imaging, specifically in relation to the [18F]MK6240 Tau PET tracer. This tracer has potential clinical limitations, such as off-target binding in dynamic imaging. NMF is a method that can overcome these limitations by accurately separating tau-specific,

non-specific, and off-target signals in the acquired data. In this thesis, the theoretical foundations of NMF are discussed, and its practical applications in dynamic PET imaging are examined. To demonstrate the effectiveness of NMF, simulations were applied to a numerical phantom and real dynamic PET images acquired from cognitively normal subjects. The results of the NMF analysis are presented and discussed, highlighting the potential of this method to improve the quantification and interpretation of dynamic PET imaging data in the context of tau pathology.

This thesis also presents and evaluates other optimization techniques, namely, motion correction, point spread function modeling, anatomical prior regularization, and projectors implementations, for a better noise control and partial volume effect correction.

# Contents

Abstract.....	5
Contents .....	7
Introduction Générale en Français.....	11
General Introduction.....	17
<b>Chapter 1 Introduction to PET and its clinical applications .....</b>	<b>21</b>
1.1 Historic of PET Imaging .....	21
1.2 General principles of PET imaging.....	22
1.2.1 The physics of PET imaging .....	22
1.2.2 Data acquisition .....	29
1.2.3 Image reconstruction.....	31
1.2.4 Data corrections.....	38
1.3 Different implementations of PET scanners.....	43
1.3.1 Combined PET-Computed Tomography .....	43
1.3.2 Simultaneous PET-MR .....	44
1.3.3 SAVANT scanner .....	45
1.4 Clinical application in neuroimaging and Alzheimer’s Disease .....	46
1.4.1 Introduction to Alzheimer’s Disease .....	47
1.4.2 PET imaging of tau protein .....	50
1.5 Conclusion.....	53
<b>Chapter 2 Challenges of PET quantification .....</b>	<b>55</b>
2.1 Resolution.....	56
2.1.1 Definition.....	56
2.1.2 Source.....	56
2.1.3 Impact.....	58
2.1.4 Improving resolution.....	58
2.2 Partial volume effect .....	59
2.2.1 Definition.....	59
2.2.2 Source.....	59
2.2.3 Impact of PVE .....	60
2.2.4 PVE Correction.....	60
2.3 Noise in PET imaging .....	61
2.3.1 Source.....	61
2.3.2 Impact.....	62
2.4 Motion .....	62
2.4.1 Source and Impact .....	63
2.4.2 Motion Correction.....	63
2.4.3 Gating.....	64
2.5 Conclusion and Research Objectives .....	67
<b>Chapter 3 Motion correction: integration of a real-time tracking camera .....</b>	<b>69</b>
3.1 Introduction .....	70
3.2 Architecture Description .....	71
3.2.1 Camera selection.....	71
3.2.2 SAVANT DAQ Overview .....	71



3.2.3	Timestamp-based bridge .....	72
3.3	Integration of the Polaris .....	76
3.3.1	PTP synchronization measurements .....	76
3.3.2	Test system for timestamp-based bridge .....	76
3.3.3	Test system for legacy bridge .....	76
3.3.4	Motion tracking and motion generation .....	77
3.3.5	Moving phantom acquisitions and reconstructions .....	77
3.4	Results .....	79
3.4.1	PTP synchronization range and stability .....	79
3.4.2	Motion correction with point sources .....	79
3.4.3	Motion correction with phantoms .....	80
3.5	Discussion .....	82
3.6	Conclusion .....	83
<b>Chapter 4</b>	<b>Super-resolution principles and a PET/MR proof of concept .....</b>	<b>85</b>
4.1	Introduction .....	85
4.2	Principle of super-resolution .....	86
4.3	Literature review .....	88
4.3.1	General SR methods in image processing .....	88
4.3.2	Super-resolution in PET .....	89
4.4	A proof of principle in PET/MR .....	91
4.4.1	Method .....	91
4.4.2	Experiment .....	92
4.4.3	Results and discussion .....	93
4.5	Discussion and Conclusion .....	94
<b>Chapter 5</b>	<b>Super-resolution in brain positron emission tomography using a real-time motion capture system .....</b>	<b>95</b>
5.1	Introduction .....	95
5.2	Super-resolution in a PET/CT setup using the Polaris tracker .....	97
5.2.1	Overview .....	97
5.2.2	High-resolution motion tracking device .....	97
5.2.3	Temporal synchronization, spatial calibration between the Polaris Vega and the PET/CT scanner and integration of the motion in PET reconstruction .....	97
5.2.4	Phantom and non-human primate experiments .....	103
5.2.5	Evaluation of image quality .....	104
5.3	Results .....	106
5.3.1	Phantom studies .....	106
5.3.2	In vivo study .....	109
5.3.3	Quantitative analysis .....	109
5.4	Discussion .....	111
5.5	Conclusion .....	115
<b>Chapter 6</b>	<b>Optimizations for PVE and noise: PSF, Projectors and Kernel Method .....</b>	<b>117</b>
6.1	PSF Modeling .....	117
6.1.1	In the image space .....	118
6.1.2	In the projection space .....	119
6.1.3	Hybrid approach .....	120
6.2	Projectors .....	124
6.2.1	Single-ray Siddon .....	124

6.2.2	Multi-ray Siddon.....	125
6.2.3	Distance-driven projector.....	126
6.2.4	Evaluation of different projectors.....	128
6.3	Kernel Method.....	130
6.3.1	Overview.....	130
6.3.2	Theory.....	131
6.4	Results.....	134
6.5	Conclusion.....	136
<b>Chapter 7 Disentangling tau-specific and off-target signals in [18F]MK-6240 PET using nonnegative matrix factorization.....</b>		<b>139</b>
7.1	Introduction.....	139
7.2	Literature review on factor analysis.....	142
7.3	Factor analysis using NMF for [18F]MK-6240.....	145
7.3.1	Introduction to Non-Negative Matrix Factorization.....	145
7.4	Simulation and human studies.....	148
7.4.1	Simulation study.....	148
7.4.2	Human studies.....	150
7.5	Evaluation of image quality.....	152
7.6	Results.....	153
7.6.1	Simulation.....	153
7.6.2	Human studies.....	155
7.6.3	Sanity check.....	157
7.7	Discussion and Conclusion.....	158
<b>Chapter 8 Conclusions and perspectives.....</b>		<b>161</b>
8.1	Conclusion.....	161
8.1.1	Real-time motion correction.....	161
8.1.2	Super-resolution.....	162
8.1.3	Factor analysis using non-negative matrix factorization.....	163
8.2	Perspectives.....	164
8.2.1	Penalized reconstruction.....	164
8.2.2	A better calibration between the camera and scanner coordinate spaces.....	165
8.2.3	Nature of movement applied to the scanned object.....	166
8.2.4	Human studies.....	166
8.2.5	Perspectives on [18F]MK-6240 NMF unmixing.....	167
<b>Publications.....</b>		<b>169</b>
<b>Appendix.....</b>		<b>171</b>
<b>Bibliography.....</b>		<b>179</b>



# Introduction Générale en Français

L'avènement des radiotraceurs se liant aux protéines mal repliées, comme l'amyloïde et les enchevêtrements neurofibrillaires de la protéine tau dans le cerveau, a instauré une nouvelle ère de l'imagerie par tomographie par émission de positons (TEP) pour les maladies neurodégénératives, apportant de nouvelles exigences pour la quantification et le traitement des images. L'imagerie de la pathologie liée à la protéine tau, surtout aux premiers stades de la maladie, alimente le besoin d'une amélioration de la quantification TEP pour permettre une imagerie précise de l'absorption de traceurs plus focalisés et de petites structures cérébrales, comme le cortex entorhinal.

La TEP est une technique d'imagerie largement utilisée qui a transformé le domaine des maladies neurodégénératives. La TEP offre une sensibilité et une spécificité élevées dans la détection de l'activité métabolique ou moléculaire de cibles spécifiques, telles que les protéines, ce qui en fait un outil indispensable pour la recherche et le diagnostic clinique. Cependant, elle présente certaines limites en matière de résolution spatiale, de bruit et d'effet de volume partiel, qui peuvent compromettre sa précision et limiter son application dans certains cas.

La résolution spatiale de la TEP est généralement de l'ordre de 3 à 5 mm, ce qui est relativement faible par rapport à d'autres techniques d'imagerie telles que l'imagerie par résonance magnétique (IRM) et la tomodensitométrie (TDM). Cette faible résolution peut entraîner un flou et une perte d'information, en particulier dans les petites structures cérébrales comme le cortex entorhinal, une zone cruciale dans la maladie d'Alzheimer. De plus, l'effet de volume partiel, qui se produit, entre autres, lorsqu'un voxel contient un mélange de différents types de tissus, peut conduire à une surestimation ou une sous-estimation de l'absorption du traceur, en fonction de la nature du mélange.

Pour pallier ces limites, cette thèse explore plusieurs méthodes pour améliorer la quantification TEP, à savoir la super-résolution (SR) et la factorisation de matrice non négative (NMF). La SR est une technique qui vise à augmenter la résolution spatiale des images TEP au-delà des limites physiques du scanner, en combinant plusieurs images de

basse résolution en une image à haute résolution. Cette approche a montré des résultats prometteurs pour améliorer la visualisation de petites structures et la précision de la quantification. NMF est une autre méthode qui décompose les images TEP en un ensemble de fonctions de base représentant différents modèles d'absorption de traceurs. Cette approche peut séparer diverses sources de bruit et d'effet de volume partiel dus à la liaison hors cible et améliorer la précision de la quantification.

Avant de nous pencher sur les contributions spécifiques de cette thèse, il est essentiel de fournir un contexte de fond sur l'imagerie TEP, son application en ce qui concerne les enchevêtrements neurofibrillaires de protéines tau, et les défis auxquels fait face l'imagerie TEP dans le contexte des maladies neurodégénératives. Ainsi une introduction approfondie de l'imagerie TEP est donnée dans le Chapitre 1 et le Chapitre 2.

Un résumé de l'histoire en imagerie TEP est donné, et les principes généraux de l'imagerie TEP sont discutés dans le Chapitre 1. Nous exposons des aspects sur la physique de l'imagerie TEP, l'acquisition des données, la reconstruction d'image, les corrections des données, et les différents types de scanners, tels que les scanners TEP-CT et TEP-IRM. De plus, le chapitre explore des applications cliniques de l'imagerie TEP, avec une attention particulière portée sur la protéine tau hyperphosphorylée, une caractéristique forte de la maladie d'Alzheimer, et le potentiel de l'imagerie TEP pour visualiser la pathologie liée à la protéine tau. La maladie d'Alzheimer est la maladie neurodégénérative la plus courante dans le monde, et l'accumulation de la protéine tau hyperphosphorylée dans le cerveau est un élément crucial du processus de la maladie. Nous examinons les signes cliniques, le diagnostic, la pathologie, et l'importance de l'imagerie TEP tau en ce qui concerne la maladie d'Alzheimer. Le chapitre discute également des différents traceurs TEP de la protéine tau disponibles et des limites de ces traceurs dans le contexte de l'imagerie de la pathologie tau.

Le Chapitre 2 de la thèse explore les défis de l'imagerie TEP, en particulier dans le contexte des maladies neurodégénératives. Ce chapitre discute de la définition, de la source et de l'impact de problèmes tels que l'intrinsèque médiocre résolution spatiale, l'effet de volume partiel, le bruit dans l'imagerie TEP, et les artefacts de mouvement et examine les méthodes actuelles pour relever ces défis, comme la modélisation de la résolution, la correction du volume partiel, et les méthodes de correction du mouvement.

En fournissant ce contexte de fond et en exposant les défis qui persistent en imagerie TEP, cette thèse prépare le terrain pour les contributions, qui visent à relever certains des défis auxquels fait face l'imagerie TEP et à explorer de nouvelles méthodes pour améliorer la précision et la résolution de l'imagerie TEP dans le contexte des maladies neurodégénératives.

Ainsi, le Chapitre 3 se concentre sur l'intégration d'une caméra de suivi en temps réel pour la correction du mouvement dans l'imagerie TEP. Les artefacts de mouvement peuvent avoir un impact significatif sur la qualité et la précision des images TEP, en particulier dans le contexte des maladies neurodégénératives, où les patients peuvent avoir du mal à rester immobiles pendant le long processus d'imagerie. Ce chapitre présente une solution robuste à ce problème, avec le développement d'un système d'intégration de caméra de suivi en temps réel qui peut mesurer et corriger précisément le mouvement. Le système utilise une caméra haute résolution et une interface basée sur des horodatages pour synchroniser les données de suivi du mouvement avec les données TEP. Des acquisitions et des reconstructions de fantômes en mouvement ont été réalisées, démontrant l'efficacité de l'interface de communication entre la caméra de suivi et différents scanners.

Le Chapitre 4 de la thèse présente un état de l'art sur les méthodes de super-résolution en traitement d'image, puis, plus particulièrement en imagerie TEP. Une preuve de concept de super-résolution en TEP/IRM est ensuite présentée, avec une application pour l'imagerie cérébrale. La méthode développée tire parti d'image IRM haute résolution pour mesurer précisément les décalages entre différentes acquisitions TEP de l'objet. Bien que cette preuve de concept démontre la faisabilité de la SR en TEP/IRM, il reste néanmoins encore de nombreux défis à surmonter afin qu'elle puisse être utilisée en pratique clinique.

À cet égard, le Chapitre 5 de la thèse introduit la première contribution principale en approfondissant le concept de super-résolution dans un contexte, cette fois, cliniquement pertinent. Ce chapitre se concentre sur le développement d'une méthode pour la super-résolution en imagerie cérébrale TEP, en tirant parti de la précision de suivi submillimétrique de la caméra de suivi infrarouge présentée dans le Chapitre 3. Il offre une description détaillée de l'architecture du système, y compris l'étalonnage spatial et l'intégration du suivi du mouvement avec la reconstruction TEP dans une configuration TEP/CT. Des expériences sur des fantômes en mouvement et sur des primates non humains qui ont été réalisées sont présentées. Les résultats montrent que la méthode de

reconstruction SR produit des images TEP avec une résolution spatiale visiblement améliorée par rapport aux acquisitions statiques standard, permettant une meilleure visualisation de petites structures. Ainsi, ce chapitre présente une nouvelle approche prometteuse de l'imagerie TEP qui pourrait aider à améliorer la précision et la résolution de l'imagerie TEP en pratique clinique.

En plus de la SR, le Chapitre 6 de la thèse donne des détails supplémentaires et explore d'autres techniques d'optimisation pour la quantification TEP, la modélisation de la fonction d'étalement du point (PSF), les projecteurs, et la méthode par noyau (« kernel method »). La modélisation de la PSF est une approche puissante pour tenir compte de l'effet de flou inhérent aux images TEP en raison de la résolution spatiale limitée. Les projecteurs sont responsables de la mise en correspondance de l'espace objet vers l'espace de projection et sont essentiels pour une reconstruction précise de l'image TEP. Ce chapitre compare différents projecteurs, dont le projecteur Siddon à rayon unique, le Siddon à rayons multiples, et le projecteur dit « distance-driven », et évalue leur impact sur la reconstruction de l'image TEP. La méthode par noyau est également discutée. Cette méthode de reconstruction fournit un moyen efficace d'incorporer un a priori anatomique dans le processus de reconstruction.

La deuxième contribution principale de ce travail est explorée dans le Chapitre 7, où est abordée la question de la liaison hors cible en imagerie TEP. La liaison hors cible des traceurs est un problème, même avec les traceurs tau les plus prometteurs et les plus récents, tels que le [ $^{18}\text{F}$ ]MK-6240. Cette liaison hors cible se produit dans les régions adjacentes, principalement extra-cérébrales, et peut entraver considérablement l'utilité clinique et de recherche du [ $^{18}\text{F}$ ]MK-6240. Pour résoudre ce problème, nous proposons d'utiliser la factorisation de matrice non négative pour désenchevêtrer la contribution de différents signaux, y compris les composants hors cible, au signal TEP du [ $^{18}\text{F}$ ]MK-6240. Cette technique peut automatiquement cibler et éliminer le signal hors cible des images TEP, améliorant ainsi la précision de la quantification du signal spécifique. L'efficacité de la NMF est démontrée par une simulation et de véritables images TEP dynamiques acquises auprès de sujets normaux sur le plan cognitif et pathologiques. Les résultats montrent que la NMF peut séparer les signaux hors cible du tau des autres sources de signal dans les données dynamiques, améliorant ainsi la précision de la quantification du tau. Cette approche pourrait fournir de nouvelles perspectives sur la pathologie sous-

jacente des maladies neurodégénératives, permettant un diagnostic plus précis et plus précoce.

Enfin, le Chapitre 8 conclut la thèse et donne des perspectives.





# General Introduction

The advent of radiotracers binding to misfolded proteins, such as amyloid and neurofibrillary tangles (tau), has ushered in a new era of positron emission tomography (PET) imaging for neurodegenerative diseases, bringing new requirements for image quantification and processing. Imaging of tau pathology, especially in early disease stages, is fueling a need for improved PET quantification to allow for accurate imaging of more focal tracer uptake patterns and small brain structures, such as the entorhinal cortex.

PET is a widely used imaging technique that has transformed the field of neurodegenerative diseases. PET offers high sensitivity and specificity in the detection of metabolic or molecular activity of specific targets, such as proteins, making it an indispensable tool for both research and clinical diagnosis. However, PET has some limitations regarding spatial resolution, noise, and partial volume effect, which can compromise its accuracy and limit its application in some cases.

PET spatial resolution is typically in the range of 3-5 mm, which is relatively low compared to other imaging techniques such as magnetic resonance imaging (MRI) and computed tomography (CT). This low resolution can result in blurring and loss of information, especially in small brain structures such as the entorhinal cortex, a critical area in Alzheimer's disease. Moreover, the partial volume effect, which occurs when a voxel contains a mixture of different tissue types, can lead to overestimation or underestimation of tracer uptake, depending on the nature of the mixture.

To overcome these limitations, this thesis explores several methods to improve PET quantification, namely super-resolution (SR) and non-negative matrix factorization (NMF). SR is a technique that aims to increase the spatial resolution of PET images beyond the physical limitations of the scanner, by combining multiple low-resolution images into a high-resolution image. This approach has shown promising results in enhancing the visualization of small structures and improving quantification accuracy. NMF is another method that decomposes PET images into a set of basis functions representing different tracer uptake patterns. This approach can separate various sources of noise and partial volume effect due to off-target binding and improve quantification accuracy.

Before delving into the specific contributions of this thesis, it is essential to provide some background context on PET imaging, its application regarding tau protein neurofibrillary tangles, and the challenges facing PET imaging in the context of neurodegenerative diseases. Hence, the foundation of this thesis lies in the introduction to PET imaging, which is provided in Chapter 1 and Chapter 2.

A historical account of PET imaging is offered, and the general principles of PET imaging are discussed in Chapter 1. We delve into the physics of PET imaging, data acquisition, image reconstruction, data corrections, and different types of scanners, such as PET-CT and PET-MR scanners. Furthermore, the chapter explores the clinical applications of PET imaging, with a particular focus on hyperphosphorylated tau protein, a hallmark feature of Alzheimer's Disease, and the potential of PET imaging to visualize tau pathology. Alzheimer's Disease is the most common neurodegenerative disease worldwide, and tau pathology is a critical element of the disease process. We examine the clinical signs, diagnosis, pathology, and importance of tau PET imaging regarding Alzheimer's Disease. The chapter also discusses the different tau protein PET tracers available and the limitations of these tracers in the context of imaging tau pathology.

Chapter 2 of the thesis explores the challenges of PET imaging, particularly in the context of neurodegenerative diseases. This chapter discusses the definition, source, and impact of issues such as poor spatial resolution, the partial volume effect, noise in PET imaging, and motion artifacts and examines current methods for addressing these challenges, such as resolution modeling, partial volume correction, and motion correction methods.

By providing this background context and challenges in PET imaging, this thesis sets the stage for its contributions, which aim to address some of the challenges facing PET imaging and explore new methods for improving the accuracy and resolution of PET imaging in the context of neurodegenerative diseases.

Hence, Chapter 3 of this thesis focuses on integrating a real-time tracking camera for motion correction in PET imaging. Motion artifacts can significantly impact the quality and accuracy of PET images, especially in the context of neurodegenerative diseases, where patients may have difficulty remaining still during the imaging process. This chapter presents a robust solution to this problem, with the development of a real-time tracking camera integration system that can accurately measure and correct motion. The system uses a high-resolution camera and a timestamp-based bridge to synchronize the motion-tracking data with the PET

data. Moving phantom acquisitions and reconstructions were performed, demonstrating the effectiveness of the communication interface between the tracking camera and different scanners.

Chapter 4 of the thesis presents a literature review on super-resolution methods in image processing, followed by a review of super-resolution in PET. A proof of principle for super-resolution in PET/MR is then presented, with a framework for brain PET imaging developed that takes advantage of a high-resolution MR to measure shifts precisely. While the proof of principle demonstrates the feasibility of SR in PET/MR, there are still many challenges to overcome before it can be used in clinical practice.

In that regard, Chapter 5 of the thesis introduces the first main contribution by expanding on the concept of super-resolution in a more clinically relevant setting. This chapter focuses on the development of a method for super-resolution in brain PET imaging, taking advantage of the sub-millimeter tracking accuracy of the infra-red tracking camera presented in Chapter 3. It offers a detailed description of the system's architecture, including the spatial calibration and integration of the motion tracking with the PET reconstruction in a PET/CT setup. Moving phantom and non-human primate (NHP) experiments were performed. The results demonstrate that the SR reconstruction method yields PET images with visibly increased spatial resolution compared to standard static acquisitions, allowing improved visualization of small structures. This chapter presents a promising new approach to PET imaging that could help improve the accuracy and resolution of PET imaging in clinical practice.

In addition to SR, Chapter 6 of the thesis gives additional details and explores other optimization techniques for PET quantification, point spread function (PSF) modeling, projectors, and the kernel method. PSF modeling is a powerful approach to account for the blurring effect inherent in PET images due to the limited spatial resolution. Projectors are responsible for mapping the object space to the projection space and are critical for accurate PET image reconstruction. This chapter compares different projectors, including the single-ray Siddon, multi-ray Siddon, and distance-driven projector, and evaluates their impact on PET image reconstruction. The kernel method is also discussed, which provides an efficient way of incorporating anatomical information to improve PET quantification. This chapter presents an overview of different optimization techniques and their impact on PET quantification and imaging independently of super-resolution.

The second main contribution of this work is explored in Chapter 7, where the issue of off-target binding in PET imaging is addressed. Off-target tracer binding is a problem even with the most promising and widely used tau tracers, such as [ $^{18}\text{F}$ ]MK-6240. Off-target binding occurs in adjacent regions, mostly extra-cerebral, and can significantly hinder the clinical and research utility of [ $^{18}\text{F}$ ]MK-6240. To address this issue, we propose using non-negative matrix factorization to disentangle the contribution of different signals, including the off-target components, to the [ $^{18}\text{F}$ ]MK-6240 PET signal. This technique can automatically target and remove the off-target signal from the PET images, improving the accuracy of specific signal quantification. The effectiveness of NMF is demonstrated through a simulation and real dynamic PET images acquired from cognitively normal and pathological subjects. The results show that NMF can separate tau off-target signals from other sources of signal in the dynamic data, improving the accuracy of tau quantification. This approach could provide new insights into the underlying pathology of neurodegenerative diseases, enabling a more precise and earlier diagnosis.

Finally, Chapter 8 concludes the thesis and gives future perspectives.

# Chapter 1

## Introduction to PET and its clinical applications

This chapter presents the general principles associated with Positron Emission Tomography (PET). After a short history of this imaging technique in Section 1.1, the main physical phenomena related to PET detection are described in Section 1.2. In that same section, we present the different formats representing the raw PET data and the different image reconstruction techniques. We present the different types of data corrections and how we can include them in a reconstruction scheme. In Section 1.3, we present different types of PET scanners. Finally, in Section 1.4, we provide an overview of some clinical applications in neurology with particular attention to Alzheimer's Disease (AD), including its clinical signs, risk factors, and methods of diagnosis.

### **1.1 Historic of PET Imaging**

PET is a type of medical imaging that reveals how the body's organs, tissues, and cells function. It differs from anatomical medical imaging methods like radiography, ultrasound, computed tomography, and standard magnetic resonance imaging, which provide information about the structure and appearance of the body's organs and tissues. PET scans can be combined with these other methods to provide a more complete understanding of the body's functions and structures.

It was in the 1950s that the idea of using short-lived positron emitters for physiological studies was born. The first research-oriented tomographic instruments appeared during the 1950s when the feasibility of a PET scan using two detectors was shown (Sweet, 1951). In 1953, Brownell and Sweet from Massachusetts General Hospital (MGH) published a comprehensive report on using coincidence detection to localize brain tumors (Brownell, 1953). In the 1970s, one of the prototypes of a PET system appeared, developed by Michel Matthew Ter-Pogossian, Edward J. Hoffman and Michael Phelps at the University of Washington (Saint Louis) (Ter-

Pogossian et al., 1975). The first in vivo images followed quickly (Phelps et al., 1975), marking the arrival of PET imaging in the clinical world.

However, the quality of the images obtained remained mediocre, given the low computing power and the lack of development of efficient image reconstruction algorithms. The instrumental and algorithmic improvements of the 1980s led to the appearance of the first whole-body PET system (Dahlbom et al., 1992). In the 1990s and at the start of the 2000s, the first PET systems coupled with a CT scanner (PET-CT) appeared, making it possible to obtain anatomical information at the same time as metabolic information (Townsend, 2008). The 2010s saw the arrival on the market of the first PET systems coupled with MRI imaging (PET-MRI) (Judenhofer et al., 2008).

Today, this diagnostic tool is increasingly used and studied, with the appearance of specific architectures, such as specialized brain PET scanners (van Velden et al., 2009), total body PET scanner (Badawi et al., 2019) or ultra-high resolution PET scanners (Lecomte et al., 2022), allowing more and more accurate diagnostics.

## **1.2 General principles of PET imaging**

PET allows imaging of the spatiotemporal distribution of a radiotracer administered to the patient. The radiotracer is composed of a biologically relevant compound, the probe, to which a specific radionuclide (a positron-emitter) is attached. PET scanners detect pairs of gamma rays produced from electron-positron annihilation by coincidence radionuclides. The radiotracer allows the binding of a compound in the organism at a specific target. It is adapted to a particular biological process studied (for instance, glucose consumption by cancerous cells).

PET is a quantitative medical imaging technique because it can measure the localized amount of radioactivity in absolute units (Bq/mL) with reasonable accuracy and spatial resolution. The quantitative capabilities of PET even go beyond the mere measurement of radiotracer concentration in the body. Indeed, dynamic PET imaging can be used to study the kinetics of radiotracer in the body and to measure specific biological properties of the tissue, such as the perfusion (in milliliters of blood per minute per gram) of tissue or the glucose metabolic rates (in mol per minutes per gram) of tissue.

### **1.2.1 The physics of PET imaging**

Radioisotopes injected into the subject are positron emitters:  $\beta^+$ . Following the disintegration of the radioisotope, the  $\beta^+$  annihilates with an electron after a short course in the tissues (called positron range), thus giving rise to two photons of the same energy, 511 keV, emitted simultaneously, at opposite and almost identical directions.

The detection of these two photons is carried out by a set of detectors arranged in rings within which the patient, animal, or phantom is positioned. These rings are made up of thousands of crystals and are coupled to processing units allowing for the processing of the signal before it is sent to a computer for storing the data and reconstruction. A detected projection (also referred to as an event or coincidence) on a pair of crystals is called a line of response (LOR) (Figure 1.1 in orange).

During the acquisition, the camera records many of those projections, or events, detected for each pair of crystals, as well as specific physical parameters (the arrival time of the two photons, their energy, etc.).

All these projections constitute the measured "raw" signal. The number of coincidences detected in each LOR of the PET scanner is an estimator of the 1-D projection of the radiotracer's distribution along that line.

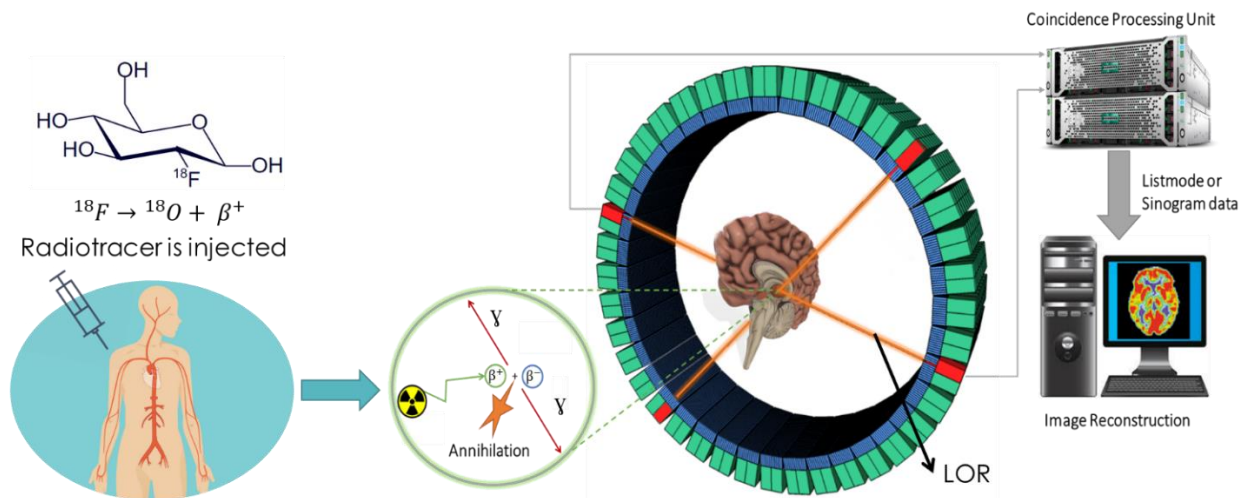


*Figure 1.1 After injecting a specific tracer, radioactive decay within the patient causes a photon pair to be emitted, forming a line of response (in orange) which, when detected by the scanner, is processed as an event by a processing unit.*

PET imaging relies on positron emission. These are emitted by atoms in an unstable state, not found in nature. They are usually produced artificially by cyclotrons or generators. These radioisotopes are partly characterized by their half-life time  $T_{1/2}$ , which corresponds to the time after which half of the radioisotopes of a sample have disintegrated. To be used in the context of nuclear medicine, a positron emitter must meet certain physical constraints. Indeed, its half-life duration  $T_{1/2}$  must be long enough to transport the radiopharmaceutical from the cyclotron to the hospital, its administration and then the observation time of the physiological phenomenon of interest. At the same time, this duration must also be relatively short in order to avoid prolonged irradiation to patients and healthcare personnel. It is also necessary to consider the additional radiation potentially emitted by the isotope: it is preferable to choose



isotopes whose branching ratio (i.e., probability of emission) of the positrons is as high as possible. Finally, the energy of the positrons must be as low as possible in order to minimize their path before annihilation. Table 1.1 summarizes the characteristics of the main isotopes used in PET.

*Table 1.1 Imaging of different physiological processes using different PET tracers.*

<i>Isotope</i>	<i>Radiotracer</i>	<i>Function</i>
$^{18}\text{F}$	$[^{18}\text{F}] - \text{FDG}$	Glucose uptake in heart, lungs, brain, and tumors
	$[^{18}\text{F}] - \text{FMISO}$	Tissue hypoxia
	$[^{18}\text{F}] - \text{FLT}$	DNA replication for tumor cell proliferation
	$[^{18}\text{F}] - \text{AV} - 1451$	Tau accumulation in the brain
$^{11}\text{C}$	$[^{11}\text{C}] - \text{Choline}$	Membrane biosynthesis for tumor cell proliferation
	$[^{11}\text{C}] - \text{PIB}$	$\beta$ -amyloid plaques in the brain
$^{13}\text{N}$	$[^{13}\text{N}] - \text{NH}_3$	Myocardial perfusion
$^{15}\text{O}$	$\text{H}_2[^{15}\text{O}]$	Myocardial and cerebral perfusion

### **Radionuclide decay: positron emission**

A positron-emitting radioisotope  $^A_Z X$  is an isotope rendered unstable by an excess of protons. During the decay process, a proton  $p$  in the nucleus is converted into a neutron  $n$ . A positron  $\beta^+$  and an electron neutrino  $\nu_e$  are then emitted to balance the process:



The  $\beta^+$  emission is not mono-energetic: we observe a continuous energy spectrum of positrons resulting from a random distribution of energy between the positron and the neutrino considered. The highest probabilities then correspond to the fairest energy sharing. The positron is thus emitted with an excess of kinetic energy which allows it to move in the surrounding medium.

### **Positron annihilation**

The positron then travels a short distance through the body while slowing down before it stops and annihilates with an electron. This process releases two gamma rays with an energy of 511 keV each. These gamma rays travel in nearly opposite directions, but they are not perfectly collinear, forming an angle that is slightly different from 180 degrees. This deviation from

collinearity can limit the spatial resolution of PET imaging, as it affects the ability to reconstruct the location of the annihilation event from the path of the gamma rays. In addition, the distance traveled by the positron before it annihilates (called the positron range) introduces uncertainty about the actual location of the tracer in the body, as the image reflects the location of the annihilation event rather than the location of the radioactive decay. For example, the positron range of the  $^{18}\text{F}$  tracer is estimated to be between 0.6 mm and 2.4 mm in water, and the angle between the annihilation photons ranges from  $179.75^\circ$  to  $180.25^\circ$  (Bailey, 2005) (Figure 1.2).

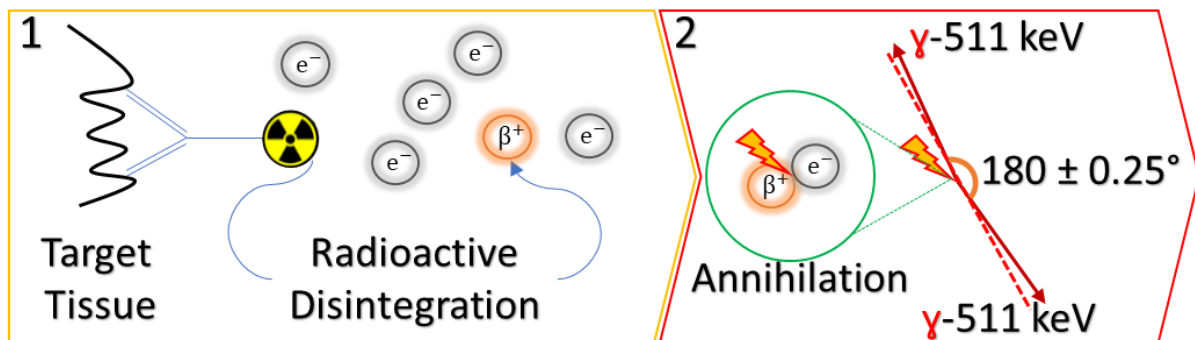


Figure 1.2 Diagram representing the different stages of decay to the generation of  $\gamma$ -511 keV photons: 1) decay and path of the positron until it meets an electron in the middle; 2) positron-electron annihilation and creation of  $\gamma$ -511 keV photons.

### Radiation-matter interactions

As the emitted photons travel through the matter, they undergo three significant types of interactions:

#### Photoelectric effect

This effect corresponds to a total transfer of energy from the  $\gamma$ -511 keV photon to an electron in a deep atomic layer strongly bound to the atom. The photon completely disappears, and the lost kinetic energy is entirely transferred to the electron which is then ejected from the atom. The energy of the incident  $\gamma$  photon  $E_\gamma = h\nu$  (with  $h$  the Planck's constant and  $\nu$  the frequency) totally transferred to the electron contributes in part to countering the binding energy  $E_b$  of this electron, and the excess is recovered in the form of kinetic energy (Figure 1.3).

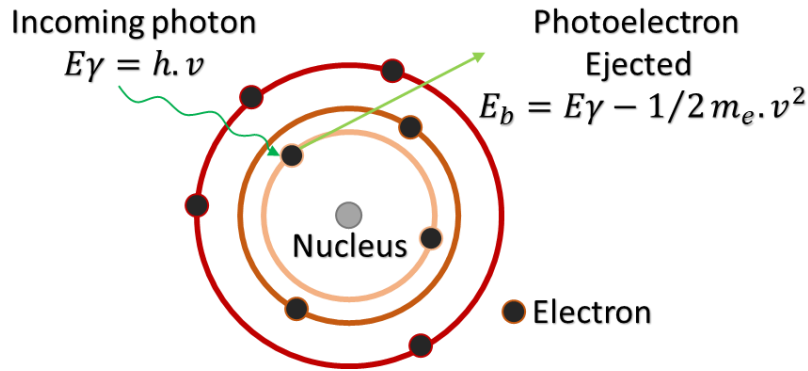


Figure 1.3 Diagram representing the principle of the photoelectric effect and the associated emissions.

#### Compton diffusion

Compton scattering is an incoherent (or inelastic) process, which means that the incident  $\gamma$ -511 keV photon loses energy. During this process, a  $\gamma$  photon interacts with an electron weakly bound to its nucleus (electron of the outer electronic shells) by giving it part of its initial energy  $E\gamma$ . This electron is torn from the procession by carrying an energy  $E_e$ , and a scattered photon is created with an energy  $E_c$  (Figure 1.4 Diagram representing the principle of Compton scattering.).

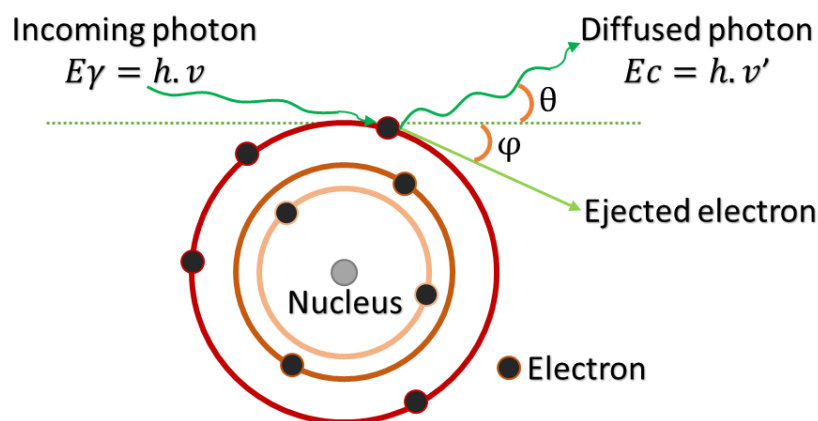
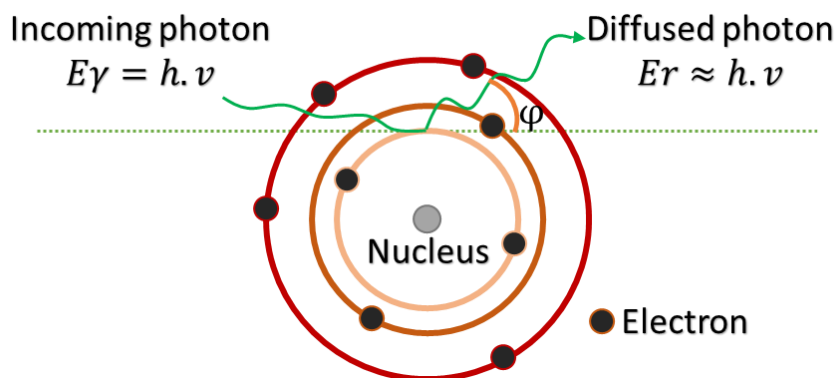


Figure 1.4 Diagram representing the principle of Compton scattering.

#### Rayleigh diffusion

Rayleigh scattering is a coherent (elastic) process, which means that the incident  $\gamma$  photon is deflected without loss of energy. This effect concerns low-energy photons which pass close to electrons strongly bound to the atom (Figure 1.5). In this case, the electron is not ejected from the procession, and the energy transfers to the atom are negligible. This process is rare and can usually be ignored in PET imaging (but not in CT imaging).



*Figure 1.5 Diagram representing the principle of Rayleigh scattering.*

As a result, the photons detected by the PET scanner may display a different energy and direction from what is expected after annihilation. These are known as scattered events.

The attenuation of annihilation photons in the object medium is the main degradation factor of the reconstructed image and is the result of those photon-matter interactions. We will study this effect in more detail in Section 1.2.4 of this chapter.

### **Detection chain**

The function of a PET system is to detect  $\gamma$ -511 keV photons that have left the object medium. The material used at the input of the detection chain must therefore have a strong propensity to stop  $\gamma$  photons with an energy of approximately 511 keV. It is preferable that the  $\mu$ Photoelectric/ $\mu$ Compton ratio is also as high as possible because the photoelectric effect corresponds to a complete local energy deposit, while Compton scattering can lead to multiple interactions with nearby detection elements, resulting in difficulties in localizing the interaction. Indeed, the photoelectric effect corresponds to a complete local energy deposition, while Compton scattering can generate multiple interactions with neighboring detection elements, leading to difficulties in locating the interaction. The other elements of the chain serve to amplify and localize as precisely as possible the place and the energy of interaction. Figure 1.6 illustrates all the elements that make up a conventional detection chain used in PET and that contribute to the optimization of detection.

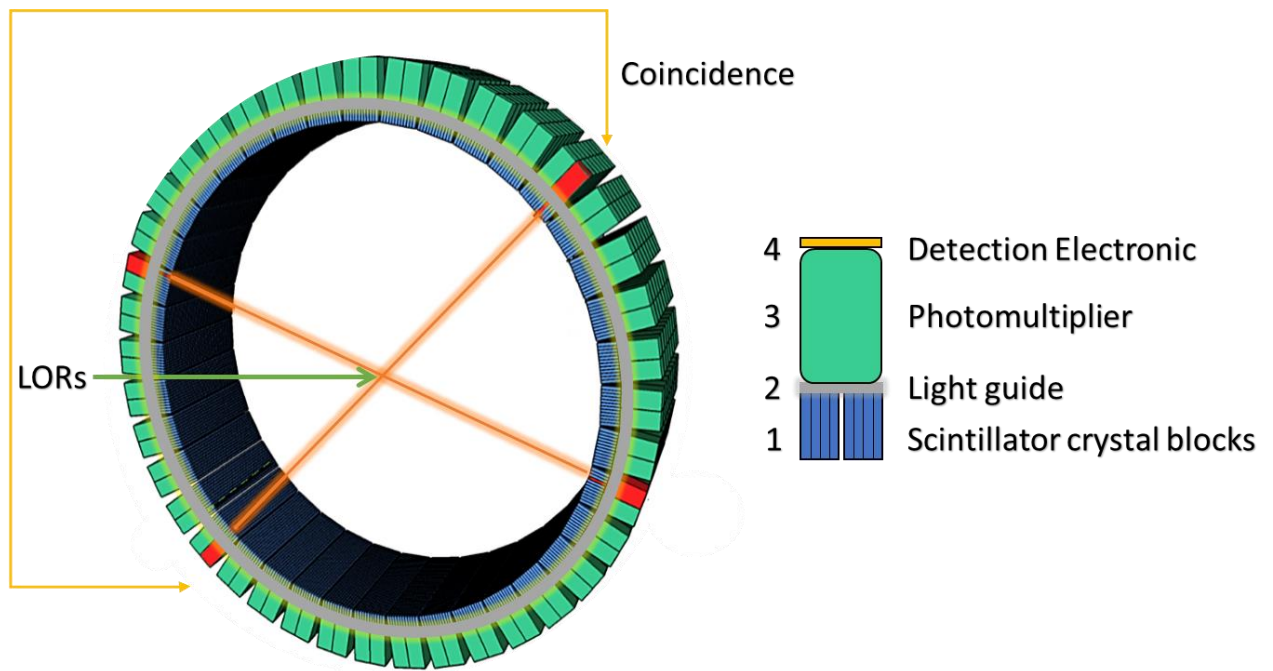


Figure 1.6 Diagram representing a cross-section of the main elements making up the detection chain of a standard PET camera.

#### Detection crystals: scintillator

The first step in the detection chain is therefore the interaction of the  $\gamma$ -511 keV photons with the scintillators (right panel of Figure 1.6). These scintillators have small dimensions and have the function of converting high-energy incident photons into light photons. The wavelengths of these light photons are compatible with the operation of photo multiplier tubes, other elements of the detection chain. The light emission is isotropic and directly proportional to the amount of energy deposited by incident  $\gamma$ -511 keV photons (Knoll, 2010). The shape of a crystal is most often parallelepiped with a square-sectioned entry face and small dimensions (of the order of 1 to 5 mm) compared to its length (greater than 10 mm). These geometric characteristics aim to optimize the detection sensitivity while preserving a good spatial resolution.

Scintillators are mainly characterized by their density  $\rho$  (directly linked to the stopping power of incident  $\gamma$ -511 keV photons), their conversion efficiency  $\eta$  of  $\gamma$ -511 keV photons into light photons, the time  $\tau$  necessary for the emission of light photons after the energy deposition of  $\gamma$ -511 keV photons, the wavelength range of the emitted light and the transparency of the scintillating crystal.

#### Light guide

After interactions within the scintillating crystals, the light signal must be transported to the photomultiplier tubes (PMTs), the next step in the detection chain. An optical guide with a

refractive index closes to that of the crystals is interposed between them and the PMT concerned. The dimensions of this guide are carefully chosen to be adapted to the shape of the PMT input interface.

#### *Photomultiplier tubes*

A photomultiplier tube is a device for detecting photons that comes in the form of an electron tube. Under the action of light, electrons are torn from a metal by photoelectric effect at a photocathode, the weak electric current thus generated is amplified by a series of dynodes using the phenomenon of secondary emission to obtain a significant gain.

#### *Detection electronics*

The analog signal at the output of the PMT is recovered by an electronic module and undergoes various processing steps before being stored for use. A first selection is applied in order to eliminate incident photons with low energy. This makes it possible to remove the photons coming from surrounding radiation and the annihilation photons having strongly diffused and therefore with energies much lower than 511 keV. Following the energy discrimination, the remaining analog signal is converted into a digital signal, in order to be stored and processed. A calculation of the energy and position of the incident photon follows. Finally comes the coincidence of events.

The first step consists in applying a new energy window with a low threshold and a high threshold to eliminate the maximum of scattered photons and high energy photons. The high threshold also makes it possible to eliminate "pile-up" effects during which several photons deposit energy almost simultaneously in the same block of crystals, leading to a detection greater than 511 keV. Each of the  $\gamma$ -photons thus discriminated is called a single event. The temporal coincidence then consists in matching the detected  $\gamma$ -photons. When a photon (1st single event) is recorded by the system, a time window of a few nanoseconds is opened. If a photon is detected in this time interval (2nd simple event), it is the second photon linked to the annihilation, and a coincidence is thus recorded within the LOR associated with the pair of involved crystals. Some PET systems have sufficient temporal resolutions to estimate the location of the annihilation site on the LOR as a probabilistic function of the detection time difference between the two photons. Systems with this technology are called time-of-flight PET (Mullani et al., 1980). However, the localization remains imprecise and does not currently make it possible to avoid an image reconstruction step.

### **1.2.2 Data acquisition**

When collecting the projections during an acquisition, the data can be stored in two different formats.

## Sinogram

The standard way of storing and structuring the PET data is the sinogram. Sinograms are multi-dimensional arrays in which a given data bin is specific to a LOR and each data bin contains the number of coincidence events detected in that LOR. Each data entry in a sinogram is a 1-D projection, i.e., an estimator of the line integral of the radiotracer's distribution along that LOR.

The sinogram data format corresponds to a histogram of the orientations and distance from the center of the scanner of the different LORs (Figure 1.7).

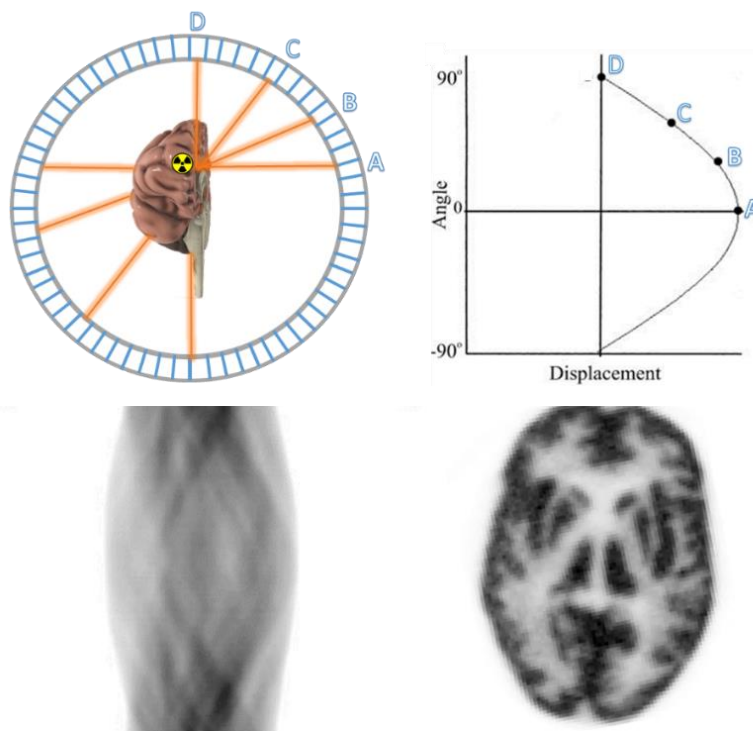


*Figure 1.7 The sinogram data format corresponds to a histogram of the orientations and distance from the center of the scanner of the different LORs.*

As the events are represented as a histogram in a fixed-sized 3D array, this allows for the computation of PET images without regard to the number of recorded events, but the disadvantage is that it does not retain physical information about individual detected events, including energy and time of arrival.

## Listmode data

In list-mode data acquisition for PET imaging, coincidences are recorded and stored sequentially in the order in which they occur, without grouping them together. This results in a list-mode file with a variable size that grows with the number of detected coincidences. The temporal information of the detected events is hence available which is crucial in certain applications, such as when the structures being imaged are in motion. This allows the data to

be synchronized with the position of the moving organs. For example, in cardiac imaging, the motion of the heart can be tracked using the temporal information of the detected events. Additionally, list-mode data allows for the reconstruction of images with a temporal dimension, which can be useful for dynamic imaging applications.

### 1.2.3 Image reconstruction

As previously mentioned, the number of coincidences detected in each LOR of a PET scanner can be used as an estimator of the one-dimensional projection of the radiotracer's distribution along that particular line. The goal of an image reconstruction algorithm is to estimate the radiotracer's spatial distribution in the FOV from these multiple 1-D projections.

The process of reconstructing an image from PET data falls within the mathematical category of inverse problem solving, where we attempt to determine a regularly sampled (voxel) representation of the object that was scanned by inverting the data acquisition process. The mathematical description of inverting projection data to create an image was formulated by J. Radon in 1917 and is known as a Radon transform (translated from German in Radon, 1986).

#### Analytical reconstruction

The 2D Radon transform can be defined as follows: consider a continuous function of two variables  $f$  on  $\mathbb{R}^2$ ; it is typically a density defined in the plane  $(X, Y)$ . Consider a line  $L$  in this plane and a vector  $v = (x, y)$ . The Radon transform of this line is the integral along the line:

$$Rf[L] = \int_L f(x, y) |dv| \quad (1.2)$$

Hence, we have:

$$Rf[L] = \int_L f(x, y) \sqrt{dx^2 + dy^2} \quad (1.3)$$

The line  $L$  can be characterized by polar parameters  $(u, \theta)$  where  $u$  is the distance of the line from the origin of the reference frame and  $\theta$  is the angle that the line's perpendicular makes with the  $X$ -axis. The coordinates  $(x, y)$  of the points on this line verify the equation:

$$u = x \cdot \cos(\theta) + y \cdot \sin(\theta) \quad \forall u \in \mathbb{R}^2, \theta \in [0, \pi] \quad (1.4)$$

According to this definition,  $L$  can be parametrized with respect to arc length  $v$ :

$$\begin{cases} x(v) = v \cdot \sin(\theta) + u \cdot \cos(\theta) \\ y(v) = -v \cdot \cos(\theta) + u \cdot \sin(\theta) \end{cases} \quad (1.5)$$



Thus, the line integral can be written in terms of the parametric equations (1.5), and we have:

$$R[f](u, \theta) = \int_{-\infty}^{+\infty} f((v \cdot \sin(\theta) + u \cdot \cos(\theta)), (v \cdot \sin(\theta) + u \cdot \cos(\theta))) dv \quad (1.6)$$

If  $p(u, \theta)$  are 1D projections for all directions, then we have  $R[f](u, \theta) = p(u, \theta)$ . The tomographic reconstruction problem then consists in inverting the Radon transform to obtain the activity distribution  $f$  at each point  $(x, y)$  from the set of measurements  $p(u, \theta)$ , for  $u$  in  $\mathbb{R}^2$  and  $\theta$  in  $[0, \pi]$ :

$$f(x, y) = R^{-1}[p](x, y) \quad (1.7)$$

The process of inverting the Radon transform is an ill-posed inverse problem, meaning that we have measurements and must determine the source of those measurements. This type of problem is considered ill-posed because the solution (the original image) does not always exist, can be non-unique or does not depend continuously on the data (the projections), meaning that a small difference in the projections can lead to significantly different reconstructed images (Bertero and Boccacci, 1998).

It is theoretically only possible to exactly invert the Radon transform for an infinite number of projections, as it is defined for continuous functions. However, in PET imaging, the number of LORs is finite, meaning that the projections are sampled, and the solution is not unique. Additionally, the acquired projections are inherently noisy and do not contain precise information about the distribution of the radiotracer, leading to an inexact reconstruction of the activity.

There are thus two basic approaches to tackle the reconstruction of images: the first which directly exploits the measurements of the projections  $p(u, \theta)$  by seeking to analytically invert the Radon transform, and the second which considers the problem in its iterative form. These two approaches are discussed below.

### **Filtered back-projection**

Reconstruction can be achieved by tracing each LOR corresponding to a list-mode event through that image and incrementing each voxel through which it passes. This process is called backprojection. This corresponds to simply estimating the activity distribution  $f(x, y)$ , by back projecting the projections  $p(u, \theta)$  onto all the angles  $\theta$ . Such a reconstruction suffers from severe artifacts such as blurring which can be corrected for, in Fourier space, by using an appropriate filter. Theoretically, the "ramp" filter aims at decreasing low frequencies causing blur in the final image, but it is not practical to use in practice, and a more practical filter such as the Ram-Lak filter, the Shepp-Logan filter, the cosine filter or the Hamming filter is often used instead. A reconstruction of this form is called filtered backprojection (FBP) (Basu and

Bresler, 2000). FBP is an analytical reconstruction, meaning that it solves the inverse problem directly, in a single step. FBP is a very quick reconstruction, but it assumes certain ideal characteristics of data acquisition and can suffer from artefacts in some cases.

### **Iterative reconstruction**

Iterative reconstruction techniques offer improvements over analytical reconstruction methods because they allow for a more accurate modeling of the system geometry and can take into account the specific noise structure of the projection data. Essentially, the goal of an iterative reconstruction algorithm is to iteratively apply corrections to an initial, arbitrary radiotracer distribution to make it as close as possible to the measured data. While this iterative process can result in a potentially more accurate estimate than analytical reconstruction techniques, it also requires more computational resources. However, advances in computation speed and the development of faster algorithms (such as OSEM, described in 1.2.3) have helped to alleviate the computational burden of iterative methods, making them the standard for clinical use.

#### *Data, image, and system modeling*

Most statistical iterative reconstruction algorithms in PET are based on the maximum likelihood (ML) estimation technique. Typically, a statistical model is chosen to model the measured dataset and the ML estimation provides estimates of the model parameters.

The PET data can be represented by a column-vector  $\mathbf{y} \in \mathbb{R}^I$  of size  $I$  containing the measured coincidences events in each LOR  $i$ . For each LOR, it is assumed that the PET scanner measures one realization of the random variable  $y_i$ , where  $y_i$  is the number of coincidences detected along LOR  $i \in [1 \dots I]$ . In most statistical iterative PET reconstruction algorithms, each element  $y_i$  of  $\mathbf{y}$  follows a Poisson distribution parameterized by its mean  $\bar{y}_i$ .

We can represent a discretized PET image by a column vector  $\boldsymbol{\rho} \in \mathbb{R}^J$  of size  $J \in \mathbb{N}$  which contains the radiotracer concentration  $\rho_j$  in each voxel  $j \in [1, \dots, J]$ .

Then, the forward PET model relates the expected PET data  $\bar{\mathbf{y}}$  to the image  $\boldsymbol{\rho}$  and is formulated as:

$$\bar{\mathbf{y}} = \mathbf{P}\boldsymbol{\rho} \quad (1.8)$$

where  $\mathbf{P}$  is a matrix of size  $I \times J$  called the “system matrix” which relates the image to the data and thus models the PET coincidence detection process. Each individual elements  $p_{i,j}$  of the system matrix is the probability of a positron emission occurring in voxel  $j$  to be detected in LOR  $i$ . The simplest approach consists in approximating each probability  $p_{i,j}$  by the portion of the line joining the center of the surfaces of the two crystals (LOR  $i$ ) going through pixel (Figure 1.8). This is often referred to as the “geometric” probability or geometric component

of the system matrix. The crystal center of mass or another point at any depth inside the crystal can be used rather than the crystal surface centers. More advanced and accurate models can be used to compute the system matrix elements, as we will see later in this thesis. Also, since this matrix has huge dimensions ( $I \times J$  elements) the system matrix is not stored, in practice, but computed on-the-fly during the reconstruction process.

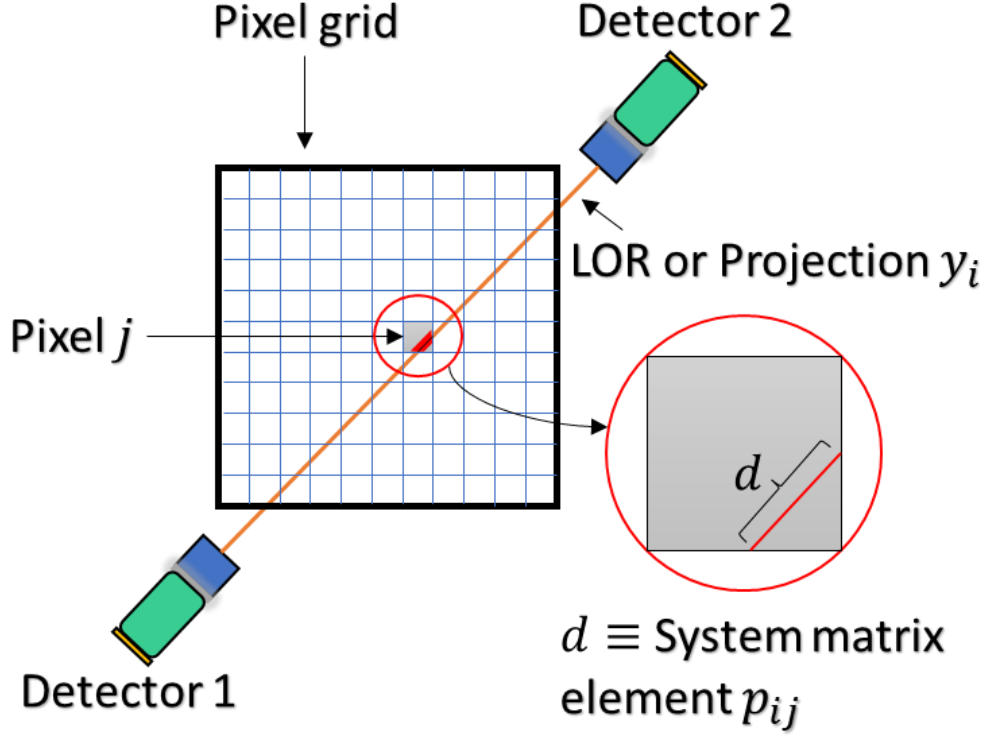


Figure 1.8 Illustration of a single geometric element of the system matrix.

Hence, the likelihood function can be written as:

$$\Pr(\mathbf{y}|\boldsymbol{\rho}) = \prod_{i=1}^I e^{-(\mathbf{P}\boldsymbol{\rho})_i} \frac{(\mathbf{P}\boldsymbol{\rho})_i^{y_i}}{y_i!} \quad (1.9)$$

Consequently, one can rewrite the ML estimation problem as:

$$\boldsymbol{\rho}_{ML} = \operatorname{argmax}_{\boldsymbol{\rho}} \Pr(\mathbf{y}|\boldsymbol{\rho}) \quad (1.10)$$

Iterative reconstruction algorithms based on the ML estimation method thus consist in estimating the image which maximizes the data likelihood function  $\Pr(\mathbf{y}|\boldsymbol{\rho})$ . The likelihood function can be seen as a cost function that needs to be optimized to reach the image maximum likelihood estimate. Maximum likelihood estimators are advantageous because they offer unbiased, minimum variance estimates as the number of measurements increases towards infinity. This means that, as the number of measurements or projections becomes large, the expected value of the image estimate approaches the true image.

*Maximum Likelihood Expectation Maximization algorithm*

The Maximum Likelihood Expectation Maximization (MLEM) algorithm has been proposed by Dempster and colleagues (Dempster et al., 1977) and used in PET for the first time by Shepp and Vardi (Shepp and Vardi, 1982). The cost function used in the MLEM algorithm is based on the logarithm of the likelihood function:

$$\ln[\Pr(\mathbf{y}|\boldsymbol{\rho})] = \ln \left[ \prod_{i=1}^I e^{-(P\boldsymbol{\rho})_i} \frac{(P\boldsymbol{\rho})_i^{y_i}}{y_i!} \right] \quad (1.11)$$

$$\Leftrightarrow \ln[\Pr(\mathbf{y}|\boldsymbol{\rho})] = \sum_{i=1}^I [- (P\boldsymbol{\rho})_i + y_i \ln ((P\boldsymbol{\rho})_i - \ln (y_i!))] \quad (1.12)$$

To find the maximum of this function, the partial derivatives with respect to each unknown  $\rho_j$  must be equal to 0:

$$\frac{\partial \ln[\Pr(\mathbf{y}|\boldsymbol{\rho})]}{\partial \rho_j} = \sum_{i=1}^I [-p_{i,j} + y_i \frac{p_{i,j}}{(P\boldsymbol{\rho})_i}] = 0, j = 1 \dots J \quad (1.13)$$

$$\Leftrightarrow \frac{1}{\sum_{i=1}^I p_{i,j}} \sum_{i=1}^I p_{i,j} \frac{y_i}{(P\boldsymbol{\rho})_i} = 1 \quad (1.14)$$

$$\Leftrightarrow \rho_j = \frac{\rho_j}{\sum_{i=1}^I p_{i,j}} \sum_{i=1}^I p_{i,j} \frac{y_i}{(P\boldsymbol{\rho})_i} \quad (1.15)$$

Replacing  $\rho_j$  by a series of image estimates  $\hat{\rho}_j^{it}$  at each iteration  $it$ , the iterative MLEM algorithm is given by:

$$\hat{\rho}_j^{it+1} = \frac{\hat{\rho}_j^{it}}{\sum_{i=1}^I p_{i,j}} \sum_{i=1}^I p_{i,j} \frac{y_i}{\sum_{j=1}^J p_{i,j} \hat{\rho}_j^{it}} \quad (1.16)$$

Equation (1.16) indicates that if the initial estimate is strictly positive, all subsequent image estimates will also be positive. Moreover, Shepp and Vardi (Shepp and Vardi, 1982) have proven the convergence of this algorithm towards an image estimate in the maximum likelihood sense, when the number of iterations approaches infinity.

Note that the first denominator in Equation (1.16) corresponds to the sum of all the LORs contributions in voxel  $j$ . An image of all these values will represent the spatial distribution of the probabilities of an annihilation originating in voxel being detected in any LOR of the PET camera. This image is called the sensitivity image.

The forward-projection operation of the image estimate along LOR  $i$  noted  $FP(\boldsymbol{\rho})_i$  is represented by the right-most denominator of Equation (1.16). Replacing  $\rho_j$  by a series of image estimates  $\hat{\rho}_j^{it}$  at each iteration it, the iterative MLEM algorithm is given by:

$$FP(\boldsymbol{\rho})_i = \sum_{j=1}^J p_{i,j} \rho_j = (\mathbf{P}\boldsymbol{\rho})_i \quad (1.17)$$

The back-projection operation evaluated in voxel  $j$ , noted  $BP_j$  is given by:

$$BP_j = \sum_{i=1}^I p_{i,j} y_i = (\mathbf{P}^T \mathbf{y})_j \quad (1.18)$$

MLEM can schematically (Figure 1.9) be summarized as follow: The MLEM algorithm consists in carrying out a first series of operations of projection of the matrix elements on the image voxels, in comparing these projection values obtained with the measured projections and then in calculating the back-projection operations. Then the whole is divided by the so-called sensitivity term. The sensitivity term  $S_j = \sum_{i=1}^I p_{i,j}$  associated with each image voxel represents the probability that a decay taking place in voxel  $j$  will be detected, whatever the associated LOR  $i$ .

Finally, the result associated with all these successive operations, called the correction term, is applied to the estimate of the image  $\hat{\rho}^{it}$  at the previous iteration  $it$  to obtain the estimate of the image  $\hat{\rho}^{it+1}$  at the current iteration  $it+1$ , for the set of voxels.

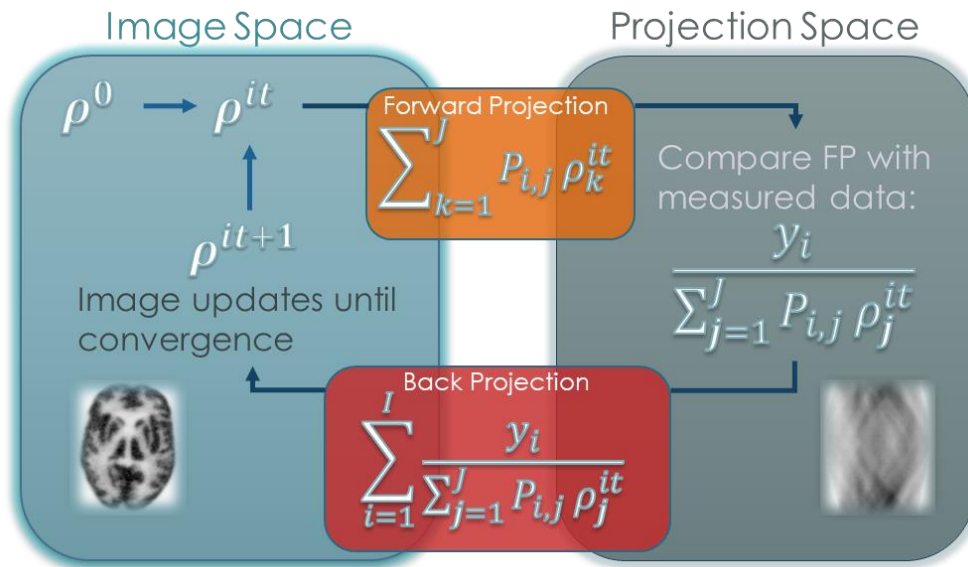


Figure 1.9 The different steps of the iterative process of the MLEM algorithm, in the image space and in the projection space (here represented by a sinogram).

The initial image, which must not contain zero elements, is generally chosen as a unit matrix. It is also possible to initialize MLEM from an image reconstructed with a faster algorithm, such as FBP, which will give as initial image an estimate closer to the real distribution. In this case, only the convergence speed of MLEM is modified.

The MLEM algorithm has the following properties:

- the total number of events returned at each iteration is kept,
- the algorithm converges slowly, especially for cold regions,
- the likelihood maximization criterion introduces noise into the images. The variance of the estimated image increases as the algorithm approaches the solution.

#### *Ordered Subsets Expectation Maximization algorithm*

The Ordered Subsets Expectation Maximization (OSEM) algorithm has been introduced by Hudson and Larkin (Hudson and Larkin, 1994) in order to accelerate the convergence of the reconstruction and make statistical iterative reconstruction methods more practical to routine applications. The cost function to maximize in OSEM is the same as the one used for MLEM in Equation (1.16) but introduces sub-steps in the computation of one iteration of MLEM. To do so, the projection data are decomposed into a number of subsets, each containing a certain portion of LORs. Subsets generally group together the LORs according to their azimuthal angle.

The basic principle behind this sub-division of the data space is that each subset should contain information covering all parts of the image to reconstruct. The OSEM algorithm iterative reconstruction loop is then given by:

$$\hat{\rho}_j^{it,s+1} = \frac{\hat{\rho}_j^{it,s}}{\sum_{i \in S} p_{i,j}} \sum_{i \in S} p_{i,j} \frac{y_i}{\sum_{j=1}^J p_{i,j} \hat{\rho}_j^{it,s}} \quad \text{if } s \in [0, (N_s - 1)[ \quad (1.19)$$

$$\hat{\rho}_j^{s+1,1} = \frac{\hat{\rho}_j^{it,s}}{\sum_{i \in S} p_{i,j}} \sum_{i \in S} p_{i,j} \frac{y_i}{\sum_{j=1}^J p_{i,j} \hat{\rho}_j^{it,s}} \quad \text{if } s = (N_s - 1) \quad (1.20)$$

with  $S$  the considered subset among the  $N_s$  defined subsets. This algorithm assumes that all separately reconstructed subsets lead to close solutions. The MLEM algorithm is first applied only to the LORs of the first subset. The next subset is then used to update the estimate, and so on until the next iteration. A complete OSEM iteration is defined by applying MLEM to all sets.

Unlike MLEM, it is impossible to prove that this algorithm converges. However, if the definition of the subsets as well as their number are rigorously chosen, it leads to a solution close to that obtained by MLEM and all the more quickly as there are  $N_S$  subsets. In this case, the OSEM solution after  $N_i$  iterations exploiting  $N_S$  subsets is very close to the MLEM solution after  $N_i \times N_S$  iterations. Also note that for a single subset, OSEM is strictly equivalent to MLEM.

#### *List-mode reconstruction*

The MLEM and OSEM algorithms can be also used to directly reconstruct list-mode data without rebinning the data into a sinogram.

Noting the measured list-mode data as  $\mathbf{y} = (i_1, \dots, i_M)^T$ , where  $i_m$  is the LOR in which event has been detected and  $M$  is the total number of coincidence events detected during the acquisition, the list-mode MLEM algorithm iterative reconstruction loop is given by:

$$\hat{\rho}_j^{it+1} = \frac{\hat{\rho}_j^{it}}{\sum_{i=1}^I p_{i,j}} \sum_{m=1}^M p_{i_m j} \frac{1}{\sum_{j=1}^J p_{i_m j} \hat{\rho}_j^{it}} \quad (1.21)$$

We can note that the iterative loop given by Equation (1.21) is very similar to the one given for the sinogram format in Equation (1.16), except that the main summation is now looping over the number of coincidences in the list-mode file rather than the LORs or sinogram bins. In particular, the forward-projection and sensitivity map calculation steps are similar to both list-mode and sinogram formats. The list-mode based MLEM algorithm is exactly equivalent to the reconstruction of a non-compressed sinogram containing the events stored in the list-mode file. For the list-mode format, the subsets used for the OSEM algorithm are defined as temporal subdivisions of the acquired data (Reader et al., 1998): for a data acquisition time  $T$ , the subset  $s$  contains the coincidences that have been stored between the times  $(s - 1)T/S$  and  $sT/S$  where  $S$  is the total number of subsets.

### **1.2.4 Data corrections**

This part exposes the classic methods of correction of specific physical effects degrading the reconstructed image among those previously described, and compatible with statistical reconstruction algorithms. Indeed, the too simplistic modeling of the system matrix does not make it possible to directly restore with precision the distribution of activity  $\rho$ . Corrections before, during, or after reconstruction are therefore necessary for better quantification.

### **Normalization**

To correct the non-uniform response of detection crystals in a PET detection system when subjected to a uniform photon flux, the most effective solution is to irradiate all the crystals uniformly. This can be achieved by using a uniform radioactive cylinder in the center of the field of view or by using a planar radioactive source parallel to the system axis and perpendicular to its radius and rotating it. This process, known as blank acquisition, is typically performed for several hours to record a large number of coincidences and decrease the statistical variance of detection. For each LOR  $i$ , the number of coincidences detected  $y_i$  at the end of the acquisition is recorded, and the average number of coincidences per LOR  $\bar{y}$  is determined from all the measurements. As each LOR should detect the same number of coincidences, defined here by  $\bar{y}$ , a multiplicative correction factor  $N(y_i) = \bar{y}/y_i$  is calculated for all the LORs.

The normalization factors can be applied directly to the measurements (before reconstruction). We have:  $y_i^* = y_i \times N(y_i)$ , with  $y_i^*$  the corrected projection  $i$ . The MLEM algorithm is then applied on  $y_i^*$  and not on  $y_i$ .

However, changing the  $y_i$  measured data destroys their Poissonian nature. We then prefer to weight the effect of normalization on the sensitivity factor (Michel et al., 1998) and apply the MLEM algorithm on the raw data  $y_i$  in order to preserve as much as possible the statistical properties of the data.

### **Randoms correction**

Random events, usually called randoms, can add noise to the data and lead to an overestimation of activity if not accounted for. The number of random coincidences in a given line of response (LOR) is closely related to the rate of true events detected by each detector forming the LOR. These random coincidences occur through two independent processes involving the emission and propagation of two photons. The average rate of randoms increases with the square of the activity in the field of view (FOV). As a result, the errors caused by randoms increase more quickly than the activity. There are two main methods for correcting for randoms: the singles-based method and the delayed coincidence window method.

The singles-based method involves measuring the average rate of singles in each detector during the acquisition. The integral of the randoms rate over the total acquisition time allows for the estimation of a randoms sinogram. However, this method does not consider defects in the coincidence detection chain, such as dead times and multiple coincidence processing, and may therefore overestimate the number of randoms.



The delayed coincidence window technique is a hardware-based method that directly measures the random coincidences in each LOR. It uses a coincidence window that is delayed by a time significantly longer than the usual coincidence timing window so that any coincidences acquired in the delayed window are necessarily randoms. Since the occurrence of random coincidences is stationary in time (assuming that the activity distribution in the FOV is stationary), these intentionally created random coincidences provide an unbiased estimate of the true distribution of randoms. The main advantage of this method over the singles-based technique is that the estimated distribution does take into account the defects in the coincidence detection and processing chain in the same way as true coincidences do.

### Attenuation correction

The attenuation of annihilation photons in the object medium is considered to be the main degradation factor of the reconstructed image (Montandon and Zaidi, 2005). The attenuation effect results in a loss of sensitivity that is all the greater, the deeper the source is. The impact of this non-uniform information loss depends largely on the object's size to be imaged. One or both 511-keV photons may be absorbed or scattered in the patient's body by photoelectric or Compton scattering effects before even reaching the detectors. Attenuation correction consists of accounting for this phenomenon by calculating the probabilities of photons absorption inside the object.

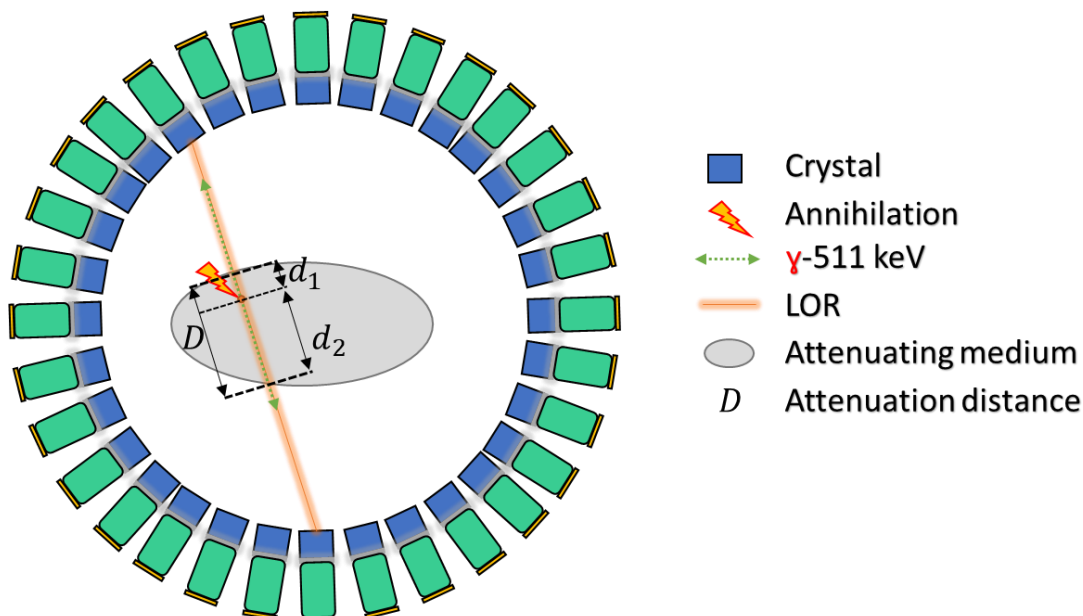


Figure 1.10 Diagram representing the phenomenon of attenuation in a uniform medium.

Consider an object of uniform density (for example, water) as in Figure 1.10. The first annihilation photon travels the distance  $d_1$  in the object before leaving it, then it is detected.

Similarly, the second annihilation photon travels the distance  $d_2$ . The absorption of  $\gamma$ -511 keV photons follows an exponential law and can be expressed as:

$$I(x) = I(0) \exp\left(-\int_0^x \mu(511\text{keV}, x) dx\right) \quad (1.22)$$

with  $\mu(511\text{keV}, x)$  ( $\text{cm}^{-1}$ ) the linear attenuation coefficient of the medium at 511 keV,  $I(x)$  the intensity of the photon flux leaving the object and  $I(0)$  the initial intensity from the source. The detection probability of each annihilation photon is proportional to the transmission probability  $I(x)/I(0)$ . We thus find, for each of the two photons, the following probabilities  $P1$  and  $P2$ :

$$P1 = \exp(-\mu \times d_1), \quad P2 = \exp(-\mu \times d_2) \quad (1.23)$$

The total probability of detection  $P$  of the LOR is therefore given by the relationship:

$$P = P1 \times P2 = \exp(-\mu \times D) \quad (1.24)$$

with  $D = d_1 + d_2$ .

It is important to note that the probability of detection does not depend on the specific location of the annihilation along the LOR, but only on the length of the LOR. This remains true in any medium, including heterogeneous ones, as long as the appropriate linear attenuation coefficients are used. This property allows for the correction of attenuation effects without any prior knowledge of the radioactive source distribution, as only the density map of the medium is needed. Attenuation correction factors (ACFs) are typically obtained using a transmission scan with a rotating source and a CT scanner for standalone PET and PET-CT systems, respectively. Many PET scanners are now combined with a CT scanner. The CT image provides a measure of the linear attenuation coefficients of tissues, so the sinogram of ACFs can be derived by forward projecting the CT image along the LORs of the PET scanner. However, the CT measurements are taken over a range of energies from 40 to 140 keV, so a conversion to the 511 keV energy used in PET is necessary. This conversion is usually performed using an approximate bilinear transformation based on the attenuation of water and cortical bone at the CT and PET energies (Burger et al., 2002).

### **Scatter correction**

The scattering of annihilation photons within the object medium can lead to the detection of scattered coincidences, which is mainly due to Compton scattering. This process causes a change in direction and a decrease in energy of the scattered photon. While some photons lose enough energy to be discriminated against by the detection chain, most are recorded due to the

mediocre energy resolutions of current PET systems (between 10% and 20%). The proportion of detected scattered coincidences in clinical 3D PET is estimated to exceed 50% of the total number of coincidences. In the reconstructed images, this effect results in reduced contrasts and spatial resolution, increased noise, and detections outside the field of view. This effect is one of the most challenging to correct in PET because there is no theoretical formulation of its distribution without prior knowledge of the activity localization.

The main approaches to scatter correction are the multiple energy window technique, and model-based analytical scatter simulation, such as the single scatter simulation technique (SSS) (Watson et al., 1996).

### **Incorporation of data corrections in the reconstruction**

The degrading effects described in the previous section can be divided into multiplicative effects and additive effects (Kadrmas, 2004). Multiplicative effects, such as detector sensitivity and attenuation, generally cause a scaling or sensitivity change for each LOR. Additive effects, including random and scattered coincidences, introduce low-spatial-frequency (i.e., relatively uniform) backgrounds on top of the useful signal. One approach to compensate for these effects in PET data is to pre-correct the raw data (i.e., the detected number of coincidences in each LOR) and then perform an iterative reconstruction of the pre-corrected data. For example, estimates of the random and scattered coincidence distributions can be subtracted from the sinogram of prompt coincidences. The resulting sinogram can then be multiplied by the normalization coefficients (NC) and attenuation correction factors and reconstructed.

However, as mentioned in Section 1.2.4, the application of these pre-correction steps destroys the Poisson nature of the data. Since maximum likelihood reconstruction methods require that the PET data being reconstructed have exact Poisson statistics, the MLEM reconstruction of such pre-corrected data converges towards a biased solution. A more accurate solution is to incorporate the corrections into the iterative reconstruction process rather than applying them as pre-corrections. This preserves the Poisson statistical distribution of the raw PET data and allows for more precise modeling of the data formation process by incorporating corrective terms into the system matrix and forward PET model. Additive effects are modeled in the description of prompt coincidences, while multiplicative effects are directly modeled in the PET system matrix.

Hereinafter, we denote by  $T_i$ ,  $S_i$  and  $R_i$  the number of true, random and scattered coincidences detected in LOR  $i$ , respectively. One can express the measured PET raw data  $y_i$  as:

$$y_i = T_i + S_i + R_i \quad (1.25)$$

We can write:

$$\bar{y}_l = \bar{T}_l + \bar{S}_l + \bar{R}_l = (\mathbf{P}\boldsymbol{\rho})_i + \bar{S}_l + \bar{R}_l \quad (1.26)$$

where  $T_i$ ,  $S_i$  and  $R_i$  are independent Poisson variables.

Corrections for multiplicative effects are incorporated inside the PET system matrix according to the following basic factorization (Qi et al., 1998):

$$\mathbf{P} = \mathbf{NAG} \quad (1.27)$$

where  $\mathbf{N} \in \mathbb{R}^{I \times I}$  is a diagonal matrix containing the NCs of each LOR,  $\mathbf{A}$  is a diagonal matrix containing the ACFs of each LOR and  $\mathbf{G}$  is a matrix whose elements are the geometric probability that a coincidence detected in LOR has been emitted in a voxel in the object. The corresponding log-likelihood-function is similar to the one given in Equation (1.12) and expressed as:

$$\ln[\Pr(\mathbf{y}|\boldsymbol{\rho})] = \sum_{i=1}^I [-(\mathbf{P}\boldsymbol{\rho})_i + \bar{S}_l + \bar{R}_l + y_i \ln ((\mathbf{P}\boldsymbol{\rho})_i + \bar{S}_l + \bar{R}_l - \ln (y_i!))] \quad (1.28)$$

Using expectation maximization, we get the MLEM /OSEM iterative algorithm:

$$\hat{\rho}_j^{it+1} = \frac{\hat{\rho}_j^{it}}{\sum_{i=1}^I p_{i,j}} \sum_{i=1}^I p_{i,j} \frac{y_i}{\sum_{j=1}^J p_{i,j} \hat{\rho}_j^{it} + \bar{S}_l + \bar{R}_l} \quad (1.29)$$

We will discuss later in this manuscript additional corrections that we can include in this formulation, such as point spread function and motion.

## 1.3 Different implementations of PET scanners

### 1.3.1 Combined PET-Computed Tomography

Standalone PET imaging lacks information about the anatomical location of the measured physiological processes, which limits its diagnostic usefulness (Shreve, 2000). In many cases, accurate anatomical information is essential for localizing the PET signal within the body. As a result, it is now widely accepted that PET should be combined with an anatomical imaging modality, such as CT, to maximize its potential.

To enable the "hardware fusion" of PET and CT data, Townsend and colleagues proposed combining PET and CT scanners in a single machine in the early 1990s (Townsend et al., 1993). The integration of PET and CT in one system is relatively simple technically. Most commercial PET-CT scanners consist of mostly unmodified standalone PET and CT scanners mounted in a common gantry and with a single patient bed (Figure 1.11). The bed can shuttle

between the two gantries, and the CT and PET exams are performed sequentially. Spatially registered CT and PET data are obtained under the assumption that the patient does not move between the two acquisitions. In addition to the clinical value, CT images can be used to generate the 511-keV photon linear attenuation correction factors, eliminating the need for time-consuming PET transmission scans (Kinahan et al., 1998) and improving patient throughput.

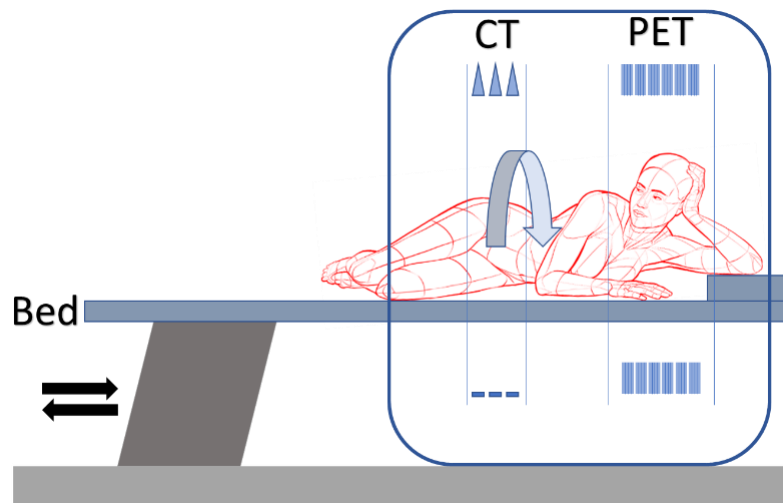


*Figure 1.11 Design of a sequential PET-CT scanner. CT is positioned in front of the PET. The bed moves back and forth between the two modalities.*

### **1.3.2 Simultaneous PET-MR**

Simultaneous PET-MR scanners, first developed in the early 2010s, allow for the simultaneous use of PET and MR scans (Figure 1.12), unlike PET/CT scanners which use the modalities sequentially (Hammer et al., 1994). However, integrating PET and MRI is more challenging than integrating PET and CT in PET-CT scanners due to the interference between the two systems (Bai et al., 2013). There are several advantages to using PET-MR scanners, including the ability to provide higher soft tissue contrast with MRI, the ability to provide additional functional information through techniques like perfusion and diffusion MRI, and the absence of ionizing radiation in MRI (Ouyang et al., 2013a). This makes PET-MR scanners especially useful for pediatric patients and reduces total radiation exposure. The Lorentz force from the main magnetic field of an MRI scanner can also reduce the positron range in PET-MR scanners, which can improve the quality of the PET data (Hammer et al., 1994). The simultaneous acquisition of PET and MRI data in PET-MR scanners also allows for better registration of the two datasets in both spatial and temporal domains, which can further improve PET image quality (Bai et al., 2013).

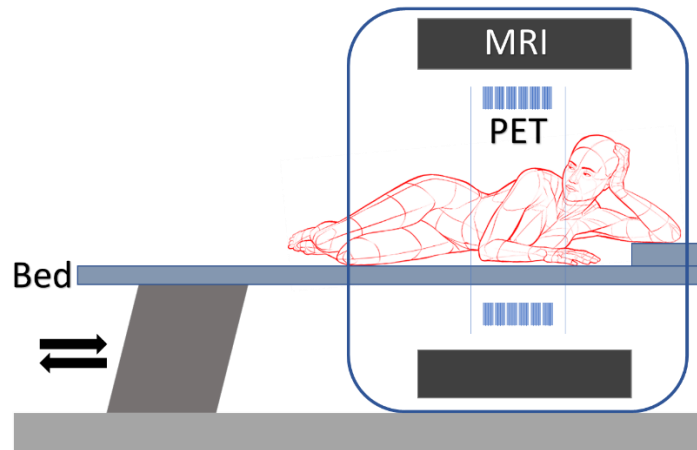


*Figure 1.12 Design of a combined PET-MR scanner. MR and PET are concentric. Scanned objects are intrinsically registered.*

### **1.3.3 SAVANT scanner**

The Gordon Center for Medical Imaging (Boston, USA), where this PhD thesis has been held and Sherbrook University (Sherbrook, Canada) are developing the Scanner Approaching in Vivo Autoradiographic Neuro Tomography (SAVANT), which is based on the LabPET-II's technology platform (Gaudin et al., 2021a) and is expected to have a volumetric resolution of under  $2 \mu\text{l}$  (Lecomte et al., 2022), a significant improvement over the HRRT's resolution.

The SAVANT (Figure 1.13) relies on the LabPET II technology platform having demonstrated unprecedented sub-mm resolution for imaging small and mid-sized animals. The basic detector elements consist of  $4 \times 8$  arrays of  $1.12 \times 1.12 \times 15$  mm 3 phoswich LGSO scintillators read out by monolithic  $4 \times 8$  APD arrays, assembled into 128-channel modules with a 2.5D architecture for thermal management and parallel signal processing by two 64-channel custom integrated circuits. Model based or machine learning classifiers are used to discriminate digitized signals from the phoswich detectors for DOI measurement. Slow ( $>44$  ns) and Fast ( $<32$  ns) decay LGSO crystals of 6.5 mm (top) and 8.5 mm (bottom) were selected as an optimal tradeoff between off-center spatial resolution and balanced coincidence detection efficiency between layers. The SAVANT uses 4032 of these detector arrays for a total of 258,048 crystals on a 39-cm diameter by 23.5-cm long cylinder with 144 rings of 896 phoswich pixelated detectors, defining an imaging field of view up to a diameter of 30 cm. Ethernet-based singles data transfer to the acquisition computer was implemented along with software coincidence processing to sort out list-mode events in real-time. To achieve the highest possible resolution in vivo, a list-mode based PET reconstruction platform supporting physiological triggers and data measured from a real-time infra-red tracking camera for event-by-event motion compensation is being developed for the SAVANT during this PhD.

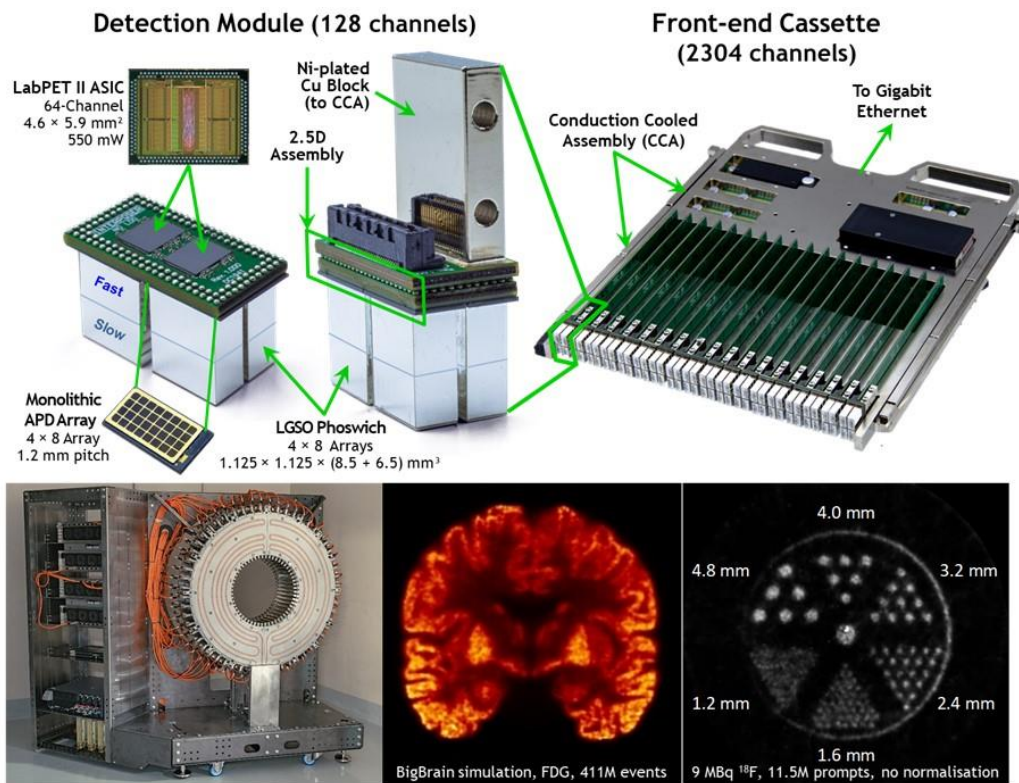


Figure 1.13 Top: Details of the SAVANT detection module showing the basic components. Eighteen modules are mounted in front-end cassettes transmitting data through a gigabit ethernet network. Bottom: SAVANT scanner during assembly (left), GATE simulation of FDG uptake based on the BigBrain atlas, and the first image of resolution phantom with a single ring prototype (right).

## 1.4 Clinical application in neuroimaging and Alzheimer’s Disease

The multitude of radiotracers and their different functions illustrated in Table 1.1 explains how prevalent PET imaging in patient diagnosis and management is.

In that regard, PET imaging is commonly used for brain pathologies, including cancer and dementia.  $[^{18}\text{F}]$ -FDG is widely used in brain cancer, and other tracers such as  $[^{18}\text{F}]$ -FMISO,  $[^{15}\text{O}]$ -H<sub>2</sub>, and  $[^{18}\text{F}]$ -FLT have also been used to assess hypoxia, perfusion, and proliferation, respectively (Bruehlmeier et al., 2004). In the case of gliomas,  $[^{18}\text{F}]$ -FDG PET imaging findings have been linked to the tumor grade and survival rates (Padma et al., 2003). In epilepsy, PET imaging can be used to localize the seizure focus, which is essential for surgical therapy (Hwang et al., 2001).  $[^{18}\text{F}]$ -FDG PET is also a biomarker for neuronal degeneration in dementia (McKhann et al., 2011), and its spatial distribution can enable early diagnosis and the distinction between different subtypes of dementia (Shivamurthy et al., 2015). In the following subsections, we focus on neurodegenerative brain disease, with particular attention given to Alzheimer’s Disease (AD).

### 1.4.1 Introduction to Alzheimer's Disease

AD is a neurodegenerative disorder characterized by a gradual decline in cognitive function, including memory, language, and problem-solving abilities. It is the most common form of dementia, accounting for 60-80% of all cases.

AD's clinical signs can be considered a continuum (Figure 1.14, Sperling et al., 2011) and typically develop slowly over several years. They may initially be noticed as mild memory problems or difficulty with language. As the disease progresses, symptoms can become more severe, significantly impairing daily functioning.

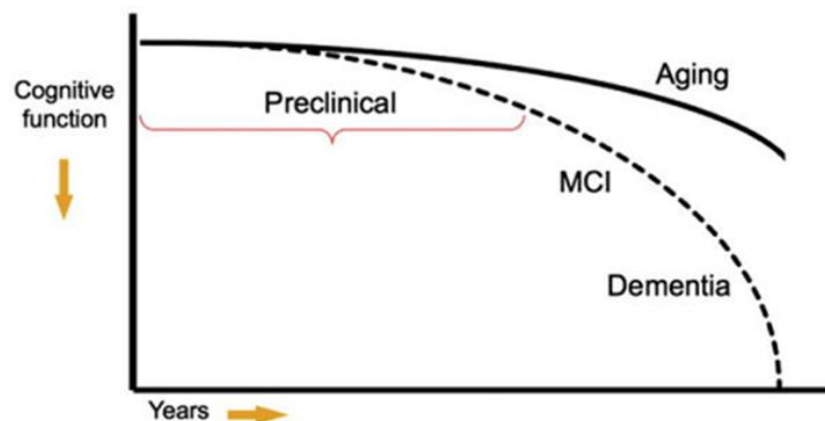


Figure 1.14 The continuum of Alzheimer Disease. (Sperling et al., 2011)

The exact cause of AD is not fully understood, but several risk factors have been identified. These include increasing age, genetics, and lifestyle factors such as a lack of physical activity and poor diet (Drachman, 2006).

#### Clinical signs and diagnostic

The symptoms of AD typically develop slowly over many years and can vary from person to person. Some common symptoms include memory loss, cognitive decline (Christie et al., 2013), changes in behavior and personality (Tsuno and Homma, 2009), language problems, and disorientation (Yesavage et al., 1993).

These symptoms can lead to significant impairments in daily functioning and can affect a person's ability to live independently. As the disease progresses, people with AD may require increasing levels of care. Improving this pathology diagnosis at earlier stages would be of great importance in order to provide the appropriate treatment options.

The diagnosis of AD typically involves a combination of cognitive and neuropsychological testing (Nasreddine et al., 2005; Tombaugh and McIntyre, 1992), brain imaging, and biomarker analysis.



Cognitive and neuropsychological tests are used to assess a person's cognitive function and determine if there are any areas of decline. These tests may include assessments of memory, language, attention, problem-solving, and other cognitive abilities.

Brain imaging techniques, such as MRI or PET, can be used to diagnose and manage AD.

Overall, the diagnosis of AD is typically based on a combination of these methods and may also involve a thorough medical history and examination, as well as input from family members or other caregivers.

### **Pathology**

The underlying pathology of AD is characterized by the formation of beta-amyloid plaques (Klunk et al., 2004) and tau tangles (Mishra et al., 2017) in the brain (Figure 1.15).

Beta-amyloid plaques are clumps of a protein called beta-amyloid that build up between nerve cells in the brain. These plaques are thought to interfere with the normal functioning of neurons and can lead to their death.

On the other hand, Tau tangles or neurofibrillary tau tangles (NFTs) are twisted fibers of another protein called tau that forms inside nerve cells. These tangles are thought to disrupt the transport of nutrients and other essential molecules within the cell, leading to its death.

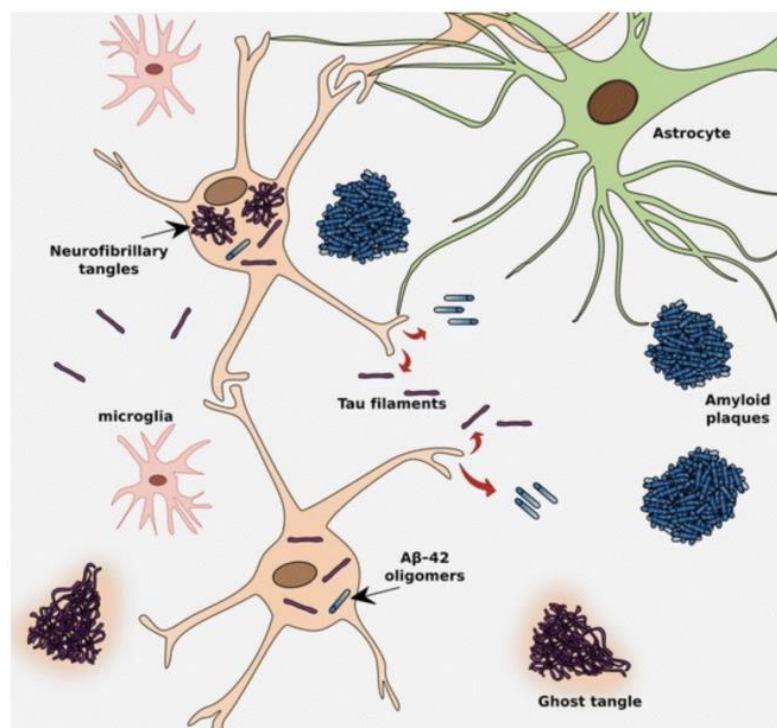


*Figure 1.15 Schematic of Amyloid plaques and Neurofibrillary Tau tangles inside the brain. (Saint Aubert, 2017).*

The formation of these plaques and tangles is thought to be a key factor in the development of the symptoms of Alzheimer's disease, such as memory loss and cognitive decline. The extent and distribution of these changes in the brain can also provide insights into the progression of the disease and the effectiveness of potential treatments. Their temporal-spatial progression is used to define stages of the disease, known as Braak stages (Figure 1.16) (Braak and Braak, 1991).

The locus coeruleus and trans entorhinal cortex are particularly susceptible to being damaged by NFTs and are the first brain structures affected by the presence of these tangles (Braak stage I). As the disease progresses, NFTs can spread from the locus coeruleus and trans entorhinal cortex to the entorhinal cortex. The entorhinal cortex is a brain region that plays a crucial role in memory and spatial navigation. (Braak stage II). These stages often occur during a long preclinical period in which an individual may not yet exhibit any disease symptoms. The presence of NFTs in the entorhinal cortex after the age of 75 may be similar to normal brain aging. Braak stage III is characterized by the presence of NFTs in the hippocampus, a brain region that plays a crucial role in learning and memory. In Braak stage IV, the NFTs extend from the hippocampus to the temporal cortex and limbic regions and all associative cortical regions. These stages correspond to the beginning of AD, as the presence of NFTs in these brain regions is associated with the development of symptoms such as memory loss and cognitive decline. Finally, stages V and VI correspond to a major impairment of the isocortex affecting the entire cortex. The primary, visual, and motor cortical regions are among the last brain regions affected by the disease (Jucker and Walker, 2011). The spreading of Tau may occur via trans-synaptic propagation through anatomically connected synapses, glial cells as oligodendrocytes, and microglia (Wang et al., 2017).

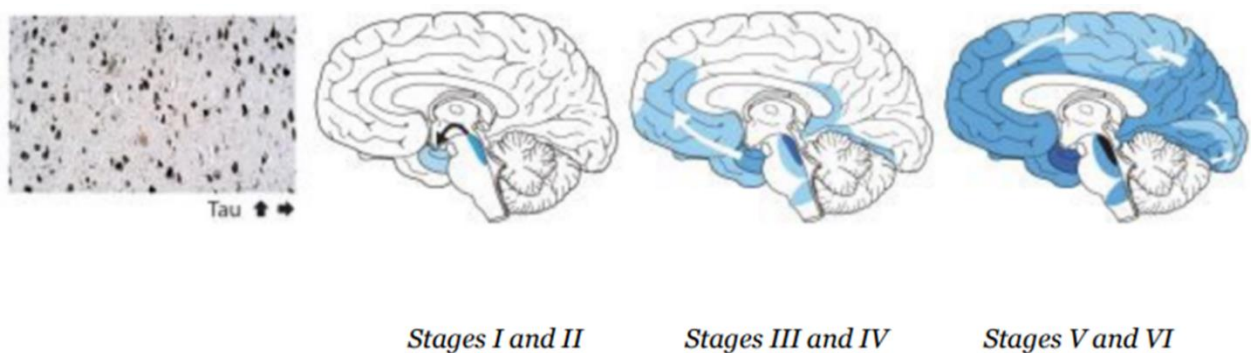


*Figure 1.16 Spatiotemporal evolution of the Tau lesions according to Braak. (Jucker and Walker, 2011)*

### 1.4.2 PET imaging of tau protein

PET can be used to visualize tau protein in the brain. As previously seen in this chapter, PET imaging works by injecting a radioactive tracer into the bloodstream, which then binds to the tau protein in the brain. The tracer emits positrons, which are detected by the PET scanner and used to create detailed images of tau distribution in the brain.

PET imaging is a valuable tool for studying AD, allowing researchers and clinicians to visualize tau protein in the brain. This can provide valuable insights into the progression of the disease and the effectiveness of potential treatments. By tracking the accumulation of tau protein in the brain over time and evaluating the impact of different interventions on tau levels, PET imaging can help researchers and clinicians understand more about the underlying causes of AD and how it can be treated. In addition, PET imaging of tau protein is increasingly being used in clinical practice to help diagnose and monitor AD, providing additional information that can help distinguish it from other forms of dementia and track its progression over time.

#### Importance of tau PET imaging in AD research

Tau PET imaging is essential for research on AD for several reasons. First, tau PET imaging (example in Figure 1.17) can provide insights into the progression of the disease by allowing researchers to track the accumulation of tau protein in the brain over time. This can help to better understand the underlying pathology of the disease and to identify potential biomarkers that can be used to monitor the disease progression and response to treatment. Moreover, there is evidence that current treatments, although symptomatic, are more effective in the early stages of the disease (Farlow, 2000).

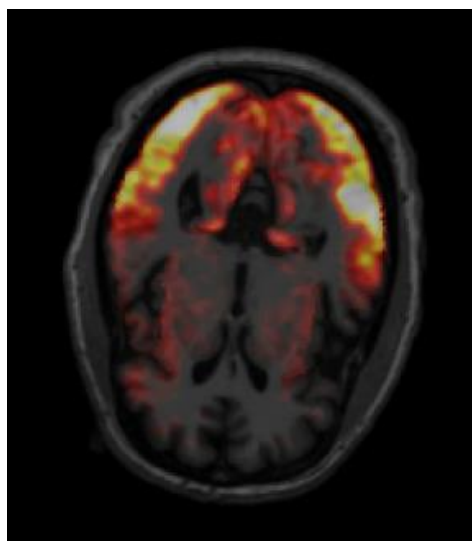


*Figure 1.17 Example of PET image overlaid on MR showing the deposition of Tau protein on an AD-positive patient.*

Secondly, tau PET imaging can be used to evaluate the effectiveness of potential treatments for AD. By measuring changes in tau levels in the brain after treatment, researchers can determine whether a particular intervention is able to slow or halt the accumulation of tau protein. This can provide valuable information on the potential benefits of different treatments and can help to guide future research and clinical practice.

Finally, tau PET imaging can also help to improve the diagnosis and monitoring of Alzheimer's disease in clinical practice. By providing detailed information on tau distribution in the brain, tau PET imaging can help to differentiate Alzheimer's disease from other forms of dementia and can provide valuable information on the progression of the disease over time.

Overall, the ability of tau PET imaging to provide insight into the progression of Alzheimer's disease and to evaluate the effectiveness of potential treatments makes it an essential tool for research in this field. It can provide valuable insight into the disease's underlying pathology and can help improve diagnosis and treatment.

### **Tau protein PET tracers**

A good candidate radiotracer for PET imaging of tau protein needs to satisfy the following requirements (Villemagne et al., 2015):

- high selectivity for tau over  $\beta$ -amyloid and high binding affinity since tau tangles,
- coexist with amyloid plaques in lower concentrations,
- ability to cross the blood-brain barrier,
- possibility to be labeled with isotopes with long half-lives,
- low binding in brain areas that do not contain tau protein.

Several different types of PET tracers are currently being used or developed for the visualization of tau protein in the brain, including [ $^{18}\text{F}$ ]-FDDNP, which binds to both  $\beta$ -amyloid and tau tangles (Smid et al., 2013), [ $^{18}\text{F}$ ]-THK5351 that selectively binds to paired helical filaments tau and exhibits low uptake in the to the white matter (Harada et al., 2016), or [ $^{18}\text{F}$ ]-T807 which presents higher selectivity for PHF-tau over  $\beta$ -amyloid (Xia et al., 2013).

Overall, the choice of PET tracer for tau imaging will depend on the specific research question and the desired information type. The tracers can provide valuable information on tau in the brain, but each has its own strengths and limitations.

In this manuscript, we will work specifically (in Chapter 7) on a non-FDA approved tracer known as [ $^{18}\text{F}$ ]MK-6240. It is a second-generation tau tracer under study that is currently considered one of the most promising in terms of the stated requirements (Guehl et al., 2019).

### **Limitation of Tau PET tracers**

Tau PET tracers are expected to detect small changes in the accumulation of neurofibrillary tangles (NFTs) at the early stages of AD, which could help evaluate the effectiveness of potential anti-tau therapies or for statistical and longitudinal analyses. However, current tau radiotracers, including both first- and second-generation tracers, have limitations with regard to off-target binding (example in Figure 1.18). For instance, quinolone derivatives, such as [ $^{18}\text{F}$ ]-THK5351, can bind to monoamine oxidase B (MAO-B), which can lead to confusion in interpreting the [ $^{18}\text{F}$ ]-THK5351 signal in relation to NFTs and may compromise the usefulness of this tracer as a tau marker. Additionally, even the most widely used and promising tau tracers have some level of off-target signal, which can arise from structures near key brain regions. This off-target signal can spill into these regions due to the limited spatial resolution of PET scans, potentially limiting the clinical and research utility of these tracers.

[ $^{18}\text{F}$ ]-T807 (also known as [ $^{18}\text{F}$ ]-AV-1451 or [ $^{18}\text{F}$ ]-flortaucipir), a first-generation tau tracer that has been extensively validated, has been shown to have off-target binding in the basal ganglia, choroid plexus, and neuromelanin-containing cells including the substantia nigra (Johnson et al., 2016; Lemoine et al., 2018; Marquié et al., 2017). The binding in the choroid plexus may hinder the accurate quantification of NFTs in the entorhinal cortex and hippocampus, which are involved relatively early in the AD process. [ $^{18}\text{F}$ ]MK-6240, also has limitations with regards to off-target binding. We will give more details and a potential solution for this problem in Chapter 7.

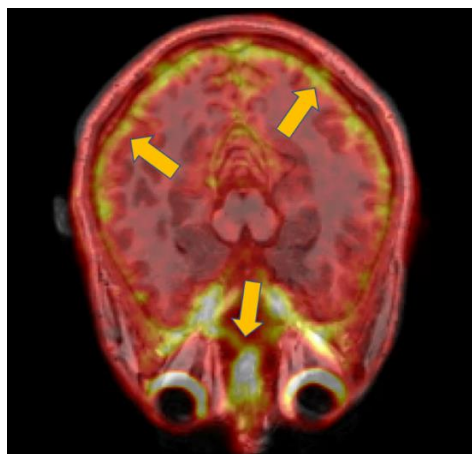


*Figure 1.18 Example of [ $^{18}\text{F}$ ]MK-6240 off-target binding to meninges and sinuses.*

## 1.5 Conclusion

In this first introductory chapter, we have presented the general principles associated with Positron Emission Tomography. We discussed the history of this imaging technique in Section 1.1, then delved into the main physical phenomena related to PET detection in Section 1.2. We have also presented the different formats representing the raw PET data and the various image reconstruction techniques, as well as the different types of data corrections and how they can be included in a reconstruction scheme. Additionally, we have discussed different implementations of PET scanners in Section 1.3. In Section 1.4, we have provided an overview of AD and its clinical signs, risk factors, and methods of diagnosis. We have discussed the symptoms of AD, including memory loss, cognitive decline, and changes in behavior, as well as the underlying pathology of AD. Additionally, we have examined the use of PET imaging to visualize hyperphosphorylated tangle of tau protein in the brain and its importance in research on AD. We have also explored the different types of PET tracers used to visualize tau protein in the brain and their limitations.

This chapter serves as a foundation for the contributions presented in Chapter 3 to Chapter 7, where we applied many of the concepts introduced to achieve improved quantification in brain PET imaging (list-mode reconstruction using an OSEM algorithm, data corrections, the use of PET/CT or PET/MR scanners, improved quantification for neuroimaging, etc.). Specifically, we attempted to improve the accuracy of brain PET imaging by implementing newer techniques such as motion correction, super-resolution, and non-negative matrix factorization. These chapters will demonstrate how some of the concepts discussed here can be used to help overcome the challenges of PET quantification (discussed in Chapter 2) and improve the diagnostic capabilities of this imaging modality for brain imaging and specifically for AD.

First, in the next chapter, we will focus on the challenges of PET quantification.



# Chapter 2

## Challenges of PET quantification

We have seen in Chapter 1 that PET is a medical imaging modality that allows for the non-invasive measurement of physiological and biochemical processes in vivo. We have outlined some of the main challenges and limitations, namely attenuation, normalization, scatter, and random correction. Accurate quantification of PET images is critical for correctly interpreting and analyzing the data, especially for studying neurochemistry and neurodegenerative proteinopathy discussed in Chapter 1, Section 1.4.

However, PET quantification is challenged by other factors that can affect the accuracy and precision of the measurements. In this chapter, we focus on the challenges, which include spatial resolution in Section 2.1, partial volume effect in Section 2.2, noise in Section 2.3, and motion in Section 2.4. Resolution refers to the ability of the imaging system to distinguish between two closely spaced objects or features. Partial volume effect occurs when structures are partially obscured by other structures or tissues due to the limited resolution or other effects, leading to underestimation or overestimation of tracer uptake. Noise in clinical PET images depends on various factors, such as the amount of radioactivity administered to the patient, the efficiency of the detection system, and the data acquisition and reconstruction techniques used. Finally, the patient's motion can introduce blur and artifact into the images, leading to errors in quantification, making PET image interpretation more challenging.

We will review the challenges and discuss their source, impact, and current approaches for addressing them.



## 2.1 Resolution

### 2.1.1 Definition

The spatial resolution of a PET system can be referred to as the smallest distance at which it is possible to distinguish two point sources on a reconstructed image. It describes the degradation of the signal acquired by the various physical limitations outlined in Chapter 1 Section 1.2.1 of this manuscript, as well as by the geometric limitations of the PET scanner.

The main limitation of PET imaging is its relatively mediocre spatial resolution compared to other medical imaging modalities. While X-ray imaging (CT) or magnetic resonance imaging (MRI) can achieve sub-millimeter resolutions, PET imaging typically struggles to achieve resolution below four to three millimeters with current technology. This low spatial resolution is due to a combination of several factors, the most important of which are the size of the scintillating crystals and the geometry of the blocks.

### 2.1.2 Source

Although some of the effects responsible for degrading spatial resolution cannot be exactly described by a Gaussian function, it is generally considered that their impacts are added in quadrature. Thus, the intrinsic radial spatial resolution at a distance  $r$  from the center of the FOV is estimated by a Gaussian function called the point spread function (PSF) (Figure 2.1) or, more generally, the system response function.

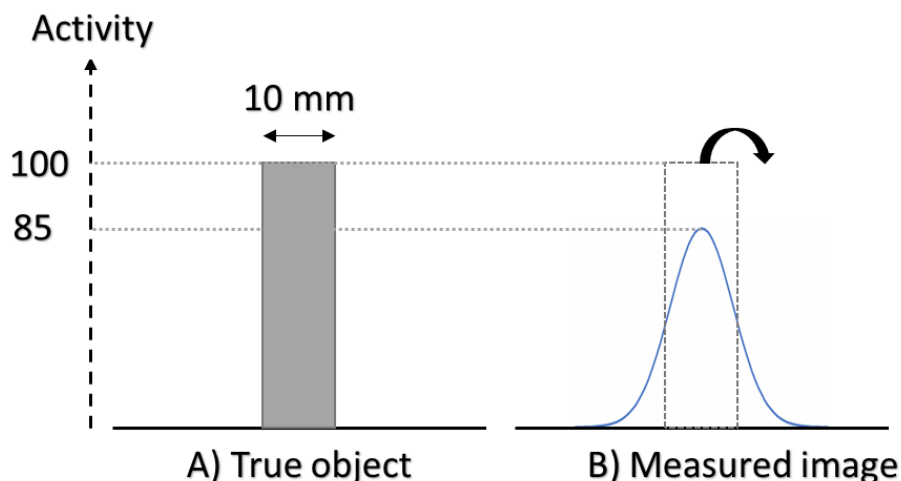


*Figure 2.1 Illustration of the deleterious effects of the PSF on PET image accuracy. A) Source of uniform activity of intensity 100 (A.U.) in a non-radioactive background produces, B) a measured image in which part of the signal is spread outside the true object, and the maximal activity of the object is under-estimated to 85 A.U. Adapted from (Soret et al., 2007).*

An empiric formula proposed by Moses and Derenzo states that the imaging spatial resolution in terms of full width at half maximum (FWMH) of a scanner system can be given by (Moses, 1993):

$$FWMH (mm) \approx a \sqrt{\left(\frac{d}{2}\right)^2 + (0.0044R)^2 + s^2 + b^2 + \frac{(12.5r)^2}{r^2 + R^2}} \quad (2.1)$$

with,

$a$ : constant factor

$d$ : the crystal width (in mm),

$R$ : is the radius of the detection rings (including photon noncollinearity in mm),

$s$ : the effective source size (including positron range in mm),

$b$ : the block effects (block size in mm),

$r$ : distance to the center of the field of view (in mm).

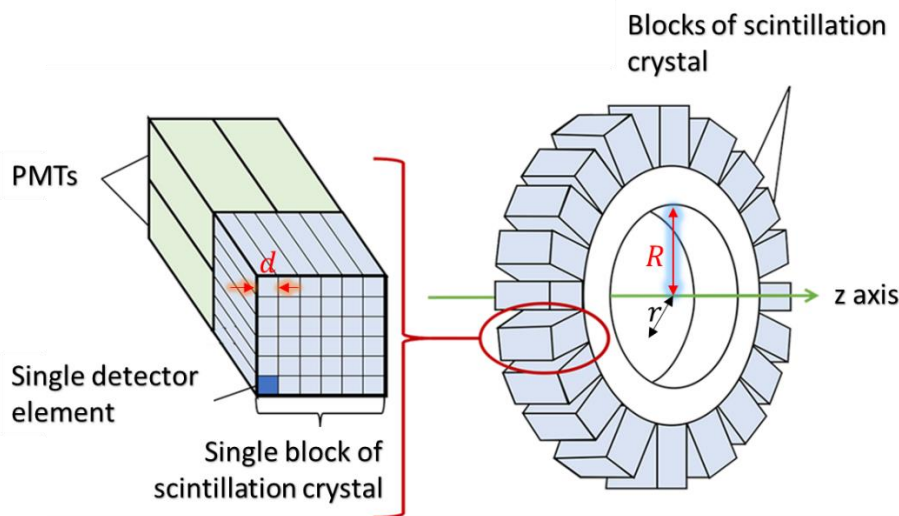


Figure 2.2 Diagram describing the elements that affect the resolution of a PET system at the ring and detector level.

The constant factor  $a$ , which varies from 1 to 1.3, is due to the image reconstruction algorithm. The factor 0.0044, expressed in radians, corresponds to the angular fluctuation between two emitted gamma rays. The crystal width is the main resolution limiting factor in most PET scanners. Decreasing crystal size is hence a way of improving resolution; however, with today's manufacturing process, this can be substantially expensive, and inter-crystal penetration can become an issue. On the other hand, most PET systems are designed for

general-purpose applications, and they cannot provide the required resolution for some specific region-of-interest (ROI) imaging (Li et al., 2014).

### 2.1.3 Impact

The limited resolution of a PET imaging device causes two types of errors in quantifying the activity distribution: underestimation of the tracer concentration in structures of size comparable to the spatial resolution and overflow of an area of activity into another (“spillover”). Several methods can partially correct these effects; however, it is important to note that the finite spatial resolution of a PET imaging device is a fundamental technological limit that cannot be completely compensated for by post-processing methods.

### 2.1.4 Improving resolution

Methods for improving resolution in PET can be divided into two subgroups based on whether they are applied to the reconstructed image or integrated into the reconstruction. Methods applied to reconstructed images are simply deconvolution methods. In fact, the reconstructed image  $\rho$  is not the original object  $f$ , but its convolution with the spatial impulse response  $h$  of the detector (Soret et al., 2007):

$$\rho(x, y, z) = (h * f)(x, y, z) \quad (2.2)$$

In reality, the impulse response of the PET imaging device is not spatially invariant, and the reconstructed image is discrete. Therefore, Equation (3.2) can be written as:

$$\rho = Hf \quad (2.3)$$

The direct inversion of Equation (2.3) is rarely used in practice because the resulting problem is ill-conditioned and therefore increases noise in the final image. To improve the conditioning of the problem, we can assume that the PET image is composed of  $K$  homogeneous compartments. This assumption reduces the dimension of the matrix  $H$  in Equation (2.3) and improves its conditioning. The compartments can be determined by segmenting a PET image or an anatomical image (MRI or CT). A major limitation of this approach is that it assumes that the PET image is homogeneous by region, which is not the case in reality and can make the identification of compartments difficult in practice (Rousset et al., 1998). Another deconvolution strategy is to regularize the iterative inversion of Equation (2.3). Several iterative methods have been proposed using different regularizations (Boussion et al., 2006).

It is also possible to integrate resolution improvement into the reconstruction process. The projection matrix of iterative reconstruction algorithms is designed to model everything that

happens to a photon, from its emission to its detection. It is therefore possible to incorporate, for example, the average free path of the positron before annihilation with an electron, the finite resolution of the detector (Panin et al., 2006), or the point spread function. In Chapter 4 and Chapter 5, we will explore a more advanced technique known as super-resolution. A literature review is presented in Chapter 4.

## 2.2 Partial volume effect

### 2.2.1 Definition

In PET imaging, partial volume effect (PVE) refers to the phenomenon whereby the measured activity concentration in a voxel is not solely from a single tissue type or region but rather is a combination of activity from multiple tissue types or regions. This can lead to an underestimation of the true activity concentration in the voxel and can affect the accuracy and precision of the PET image.

### 2.2.2 Source

More precisely and as explained by (Soret et al., 2007), the term “partial-volume effect” refers to two distinct phenomena that make intensity values in images differ from what they ideally should be. The first is the 3D image blurring introduced by the finite spatial resolution of the imaging system, which can result in spillover between regions and cause the image of a small source to appear larger and dimmer. The second phenomenon referred to as the “tissue fraction effect,” is due to image sampling. The radiotracer distribution is sampled on a voxel grid, resulting in most voxels including different types of tissues and a signal intensity that is the mean of the underlying tissues.

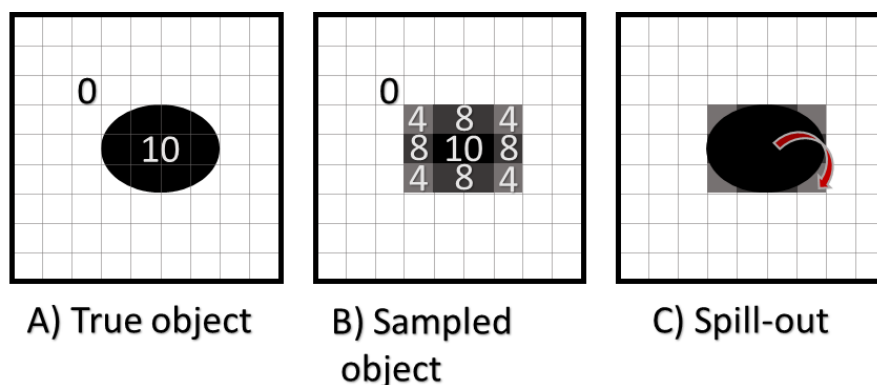


*Figure 2.3 Influence of image sampling on PVE. Pixels on the edge of the source include both source and background tissues. A part of the signal emanating from the source is outside the actual object and therefore is described as spilling out. Adapted from (Soret et al., 2007).*

Ideally, compensation for PVE should consider both the finite resolution effect and the tissue fraction effect. This phenomenon is why PVE is a concern in both emission tomography, which

has poor spatial resolution compared to other imaging modalities, and high-resolution imaging, such as MRI or CT. Note that even if the imaging system had an infinite spatial resolution, there would still be some PVE due to image sampling. Mathematically speaking, the finite resolution effect is described by a 3D convolution operation, where the image is formed by the convolution of the actual source with the 3D point spread function of the imaging system. This specific source of PVE will be covered in Chapter 6.

In summary, there are several sources of PVE in PET imaging:

- Spatial resolution: The finite size of the PET detectors limits the ability to accurately localize the origin of the emitted gamma rays, leading to PVE,
- Anatomical structures: The presence of anatomic structures with different activity concentrations nearby can contribute to PVE. For example, the boundary between two tissues with varying levels of activity can lead to PVE.

Overall, PVE can be a significant source of error in PET imaging and can affect the accuracy and precision of the images. It is essential to carefully consider the sources of PVE and take steps to minimize their impact when interpreting PET images.

### **2.2.3 Impact of PVE**

Partial volume effect can significantly affect the quality and accuracy of images. PVE spreads out the signal from small, hot lesions embedded in a colder background, making the lesion appear larger but less aggressive than it actually is. This is particularly problematic when using PET for radiotherapy treatment planning, as the contours of the lesion on the PET image may include more than the metabolically active part of the tumor due to the limited spatial resolution of PET images. PVE can also cause difficulty in accurately assessing the viability of necrotic tissue in tumors, as activity from outside the tumor can spill into the tumor, leading to an overestimation of viable tissue. PVE does not cause any signal loss but displaces the signal in the image. In the absence of background activity, PVE does not affect the total activity in the tumor as long as a large enough region is drawn around the tumor to capture the total activity accurately. The quest for higher-resolution PET systems remains important to more accurately determine the metabolically active part of tumors and improve treatment planning.

### **2.2.4 PVE Correction**

Various methods are being researched to correct for PVE, including the recovery coefficient (RC) method (Krempser et al., 2013), the geometric transfer matrix (GTM) method (Rousset et al., 1998), deconvolution (Golla et al., 2017), the multiresolution method (Boussion et al.,

2006), the fitting method (Santago and Gage, 1995), and the maximum a posteriori approach (Baete et al., 2004).

The RC method involves multiplying the measured uptake value in an ROI by a correction factor. In contrast, the GTM method consists in dividing the image into compartments and calculating the proportions of the signal emanating from each compartment and detected in the other compartments. Deconvolution is a method that involves an iterative process where the image that would be obtained if the true image was known is compared with the actual image acquired. The difference is used to update an estimate of the PVE-corrected image. The multiresolution method involves extracting and transforming details from a high-resolution image and incorporating them into a low-resolution PET image. The fitting method involves modeling a tumor as a sphere with uniform uptake and estimating the model's unknown parameters by minimizing an objective function. The maximum a posteriori approach involves incorporating previously determined anatomic information into the reconstruction process and allowing noise suppression in specific compartments with anatomically based smoothing.

Other methods will be exposed as part of the contribution of the Ph.D. work in Chapter 4, Chapter 5, Chapter 6, and Chapter 7.

## 2.3 Noise in PET imaging

### 2.3.1 Source

There are other sources of errors that are more difficult to correct and represent limitations to the use of PET imaging. On the one hand, PET images are very noisy. Noise comes from two distinct sources. The first is directly related to the statistical nature of the observed phenomenon, that is, the radioactive disintegrations of the marker associated with the molecule injected into the patient. The noise level due to this source depends on the amount of injected activity (Figure 2.4).

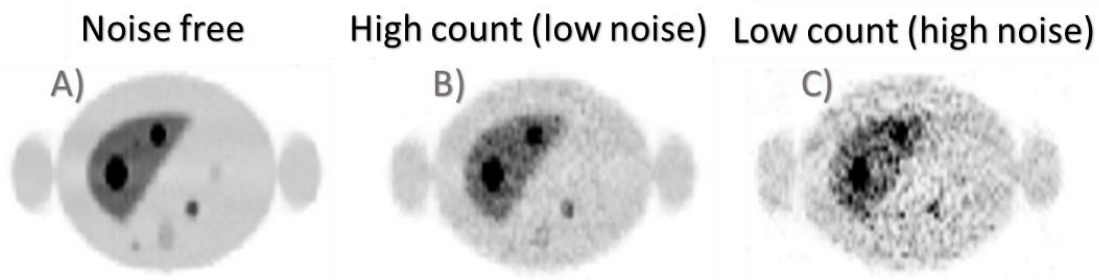


*Figure 2.4 OSEM image showing the effect of the number of counts considered for the reconstruction. A) is the ideal noise-free object, B) is the high count displaying a lower amount of noise, and C) is the low count reconstruction displaying a higher amount of noise.*

The second source of noise is the iterative reconstruction of the image. The noise found in the images after reconstruction depends heavily on the reconstruction algorithm used. Each reconstruction introduces noise and artifacts specific to its operating mode. Although reconstruction algorithms have benefited from many improvements over the years, unregularized approaches still produce imperfect images with variable properties, often noisy and affected by artifacts related to the approach used. Iterative algorithms that produce the best results are also subject to noise, usually proportional to the number of iterations.

In addition to the intrinsic resolution allowed by the PET device, the size of the voxels used to reconstruct the image significantly impacts its final quality. The smaller the voxels, the better the objects are represented, but the fewer the LOR passing through each voxel. In practice, reducing the size of the voxels results in an increase in noise in the image.

A compromise must therefore be found between the ratio between the size of the voxels and the imaged object and the quality of the image. In clinical routine, the size of the voxels is generally between 2- and 5 mm.

Other sources of noise can include random coincidences, scattered photons, and electronic noise.

### **2.3.2 Impact**

Noise in PET imaging can significantly impact the overall quality of the images produced and can affect the accuracy of the measurements obtained from those images. High noise levels can make it difficult to distinguish small or subtle changes in tissue activity, which can lead to false positive or false negative results. Additionally, noise can make detecting small lesions or tumors difficult, leading to delayed or missed diagnoses. Furthermore, high noise levels can increase the radiation dose required to achieve a given image quality, increasing the risk of radiation-induced cancer and other adverse effects. Noise can also impact the ability to perform quantitative analysis, such as measuring the binding potential of a tracer in a specific region of interest.

## **2.4 Motion**

Movement during a PET acquisition is another source of resolution degradation. During a PET scan the data is accumulated over some time, depending on the study, a single brain scan can last up to an hour. Any substantial motion of the subject during the scan will result in motion blur in the final reconstructed image. It is a common practice to physically restrain the head to minimize the possible motion of the patient. Nonetheless, even with a head restraint, some

patients struggle to remain motionless through the scan (for instance in pediatric or psychiatric imaging) (Daou, 2008).

In this section, we first discuss the source and deleterious consequences of physiologic motion in PET and PET-CT applications. We then present the different methods that have been proposed in the literature to alleviate the impact of motion in these applications.

### **2.4.1 Source and Impact**

Physiologic motion, such as respiratory, cardiac movement, or any rigid body motion can have a negative impact on the quality of PET and PET-CT images, particularly in areas such as the heart, thorax, abdomen and head where the movements can be substantial. This motion can cause blurring of the signal, leading to an underestimation of the local tracer uptake and an overestimation of the volume of the organ or lesion being imaged (Liu et al., 2009) (see an example in Figure 2.5). In addition, motion can create inconsistencies between the emission and attenuation data in PET-CT studies, resulting in image artifacts and degrading the quantitative accuracy of the images (Gould et al., 2007). These issues can be particularly problematic in neurology, oncologic and cardiac imaging, where an accurate assessment of tracer uptake and lesion size is critical.

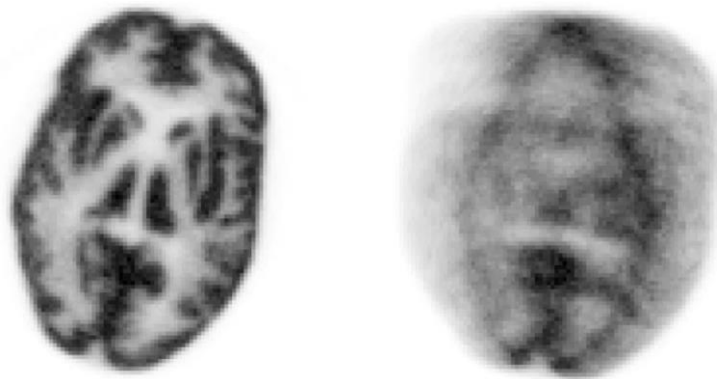


*Figure 2.5 Effect of extreme continuous motion degrading the image resolution on a Hoffman brain phantom.*

To address these issues, various methods have been proposed in the literature to alleviate the impact of motion on PET and PET-CT images. These methods include respiratory gating, external surrogates, internal surrogates, and image-based motion correction.

### **2.4.2 Motion Correction**

The gating method is a common approach to compensate for motion in PET, but it can result in an increased noise level due to the reduced number of events in each phase and is only useful for pseudo periodic types of movement. To overcome the limitations of gating, various PET



motion correction methods have been developed, which involve two steps: estimating the motion vector field and correcting for motion through the application of the vector field to gated images or modeling it in motion-compensated PET image reconstruction. PET motion correction methods can hence be divided into three categories based on how the motion field is estimated: PET-based, MR-based, or external tracker-based.

### 2.4.3 Gating

There are two types of gating: prospective and retrospective. In prospective gating, data acquisition is restricted to certain points in the motion cycle, such as the end of exhalation in respiratory gating or the end of diastole in cardiac gating. In retrospective gating, data is collected throughout the entire acquisition and is sorted and reconstructed based on the gating signal after the acquisition. Retrospective gating is preferred for motion correction because it allows for all available data to be used to improve image quality. Cardiac gating uses the electrical activity of the heart as the gating signal, and respiratory gating uses sensors placed on the patient's chest or abdomen to measure the motion of the rib cage or belly during respiration (Figure 2.6).

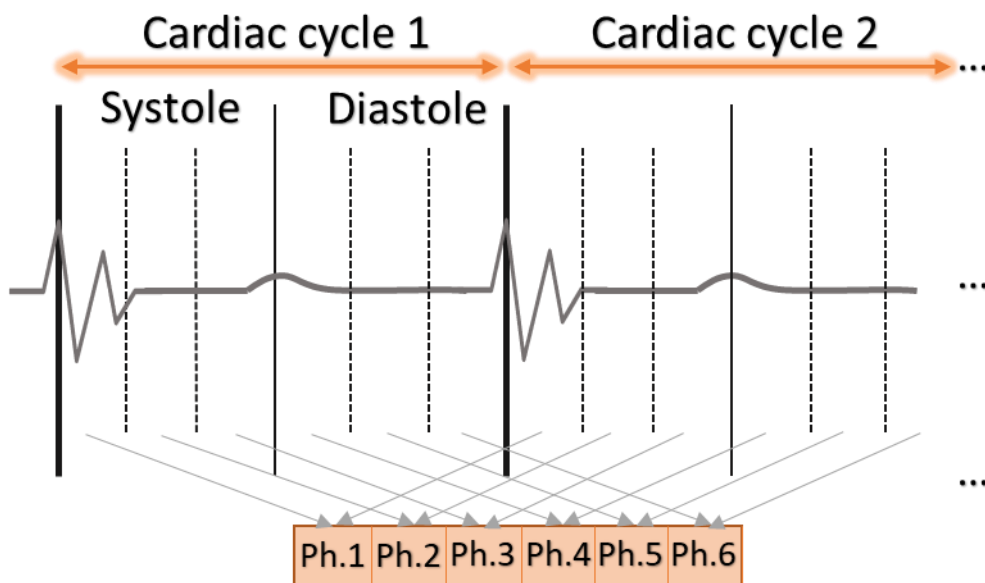


Figure 2.6 Illustration of the concept of EKG-based cardiac gating with an example of 6 cardiac gates (Ph.1 ... Ph.6). Cardiac gating is achieved by grouping data detected in the same cardiac gate but acquired in different cardiac cycles.

To determine the movement of voxels between different gates in a gated PET data acquisition, a motion field must be calculated. This is typically done using image registration, a process that finds a point-to-point correspondence between two images by identifying a spatial transformation that links their coordinate systems. The resulting motion field describes the

movement of voxels between the gates and a reference point. Image registration is typically formulated as an optimization problem, minimizing a cost function that measures the discrepancy between the two images being registered. The cost function is typically composed of an image matching criterion and a regularization criterion. There are two main types of image registration methods: non-parametric, local methods such as optical flow, and parametric, global methods that use a global transformation model defined by a small number of parameters. Both of these methods have been widely used in the PET literature for motion correction.

However, gating results in increased noise levels due to the reduced number of events in each motion phase. To address the limitations of the gating method, many PET motion correction methods have been developed, which consist of two consecutive steps: motion vector field estimation, and motion correction by either applying the estimated motion vector fields to the gated images or modeling it within motion-compensated PET image reconstruction (Rahmim et al., 2013).

Depending on how the motion field is estimated, PET motion correction methods can be divided into two major subcategories: PET-based methods and Magnetic Resonance (MR)-based methods.

### **PET based**

In the PET-based motion correction methods, the measured emission data are first assigned to specific motion phases based on surrogate signals (Jin et al., 2013), e.g., EKG, respiratory bellow, etc. (Roger R Fulton et al., 2002; Montgomery et al., 2006; Yu et al., 2016), or the PET-data themselves (Kesner et al., 2009; Lu et al., 2019; Sun et al., 2019), e.g., center of mass, time-of-flight information, frame-by-frame images, etc. Motion vector fields are then estimated by registering the reconstructed image of each phase to a reference phase (Dawood et al., 2008). However, the accuracy of the motion vector fields estimated by the PET-based methods is limited by low signal-to-noise ratio (SNR), especially in the case of dual gating, and the overall lack of anatomical structural information of PET images (Ouyang et al., 2013b; Petibon et al., 2019).

### **MR based**

The increasing availability of hybrid PET/MR systems provides a unique opportunity for mitigating effects of motion in PET using MR-based motion correction. Because of its excellent soft-tissue contrast, high spatial resolution, and high SNR, MR provides more accurate estimation of motion vector fields than the PET-based methods. MR-based PET

motion correction methods have been successfully applied to compensate respiratory and cardiac motion in various applications involving both static and dynamic PET imaging (Catana, 2015; Gillman et al., 2017; Huang et al., 2014; Petibon et al., 2019, 2013).

One major limitation of the MR-based motion correction methods is that the conventional Fourier-based MR imaging method could not resolve cardiac or respiratory motion in real time due to its slow imaging speed. The binning-based MR imaging methods (Feng et al., 2016; Grimm et al., 2015; Munoz et al., 2018; Rank et al., 2016; Robson et al., 2018) are often used to address this issue, where MR k-space data are grouped into different motion phases based on surrogate signals (e.g., EKG), navigator signals, or k-space data alone, and images of each motion phase are then reconstructed for the estimation of motion vector fields. However, the binning-based MR imaging methods suffer from three noticeable limitations. First, they assume pseudo periodic motion, which does not hold well in the case of arrhythmia and irregular respiratory motion. Secondly, they rely on either surrogated signals or navigator signals acquired along a single direction to assign k-space data to specific motion phases, which cannot reliably capture voluntary body motion. Thirdly, their performance is limited by the inherent trade-off between the number of motion phases (and thus the accuracy of motion field measurement) and data acquisition time.

In Chapter 4, we demonstrate how we were able to correct motion and to improve resolution from multiple shifts of a phantom during a PET scan using MR in a PET/MR setup.

### **External tracking devices**

Since standard motion correction techniques, which typically rely on registration of reconstructed PET images, have limited temporal resolution and often fail to correct the effects of rapid or continuous head motion, an alternative approach is to use external optical tracking systems, which provide motion information with excellent temporal and spatial resolution. Those features are essential in the context of brain studies which was the main application of this PhD work.

There have been various approaches to tracking head motion using external devices in PET imaging. Some early methods used transducers (Green et al., 1994) or miniature lamps attached to the patient's head (Goldstein et al., 1997), which were tracked by external radio devices or optical cameras, respectively. Other methods used mechanical arms (R.R. Fulton et al., 2002a) or infrared cameras to track reflective markers attached to the head. More recently systems using infrared cameras to track reflective markers, have been widely implemented (Lopresti et

al., 1999). Other systems use visible spectrum stereo-optical cameras to track small markers attached to the head and have been successful in accurately resolving the motion of small subjects. These systems typically rely on the assumption that the motion of the markers accurately represents the motion of the brain. In general, this assumption is justified.

To make proper use of the tracking information for motion correction of PET, the signal must be spatially and temporally aligned to the PET acquisition system. However, newer optical tracking devices do not necessarily provide an external trigger input or output signal, like previous-generation models did. For example, the Polaris Vega (NDI), that we used for our studies, offers overall desirable performance, but only provides a network interface, and therefore needs an alternative integration scheme that should be adaptable to any similar device. Robust methods for the temporal and spatial alignment of a high-performance optical motion tracking system (Polaris Vega, NDI) with a state-of-the-art clinical PET/CT scanner (GE Discovery MI) to perform motion correction for brain PET studies will be presented in the next chapter.

## **2.5 Conclusion and Research Objectives**

This chapter concludes the introductory part of this manuscript. We discussed the challenges of PET quantification, including resolution, motion, partial volume effect, and noise. We have defined these challenges, discussed their source and impact on the accuracy of PET imaging, and reviewed the correction methods that are currently used to address them. We highlighted the importance of addressing these challenges in order to improve the diagnostic capabilities of PET imaging.

Through the course of this PhD, we have aimed to address these challenges and improve the accuracy of PET quantification through the implementation of various techniques and methodologies. Specifically, in Chapter 3, we will present a motion correction method that integrates an optical tracking device, and in Chapter 4 and Chapter 5, we will demonstrate the implementation of super-resolution techniques in PET/MR and brain PET imaging using a real-time motion capture system. In Chapter 7 we will explore a technique called non-negative matrix factorization to disentangle specific, non-specific, and off target signal of [ $^{18}\text{F}$ ]MK-6240 in Tau dynamic sequences.



# Chapter 3

## Motion correction: integration of a real-time tracking camera

This chapter introduces the prerequisite steps to achieve motion correction and, ultimately, super-resolution. We explained in Chapter 2 how head motion degrades the spatial resolution and quantitative accuracy of brain PET images. While a subject's head can be mechanically restrained to minimize movement, most brain studies exhibit motion artifacts in practice. Standard motion correction techniques, which typically rely on the registration of reconstructed PET images, have limited temporal resolution and often fail to correct the effects of rapid or continuous head motion. An alternative approach, presented in Section 3.1, is to use external optical tracking systems, which provide motion information with excellent temporal and spatial resolution. To properly use such information for motion correction of PET, the tracking signal must be spatially and temporally aligned to the PET acquisition system. However, newer optical tracking devices don't necessarily provide an external trigger input or output signal, as previous-generation models could have. In Section 3.2, we describe the architecture of the hardware interface that we built for the communication and temporal alignment of a high-performance optical motion tracking system (Polaris Vega, NDI) with a state-of-the-art clinical PET/CT scanner (GE Discovery MI) and on the SAVANT scanner that we described in Chapter 1, to perform motion correction for brain PET studies. Section 3.3 describes how the measured external motion information is used in a list mode MLEM reconstruction framework to correct PET lines of response for motion directly. We performed experiments with moving point sources, a Derenzo resolution phantom, and a Hoffman brain phantom to assess the motion correction performance we present and discuss in Sections 3.4 and 3.5. In all experiments, the developed approach produced PET images exhibiting fewer motion artifacts than non-corrected ones, with quality approaching that of the static reference images.

### 3.1 Introduction

The High-Resolution Research Tomograph (HRRT), developed 20 years ago by CTI/Siemens, remains the standard-bearer for performance in brain PET with  $\sim 16 \mu\text{L}$  volumetric resolution, but better performance is required to push cutting edge neurological degenerative disease studies (Carson and Kuo, 2019). We are building the Scanner Approaching in Vivo Autoradiographic Neuro Tomography (SAVANT) (Figure 3.1). Based on the LabPET-II technology platform (Gaudin et al., 2015), it is expected to achieve under  $2 \mu\text{L}$  volumetric resolution (Gaudin et al., 2019), nearly one order of magnitude better than the HRRT. Technical information on the SAVANT scanner's architecture is given in Section 1.3.3 of Chapter 1.

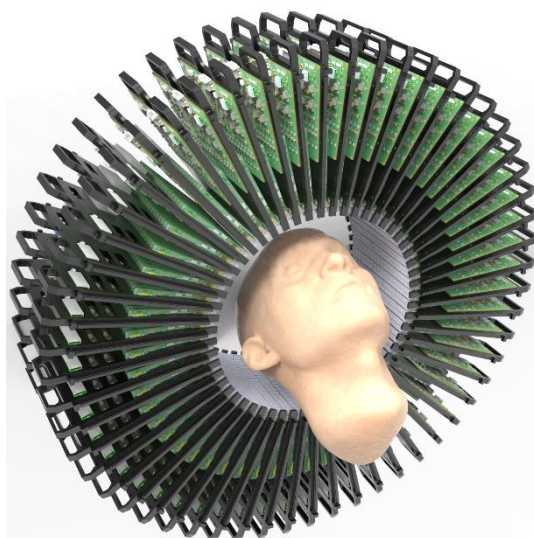


*Figure 3.1 SolidWorks model of the SAVANT scanner geometry.*

The very high resolution of the SAVANT will unavoidably be smeared by involuntary motion from the patient during the measurement, therefore requiring correcting data for those displacements as accurately as possible. Head motion tracking can be performed using infrared markers (R.R. Fulton et al., 2002a), or using PET data driven methods (Lu et al., 2019). However, given the unprecedented resolution of this scanner, it is important to begin with a well understood reference methodology for motion correction, and motion tracker-based correction schemes have been recognized as excellent baseline references for rigid-motion scenarios like brain imaging.

We chose to integrate a motion tracker from the NDI Polaris family, which has shown very reliable performance in the past (R.R. Fulton et al., 2002a), (Jin et al., 2014). However, more recent models with improved accuracy often no longer offer an output synchronization trigger

port. Many models now only provide an Ethernet port, but with support for network synchronized Precise Timing Protocol (PTP, IEEE-1588 standard). This, on the other hand, presents an opportunity to directly merge the motion data with the PET data using the PTP timestamps and enable real-time corrections to the list mode data, and thus real-time, event-by-event motion-corrected image reconstruction. The overall synchronization design also applies to any other type of Ethernet-enabled peripheral to be integrated into the SAVANT or other timestamp-based scanners. Lastly, it is highly desirable to also support a so-called legacy mode to easily share the motion capture camera among PET systems available in an institution.

In the next parts, we describe the firmware and software architecture bridging the PET Data Acquisition System (DAQ) with a PTP enabled network-based motion capture camera. The architecture is structured to support both the SAVANT's fully timestamp based DAQ, as well as a legacy mode for compatibility with other scanners by using their gating input ports. Experimental results are presented for each bridge type using two different scanners to demonstrate its effectiveness and portability.

## **3.2 Architecture Description**

### **3.2.1 Camera selection**

With an anticipated volumetric spatial resolution for the SAVANT scanner that is better than  $2\ \mu\text{L}$ , the NDI Polaris Vega motion capture camera (MCC) was selected. It is a device approved for medical environments with  $0.12\ \text{mm}$ , or  $0.022\ \mu\text{L}$  FWHM volumetric accuracy, that locates infrared reflective beads fixed on a rigid frame. The NDI Polaris Vega is controlled through a gigabit Ethernet port (instead of USB as in older models), simplifying its hardware connection interface to any remote client over a local area network, including embedded systems. The MCC provides complete 6 degrees of freedom (6DoF) information (position and rotation quaternion) in the standard operation mode, with selectable frame rates of 20, 30 and 60 Hz. The exposure time ranges between 400 and 1200 microseconds, with default at 800 microseconds. The internal image capture trigger is derived from an onboard clock, which also provides the timestamps attached to the 6DoF and local ancillary subsystems. The onboard clock is PTP compliant (IEEE-1588) and includes hardware-assisted PTP synchronization support for optimal results.

### **3.2.2 SAVANT DAQ Overview**

The SAVANT DAQ is a modified version of the one used in the LabPET-II preclinical systems (Njejjimana et al., 2016, 2013). Time synchronization is enabled by the distribution of a high precision 100 MHz reference clock incrementing a reference counter (Arpin et al., 2011). Every



module in the system (front-end ASICs and FPGAs) has a copy of this counter, synchronized on a slow-period “sync” signal distributed side-by-side with the reference clock (Figure 3.2, right side).

Instead of using customized or vendor-defined multigigabit protocols, the detector boards for the SAVANT push out the detected single events through standard gigabit Ethernet connections. Two Ethernet switches act as data concentrators and transfer the raw data to the software coincidence engine through their respective 10 Gbps uplink ports, sufficient to support the maximum event rate of the system. The coincidence engine then proceeds to extract coincidences from the flow in real time (Figure 3.2, upper-left side). Other types of ancillary data such as gating inputs, temperature sensors and per-channel count rates are then inserted in the list mode data, time-aligned with coincidences with their respective attached timestamps obtained from a copy of the system counter.

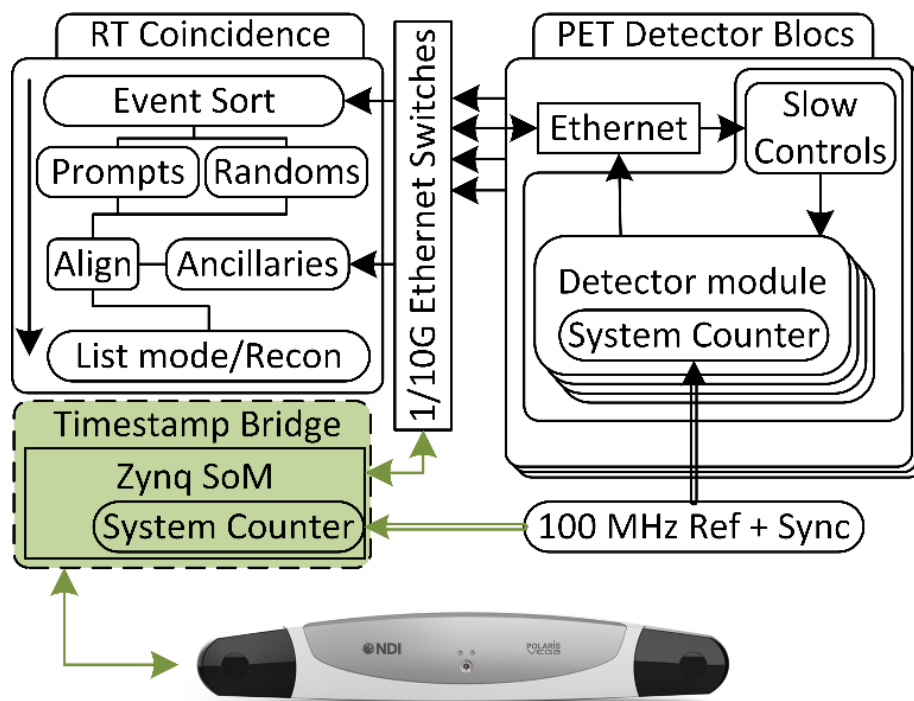


Figure 3.2 Overview of the DAQ for the SAVANT system. The motion capture camera is integrated through a timestamp synchronizing bridge (green).

### 3.2.3 Timestamp-based bridge

The SAVANT DAQ’s building block is the Zynq-7000 System on Chip (SoC), which includes an ARM processor and FPGA fabric. The MCC host board acting as the timestamp bridge (Figure 3.2, in green) has two Ethernet ports: one connected to the SAVANT DAQ Ethernet switch, while the other is connected to the MCC for control, data collection and PTP

synchronization. Hardware PTP support in the embedded Ethernet core has been disabled by Xilinx due to known issues in the processor-side hardware (Cherukupally, 2017). However, this high precision mode is still possible in the Zynq-7000 using a logic core for serial Ethernet interfaces (i.e., with a SFP module). Without an SFP module interface, the alternative is to fall back to software PTP alignment (without hardware assistance), with increased but acceptable time alignment jitter, that is, smaller than the MCC’s exposure time.

To run the SAVANT DAQ counter and PTP time in lockstep, a PTP-compliant timer is implemented in the programmable logic fabric using the open-source ha1588 module and paced with the DAQ’s 100 MHz reference clock (Figure 3.3). A register is configured to simultaneously capture the DAQ counter and PTP-compliant timer on request, providing the exact relationship between the two and enabling a cycle-accurate substitution of the PTP time for the DAQ timestamp.

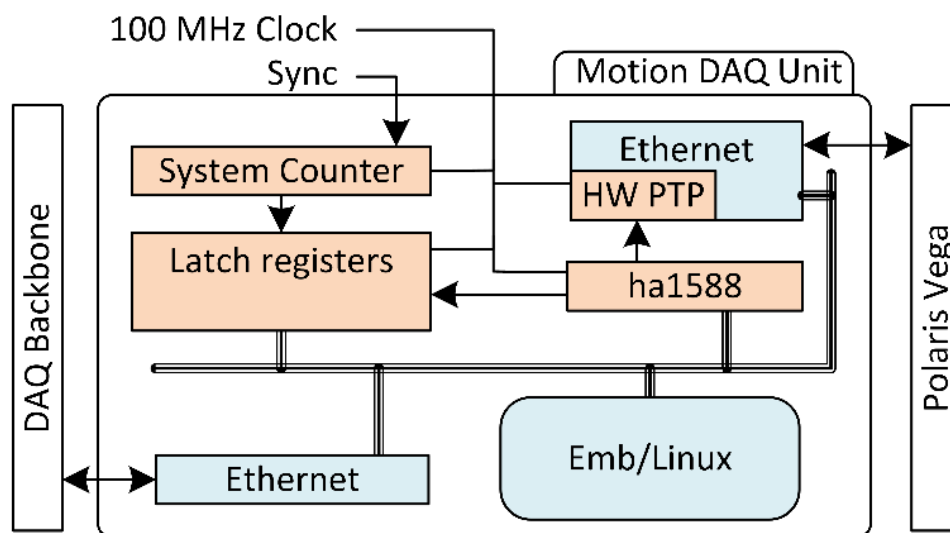


Figure 3.3 Embedded system implementation for the timestamp bridge. Blue boxes are fixed processor system components, and orange blocks are in the programmable logic fabric. The PET system counter and PTP/ha1588 modules run in lockstep and can be latched together in order to remap the PTP timestamps to scanner timestamps.

### Software

The embedded processor inside the Zynq-7000 SoC runs a Debian variant of Linux using a kernel provided by Xilinx. It therefore has access to almost every mainstream Linux software component, such as the GCC compiler toolchain and system services including *linuxptp*. This service is configured here to act as a PTP Master node. The MCC thus has its internal PTP counter continuously synchronized with the PET scanner. The ha1588 VHDL module is made visible to the Linux OS through an open-source device driver. In cases where the hardware-

assisted PTP synchronization is enabled (requiring the SFP module for Zynq-7000), the driver provides seamless integration with the *linuxptp* program. Without the SFP support, the *linuxptp* source code needs to be slightly modified to fetch the lockstep PTP-compliant time hosted in the FPGA fabric instead of the Linux kernel time.

The second software component is a custom application whose role is to control the MCC, recover the motion capture frames, substitute their PTP timestamp and then send the packet to the main DAQ. NDI provides the full source code for a C/C++ API and control library for their devices, on top of which the application was prepared. Its tasks cover configuring the MCC, requesting start and stop of motion capture, converting the PTP timestamp to scanner timestamp by accessing the VHDL registers (Figure 3.3), formatting the data in a PET list mode packet and sending them to the main DAQ system (Figure 3.2). The application also monitors error codes issued by the MCC, such as the PTP synchronization status and visibility of the motion tracking tool. This ensures that these error flags are available in the list mode file to clearly indicate data portions that have potentially unusable motion information.

### **Legacy bridge**

The legacy variant sends electrical pulses to indicate to the PET scanner when a frame is captured by the MCC (Figure 3.4), where the pulse must be aligned with the MCC's capture time. To determine when to generate pulses, after the MCC starts capturing motion frames, a monitoring thread picks up the PTP timestamp from initial 6DoF frames. Since the embedded system and the MCC share a synchronized PTP time counter, the embedded system can then use its own local clock and the configured motion capture period to determine when to send pulses for the upcoming capture times. Pulses are sent through a general-purpose input/output (GPIO) interface, connected to one of the PET scanner's gating input ports (Figure 3.4).

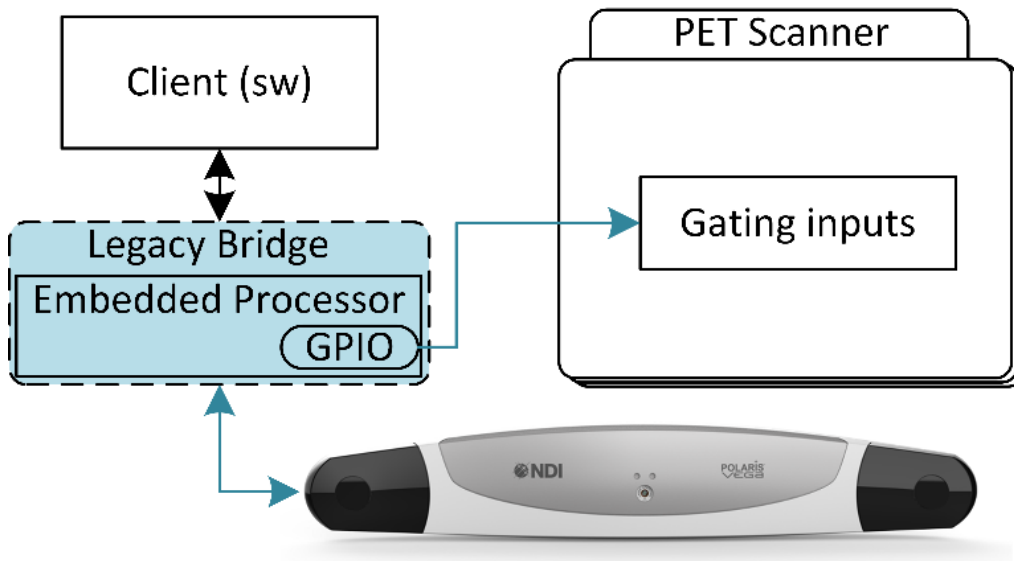


Figure 3.4 Legacy-mode connection scheme with available PET gating input.

To align the list mode gating flags with the MCC 6DoF data, the operator requests the injection of a burst of pulses shortly after the start of the PET acquisition sequence, creating a signature early in the PET list mode data. By having the software log the pulse times and marking the signature insertion time as such (Figure 3.5), it becomes possible to find the signature in both files, and then use the pulse times to match the 6DoF data with a corresponding gating flag. The signature can also be inserted at user chosen times, for example between bed positions.

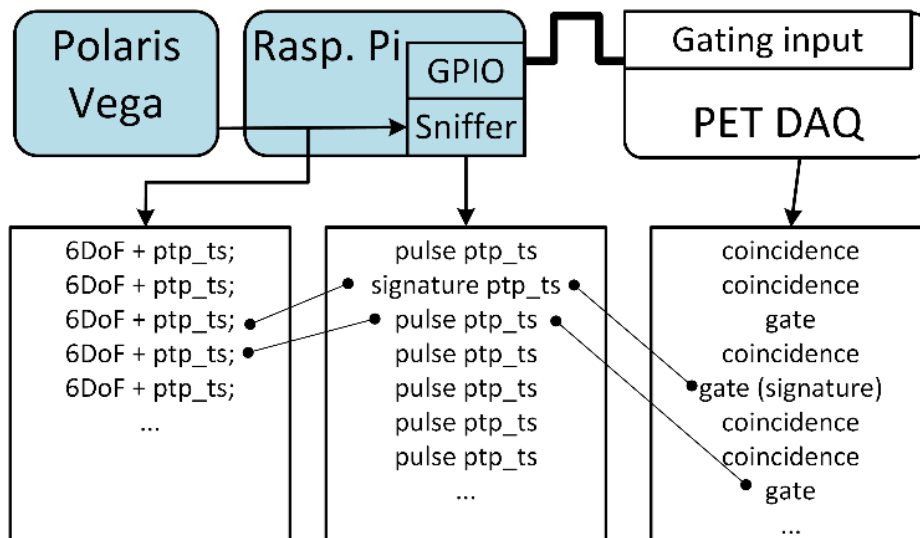


Figure 3.5 Legacy bridge using Raspberry Pi. Synchronization between motion data and list mode PET data (either coincidence or single events) uses a gating input port to insert either a short sequence (start signature) or single triggers aligned with position capture. Correspondence between the motion data and list mode data is then determined post-acquisition.

Although software-based pulse generation does not nearly have the same precision as FPGA fabric timing, in this case the MCC's (NDI Polaris Vega) exposure time ranges between 400 and 1200  $\mu$ s. A high priority software thread is therefore sufficiently precise to align the pulses with the exposure window, even accounting for some jitter caused by delays in the standard, non-real-time Linux operating system. In that case, any embedded system with general purpose input/output (GPIO) connectors can host the synchronization interface, such as a Raspberry PI. Understanding this, the software can be programmed to support various embedded platforms and select the appropriate GPIO library and configuration.

### **3.3 Integration of the Polaris**

#### **3.3.1 PTP synchronization measurements**

The synchronization stability between the MCC and embedded Linux was evaluated using the value reported by the MCC's internal PTP offset register. Stability is compared using hardware-assisted PTP (PC network card), using the hybrid timestamp bridge firmware design (Section 3.2.3), and using software-only synchronization (Raspberry Pi3 and Pi4). Offset data was recorded every second for 3 minutes while the MCC was transmitting motion data. The minimum and maximum offset values were noted providing the total offset range (max – min). The standard deviation was also calculated to indicate variation during an acquisition.

#### **3.3.2 Test system for timestamp-based bridge**

Because a full SAVANT detector ring is not yet available, initial integration tests were conducted using a LabPET-II mouse scanner, offering 0.78 mm FWHM spatial resolution (Gaudin et al., 2021b). Both PET systems share the same front-end electronics and synchronization scheme, allowing this substitution for system integration tests and validation with phantoms. The timestamp-based bridge host board was connected to the mouse scanner system clock and synchronization signal through an available expansion connector, and motion data merged using available time markers in the list mode file. Two imaging targets were used: a 0.4 mm  $^{22}\text{Na}$  point source and an ultra-micro hot spot resolution phantom with 0.75, 1.0, 1.35, 1.7, 2.0, and 2.4 mm hollow channels filled with  $^{18}\text{F}$  solution.

#### **3.3.3 Test system for legacy bridge**

The legacy variant was tested using a Raspberry Pi4, which also serves to demonstrate the architecture's portability. The MCC was connected to the Pi's main gigabit Ethernet port, while a USB-Ethernet dongle provided the connection with a control computer. The Pi's embedded Linux OS runs the standard *linuxptp* program and the MCC client application. Pulses were generated through the Pi's GPIO port and connected through a level shifter buffer circuit to the

gating port of the GE Discovery MI PET/CT scanner. This scanner provides a 4.3 mm FWHM spatial resolution in the center of the field of view (Pan et al., 2019). Two imaging targets were used: a 6.0 mm  $^{22}\text{Na}$  point source and a Hoffman brain phantom filled with 185 MBq  $^{18}\text{F}$  activity.

### **3.3.4 Motion tracking and motion generation**

The NDI Polaris Vega acts as MCC. It was shipped with a pre-calibrated marker tool which holds four reflective infrared beads. The tool can then be attached to a rigid body (i.e., the phantom) and thus reports its displacements with six degrees of freedom. For consistent results across different measurements, reflective stickers can be affixed to the PET scanner's frame, in which case the relative position between the marker tool and the scanner can be obtained instead of a position relative to the MCC. The motion capture and reconstruction coordinates grids thus become consistent throughout different imaging sessions even if the MCC is moved. This was done on the GE Discovery MI with NDI providing software tools, but not on the LabPET-II as the MCC will not be repeatedly used with this system. Manual grid alignment was chosen instead for the tests on the preclinical system.

A limitation for this test on the LabPET-II is the very small bore opening, smaller than the smallest supported tracking tool configuration. Free motion is therefore not mechanically feasible. Instead, a motorized stage induced a 1 cm linear, cyclic and continuous motion on the scanner's bed, to which was affixed the marker tool outside the bore. The bed, phantom and tracking tool behave as one rigid body.

Bore size is not an issue with the GE Discovery MI, so the marker tool was affixed directly on the Hoffman phantom. The phantom was then rolled back and forth on an inclined plank by a motorized piston, providing continuous translation and rotation displacements. Furthermore, the plank was positioned diagonally from the scanner central axis to create blurring across the field of view. For the point source, a motorized stage was placed on the bed, with the marker tool affixed to the stage. Here, it provided a 4 cm linear, cyclic and continuous motion.

### **3.3.5 Moving phantom acquisitions and reconstructions**

In all cases, the point sources and phantoms were first measured without motion to obtain a static reference. A second acquisition was then immediately acquired with induced motion. Static and motion corrected images are obtained with GCREcon, an in-house, image reconstruction engine with an event-by-event motion correction module. However, the used version implemented simple single-ray Siddon projection (Siddon, 1985).

While the engine is sufficient to match the spatial resolution reached by the GE system, the projectors implemented so far with motion correction cannot resolve the finest hot spots of the mouse scanner. To show that the issue is due to the engine in development rather than the detectors or motion correction, the static data set were reconstructed with the LabPET-II's default closed-source engine (same as in (Gaudin et al., 2021b)). In this case the reconstruction parameters were set to 4 and 16 OSEM iterations with 8 subsets,  $0.3 \times 0.3 \times 0.3$  mm pixels and all corrections enabled (normalization, attenuation, randoms and scatter).

With the LabPET-II mouse scanner, 3.1 million prompts were acquired from the small point source and reconstructed from 4 OSEM iterations with 8 subsets using GCREcon. For the resolution phantom case, 100 million prompts were obtained from the resolution phantom filled with  $^{18}\text{F}$  and reconstructed from 4 OSEM iterations with 8 subsets. No corrections were applied to static and motion image reconstructions (no normalization, attenuation, randoms or scatter corrections). Images were reconstructed with  $0.3 \times 0.3 \times 0.3$  mm pixels.

With the GE Discovery MI clinical scanner, a first test acquired 4 million prompts from the larger point source and reconstructed with 20 MLEM iterations. For the second test case, the Hoffman brain phantom was filled with  $^{18}\text{F}$  from which a total of about 1.2 billion prompts were acquired and reconstructed from 3 OSEM iterations with 12 subsets. Normalization, attenuation, randoms and scatter corrections were applied to static and motion image reconstructions. Images were reconstructed with  $2.0 \times 2.0 \times 2.8$  mm pixels.

For motion corrected reconstruction, the motion data obtained from the tracker was used to transform the endpoints of measured lines-of-response (LORs) on an event-by-event basis at the corresponding MCC frequency rate (60 Hz). A list-mode OSEM reconstruction algorithm modified from (Rahmim et al., 2004) was implemented using the formulation (1.29) introduced in Chapter 1F:

$$\hat{\rho}_j^{it+1} = \frac{\hat{\rho}_j^{it}}{\hat{S}_j} \sum_{m=1}^M P_{i'_m j} \frac{1/I'_{i'_m}}{\sum_{k=1}^J P_{i'_m k} \hat{\rho}_k^{it} + S_{i'_m} + R_{i'_m}} \quad (3.1)$$

where  $\hat{\rho}_j^{it}$  is the image value at voxel  $j$  and iteration  $it$ ,  $M$  is the total number of events in the list-mode file,  $P_{ij}$  is an element of the system matrix accounting for the geometric probability that an event generated in voxel  $j$  is detected along a LOR  $i$ ,  $i'_m$  is the LOR  $i$  associated with list-mode event  $m$ , with  $i'_m$  being the LOR after motion correction (MC),  $I'_{i'_m}$  is the *in vivo* attenuation correction factor for LOR  $i'_m$ ,  $S_{i'_m}$  and  $R_{i'_m}$  account the scatter and random

contributions, and  $\tilde{S}_j$  is the time-averaged sensitivity image (Rahmim et al., 2004) that accounts for LOR normalization factors and hardware attenuation.

## 3.4 Results

### 3.4.1 PTP synchronization range and stability

The NDI Polaris Vega MCC showed very stable time alignment when controlled through hardware assisted PTP master node, with a range of less than 50 ns (Table 3.1). Hybrid PTP synchronization from the timestamp bridge also showed very good performance with less than 3.5  $\mu$ s min-max range. The Raspberry Pi3 gave less stable results with a min-max range of 90.5  $\mu$ s and drifted twice beyond a 50  $\mu$ s offset over a 3-minute period. This is likely due to delays induced by an onboard gigabit Ethernet chip which uses USB2 to link with the processor, causing less deterministic behavior in the PTP handshake protocol. Tests executed on the Pi4, which has a true gigabit Ethernet link with the processor, were better with a min-max range of 4.2  $\mu$ s, supporting this hypothesis. Except for the Pi3, the offset travel/swing is at or below 1/100<sup>th</sup> of the MCC's minimal exposure time (3.2.1), thus providing suitable synchronization for both the timestamp-based and legacy pulse bridges.

Table 3.1 - PTP offset measurement results

	Min (ns)	Max (ns)	SD (ns)
<b>HW/PTP</b>	-23	19	7.6
<b>TS Bridge</b>	-1,098	2,428	495.6
<b>SW/Pi3</b>	-45,427	55,154	11,119.0
<b>SW/Pi4</b>	-2,214	2,015	687.8

### 3.4.2 Motion correction with point sources

Point source experiments in both scanners show good motion recovery for the induced linear movement. For the LabPET-II, without source size and annihilation photon non-collinearity correction and without physical modeling of the transition matrix, the motion-induced point source line profile obtains 1.62 mm FWHM, compared with 1.32 mm FWHM for the motionless condition (Figure 3.6). Similarly, with the GE Discovery MI, the motion compensated image reconstruction obtained 6.8 mm compared with 6.7 mm for the motionless data set (Figure 3.7).



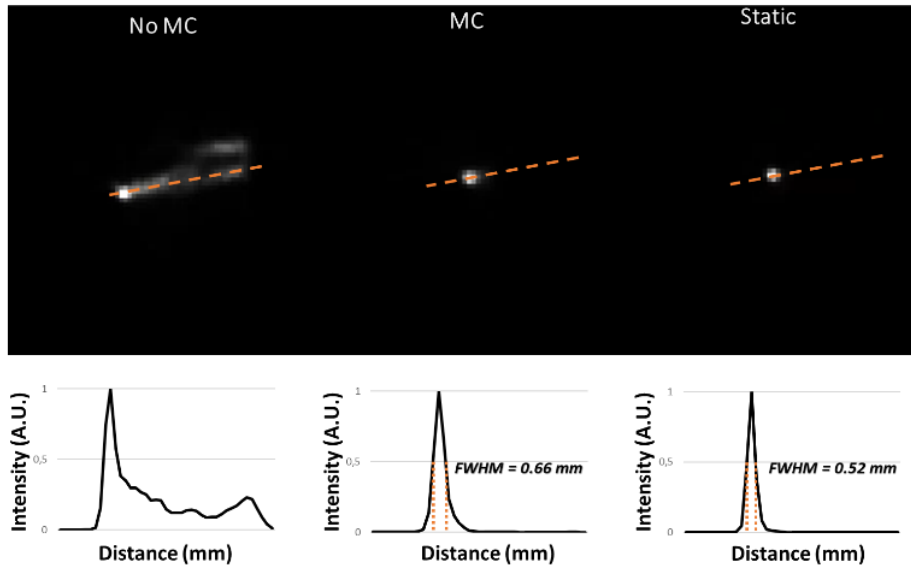


Figure 3.6 Point source reconstruction on the LabPET-II system with motion capture synchronized using the real-time timestamp-based bridge. Top row, left to right: no MC, MC, static reference. Bottom row: associated line profiles passing through the point source reconstructions.

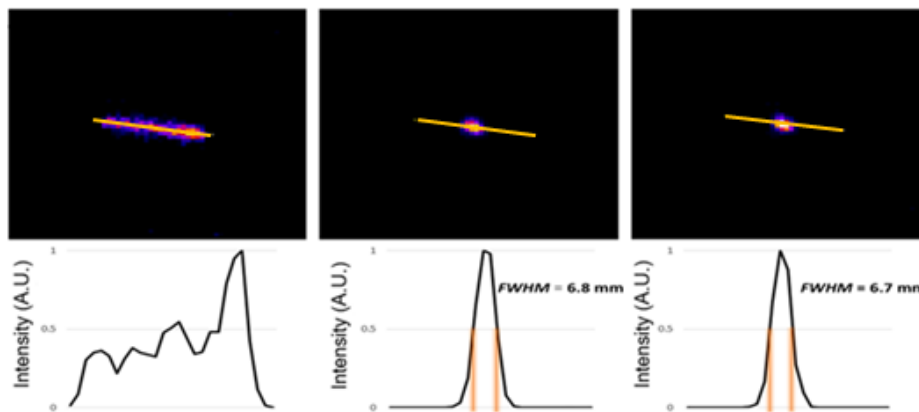


Figure 3.7 Point source reconstructions on the GE Discovery MI PET/CT system, with motion capture synchronized using the legacy mode on the Raspberry Pi4. Top row, left to right: no MC, MC, static reference. Bottom row: associated line profiles passing through the point source reconstructions.

### 3.4.3 Motion correction with phantoms

The resolution phantom static data was first reconstructed using a closed-source commercial engine optimized for the LabPET-II, showing in Figure 3.8 features on par with previously reported results (Gaudin et al., 2021b).

The same static data set was reconstructed with the event-by-event engine and compared with the motion-induced acquisition without and with motion correction. The motion-corrected image demonstrates recovery on par with the point source, where the 1.7 mm resolution spots are resolved nearly as well as with the static data set (Figure 3.9). While the reconstruction

engine does not reach the full potential of the LabPET-II, it does demonstrate correct integration between the system and the MCC.

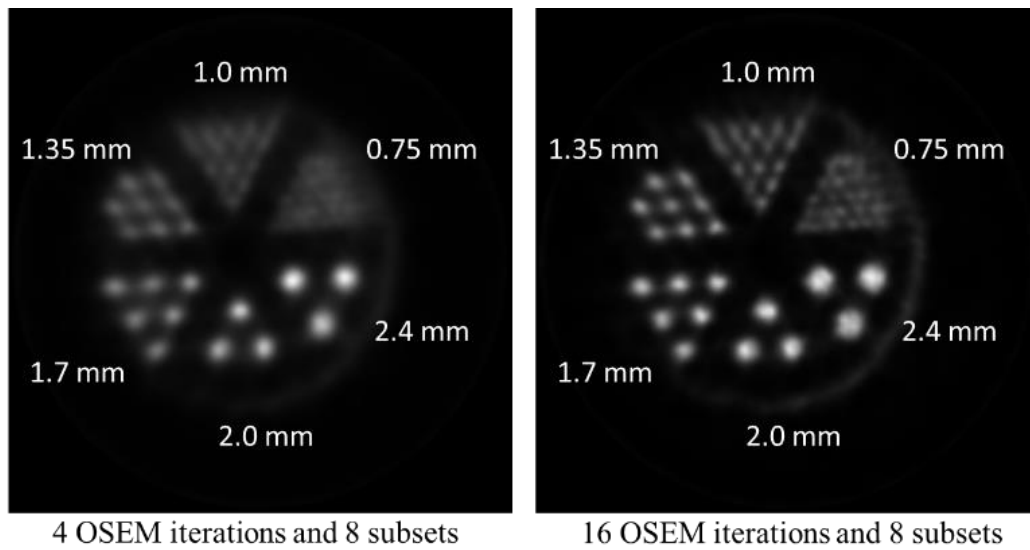


Figure 3.8 Resolution phantoms reconstructed with the default LabPET-II engine. Left: 4 OSEM iterations and 8 subsets; Right 16 OSEM iterations with 8 subsets.

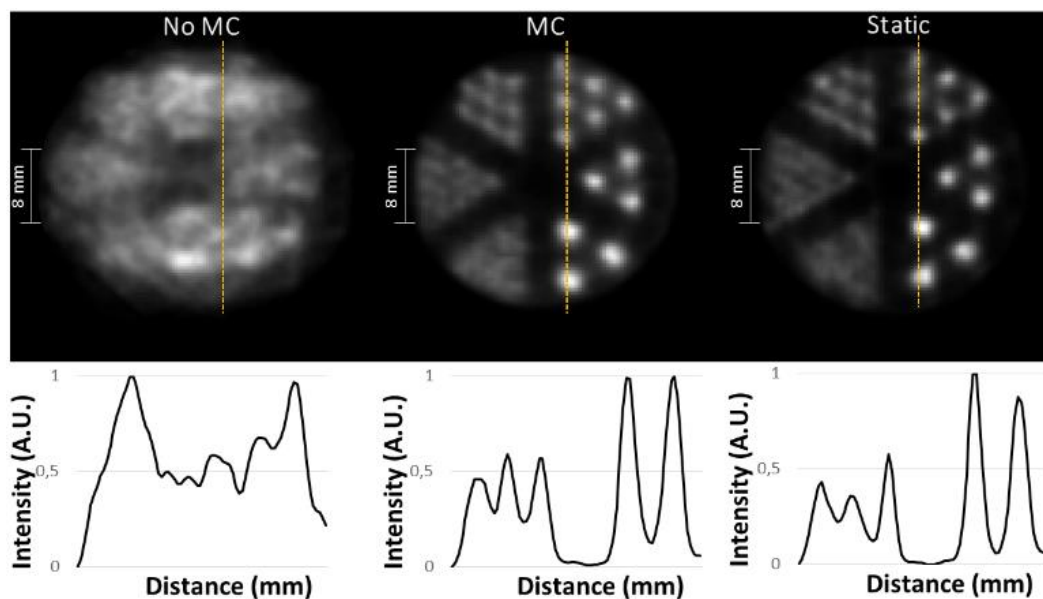


Figure 3.9 Images from the LabPET-II system reconstructed with the in-house OSEM engine GCRecon. The static data is the same as in Figure 3.8, but different coordinates space. Top row, left to right: no MC, MC, static reference. Bottom row: associated line profiles passing through the point source reconstructions.

Similarly, with the GE Discovery MI, the motion-induced Hoffman brain phantom is unblurred, with some differences with the static image in the line profile but still providing significant recovery from motion blurring (Figure 3.10).

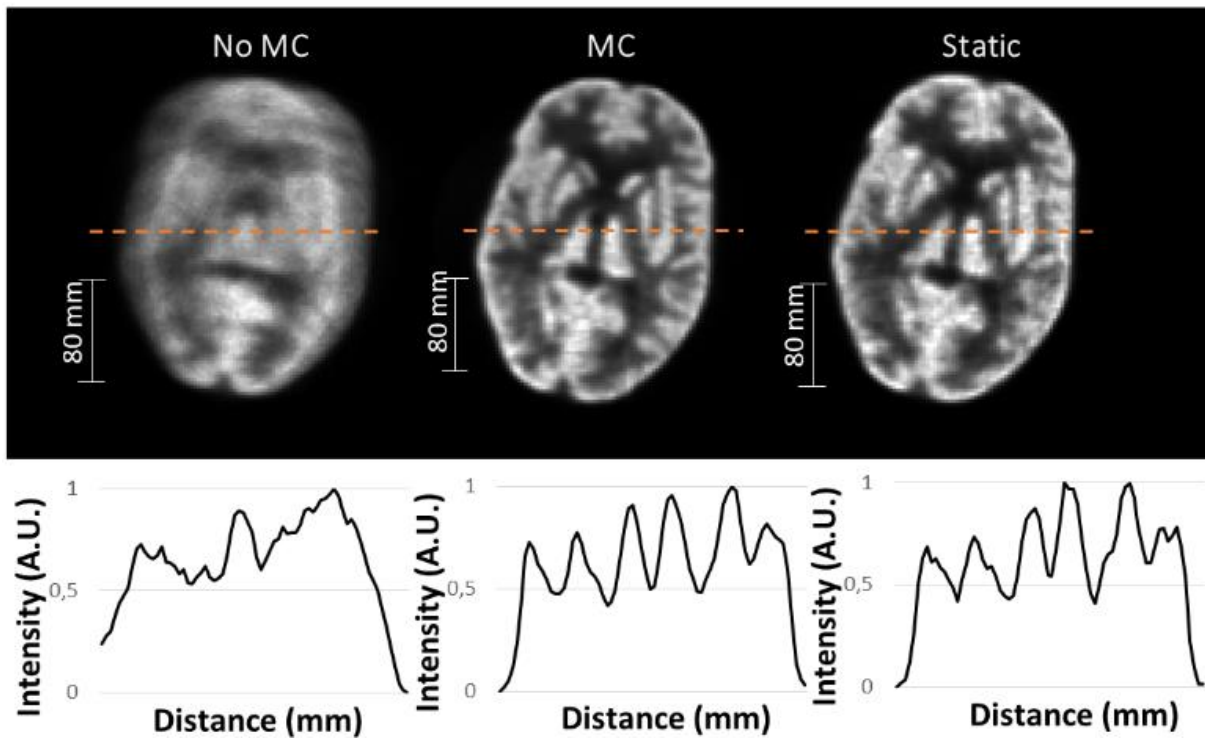


Figure 3.10 Hoffman phantom reconstructions on the GE Discovery MI PET/CT system, with motion capture synchronized using the legacy mode on the Raspberry Pi4. Top row, left to right: no MC, MC, static reference. Bottom row: corresponding line profiles.

### 3.5 Discussion

Unlike early head motion tracking schemes (R.R. Fulton et al., 2002b), the approach here does not need to wait post-acquisition to merge the two data streams thanks to the PTP timestamps now available from the MCC and translated by the bridge into PET timestamps. The coincidence engine can now directly insert and align the motion data with PET coincidence data in (Figure 3.2). This enables support for real-time, motion-corrected, event-by-event image reconstruction, which could prove quite useful with short-lived radiolabeled tracers for cognitive brain studies in the SAVANT system, allowing the operator to monitor if the measurement was successful and administer an additional dose if not.

The point source on the GE Discovery MI shows excellent motion recovery, in good part thanks to the alignment of the motion capture and PET coordinates grids. This alignment is not possible with the LabPET-II because the procedure requires placing a marker tool at several different positions inside the bore, and the marker does not fit even for a single position. It is then difficult to avoid slight blurring resulting from manually aligned coordinates grids, as seen along and perpendicular to the point source's line profile (Figure 3.6, center). This blurring then also similarly affects the resolution phantom images, making the spots smaller than 1.7 mm difficult to distinguish. Once assembled, the SAVANT will have a large enough bore

to complete the alignment procedure, and blurring caused by grid misalignment will be significantly reduced or completely removed. This step will also be critical when testing super-resolution reconstruction on the SAVANT.

It is also important to note that the event-by-event motion corrected image reconstruction engine does not implement corrections like scatter, randoms and attenuation for the LabPET-II. It also uses the much simpler single-ray Siddon projector. Because of this, the smaller hotspots are not resolved unlike with the dedicated engine. Full corrections and a better projector are being prepared for the SAVANT system.

Lastly, while PET single events require better time alignment than provided by software or hardware based PTP, PTP is accurate enough to time-align the motion data. In addition to the MCC, the timestamp bridge is also suitable for other scanner peripherals such as blood counters (Convert et al., 2022) or ECG monitors. The bridge avoids the need for device-specific customized cabling and connectors, requiring only a network interface, a major trend in modern radiation instrumentation.

### **3.6 Conclusion**

This work detailed how a network-synchronized motion tracking camera (MCC) approved for medical environments was integrated and synchronized with a timestamp-based PET data acquisition system. Even when using lower accuracy software synchronization on an embedded processor, the offset range is less than a few microseconds, well within the MCC's exposure time window. The data stream from the MCC is then seamlessly merged into the PET list-mode data, enabling real-time motion corrected, event-by-event image reconstruction for rigid bodies. The system also supports a legacy mode, allowing the MCC to be used on other PET systems with available gating input connections. Integration tests were successfully conducted with both timestamp based and legacy PET DAQ systems, and motion corrected images nearly match the phantom motionless reference images.

Once the full SAVANT system is available on the GE DMI scanner, future experiments will focus on validating the overall motion correction scheme with volunteers instead of phantoms. Furthermore, it will be possible to attempt super-resolution reconstruction (Chemli et al., 2021), which could further increase the reconstructed resolution of the GE PET/CT or the SAVANT, ultimately providing a brain dedicated PET scanner with unmatched very high spatial resolution. The following contribution regarding super-resolution were achieved on our

GE Discovery scanner and used with the legacy mode using the cardiac gating input connection of the scanner.

In the next chapter, we present a literature review as well as a proof of concept for super-resolution in brain PET imaging using a PET/MR.

# Chapter 4

## Super-resolution principles and a PET/MR proof of concept

This chapter presents the principles and techniques of super-resolution (SR) in image processing and in PET imaging as well as a proof concept in PET/MR. In Section 4.1, we recall some of the challenges of PET imaging and emphasize the need for improved resolution. In Section 4.2, we explore how super-resolution methods aim to generate a high-resolution image from one or multiple low-resolution images by combining the partial non-redundant information contained in the low-resolution images. Different methods are presented in Section 4.3, where we discuss the state-of-the-art of super-resolution in image processing and PET imaging. In the context of PET imaging, Section 4.4 presents a proof of principle for using super-resolution techniques in a PET/MR setup to improve the spatial resolution of PET images. The proposed method involves using the OSEM algorithm to maximize the log-likelihood function and iteratively estimate the high-resolution PET image from sinograms obtained from multiple scans. The method was tested on a Hoffman brain phantom, resulting in improved spatial resolution and better correspondence with high-resolution MRI images compared to standard OSEM. These results, presented and discussed in Section 4.4.3, demonstrate the usefulness of super-resolution techniques in PET/MR imaging to potentially improve the accuracy and reliability of PET images for diagnosis and treatment planning.

### **4.1 Introduction**

For the last several decades, PET neuroimaging has provided unique insights into the brain function, including quantitative measurements of cerebral glucose metabolism and blood flow as well as numerous receptors, transporters, and enzymes (Gunn et al., 2015). In Chapter 1, we saw that more recently, the advent of radiotracers binding to misfolded proteins such as amyloid and hyperphosphorylated neurofibrillary tangles (tau), has ushered in a new era in

PET imaging of neurodegenerative diseases, accompanied by new requirements in terms of image quantification and processing. In particular, imaging of tau pathology, especially in early disease stages, is fueling a need for improved PET spatial resolution (Lecomte et al., 2022) to allow for accurate imaging of more focal tracer uptake patterns and small brain structures (e.g., entorhinal cortex) (Schöll et al., 2016).

In Chapter 2, we established that the effective spatial resolution of PET images is limited by several factors. One relates to the physical effects of positron emission and annihilation, such as the positron range and photon non-collinearity. The other pertains to limitations of hardware and instrumentation, including block effects and the width of the crystals, the latter being by far the main resolution-limiting factor in clinical PET scanners (Li et al., 2014). Another critical effect limiting PET resolution is the subject's movement during the acquisition. Indeed, a brain scan typically extends several minutes up to hours for some dynamic acquisitions. Any substantial head motion during the scan will introduce blurring in the final reconstructed image.

The PET spatial resolution could be enhanced by improving detector designs (e.g., reducing crystal size) and electronics; however, these modifications would incur additional costs and would be challenging to implement in existing PET scanners. In this chapter, we show that it is possible to enhance the spatial resolution of brain PET images using SR.

## 4.2 Principle of super-resolution

Super-resolution methods use a single or multiple acquisition of low-resolution (LR) images to generate one high-resolution (HR) image. The basic idea is to combine the partial non-redundant information contained in several LR images to generate the HR image (Figure 4.1). The partial non-redundant information contained in these LR images is generally introduced by subpixel shifts therebetween.

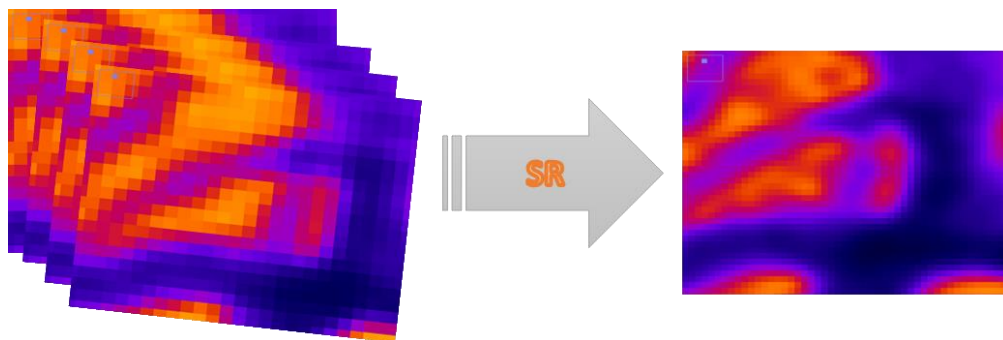


*Figure 4.1 Illustration of SR principle. From multiple shifted captures of the same scene, SR techniques allow reconstructing a high-resolution image with finer details.*

These subpixel offsets can occur due to uncontrolled or controlled movement between the imaging system and the object. SR construction reverses this shifting process by aligning the LR observations to subpixel accuracy and by combining them into an HR image grid (Figure 4.2).

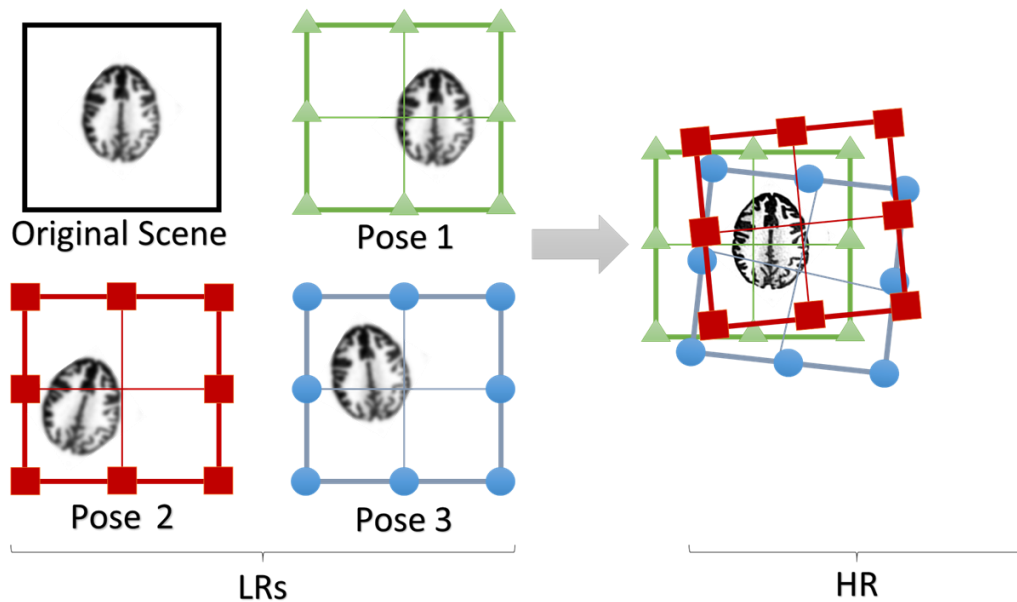


Figure 4.2 The basic idea of SR reconstruction in the image space: In the imaging process, the sensor captures several LR frames downsampled from the HR scene with subpixel shifts between each other. We obtain an image with an improved spatial resolution by fusing the information within all three poses.

To understand the SR problem, we must define an image observation model that relates the original HR image to the different  $k$  ( $k \in \mathbb{N}$ ) observed LR images. Schematized in Figure 4.3, It can be modeled as follows: a low-resolution observation LR of the original image HR is obtained by applying an operator  $L$  modeling the motion (the geometrical transformation), a blur operator  $B$  (modeled by the Point Spread Function) and a down sampling operator  $D$ .

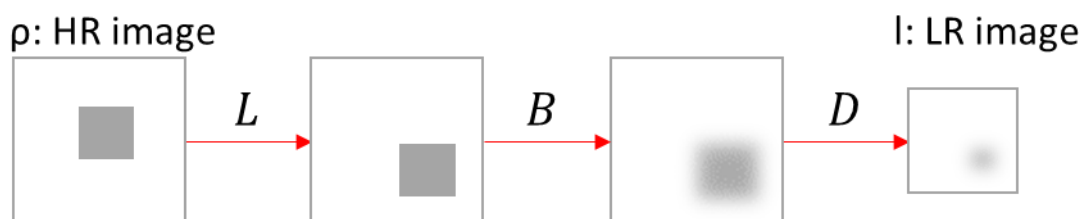


Figure 4.3 Image observation model: the expected HR image undergoes a shift ( $L$ ), a blurring effect ( $B$ ), and a down-sampling operation ( $D$ ).

From this image observation model, we can draw the forward model, which can be written as:



$$l_k = DBL_k \rho \quad (4.1)$$

where  $l_k$  and  $L_k$  denote, respectively, the  $k^{\text{th}}$  LR image shifted by the corresponding  $k^{\text{th}}$  geometrical transformation  $L$ , and  $\rho$  denotes the HR image.

SR usually seeks to invert this forward model, which is a hard inverse problem in the sense that it is ill-posed. A problem is said to be well-posed or well-conditioned, in the sense of Hadamard, if it satisfies the following three conditions:

- there exists a solution,
- the solution is unique,
- it depends continuously on the data.

A problem is said to be ill-posed if at least one of these three conditions is not met. In general, super-resolution problems are ill-posed. They can violate any of the above three conditions. The non-existence of a solution can result from noise in the data. If the imaging operator is not injective, or if there is not a sufficient amount of data, there may be multiple solutions. Additionally, since super-resolution aims to recover information lost during the imaging process, it is intuitive that the solution will likely not be unique. Finally, depending on the characteristics of the imaging system, the solution to the super-resolution problem may be very sensitive to data perturbations and thus violates the last condition of Hadamard.

In the next section, a brief state of the art is presented where authors have attempted to use SR for different applications based on this forward model as well as other formulations.

## 4.3 Literature review

### 4.3.1 General SR methods in image processing

Several super-resolution approaches have been applied in signal and image related fields. We can separate them into four main categories:

- Super-resolution in the frequency domain

Tsai and Huang (Huang and Tsai, 1984) were the first to explore solutions to the problem of super-resolution. These methods aim at finding a continuous, band-limited image from several sampled and translated versions of this image based on the shift and aliasing properties of the continuous and discrete Fourier transforms.

- Interpolation-restoration techniques

Interpolation-restoration techniques are spatial approaches that achieve super-resolution by registering different LR images to a common position (Ur & Gross, 1992). An image is then obtained in non-uniformly spaced samples. These samples are then resampled on a finer grid than the initial one. A method of image restoration (deconvolution for example) is then applied to the resampled image to reduce the effects of blur and noise (Elad & Feuer, 1997).

- Iterative methods

The idea introduced by Peleg in (Peleg, Keren, & Schweitzer, 1987) consists of a back-projection method using the reconstruction constraint as a regularizer. The idea is to start from an estimate  $\mathbf{X}_0$  of the sought image, to compute the corresponding observation  $\mathbf{L}_0$ , and finally to project the error  $\mathbf{L}_0 - \mathbf{L}$  in a high-resolution space to update the current estimate. These operations are repeated until a convergence criterion is reached. The result often depends on the initialization.

Another idea is to estimate a HR image  $\boldsymbol{\rho}$  using the observations of the low-resolution images  $\mathbf{l}$  as well as the projection operator  $\mathbf{P}$  knowledge ( $\mathbf{P} = \mathbf{DBM}$ ). Using the forward model, an HR image can be obtained from the LR images by inverting Equation (4.1). As mentioned above, this is an ill-posed problem, (there is no uniqueness of the super-resolution result), but we can obtain satisfactory results by establishing an iterative scheme for the resolution of this inverse problem.

- Deep learning-based methods:

With the rapid development of deep learning techniques in recent years, deep learning-based SR models have been actively explored and often achieve state-of-the-art performances on various benchmarks of SR. A variety of deep learning methods have been applied to tackle SR tasks, ranging from the early Convolutional Neural Networks (CNN) based method (e.g., SRCNN (Dong, Loy, He, & Tang, 2014)) to recent promising SR approaches using Generative Adversarial Nets (GAN) (e.g., SRGAN (Ledig, et al., 2017)).

### 4.3.2 Super-resolution in PET

Different methods have been proposed over the years to achieve SR in PET imaging. Dagher and Thompson’s work consisted in physically moving the scanner detector rings by a precession or “wobbling” movement, leading to oversampled projections (Dagher and Thompson, 1985). Wernick and Chen showed that further resolution enhancement can be obtained by applying the same super-resolution approach, utilizing detector motion, to directly

improve the quality of the projection matrix before tomographic reconstruction (Wernick and Chen, 1992). In their work, a filtered backprojection using the super-sampled projection matrix was applied on the data yielding substantially improved images in contrast and SNR. Later, instead of moving the detectors, Kennedy et al. created multiple low-resolution frames by shifting and rotating the scanned object. For precise control of the motion, they used a special motorized apparatus comprised of a translational stage and a micrometer. They showed an increase in both resolution and contrast on a clinical scanner (Kennedy et al., 2006). Instead of reconstructing the separately constructed HR sinograms or applying SR to already reconstructed low-resolution images, more recent work integrated the SR estimation directly into the iterative process of the Maximum Likelihood Expectation Maximization (MLEM) image estimation. In (Li et al., 2014) the authors present a super-sampling data acquisition model based on the physical processes of PET acquisition including, the forward model, blurring, downsampling, and motion as its building blocks. Based on their model, they used and extended MLEM algorithms to reconstruct images directly from oversampled data sets leading to improved resolution, contrast, and signal to noise ratio (SNR). In (Verhaeghe and Reader, 2010), a SR PET data framework was introduced to generalize the image reconstruction process in the presence of any type of acquisition motion. The authors studied and exploited wobble or random motion to increase resolution. However, they discretized motion, underexploiting the benefits of continuous motion. With the recent advances in machine learning, PET super-resolution using deep learning has emerged in recent years. Song et al. (Song et al., 2020) used a convolutional neural network to achieve super-resolution on a single acquisition without making use of object motion. Instead, they incorporated high resolution (HR) anatomical information based on magnetic resonance (MR) imaging as well as spatial location information to model the spatially varying blur inherent to PET images, inducing visually finer structural details.

It is important to note that, for any of the previous methods, image registration is critical for the success of SR reconstruction, where complementary spatial samplings of the HR image are fused. Image registration is a fundamental image processing problem that is ill-posed. The problem is harder in the SR setting, where the observations are low-resolution images with heavy aliasing artifacts. The performance of image-based registration algorithms degrades as the resolution of the observations goes down.

In this chapter and the next one, we expose how we achieved SR in two different setups. We started our studies with proof of concept, using a PET/MR machine where the registration was

achieved using simultaneously acquired MR images in a step and shoot fashion. Then, a clinically practical method was studied where the registration was achieved using a high-resolution optical tracking device integrated in a PET/CT setup.

## 4.4 A proof of principle in PET/MR

As a proof of principle, we developed and evaluated a sinogram SR PET reconstruction algorithm for PET/MR, modeling all the physics of projection data formation and taking advantage of simultaneously acquired high-resolution MRI scans to precisely measure the object shifts. We used a sinogram reconstruction approach because the object shifts were acquired at five fixed positions, hence the time information of arrival of the projections was not required.

### 4.4.1 Method

The forward model for the SR reconstruction method was defined according to:

$$\begin{bmatrix} \mathbf{y}_1 \\ \vdots \\ \mathbf{y}_K \end{bmatrix} \sim \text{Poisson} \left\{ \begin{bmatrix} \Delta t_1 \mathbf{N} \mathbf{A}_1 \mathbf{P} \mathbf{D}_{H \rightarrow L} \mathbf{B}_{PSF} \mathbf{L}_{ref \rightarrow 1} \\ \vdots \\ \Delta t_K \mathbf{N} \mathbf{A}_K \mathbf{P} \mathbf{D}_{H \rightarrow L} \mathbf{B}_{PSF} \mathbf{L}_{ref \rightarrow K} \end{bmatrix} \times \widehat{\boldsymbol{\rho}}_{HR} \right\} \quad (4.2)$$

where  $\mathbf{y}_k$  contains the sinogram measured in position  $k$ ,  $\widehat{\boldsymbol{\rho}}_{HR}$  is the unknown HR PET image we want to estimate,  $\mathbf{L}_{ref \rightarrow k}$  is an MR-based interpolation operator that transforms an image from the reference position to the position corresponding to scan  $k$ ,  $\mathbf{B}_{PSF}$  models point spread function (PSF) blurring effects in the image domain,  $\mathbf{D}_{H \rightarrow L}$  is an image down-sampling operator,  $\mathbf{P}$  is the forward-projection operator,  $\mathbf{A}_k$  models attenuation effects for scan  $k$ ,  $\mathbf{N}$  contains the detector sensitivity coefficients, and  $\Delta t_k$  represent the scan fraction time for each scan  $k$ . Hence, the SR reconstruction method treats the sinogram data of a particular scan as a blurred, low-resolution, Poisson-distributed projection of an unknown HR 3-D PET image shifted to a known position. The Ordered Subset Expectation Maximization algorithm (OSEM) was used to maximize the corresponding log-likelihood function.  $\rho_{HR}$  was iteratively estimated from sinograms  $\begin{bmatrix} \mathbf{y}_1 \\ \vdots \\ \mathbf{y}_K \end{bmatrix}$  using:

$$\widehat{\boldsymbol{\rho}}_{HR}^{it+1} = \frac{\widehat{\boldsymbol{\rho}}_{HR}^{it}}{\mathbf{S}} \left[ \sum_{k=1}^K \mathbf{L}_{ref \rightarrow k}^T \mathbf{B}_{PSF}^T \mathbf{D}_{H \rightarrow L}^T \mathbf{P}^T \frac{\mathbf{y}_k}{\mathbf{P} \mathbf{D}_{H \rightarrow L} \mathbf{B}_{PSF} \mathbf{L}_{ref \rightarrow k} \widehat{\boldsymbol{\rho}}_{HR}^{it}} \right] \quad (4.3)$$

with  $\mathbf{S}$  being the sensitivity image that includes the attenuation and sensitivity of the scanner detectors:

$$\mathbf{S} = \sum_{k=1}^K [\Delta t_k \mathbf{L}_{ref \rightarrow k}^T \mathbf{B}_{PSF}^T \mathbf{D}_{H \rightarrow L}^T \mathbf{P}^T \mathbf{A}_k^T \mathbf{N}^T \mathbf{1}_I] \quad (4.4)$$

Scatter and random events contributions were ignored for this study.

#### 4.4.2 Experiment

A Hoffman phantom filled with 2mCi 18F was scanned on a whole-body integrated PET/MR scanner (Biograph mMR, Siemens). A total of five 5-min PET list mode acquisitions were performed, each corresponding to a different phantom position and orientation (Figure 4.4). To measure the precise phantom location for each scan, a high-resolution MRI volume was simultaneously acquired using a Gradient-Recalled Echo sequence (TE = 2.48ms, TR = 6ms, flip angle = 20°, in-plane pixel size = 1×1mm<sup>2</sup>, slice thickness = 1mm). A reference MR image was selected, and all other four MR images were rigidly co-registered to the reference to estimate the spatial shift parameters for each scan. The HR PET image that we seek to estimate depicts the object in the reference position and is estimated iteratively using sinogram data from all five scans.

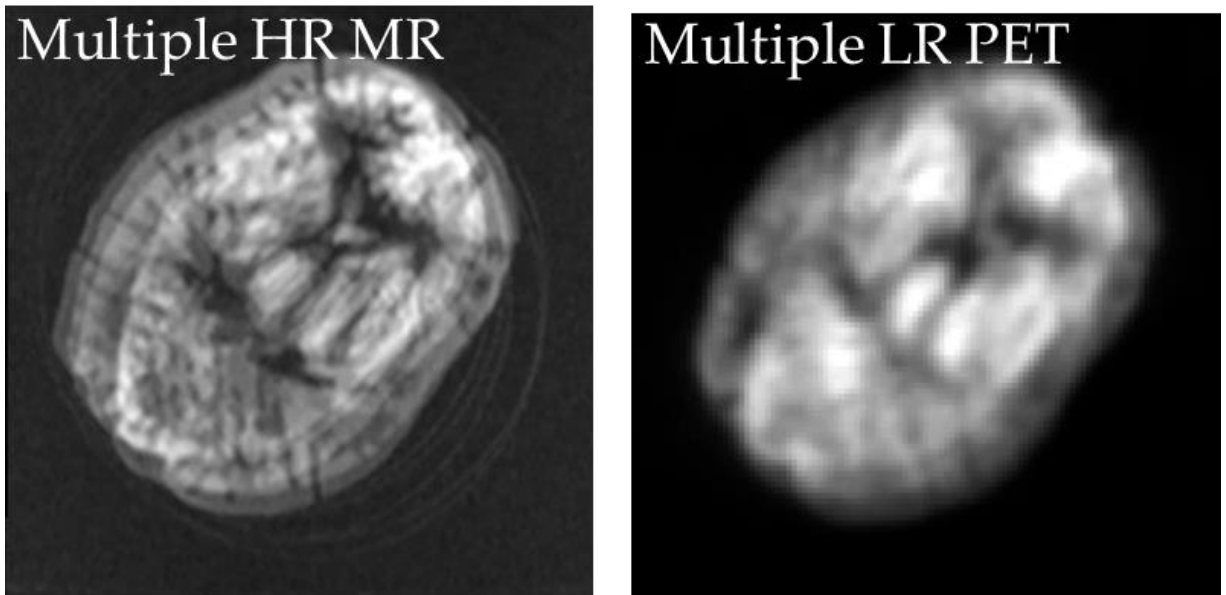


*Figure 4.4 Superposition of the five different PET and MR simultaneous scans.*

The SR reconstruction algorithm was implemented using Equation (4.3), by modeling the estimated MR-derived shift parameters, image down-sampling, point spread function (PSF) blurring, forward-projection, and detector sensitivity coefficients inside the PET system matrix. PET images were reconstructed with three different methods:

- standard OSEM algorithm applied to the reference scan data (2x2x2mm<sup>3</sup> voxel grid),

- standard OSEM algorithm with PSF (OSEM-PSF) modeling applied to the reference scan ( $2 \times 2 \times 2 \text{mm}^3$ ),
- proposed SR algorithm applied to data from all five scans ( $1 \times 1 \times 1 \text{mm}^3$ ).

Each method used the same number of coincidence events to form the final images. Iteration numbers were chosen to match noise levels across methods (the noise was defined as the variance inside a region where the activity is relatively uniform). Line profiles were drawn across a small region of the brain phantom in order to observe potential details improvement for the SR.

#### 4.4.3 Results and discussion

The proposed SR reconstruction method yielded PET images with visibly improved spatial resolution as compared to both OSEM and OSEM-PSF reconstruction (Figure 4.5).

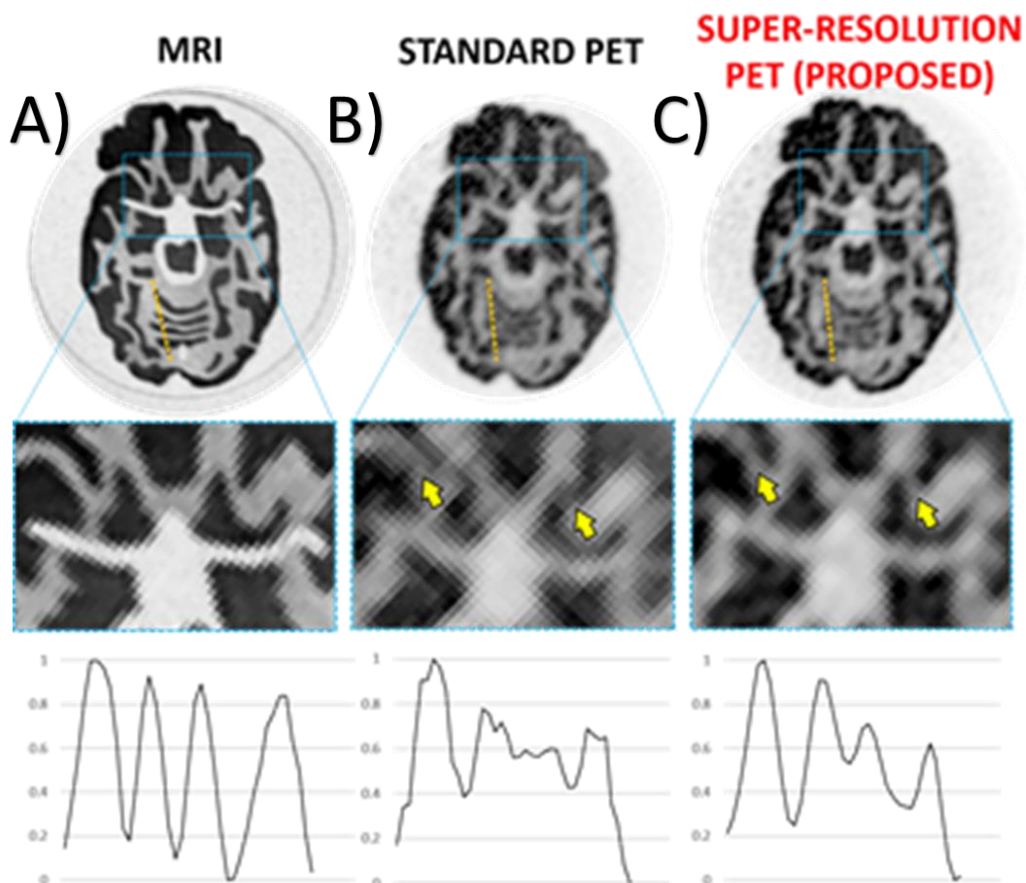


Figure 4.5 Results of the Hoffman brain phantom study. Top row: same PET slice reconstructed with A) corresponding MRI slice, B) standard OSEM, and C) proposed SR method. Bottom row: Line profiles for the corresponding data.

By visual inspection, it is clear that PET images reconstructed with the proposed SR algorithm have higher spatial resolution than those obtained with standard PSF-OSEM, enabling

improved characterization of small cortical and subcortical brain phantom structures. Line profiles confirmed the increase in spatial resolution for the SR image as well as improved correspondence with high-resolution MRI as compared to the conventional methods. We can observe higher peaks and deeper valleys for the line profile measured in our proposed SR method, while the line profile measured in the standard reconstruction method present a lessened dynamic between the peaks and valleys. This was true for most of the line profiles we measured in small regions of the phantom.

## 4.5 Discussion and Conclusion

The goal of super-resolution in PET imaging is to improve the spatial resolution of the images, i.e., to make the images appear more detailed. This is particularly important for small structures, such as tumors, which can be difficult to detect with the lower resolution images produced by traditional PET scanners. Authors have attempted to apply SR in PET imaging through methods such as physically moving the scanner, leading to oversampled projections. Other approaches applied SR to the projection matrix before tomographic reconstruction, and more recently, authors have integrated SR estimation directly into the iterative process of the MLEM image estimation, keeping the Poisson nature of the data. In that context we conducted a proof of concept that sought to apply SR in a PET/MR setup. This study indicated that super-resolution PET reconstruction using simultaneously acquired HR MRI data for shift estimation is a promising way of improving PET image quality and resolution in PET/MR scanners.

However, to the best of our knowledge, this method and all the mentioned methods in the literature review still rely on having multiple fixed positions of the scanned object or a “step and shoot” fashion, or end up discretizing and binning continuous movement (Verhaeghe and Reader, 2010). In addition, as mentioned by the authors in (Song et al., 2020), the main limitation of CNN-based SR method is the intrinsic dependence on supervised learning and therefore, the requirement of paired low resolution and high-resolution PET images for training. Hence, those SR implementations remain clinically not convenient for brain imaging, especially for animal studies or human patients. In fact, a patient would have to stay still in multiple positions for an extended period of time, which can be in many cases impracticable. What we want to achieve is allowing subjects to move freely during the acquisition, and take advantage of the head movement to achieve SR. In Chapter 5, we propose a method for that, using the Polaris optical tracking device presented in Chapter 3. The device uses near-infrared light to track 3D positions of passive markers in real time at a sub-millimeter precision, making it suitable for SR applications.

# Chapter 5

## Super-resolution in brain positron emission tomography using a real-time motion capture system

This chapter presents a super-resolution framework for improving the resolution of brain PET images, which here is potentially applicable in a real clinical setting. We introduce in Section 5.1 the importance of resolution in clinical brain PET imaging and recall some SR principles. The framework takes advantage of a high-resolution infra-red tracking camera, introduced in Chapter 3, to continuously and accurately measure sub-resolution shifts of an object during a PET acquisition. In Section 5.2, we explore how the tracking camera is integrated with the GE PET/CT scanner through our custom-built interface that was studied in Chapter 3. The SR framework was evaluated through experiments on both a moving phantom and a non-human primate using  $^{18}\text{F}$ -labeled tracers. The results are shown in Section 5.3 and discussed in Section 5.4. The SR method was found to improve the visualization of small brain structures and achieved better noise control compared to static reconstructions with the same voxel size.

### 5.1 Introduction

In Chapter 4 we provided a literature review, a formalization of the problem of super-resolution and a proof of concept in a non-clinical PET/MR setup. In Figure 4.2, we illustrated how we could achieve SR in that setup by combining the partial non-redundant information contained in multiple low-resolution images. Ultimately, SR was achieved by accurately correcting the motion in the image space.



As it is still an open problem to find a way to achieve SR in an actual clinical setup using commercial scanners and in scenarios where a patient can be subject to small uncontrolled movements, in this work, we undertook a different approach where we explored the potential of using real-time motion correction to obtain non-redundant information, by moving the scanned object inside the field of view of the scanner in a continuous manner, and by directly correcting the position/orientation of the line of responses at a sub-voxel accuracy to a common reference (Figure 5.1) during reconstruction. Fundamentally, the SR is achieved directly into the projection space in this setup.

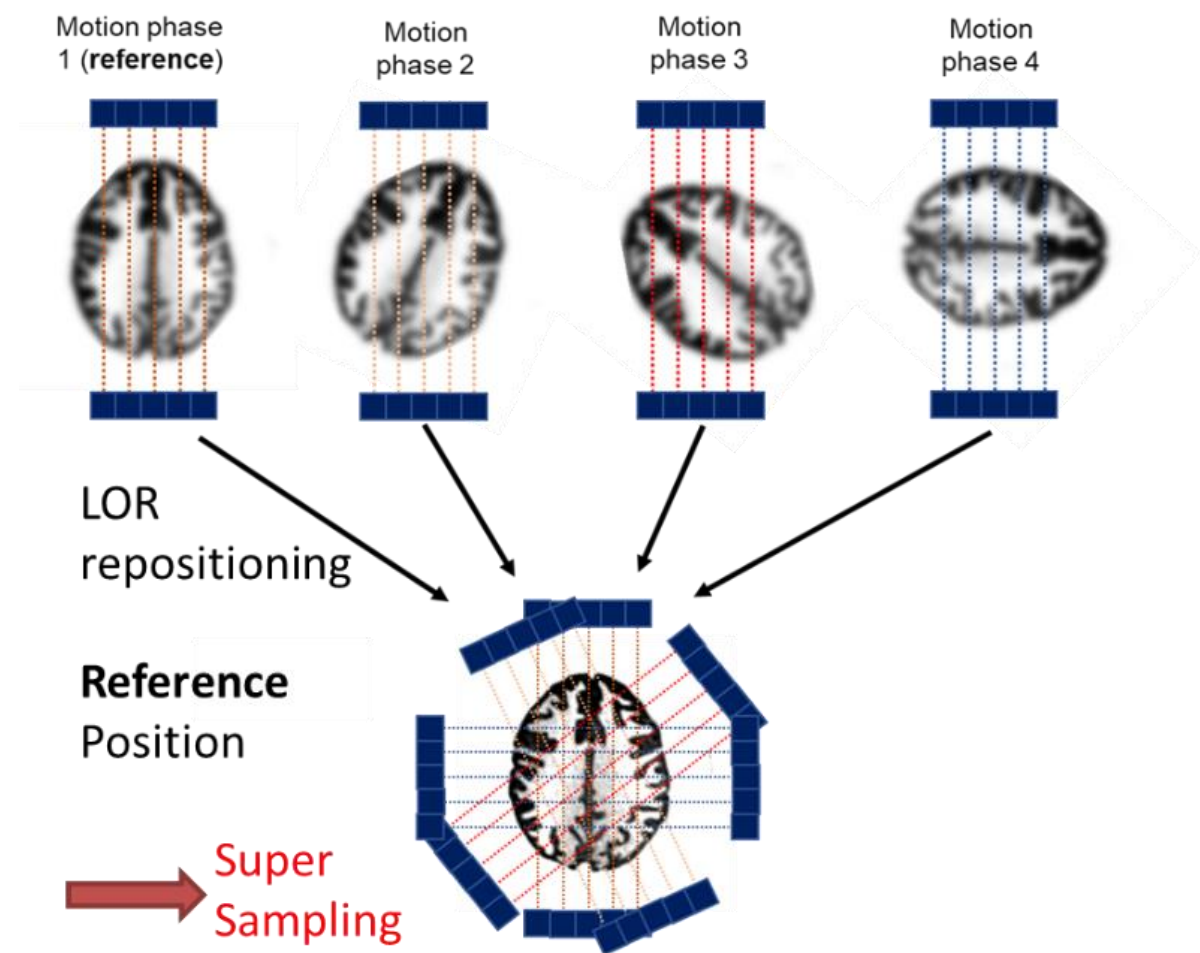


Figure 5.1 Principle of super-resolution in brain PET directly in the projection domain. The object is sampled in different positions due to motion. To achieve SR, motion transformations measured by a high-resolution optical tracking are applied to the acquired LORs during image reconstruction to estimate a higher resolution PET image in a common oversampled reference grid.

Hence, the purpose of this work is to show that SR can be achieved with the state-of-the-art high-resolution optical tracking device (presented in Chapter 3) that is used to measure continuously, in real-time, the undesired random head movement with a very high spatial and

temporal accuracy during a PET acquisition, achieving SR using a commercial clinical scanner. The main contributions are the robust temporal synchronization, the accurate spatial calibration between the optical tracking device and a PET/CT scanner and the use of real time motion information into a list-mode based reconstruction scheme.

## **5.2 Super-resolution in a PET/CT setup using the Polaris tracker**

### **5.2.1 Overview**

Our objective is to harness the usually undesired head motion that typically degrades PET spatial resolution to actually enhance it using SR. To accomplish that, we need to measure the unpredictable and potentially continuous head motion occurring during a PET scan with high spatial and temporal resolution.

Standard motion tracking techniques, which typically rely on registration of reconstructed PET images, have limited temporal and spatial resolution, and often fail in presence of rapid or continuous head motion. An alternative approach is to use external optical tracking systems (Rahmim et al., 2007), which usually provide motion information with excellent temporal and spatial resolution.

### **5.2.2 High-resolution motion tracking device**

Several 3D external motion tracking systems have been employed for motion correction of brain PET (Picard and Thompson, 1997), (Roger R Fulton et al., 2002). Here, we use the Polaris Vega, a tracking system manufactured by Northern Digital Inc. (NDI, Canada) that we introduced in Chapter 3. We recall that the Polaris Vega is a device approved for medical environments that tracks a “tool” or “target” where spherical reflective markers are mounted in a specific geometry recognized by the tracker. It can track a target with 0.12 mm volumetric accuracy. The motion capture frame rate can be selected from 20, 30, to 60 Hz. Temporal synchronization with external devices is only supported through the IEEE 1588 PTP (Precise time Protocol) standard. However, the GE Discovery MI that we used for our experiments cannot directly be interfaced in this manner, thus requiring an alternate method to align the system with the PET scanner’s clock. Accurate spatial calibration of both devices is required as one must relate the tracker and scanner coordinate frames.

### **5.2.3 Temporal synchronization, spatial calibration between the Polaris Vega and the PET/CT scanner and integration of the motion in PET reconstruction**

There are three key steps to achieve our SR: the first is to temporally synchronize Polaris Vega and the GE PET/CT scanner. The second step is to perform an accurate spatial calibration

between the apparatuses. The last step consists in integrating the motion information from the Vega into a list-mode event-by-event based motion-compensated PET reconstruction framework to achieve SR. Those steps are explained in the following sections.

All the important elements of the system (scanner, tracker, target, communication interface...) and their relations are presented in Figure 5.2.

We tested and validated the developed method with three different experiments: one using a mini hot spot phantom (Data Spectrum) for validation, another using a brain Hoffman phantom, and an in vivo study with a non-human primate.

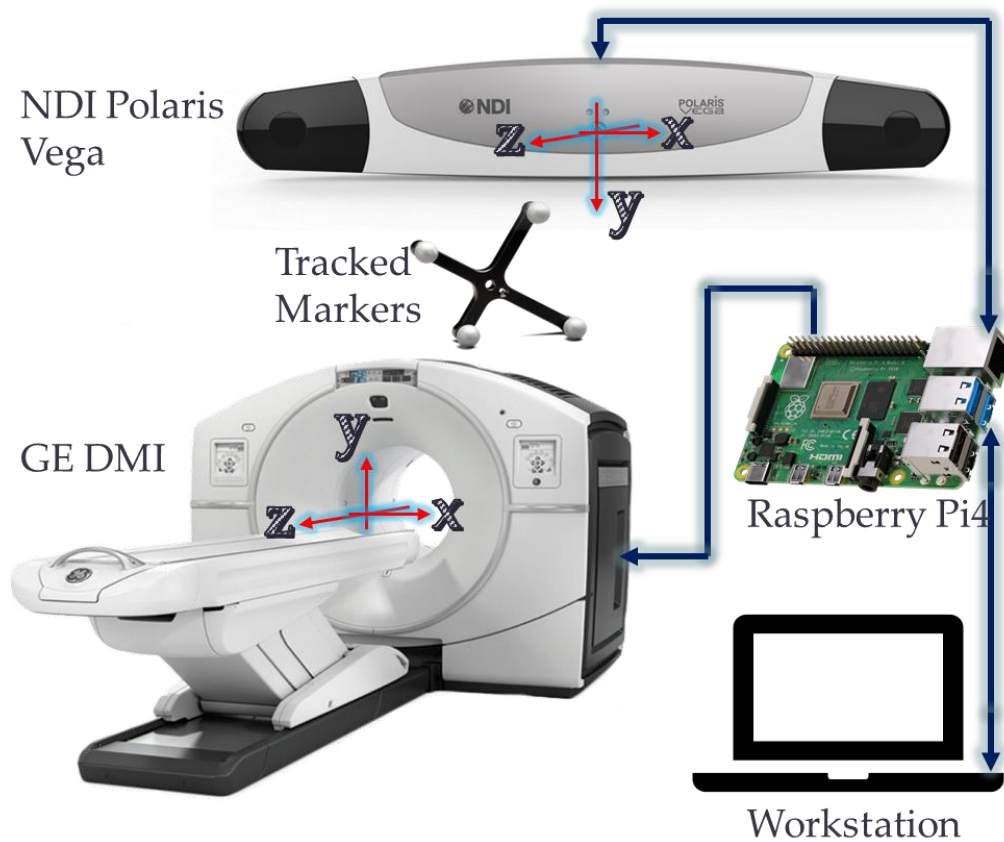


*Figure 5.2 Integration scheme of a high-resolution optical tracking device in a PET/CT setup.*

### **Temporal Synchronization**

Chapter 3 presented extensively a hardware and a software approach to temporally align the two systems. We chose the software approach with the GE DMI scanner for its portability and to allow the relatively easy implementation of potential future updates and improvements. At the time of our experiments, to achieve the temporal alignment between the tracking device and the PET scanner, the Raspberry Pi4 (Rpi) platform (Figure 5.2) was used as a host to

control PTP synchronization and to generate pulses to be injected into the scanner’s gating signal input and incorporated into the PET listmode data stream (Figure 5.3). The PTP is a protocol used to synchronize clocks throughout a computer network. It achieves synchronization accuracy in the sub-microsecond range on a local area network, making it suitable for measurement and control systems (Eidson, 2006). Thanks to this tool, no specific time delay correction implementation is needed (Spangler-Bickell et al., 2016). The Raspberry Pi4 first achieves synchronization with the Vega by providing a PTP master reference. Since the Vega provides a PTP timestamp with every frame, the Raspberry Pi4 can then determine when to generate a pulse synchronized with motion frame capture.

After the PET acquisition starts, a pattern of pulses is sent to the gating interface to define the starting frame time and position. In addition, pulses are sent periodically to the list mode data stream to ensure that no time drift occurs between the PET system and the PTP master counter (Figure 5.3).

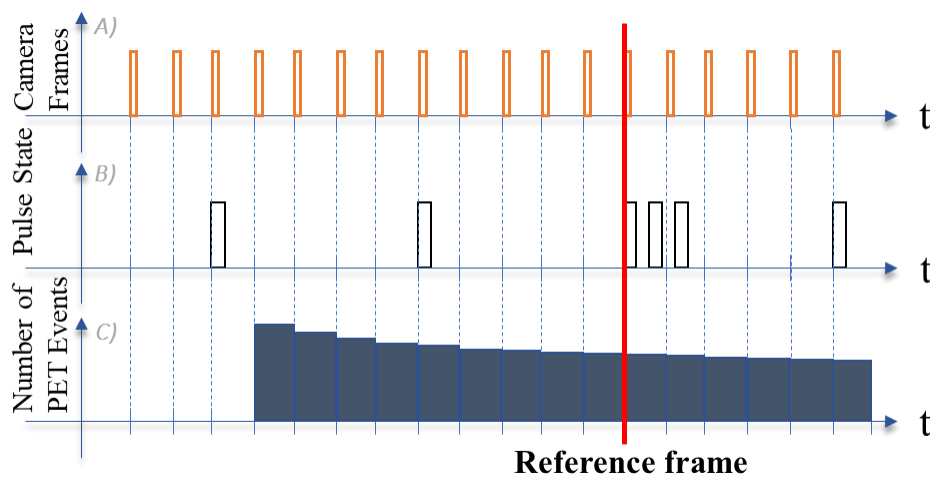


Figure 5.3 Temporal synchronization between the Polaris Vega and the PET/CT scanner. A) Camera frame timestamps are sent in the RPi. B) Aligned RPi timestamps are generated and sent to the listmode data stream, and a reference frame is defined by a specific pattern of pulses. C) PET events are aligned with the camera stamps post-acquisition.

### Spatial calibration

Since the PET and Polaris Vega coordinate systems are not intrinsically aligned, a transformation matrix must be determined to convert the recorded motion tracking data from the Polaris Vega into the PET coordinates. A standard solution is to use a radioactive point source that is rigidly placed on the origin of a tracked target, and simultaneously scan and measure them at various positions within the PET scanner’s and tracker’s fields of view. It is then possible to determine a suitable transformation between the coordinate systems by finding

the relationship between the two sets of coordinates (Roger R Fulton et al., 2002). However, such an approach could potentially limit resolution recovery gain of SR since the accuracy of the spatial calibration matrix would be close to that of the intrinsic PET resolution. For SR, the accuracy of the spatial calibration should be higher than the intrinsic PET resolution. Here, rather than relying on PET point sources, we determined the calibration matrix using the CT, which shares the same image space as the PET component but has a much higher spatial resolution.

The spatial alignment transformation between the Polaris Vega and the scanner coordinate spaces is determined by six paired measurements of high-resolution CT scans ( $0.7 \times 0.7 \times 0.6$  mm<sup>3</sup>) and Polaris tracking of individual reflective markers. The markers positions are chosen regularly spaced across the field of view of the CT. In the Polaris camera space, the different positions of the center of a marker (which is a sphere) are directly given by the camera. The corresponding positions of the markers in the CT space are manually spotted in the acquired 3D volumes. A matrix  $\mathbf{M}_c$  representing the 3-D rigid transformation between the two coordinate systems (PET scanner and Polaris camera coordinate frames) is found by measuring the position of the same set of points in both spaces simultaneously. Using the two sets of corresponding 3-D point data, the optimal solution for  $\mathbf{M}_c$  in terms of least square optimization is found using singular value decomposition (SVD) on the covariance matrix built from the sets of points (Arun et al., 1987). Using high-resolution CT rather than multiple tracked PET point sources ensures that the accuracy of the measured transformations is greater than the PET intrinsic spatial resolution, which is required to achieved super-resolution.

To apply the spatial alignment in subsequent experiments in which the relative position of the Polaris and scanner may have changed, we use a reference target built with marker rigidly affixed to the gantry (Figure 4). The camera simultaneously tracks the position of the mobile target and the reference target relative to the Polaris reference frame. This allows positioning the camera anywhere for each experiment without having to recalibrate the system.

The global transformation matrix  $\mathbf{L}$  allowing to express the position of the tracked marker from the reference camera space to the PET image space, is given by:

$$\mathbf{L} = \mathbf{M}_c \mathbf{M}_{RefT} \mathbf{M}'_T^{-1} \mathbf{M}_c^{-1} \quad (6.1)$$

where  $\mathbf{M}_c$  is the aforementioned calibration matrix relating the PET image space and Polaris Vega coordinate space,  $\mathbf{M}_{RefT}$  is the reference rigid transformation matrix that represents the

position where all the other positions are registered to, and  $M'_T$  is the current rigid transformation matrix given by the Polaris Vega at each time point.

Using this set of transformations with our calibration method, we can relate the coordinates of the tracked target from the camera space to the PET image space with high accuracy (example in Figure 5.4).

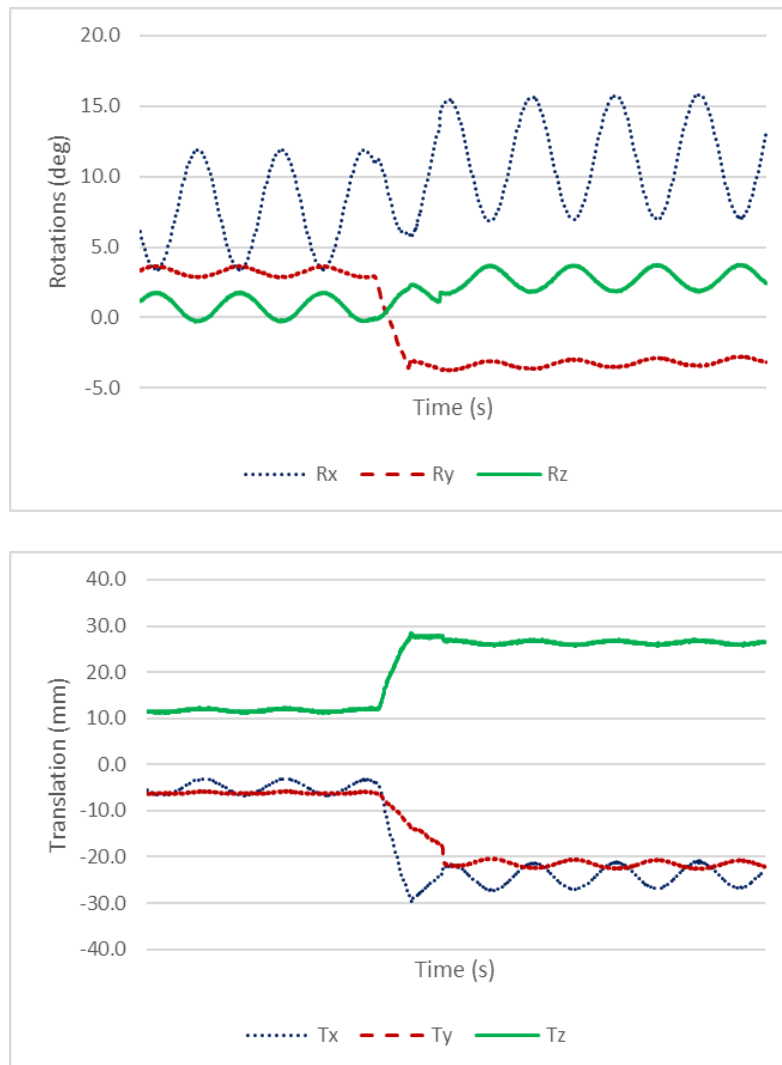


Figure 5.4 Examples of motion transformations measured by the Polaris Vega camera in the PET image space for a phantom experiment with continuous movement.  $R_x$ ,  $R_y$  and  $R_z$  are the rotation angles and  $T_x$ ,  $T_y$ ,  $T_z$  are the translations of the tracked target in the image space spanned by  $x$ ,  $y$ , and  $z$  axis.

**List-mode based Ordered Subset Expectation Maximization (OSEM) motion corrected reconstruction for SR**

For a given scan, the motion data obtained by the Polaris is used to transform the endpoints of measured LORs to a common reference frame on an event-by-event basis at the corresponding time. Let  $L_t$  model the effect of motion at time frame  $t$  (i.e., rigid-body transformation from

the reference frame to  $t$ ) in the LOR space and  $i_m$  represent LOR  $i \in [1 \dots I]$  associated with list-mode event  $m$  detected during frame  $t$ ; thus we have  $i'_m = \mathbf{L}_t^{-1}(i_m)$  where  $i'_m$  denotes the transformed LOR for event  $m$  after motion correction. To achieve SR, a list-mode OSEM reconstruction algorithm with LOR-by-LOR motion compensation was implemented using the formulation in (Spangler-Bickell et al., 2019). Derived from a classic list-mode, this formula integrates motion information directly into the system matrix  $\mathbf{P}$ :

$$\hat{\rho}_{SR_j}^{l+1} = \frac{\hat{\rho}_{SR_j}^l}{\bar{S}_j} \sum_{m=1}^M P_{i'_m,j} \frac{1/I_{i'_m}}{\sum_{k=1}^J P_{i'_m,k} \hat{\rho}_{SR_k}^l + \frac{S_{i'_m} + R_{i'_m}}{a_{i'_m} N_{i'_m}}} \quad (5.1)$$

where  $\hat{\rho}_{SR_j}^{it}$  is the SR image value at voxel  $j \in [1 \dots J]$  and iteration  $l$  in the reference frame,  $M$  is the total number of events in the list-mode file,  $I_{i'_m}$  is the attenuation correction factor for attenuating material undergoing motion (e.g., head) for the transformed LOR  $i'_m$ ,  $S_{i'_m}$  and  $R_{i'_m}$  are respectively the estimated scatter and random contributions,  $a_{i'_m}$  is the combined moving (e.g., head) and non-moving (e.g., scanner bed) attenuation correction factor for uncorrected LOR  $i_m$ ,  $N_{i'_m}$  is the detector sensitivity for LOR  $i'_m$ .

$P_{i,j}$  is an element of the PET system matrix defined as:

$$P_{i,j} = \sum_{l=1}^I B_{proj_{i,l}} \sum_{k=1}^J G_{l,k} B_{img_{k,j}} \quad (5.2)$$

where  $G_{i,j}$  accounts for the geometric probability that an event generated in voxel  $j$  is detected along LOR  $i$ ;  $B_{img_{k,j}}$  and  $B_{proj_{i,l}}$  are elements of PSF kernel matrices in the image space and in the projection space, respectively. The kernel values for each component were given by the scanner manufacturer. PSF effects are accounted for in two steps during reconstruction: the spatially invariant 3D Gaussian smoothing kernel  $\mathbf{B}_{img}$  is first applied to the image at each update and then LORs are spread in the projection step according to the spatially varying PSF kernel  $\mathbf{B}_{proj}$ , and vice-versa during back-projection. The image-space component models the positron range and allows using slightly narrower PSF kernels in the projection space, which speeds up the projection and back-projection operations during each update. Integrating smoothing also makes the reconstruction more robust to slight high-frequency artifacts that might appear during the iterations (Deller et al., 2021). We develop the principles of PSF in PET imaging in Chapter 6.

In motion-corrected super-resolution reconstruction, the sensitivity image  $\tilde{S}_j$  is a crucial component that needs to be accurately calculated to avoid artifacts and improve image quality. Due to patient or object motion, in vivo attenuation correction factors (ACFs) move while normalization factors and ex vivo ACFs do not, requiring these factors to be handled separately. To ensure accuracy and avoid artifacts, a time-averaged sensitivity image is created, including PSF modeling and a multi-ray Siddon approach (Moehrs et al., 2008). These techniques, discussed in Chapter 6, help to minimize the common one-ray Siddon (Siddon, 1985) high frequency artefacts in the sensitivity image and produce higher quality, especially in the presence of motion where any mismatch between the current estimate  $\hat{\rho}_{SR}^{it}$  and  $\tilde{S}_j$  is detrimental. Hence  $\tilde{S}_j$  is the time-averaged sensitivity image value at voxel  $j$  that accounts for LOR normalization factors and hardware attenuation. It is defined as (and adapted from Spangler-Bickell et al., 2019):

$$\tilde{S}_j = \frac{1}{T} \sum_{t=1}^T \sum_{j'=1}^J L_{t,j \rightarrow j'} \sum_{i=1}^I P_{ij} H_i N_i \quad (5.3)$$

where  $T$  is the total number of motion frames and  $H_i$  is the attenuation correction factor for non-moving components for LOR  $i$ .

$L_t$  being measured at a very high resolution, we can increase spatial sampling by providing complementary information which can be exploited by the OSEM algorithm to reconstruct a PET image on a finer voxel grid.

#### 5.2.4 Phantom and non-human primate experiments

Two phantoms, a Mini Hot Spot and a Hoffman, respectively filled with 74 MBq and 111 MBq of  $^{18}\text{F}$ , were scanned for 15 min in list-mode on the PET/CT scanner while undergoing continuous rotation/translation movements introduced by a QUASAR system (Modus QA) (see the Hoffman experiment setup in Figure 5.5). Similarly, an anesthetized male rhesus monkey administered with 407 MBq  $^{18}\text{F}$ -FDG was scanned for 15-min (60 min after tracer injection) in list-mode with continuous and random head motion induced manually. This experiment complied with the ARRIVE guidelines and was carried out in accordance with the National Institutes of Health guide for the care and use of Laboratory animals (NIH Publications No. 8023, revised 1978).



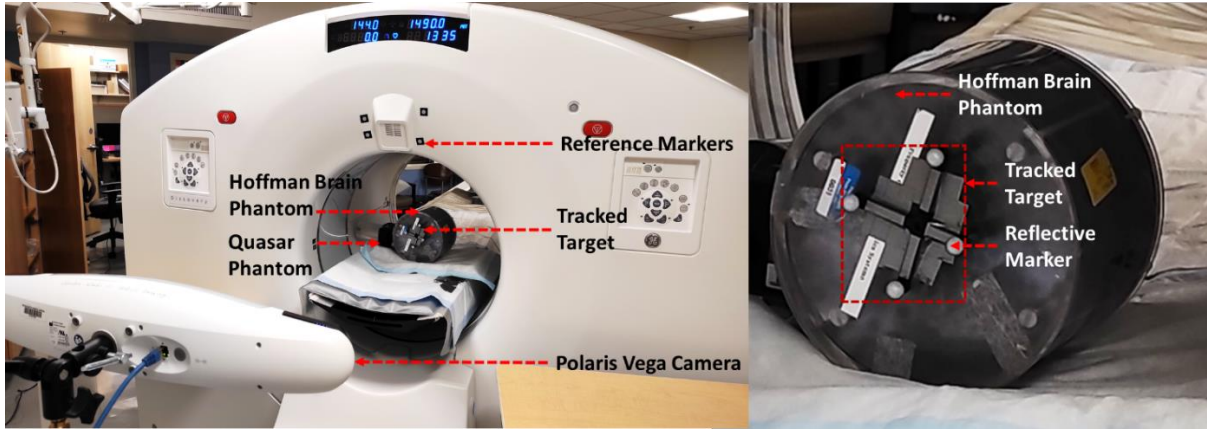


Figure 5.5 Experimental setup used for the Hoffman phantom experiment showing the placement of Polaris Vega relative to the GE DMI scanner, the Hoffman phantom on which is attached the tracked markers, the Quasar phantom, and the reference markers.

For all the scans, motion was tracked at all times using the Polaris and reflective markers rigidly attached to the targets (see Figure 4 for the Hoffman phantom study). For the NHP, markers were rigidly attached to the skull using an adhesive bandage. For each study, reference static PET acquisitions were also performed without inducing movement. List-mode data were reconstructed with three different methods: (A) OSEM algorithm with PSF modeling applied to the static reference scan data (2 mm voxel size), (B) OSEM with PSF modeling applied to the static scan on smaller voxel size (0.8 mm for the mini hot spot and 1 mm for the Hoffman), (C) proposed SR algorithm applied to the moving scan with 0.8 or 1 mm voxel size. The iteration numbers were chosen to match image noise levels for all methods.

### 5.2.5 Evaluation of image quality

We evaluate the quality of the super-resolved PET images via two conventional measures in image processing, namely the Contrast-to-Noise Ratio (CNR) and the Structural Similarity Index (SSIM) (Wang et al., 2004). The CNR gives a contrast index between different regions in the brain relative to the noise level. Here, it was computed as:

$$CNR = \frac{\mu_{Target} - \mu_{Background}}{\sigma_{Background}} \quad (5.4)$$

$\mu_{Target}$  is the mean value in gray matter,  $\mu_{Background}$  is the mean value in the background, and  $\sigma_{Background}$  is the standard deviation in background, modeling the noise level.

The SSIM evaluates the structural similarity between two images (e.g., ground truth or reference image vs. estimated image). It combines three terms: luminance, contrast features, as well as an image correlation term. For both the mini hot spot and Hoffman phantoms, CT provides high-resolution reference images for SSIM calculation. Hence, it was computed as:

$$\text{SSIM}(\text{PET}, \text{CT}) = \frac{(2\mu_{\text{PET}}\mu_{\text{CT}} + C_1)(2\sigma_{\text{PETCT}} + C_2)}{(\mu_{\text{PET}}^2 + \mu_{\text{CT}}^2 + C_1)(\sigma_{\text{PET}}^2 + \sigma_{\text{CT}}^2 + C_2)} \quad (5.5)$$

where  $\mu_{\text{CT}}$  is the mean CT value in the ROI,  $\mu_{\text{PET}}$  is the mean PET value in the ROI,  $\sigma_{\text{CT}}$  is the standard deviation of CT values in the ROI,  $\sigma_{\text{PET}}$  is the standard deviation of PET values the ROI,  $\sigma_{\text{PETCT}}$  is the cross-covariance for PET and CT in the ROI and  $C_1$  and  $C_2$  are regularization constants that helps avoiding instability for image regions where the local mean or standard deviation is close to zero.

The SSIM was only calculated for the two phantoms which had a CT reference available. The regions of interest were randomly selected across multiple slices on windows centered in regions where structures are small, while the CNR was calculated by selecting multiple regions with activity and a unique background region (Figure 5.6).

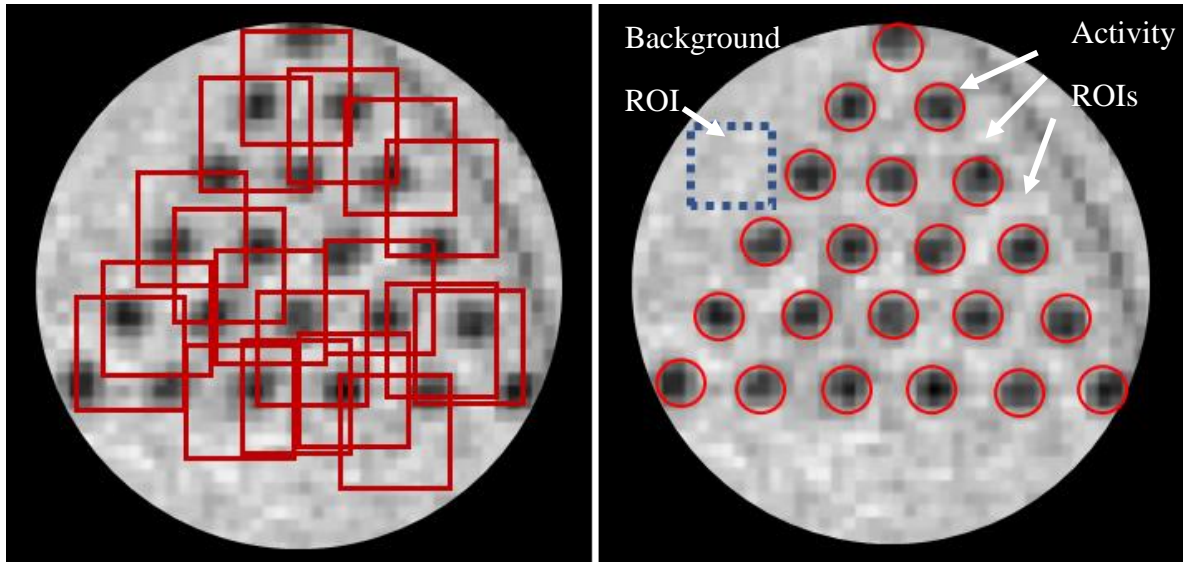


*Figure 5.6 Illustration of ROIs selection for SSIM and CNR calculation in the Mini Hot Spot phantom. Left: Examples of randomly selected ROIs in a window drawn around the 2.4mm rods in the reference CT image. Right: Selection of ROIs for CNR calculation. The dashed blue square shows the background ROI.*

Line profiles were used to further quantitatively assess resolution recovery from the SR method. Those were drawn across small structures, typically at the limit of the scanner resolution capabilities.

## 5.3 Results

### 5.3.1 Phantom studies

#### Mini Hot Spot Phantom

The mini hot spots phantom was moved with a range of approximately  $\pm 20^\circ$  and  $\pm 40$  mm, with motion along all 6 degrees of freedom (see sample in Figure 5.4). The data set consisted of about 1 billion events spanning 15 min for both the static and moving acquisitions. Figure 5.7 shows the results of the listmode based reconstructions of the static data for the standard  $2 \times 2 \times 2.8$  mm<sup>3</sup> voxel size as well as in  $0.8 \times 0.8 \times 2.8$  mm<sup>3</sup> voxel size (that we refer to as static 2mm and static 0.8mm, respectively). The data from the moving acquisition were reconstructed with voxel a size of  $0.8 \times 0.8 \times 2.8$  mm<sup>3</sup> to generate SR images (referred to as SR 0.8mm). Figure 5.7 also shows the aligned CT with a voxel size of  $0.7 \times 0.7 \times 0.625$  mm<sup>3</sup> as the reference.

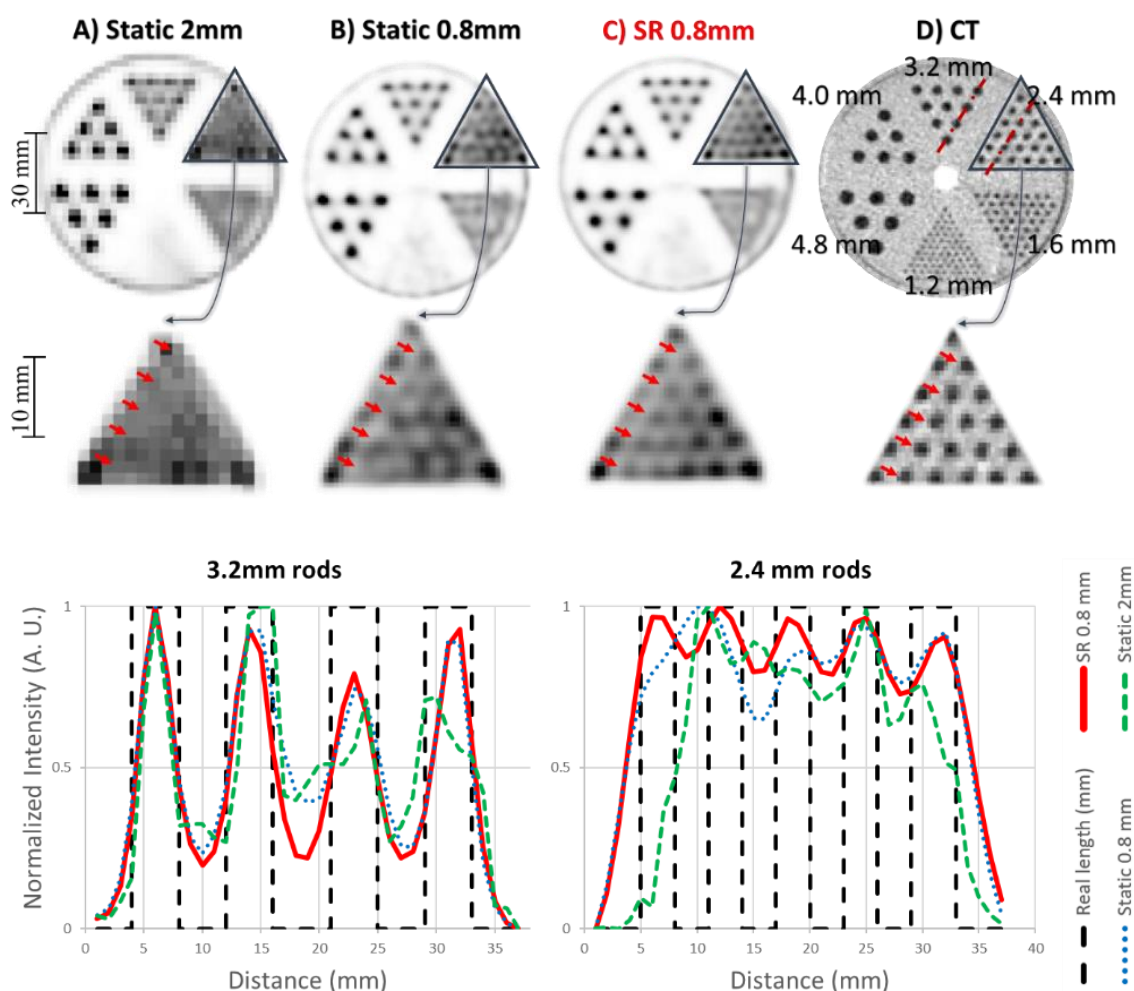


Figure 5.7 Results of the Mini Hot Spot phantom study. Top row: same PET slice reconstructed with A) static OSEM-PSF with 2mm voxels, B) static OSEM-PSF with 0.8 mm voxels, C) proposed SR method with 0.8 mm voxels, and D) corresponding CT slice (note that the CT image can be treated as a high-resolution reference image for the experiment). Bottom row: Corresponding line profiles for the different methods.

The line profiles passing through 3.2 and 2.4 mm rods across all these reconstructions are shown in the bottom panel of Figure 5.7. Note that the reference frame for SR reconstruction was that of the static data. Therefore, the SR reconstruction is well aligned with the static reconstruction without needing additional image registration. Hence, for clinical studies, the PET data can be corrected to the reference frame of the attenuation map to ensure that these are well aligned.

As shown visually and by the line profile in Figure 5.7, the 3.2 mm rods of the static and SR reconstructions are all resolved correctly. This is expected as the intrinsic resolution of the scanner allows resolving structures of this size. However, the 2.4 mm rods cannot be resolved in both static reconstructions, whereas they can clearly be visualized with the SR reconstruction, indicating an improvement in spatial resolution.

### **Hoffman Phantom**

Similar results were obtained using the Hoffman brain phantom, which was moved in a similar manner as the mini hot spot phantom albeit with more movement amplitude along the axial direction of the scanner.

The reconstructed list-mode data for each method and a line profile passing through small structures of the brain across all these reconstructions are shown in Figure 5.8.

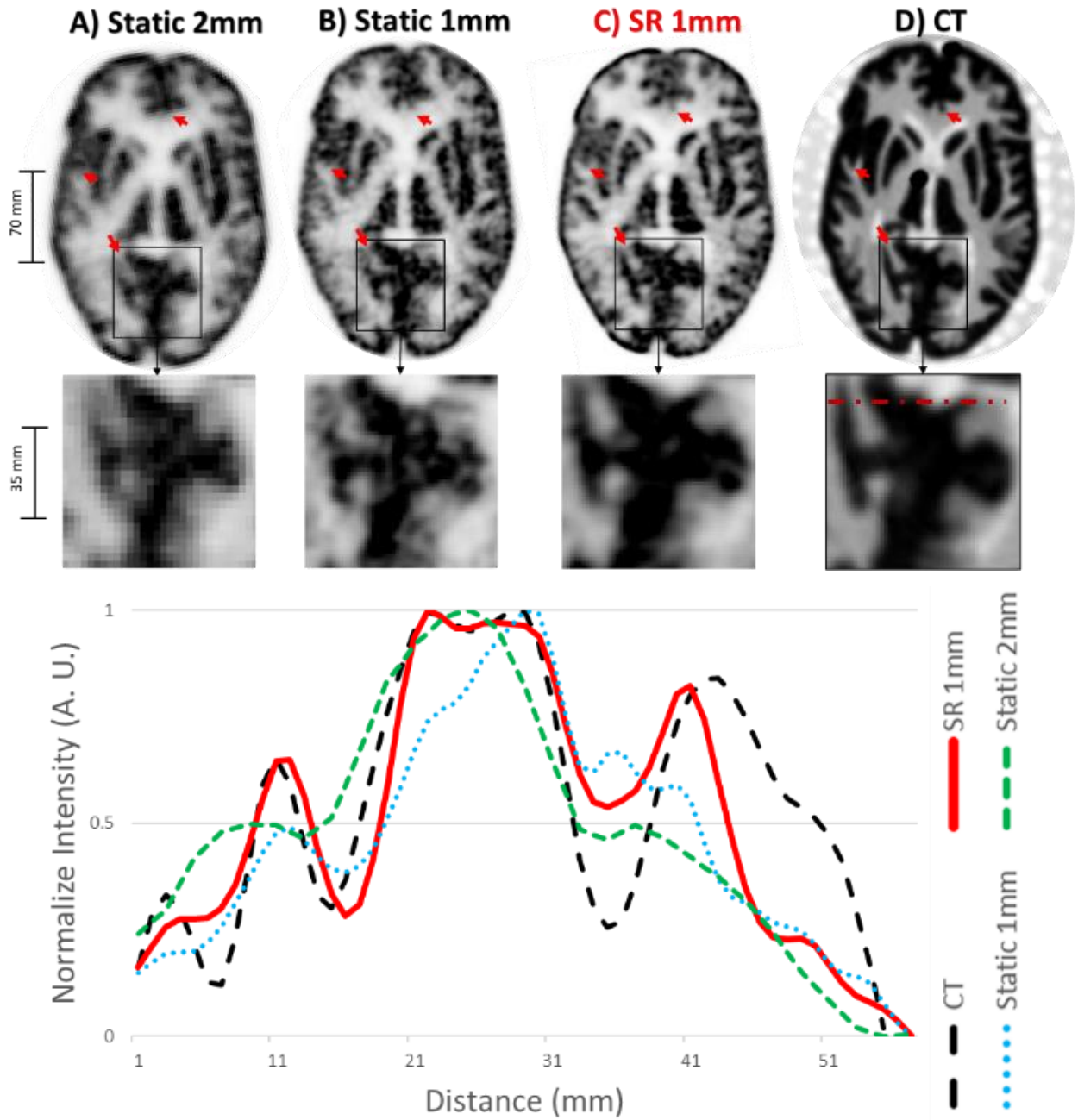


Figure 5.8 Result of the Hoffman phantom study. Top panel: same PET slice reconstructed with A) static OSEM-PSF with 2mm voxels, B) static OSEM-PSF with 1mm voxels, C) proposed SR method with 1mm voxels, and D) corresponding CT slice (the CT image can be considered as a high-resolution reference). Bottom panel: corresponding line profiles.

The proposed SR reconstruction method yielded PET images with visibly improved spatial resolution compared to standard and static reconstructions with the same  $1 \times 1 \times 1 \text{ mm}^3$  voxel size (here referred to as static or SR 1mm), allowing for a better characterization of small cortical and subcortical brain phantom structures (see Figure 5.8). Line profiles confirmed the

improvement in spatial resolution for the SR image as well as an improved correspondence with high-resolution CT as compared to the conventional methods.

### 5.3.2 In vivo study

The rhesus monkey administered with 11 mCi  $^{18}\text{F}$ -FDG was sedated and scanned for 15-min in list-mode without motion, followed by a 15 min acquisition with continuous head motion induced manually. The same reconstruction parameters as in the Hoffman Phantom experiment were used with a voxel size of  $1\times 1\times 1\text{mm}$  for SR.

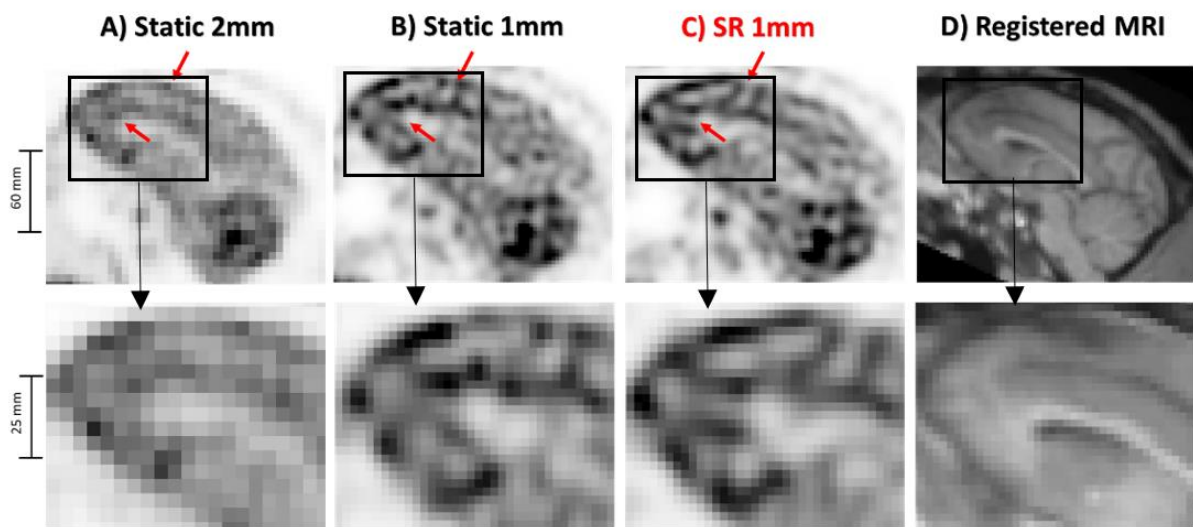


Figure 5.9 Results of the  $^{18}\text{F}$ -FDG NHP in vivo study. Same PET slice reconstructed with A) static OSEM with 2 mm voxels, B) static OSEM with 1 mm voxels, C) proposed SR method with 1 mm voxels, and D) corresponding MR slice.

Figure 5.9 shows a sagittal slice through the brain for the NHP study. Specific brain regions, such as the frontal lobe, can be better resolved after SR.

### 5.3.3 Quantitative analysis

A quantitative analysis in terms of SSIM and CNR is presented in Figure 5.10 and Figure 5.12 for the three experiments.

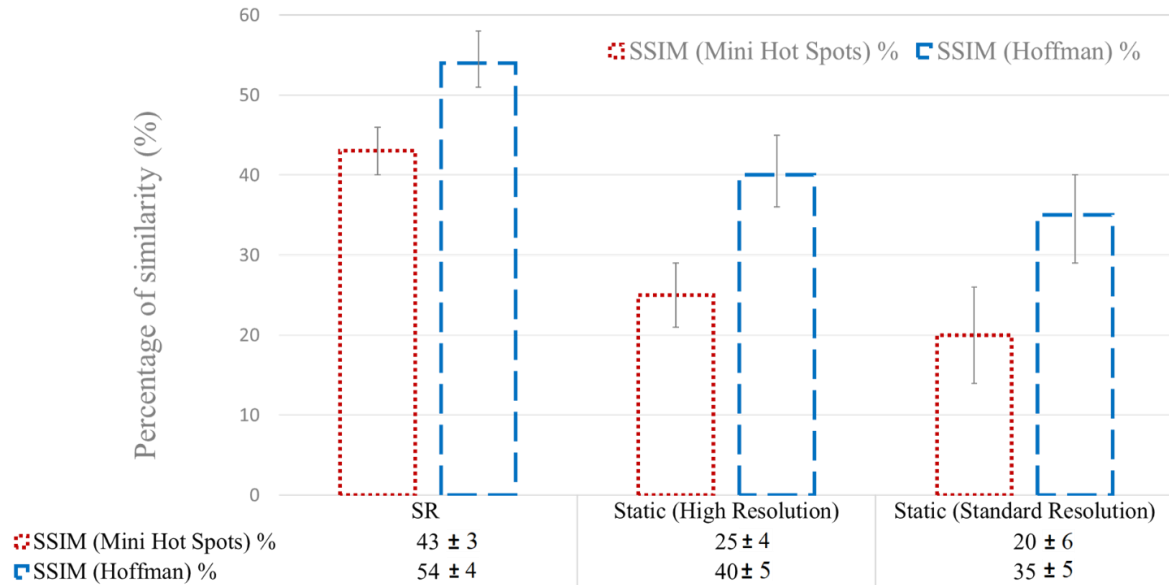


Figure 5.10 SSIM results for the Mini Hot Spots Phantom (dotted red) and the Hoffman Phantom (dashed blue). The bar plot shows the mean SSIM as described in Figure 6. Error bars representing the standard deviation are also plotted.

The results are in agreement with what was observed visually and with the line profiles shown in Figure 5.7 and Figure 5.8. Standard 2mm and 1mm (or 0.8mm) static reconstructions exhibit lower SSIM than SR images, which showed a higher percentage of structural similarity in the order of 15-20 % due to the oversampling introduced by the precisely corrected movement. We demonstrate for the Mini Hot Spots phantom that this quantitative analysis at different iterations yielded similar results in Figure 5.11. Although not shown here, the results were similar with the Hoffman Phantom.

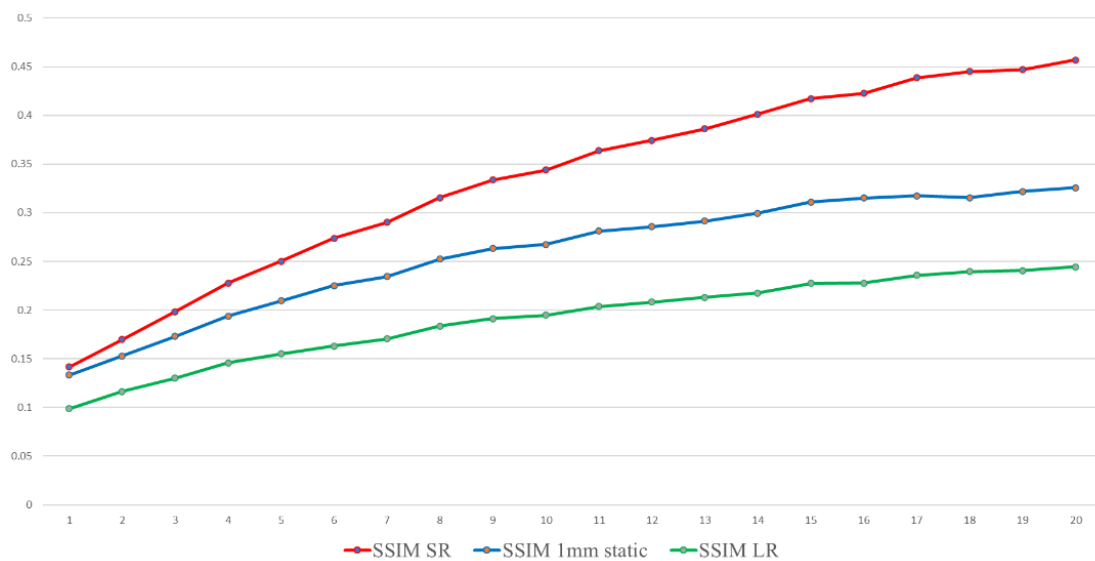


Figure 5.11 SSIM results across OSEM iterations for the mini hotspot phantom. SR always presents a higher similarity with the CT.

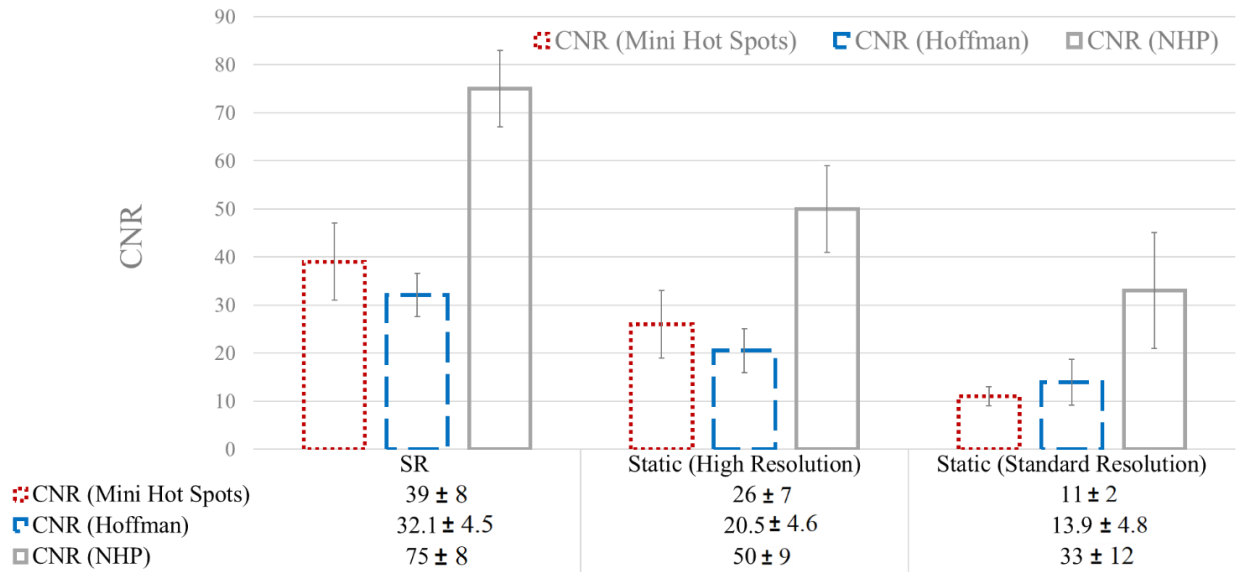


Figure 5.12 CNR results for the Mini Hot Spots Phantom (dotted red), the Hoffman Phantom (dashed blue), and the NHP (plain gray).

Similarly, CNR results are in accordance with what was observed. Standard and 1mm (or 0.8mm) static reconstructions exhibit higher CNR in the order of 50% of increase due to the improved contrast recovery in small structures.

## 5.4 Discussion

This work shows that one can estimate PET images with a resolution that outperforms the intrinsic scanner resolution by harnessing, counter-intuitively perhaps, the usually undesired target motion, if measured at a higher resolution than the scanner's intrinsic resolution. In other words, it is possible to not only compensate for the deleterious effects of motion on PET image quality, but to also leverage the increased sampling information associated with moving targets to enhance the effective PET resolution based on super-resolution principles.

Although SR has been investigated in PET before, to the best of our knowledge, this is the first study showing that it can be achieved with an external optical tracking device that is used to continuously measure head movement with a very high spatial and temporal precision during the listmode PET acquisition. The Polaris Vega tracking camera can indeed measure rigid-body transformations at a sampling rate of 60Hz (~16.6 ms/frame) and with a much higher accuracy than the spatial resolution of the GE Discovery MI PET/CT scanner (0.12mm vs. ~4 mm). Here, we exploited the measured subpixel motion in a listmode reconstruction framework with event-by-event repositioning which handles any type of movement in the 3D space, including unintentional motion, to achieve super-resolution.



An important step of the reconstruction is the generation of the sensitivity image. There are two main approaches to calculating the motion averaged sensitivity image (Rahmim et al., 2008). One approach consists in applying motion correction to the projection space followed by backprojection of all LORs, repeating this process for all poses ((Rahmim et al., 2008), Equation 16). Another strategy consists in performing only one backprojection and applying motion correction in the image space for all poses ((Rahmim et al., 2008), Equation 10). The first method can handle the attenuation correction properly but can be computationally expensive and very slow as the frame rate we are dealing with is very high (60Hz). The second method is much faster but requires that the attenuation of the moving object is calculated during forward projection in the iteration process. Moreover, it requires segmenting the moving object from the static parts (scanner bed, static body etc.) in the attenuation map. Our results showed that the second approach, which was the one we used, works rather well. However, another disadvantage of this method is that by moving and averaging the sensitivity image, high frequency artifacts (in the form of Moiré patterns) gets propagated when a single ray Siddon projector (Siddon, 1985) is used for projection/backprojection and when the predefined voxel size is smaller than the scanner detector size. Using a multi-ray Siddon projector (Moehrs et al., 2008) allowed to overcome this issue. The use of PSF modeling in the image space also contributed to alleviate most of the high frequency artifacts. However, multi ray Siddon algorithm is very computationally expensive, scaling with the number of rays used for each LOR. An alternative projector using a distance driven approach (Manjeshwar et al., 2006) is being studied to improve reconstruction time (details are given in Chapter 6).

As previously described, we calibrated our system (Polaris tracker and PET/CT scanner) using paired position measurements in both respective spaces. Using CT image for spatial calibration offers arguably more accurate results than PET-based methods that use markers attached to a radioactive point source (Roger R Fulton et al., 2002) (super-resolution would be difficult to achieve with such methods since the movement would be tracked at a resolution close to that of the PET scanner). However, determining the position of the center of a marker using CT images can be challenging. Instead of comparing absolute positions of the object in the scanner and Polaris coordinate frames, we can compare the relative motion between two static positions in both spaces. This relative motion in the two systems is independent of any offset between the object position in the CT and Polaris coordinate frames. The advantage of this method is that it requires no careful measurement of the center of the marker sphere in the CT space, and, since a complex phantom can be measured, the relative position matrices for the CT data can

be determined to a greater precision than the absolute position of the points in the former method.

During all our experiments, the movements applied to the phantoms were mostly back and forth (translation and rotation). Hence, there was a predominant motion direction for each SR acquisition used in this work. It is possible that the applied motion patterns were not optimal to achieve oversampling and that the non-homogeneous nature of the movement implies a non-homogeneous resolution recovery. For instance, if the object is only rotating around a specific axis, the points belonging to that axis will not undergo motion and therefore will not benefit from the improvement offered by oversampling.

In a clinical context, the type and magnitude of motion can vary depending on the targeted population and disease. From our recent study (Tiss et al., 2022) on the impact of motion correction on longitudinal [ $^{18}\text{F}$ ]MK-6240 tau clinical brain scans, we found that 95% of the cohort of 65 subjects (55 Cognitively Normal, 7 with Mild Cognitive Impairment, and 3 with Alzheimer's Disease) exhibited motion with an average displacement of 0.66mm in X, 1.04mm in Y, and 0.83mm in Z axis. While this motion is within the accuracy range of the tracking setup, it's at the lower bound of 0.7mm, which is the limit imposed by the spatial calibration used in the study. To ensure isotropic enhancement of spatial resolution, it may be useful to impose motion on a patient's head, for example, with a motorized massage pillow that provides continuous pseudo-random motion. Combined with the movement of the bed, this could provide sampling in all three directions.

To investigate the optimal motion patterns and amplitudes required for super-resolution, we conducted a simulation study using a high-resolution 2D phantom image consisting of nine hot spots of 2.4mm in size. Six specific patterns of motion, including linear, circular, a combination of linear and circular (similar to that which was applied to our phantom experiments), Brownian-like, spiral, and random back and forth, were applied to the object on a hundred frames. The resulting list-mode data were then reconstructed using our super-resolution method and compared to a static reference. The mean peak-to-valley ratios (MPVR) of line profiles were calculated to quantify the benefits of super-resolution compared to the static reference. Our results showed that linear motion provided the highest super-resolution improvement, with a peak MPVR of 10 compared to an average of 3.5 for the static reference. Brownian-like motion, spiral motion and the combination of linear and circular motion also yielded significant

super-resolution benefits, while circular motion and random back and forth motion resulted in less improvements.

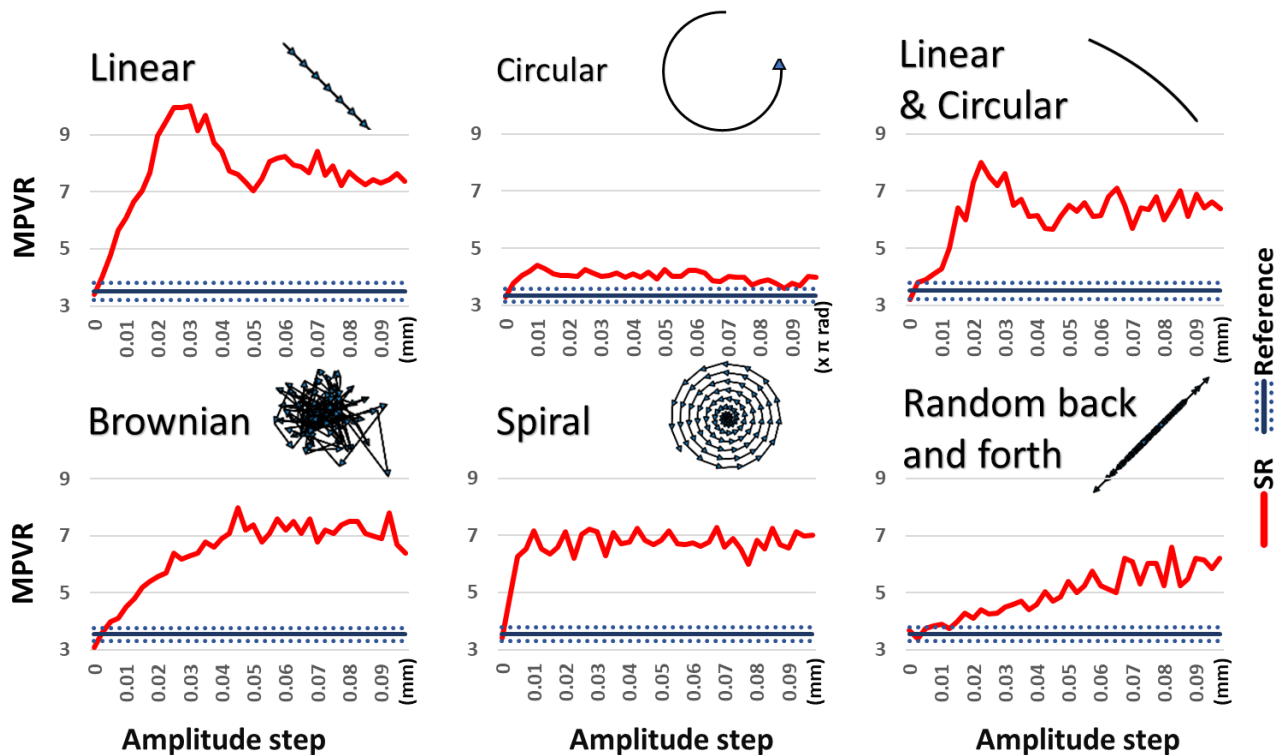


Figure 13 Illustration of the six patterns shapes we defined and plots of corresponding graphs displaying the measured resolution in terms of MPVR as a function of the amplitude step. The displayed patterns were obtained by applying the motion on a single point to have a sense of the path taken by the digital phantom for a given amplitude step. The MPVR were calculated on line profiles drawn on the reconstructed SR (red MPVR) and static reference images (blue MPVR). The dashed lines indicate one standard deviation around the mean reference MPVR.

These simulations showed that the specific motion amplitude required for optimal super-resolution benefits depends on the type of motion pattern used, but any type of pattern will lead to an increase in resolution as long as the amplitude is sufficient. We believe that any of these patterns or their combination will result in an increase in resolution in a clinical setup. However, these quantitative results depend on several parameters that we chose to fix for this study and may not be generalizable to other scenarios. Overall, our findings provide valuable insights into the optimal motion patterns and amplitudes required for super-resolution, which can guide future clinical studies in this area. Further details on the evaluation measure are provided in the Appendix.

It is possible to further improve super-resolved PET images quality by guiding the reconstruction using anatomical prior information (in a Bayesian sense). Such a regularization, allowing for better noise control, could be important in SR as noise is exacerbated with smaller

voxel size. Moreover, OSEM algorithm generally cannot be run to full convergence because the noise in the image grows with each iteration (Mettivier et al., 2011). To compensate for this, the algorithm is generally stopped after a determined number of iterations, resulting in an under-converged image. To address the effects of convergence and provide a more accurate PET quantitation, a regularized reconstruction iterative algorithm will be studied in Chapter 6, incorporating prior knowledge about the image into the reconstruction to better control noise propagation during SR reconstruction. This prior knowledge can be incorporated as segmented anatomical information from MR or CT images.

While we only tested this super-resolution technique in preclinical studies, we are currently working on extending it to human subjects. It is essential that no relative movement occurs between the markers and the head as those would decrease motion tracking accuracy and thus the performance of SR. Moreover, the attachment device must be comfortable for long scans and must have minimal impact on CT and PET attenuation. Hence, we are working on developing a solution to rigidly attach markers to a subject's head, consisting of a pair of swimming goggles to which a 3-D printed rod has been mounted to bring the Polaris markers to the top the head.

One of the end goals of this work is to provide a methodology that will enable the detection of very early neurofibrillary tangles (NFTs) in regions. One of them is the locus coeruleus (LC), a small structure where tau pathology appears first in Alzheimer's Disease, decades before symptoms. New data suggest that the LC is one of the earliest sites of tau pathology in AD and the initiator in the transmission of NFT during the progression of AD; however, its elongated shape and ultra-small dimensions,  $\sim 6\text{-}22 \text{ mm}^3$  (Theofilas et al., 2017), pose a significant challenge for PET even with state-of-the-art scanners. Super-resolution may allow improved imaging of the LC.

## **5.5 Conclusion**

In both phantom and animal studies, we demonstrated that super-resolution can be achieved in brain PET by precisely measuring head movement in real-time using a high-resolution infrared tracking camera. We built a robust and accurate spatial and temporal calibration interface between a clinical scanner and the tracker to attain this. For both phantoms and NHP studies, the developed SR reconstruction method yielded PET images with visibly improved spatial resolution as compared to static acquisitions, allowing for improved visualization of small cortical and subcortical brain phantom structures. Improved PET resolution might allow for

earlier and more accurate diagnoses of neurological disorders such as Alzheimer's Disease. It may also enable more accurate estimation of image-based input functions to quantify dynamic brain PET studies.

In the next chapter, we detail some optimization in terms of resolution and PVE that were addressed during the Ph.D. We explain in more detail and extend the study of PSF modeling that we used in this chapter and the previous one. We also explore other techniques to improve PET image quality through different projector implementations and the inclusion of anatomical priors into the reconstruction.

# Chapter 6

## Optimizations for PVE and noise: PSF, Projectors and Kernel Method

In this chapter, we explore different types of optimizations that were implemented or studied. These optimizations aim to improve image quality, regardless of super-resolution. First, we study and evaluate the impact of the point spread function (PSF) modeling. The PSF, which was briefly introduced in Chapter 2 and Chapter 5, represents the impulse response or the imaging system's response to a point source in the context. Its modeling is fundamental in PET because its incorporation in an iterative reconstruction scheme can alleviate some of the inherent partial volume effects. We then discuss projectors, which are at the core of estimating the system matrix. The importance of different projectors, such as Siddon, multi-ray Siddon, and Distance Driven, and their effects and performance on image reconstruction are explored. Finally, we discuss how anatomical prior information can be incorporated into kernel-based reconstruction methods. Including prior information in PET reconstruction, whether a mathematical model or structural information, can help control the noise behavior by introducing a priori information. Such a prior plays the role of a smoothness constraint that penalizes the roughness of the image estimate and then reduces the noise level. Here we explore the kernel method, which models PET image intensity in each pixel as a function of a set of features obtained from prior information.

### 6.1 PSF Modeling

The point spread function describes the response of an imaging system to a point source. In PET imaging, accurately modeling the physical measurement process to account for the point spread function can improve the subsequent resolution of the reconstruction by alleviating

some of the effects of the detector response function, the non-collinearity of the photon pair, and the positron range.

The PSF models are usually based on theoretical derivation, analytical approximation, computer simulation, or experimental measurements. In PET, several methods have been developed for estimating and modeling PSF in the projection space or image space. These methods can be broadly classified into three categories: analytical approaches (Rahmim et al., 2008; Selivanov et al., 2000; Strul et al., 2003), Monte Carlo simulations (Alessio et al., 2006), and physical measurements using point or line sources (Alessio et al., 2010; Cloquet et al., 2010; Panin et al., 2006; Sureau et al., 2008).

The PSF can be corrected directly in the image space, in the projection space, or in a hybrid fashion, i.e., both in the image and projections space.

### **6.1.1 In the image space**

Incorporating the PSF in the image space involves using a pre-defined or estimated PSF to directly model the degradation of the image due to the system's response to the point source. This can be done by convolving the estimated or measured PSF with the reconstructed image in order to account for the spread of the emitted radiation as it passes through the system. This is the method we used for our SR reconstructions in Chapter 4. One advantage of this approach is that it is relatively simple and can be easily implemented. However, it does not consider the spatially varying nature of the PSF, which can lead to suboptimal results in some cases (Deller et al., 2021).

The PSF in the image space is a function that describes how a voxel is blurred into other voxels in the field of view (FOV). In theory, it would be necessary to measure the PSF at every voxel in the FOV to understand the blurring effects fully, but this is a very time-consuming and complex task. As a result, the PSF is usually measured at a limited number of locations in the FOV, and the characteristics of the PSF at other locations are estimated using interpolation or extrapolation based on the symmetry of the FOV. The PSF at a given location can then be estimated by reconstructing point source data using an algorithm that does not model PSF-related effects and then by fitting the reconstructed data to an analytical function. Some studies have used shift-invariant Gaussian kernels to model the PSF based on a single measurement at the center of the FOV (Reader et al., 2003). However, this method had limited success for scanners with depth-of-interaction measurement capabilities. More accurate approaches, out of

the scope of this manuscript, take into account the anisotropic, asymmetric, and potentially non-Gaussian characteristics of a PSF kernel.

### 6.1.2 In the projection space

Incorporating the PSF in the projection space involves using the PSF to directly model the degradation of the projection data due to the system's response to the point source. This can be done by convolving the estimated or measured PSF with the projection data before it is used in the reconstruction process. This approach allows for the spatially varying nature of the PSF (*Figure 6.1*) to be taken into account, which can lead to more accurate reconstruction results (Deller et al., 2021). However, it is generally more computationally complex than incorporating the PSF in the image space, and in practice, it is not feasible to measure the PSF for each LOR.

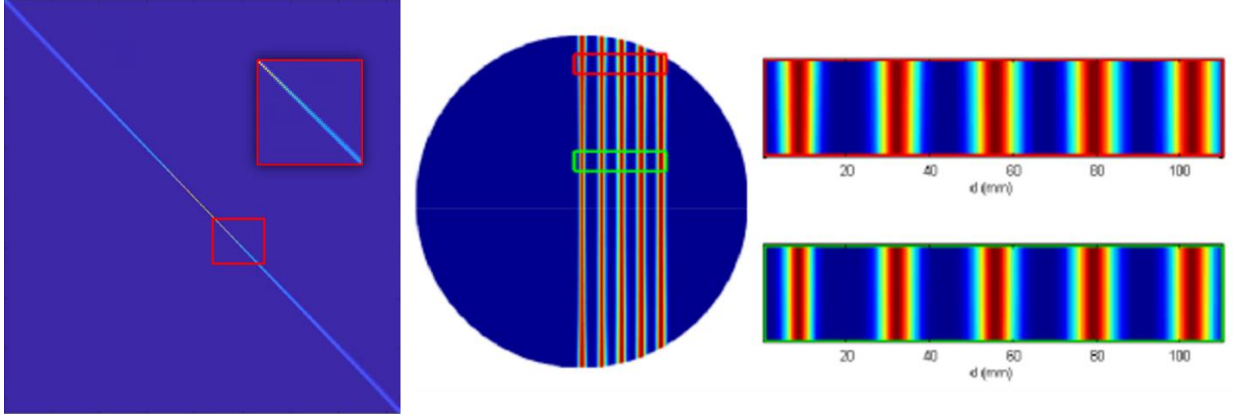


*Figure 6.1 Visualization of the contributions of the voxels to typical LORs with varying distances to the isocenter. Magnified partial LORs are shown on the right. Adapted from (Cui et al., 2011).*

During an MLEM/OSEM reconstruction, to account for the spatially variable nature of the PSF, we can apply it in the projection space by spreading the LORs only along their radial neighbors. Hence, for a treated LOR, we determined its radial neighbors, which number is given by the width of a kernel corresponding to that LOR. Then, we weighted the projected or back-projected values of the neighboring LORs according to that kernel's values.

More precisely, the forward projection model introduced in Chapter 1 in (1.7) by  $FP(\boldsymbol{\rho})_i = \sum_{j=1}^J p_{i,j} \rho_j$  becomes:

$$FP(\boldsymbol{\rho})_i = \sum_{k=1}^K \sum_{j=1}^J p_{i_{kj}} \cdot \rho_j \cdot Bproj_i[k] \quad (6.1)$$



where,  $j = (1, \dots, J)$  is an image voxel,  $J$  is the total number of voxels,  $K$  is the size of a discrete PSF kernel  $B_{proj_i}$  defined for a radial bin of LOR  $i$  and  $i_k$  is the radial neighbor of LOR  $i$  indexed by  $k$ .

Since we only consider the radial neighboring LORs for a specific event, the PSF is not fully characterized for each LOR. However, this approximation yielded sufficient improvement for a reasonable increase in computation time (each LOR being projected and back-projected multiple times according to the width  $K$  of a PSF kernel given for a radial position).

The kernel values we used for our reconstruction were based on experimental measurements of a sodium point source, which the constructor scanned at different radial positions.

### 6.1.3 Hybrid approach

A hybrid approach incorporating the PSF into the reconstruction process in PET imaging involves combining the techniques of incorporating the PSF in both the image space and the projection space.

This approach first incorporates the PSF into the projection space, as described above. The modified projection data are then used to reconstruct an initial estimate of the image, which is then convolved with the PSF in the image space to obtain a final estimate of the image. This hybrid approach can potentially combine the benefits of both image space and projection space incorporation of the PSF, while mitigating some of the limitations of each approach.

This is the method we used for our SR reconstructions in Chapter 5. In our MLEM/OSEM formulation  $p_{i,j}$  is an element of the PET system matrix defined as:

$$p_{i,j} = \sum_{l=1}^I B_{proj_{i,l}} \sum_{k=1}^J g_{l,k} B_{img_{k,j}} \quad (6.2)$$

where  $g_{i,j}$  accounts for the geometric probability that an event generated in voxel  $j$  is detected along LOR  $i$ ;  $B_{img_{k,j}}$  and  $B_{proj_{i,l}}$  are elements of PSF kernel matrices in the image space and in the projection space, respectively. PSF effects are accounted for in two steps during reconstruction: the spatially invariant 3D Gaussian smoothing kernel  $\mathbf{B}_{img}$  is first applied to the image at each update and then LORs are spread in the projection step according to the spatially varying PSF kernel  $\mathbf{B}_{proj}$ , and vice-versa during back-projection.

We found that using a hybrid approach in our super-resolution reconstruction has several benefits. Firstly, the image-space component models the positron range (in soft tissues) and

allows for the use of slightly narrower PSF kernels in the projection space, which speeds up projection and back-projection operations during each update. Secondly, integrating image smoothing makes the reconstruction more robust to high-frequency artifacts that might appear during the iterative process. This is especially important when computing the sensitivity image, as high-frequency artifacts can be propagated and not compensated for during maximum likelihood expectation maximization (MLEM) reconstruction. Smaller voxel sizes in SR reconstructions can lead to more artifacts, but using a PSF model in the sensitivity image can help smooth these artifacts and improve the overall quality of the reconstruction.

*Figure 6.2* shows the difference between reconstruction with and without PSF modeling for standard, 1mm, and SR reconstructions for the Hoffman phantom.

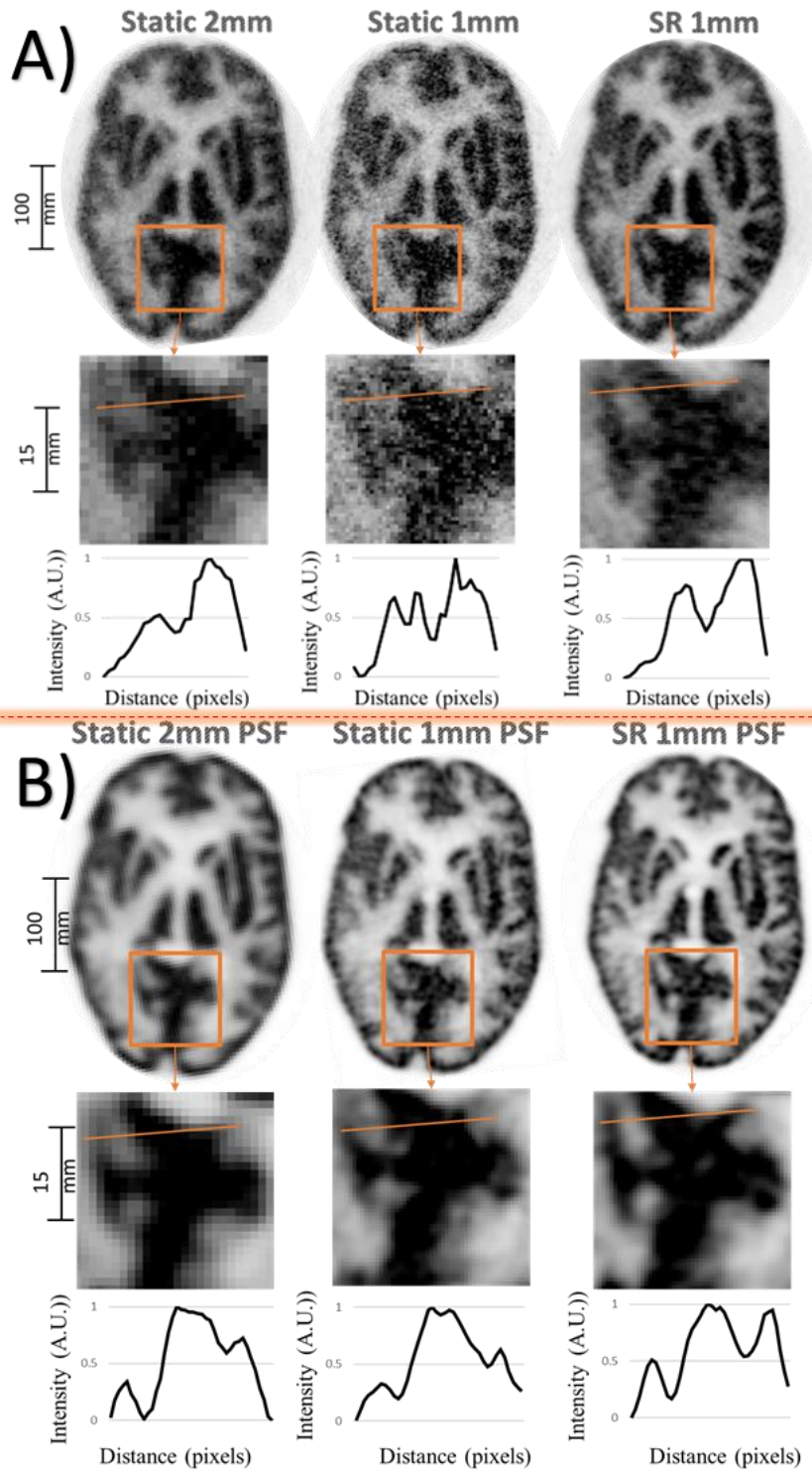


Figure 6.2 Hoffman phantom reconstruction at 1mm, 2mm, and SR A) without PSF, B) with the hybrid implementation of the PSF modeling.

Similarly, Figure 6.3 displays in vivo data with and without PSF modeling.

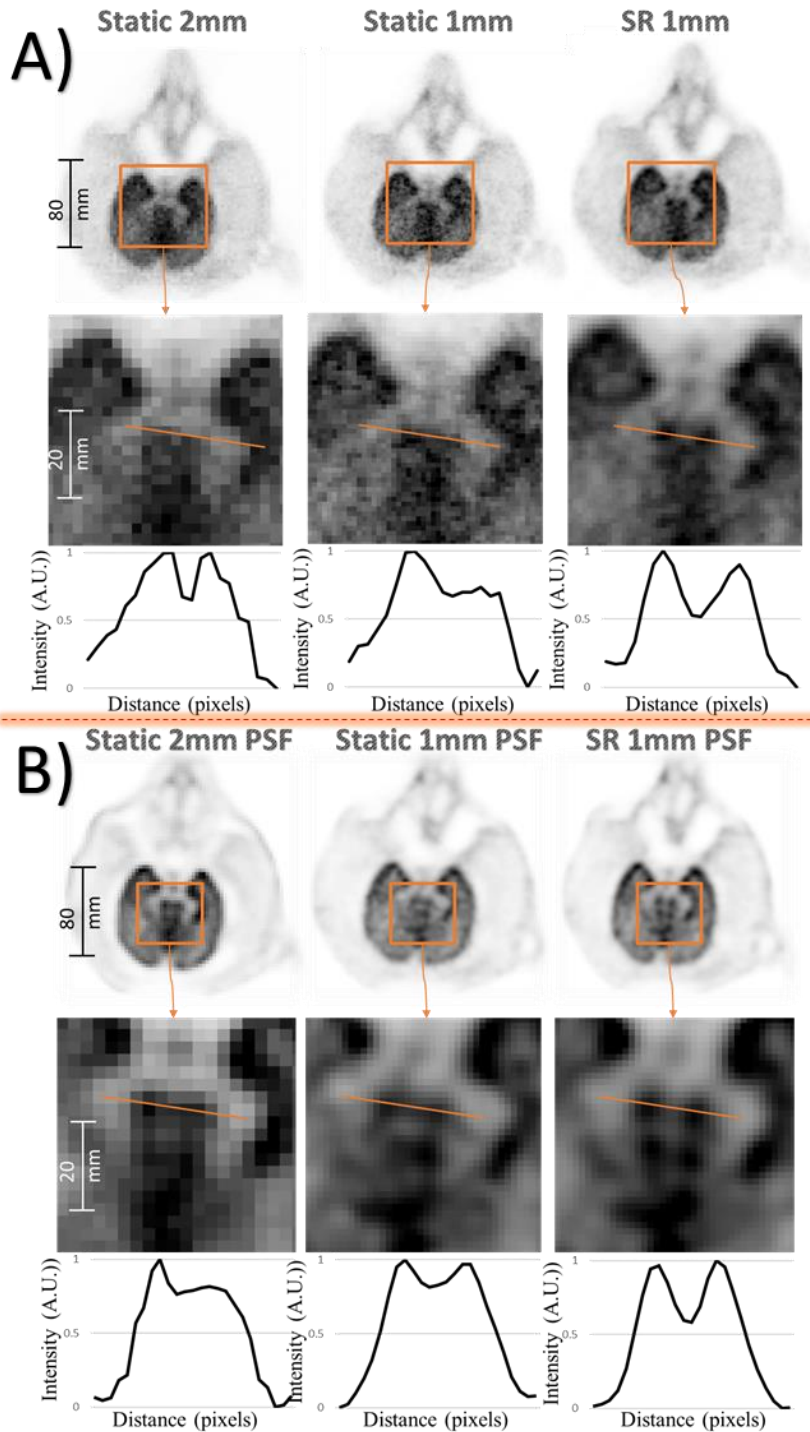


Figure 6.3 Nonhuman primate reconstruction at 1mm, 2mm, and SR A) without PSF, B) with the hybrid implementation of the PSF modeling.

We note increased resolution for both the Hoffman and NHP experiment and better noise control thanks to the PSF modeling. We can visually see improvement in details and contrast in small regions of the brains over the reconstructions that do not include the PSF modeling. We could also appreciate fewer artifacts thanks to the PSF smoothing effects. To give a quantitative idea of the impact of the PSF modeling, the contrast to noise ratio (CNR, defined

in 5.2.5) for the Hoffman phantom with and without PSF. The reconstruction with the PSF modeling led to a CNR of 20.62, while the reconstruction without the PSF modeling led to a CNR of 15.91.

## 6.2 Projectors

The projectors are essential to an iterative image reconstruction algorithm; it is the function linking an event, i.e., the record of two coincident photons by two detectors, and the activation (i.e., value) of the voxels of the image. As the projector function is called for each list-mode event twice per iteration (forward and backward projections), it must be both computationally effective and accurate for the voxel's activation. Unlike the Siddon projector (Siddon, 1985), which uses a ray-based approach, the distance-driven projector (Manjeshwar et al., 2006) uses a boundary-based approach, computing the boundaries of the "TOR" (tube of response) and activating the voxels within it.

### 6.2.1 Single-ray Siddon

A projector often used in practice is the Siddon Ray-Tracing algorithm, published for the first time in 1985 (Siddon, 1985). It models an event by a single line joining the centers of the two detectors. Instead of computing the intersection of the line of response with the voxels, which scales in  $N^3$  (the total number of voxels in the image), with  $N$  the number of voxels in a given axis, the Siddon projector computes the intersection of the LOR with the three sets of orthogonal planes defining the grid, which scales in  $3N$  (the number of orthogonal planes).

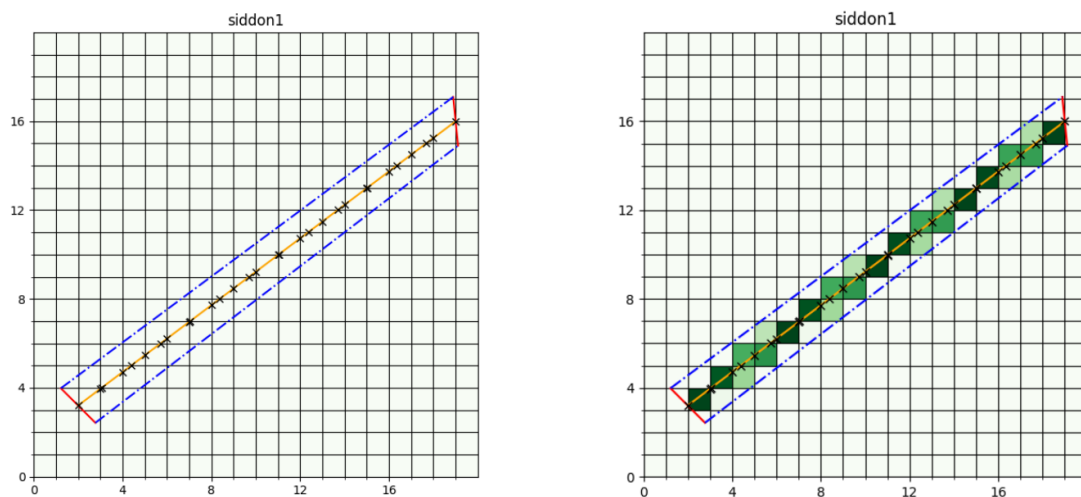


Figure 6.4 Siddon 1 ray - calculated points (left) and resulting voxels activation (right).

On the left side of Figure 6.4, the black crosses are the calculated intersections between the LOR (yellow) and the planes. The voxel activation is the length of the LOR inside the voxel.

The minimum value is when the segment has a null length, and the maximum value is when the segment is one of the big diagonals of the voxel (the longest segment that can fit inside a cube/rectangle). However, we can see on the right of Figure 6.4 that the Siddon projector only activates the voxels at the center line of the “Tube of Response” or TOR, leaving the outer voxels inactivated.

### 6.2.2 Multi-ray Siddon

Instead of just one line of response, we can use more lines inside the TOR to activate more voxels, allowing for better sampling. This becomes necessary when the voxel size gets smaller (relative to the scanner detector size). Instead of a single line, multiple lines joining random points located on the face of a detector are used (Moehrs et al., 2008). In Figure 6.5, we can see four simulated lines and the resulting activation. We can see a substantial improvement when it comes to the activation of the voxels inside the TOR.

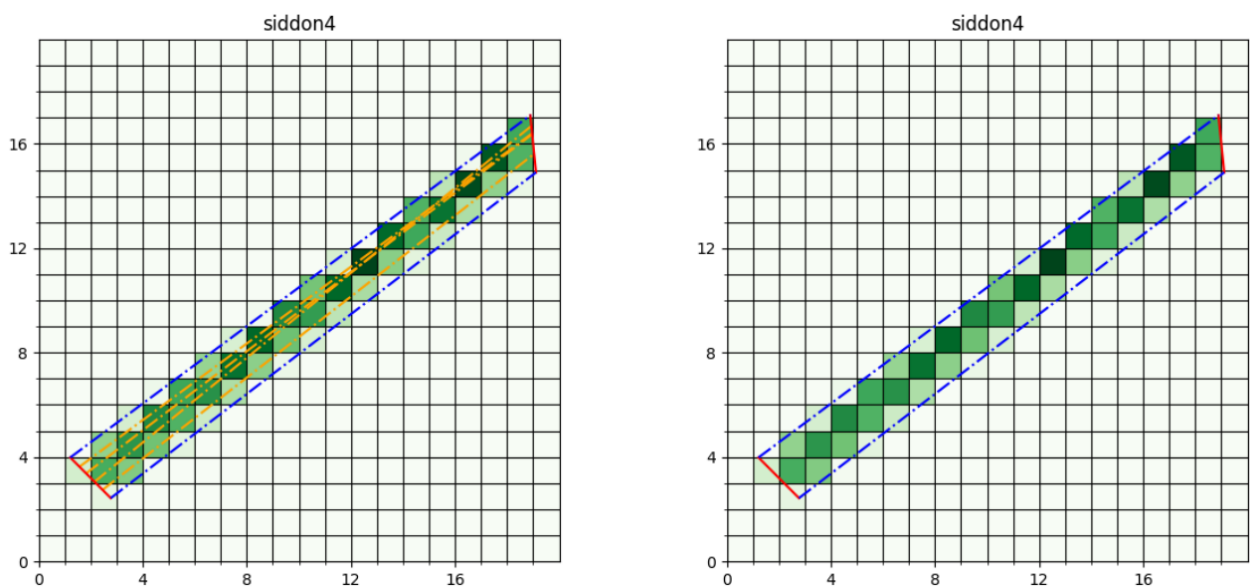
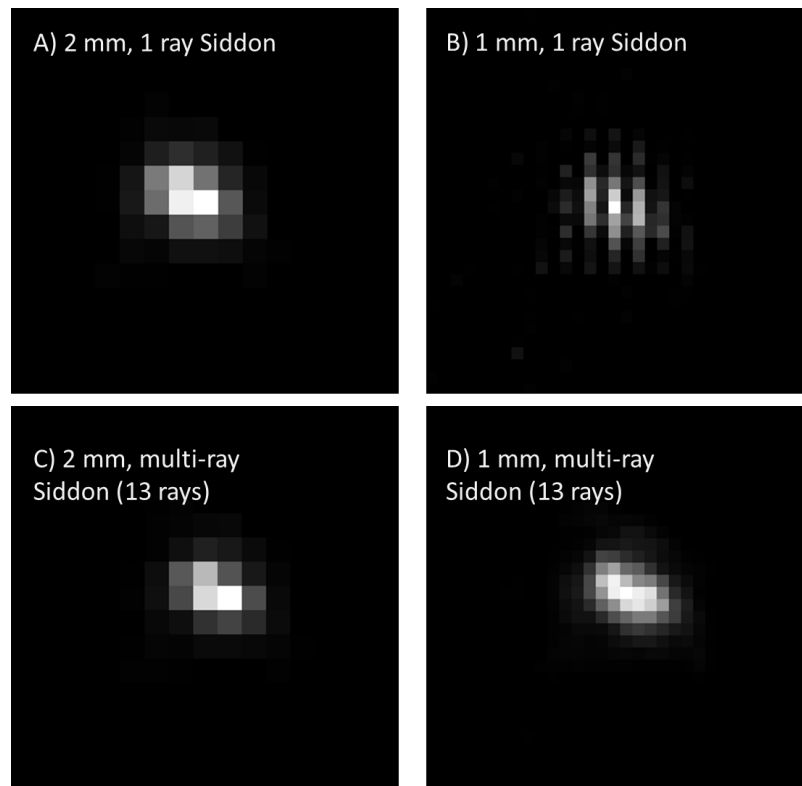


Figure 6.5 Siddon 4 rays - 4 rays used for computation (left) and resulting voxels activation (right).

In our SR experiments, the results were noticeable, and we found that using a multi-ray or TOR approach was necessary because of the voxel size we used. There are multiple ways of implementing multi-ray Siddon, depending on how we want the rays to be distributed.

Figure 6.6 displays the results of a point source experiment conducted on the GE DMI system, which was reconstructed using four different methods: A) using a single ray Siddon with a 2mm voxel size, B) using a single ray Siddon at a nonstandard voxel size of 1mm, C) using 13 rays Siddon at 2mm voxel size, and D) using 13 rays Siddon at 1mm voxel size. The decrease

in voxel size in B) leads to the appearance of gap artifacts, which was expected since a single ray Siddon lacks sufficient voxel sampling. This issue is resolved using multiple rays, as seen in D).



*Figure 6.6 Comparison between single- and multi-ray Siddon. A) Standard reconstruction with 2 mm voxel size and single-ray Siddon. B) Non-standard reconstruction with 1 mm and single-ray Siddon sampling artifacts appear. C) Standard reconstruction with 2 mm voxel size and multi-ray Siddon. D) Non-standard reconstruction with 1 mm and a multi-ray Siddon, no sampling artifacts appear.*

Using a multi-ray approach accounts for the TOR having a non-null width instead of a single ray. As expected, using a Siddon projector with more rays slows the reconstruction, for it scales in  $m \times 3N$ , with  $m$  the number of rays used and  $N$  the number of voxels along a given axis. However, computation time becomes detrimental. In the case of SR, with a need for more than 20 rays per event, the computation time becomes impractical (in the order of a few days, depending on the experiment).

### **6.2.3 Distance-driven projector**

The distance-driven projector in PET (Manjeshwar et al., 2006) is another state-of-the-art projector used in tomography. In contrast to the Siddon projector, which is a ray-driven projector, the distance-driven projector computes the boundaries of the tube of response and

activates the voxels inside it. The computing is done by iterating on a given direction (x, y, or z), calculating the intersections of the TOR with the two other directions (Figure 6.7).

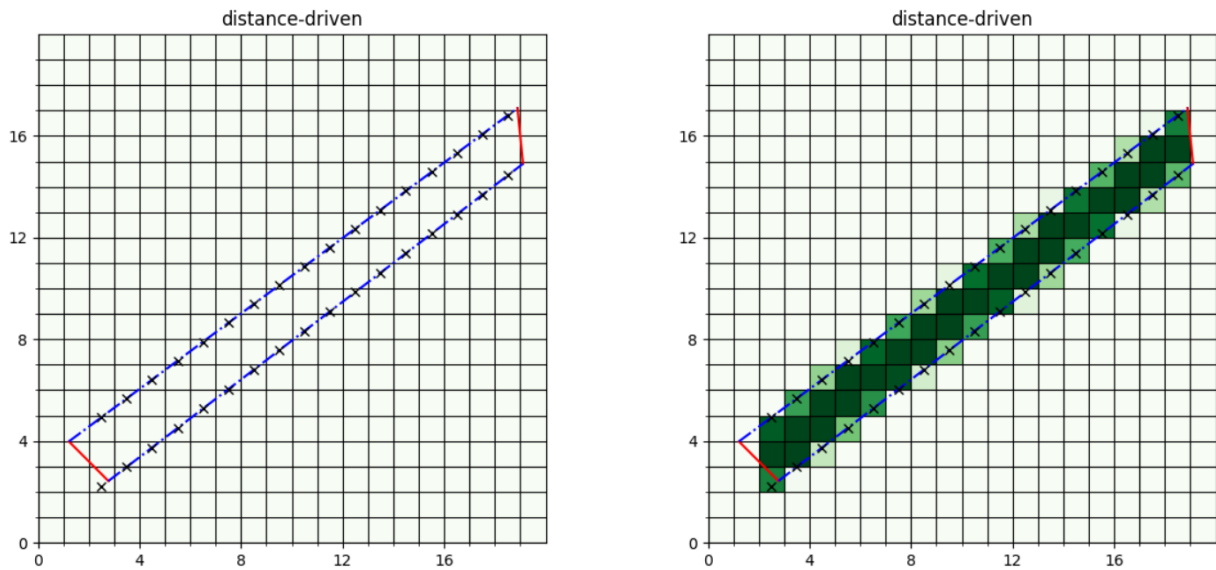


Figure 6.7 Distance-driven projector - calculated points (left) and resulting voxels activation (right).

The activation is based on the intersections of the TOR with the two other directions. The weight is the product of the weights of the two directions. The weight of one direction is the percentage of the voxel inside the TOR boundaries. If a voxel is fully inside, the weight is one.

Figure 6.8 compares the activation voxel grids between the one-ray Siddon (left) and the DD (right).

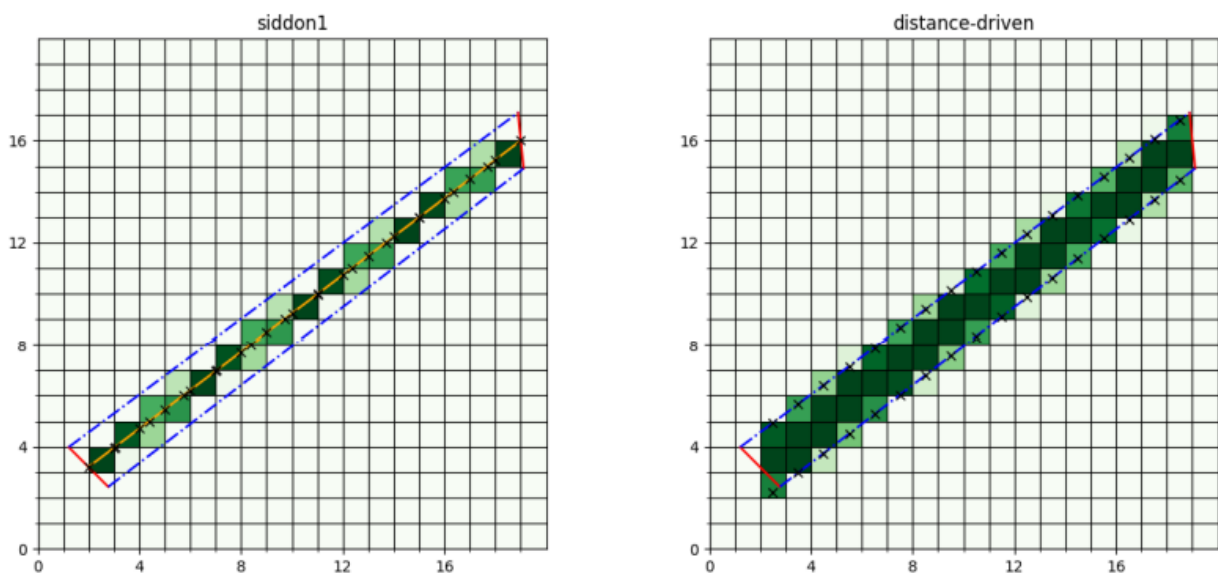
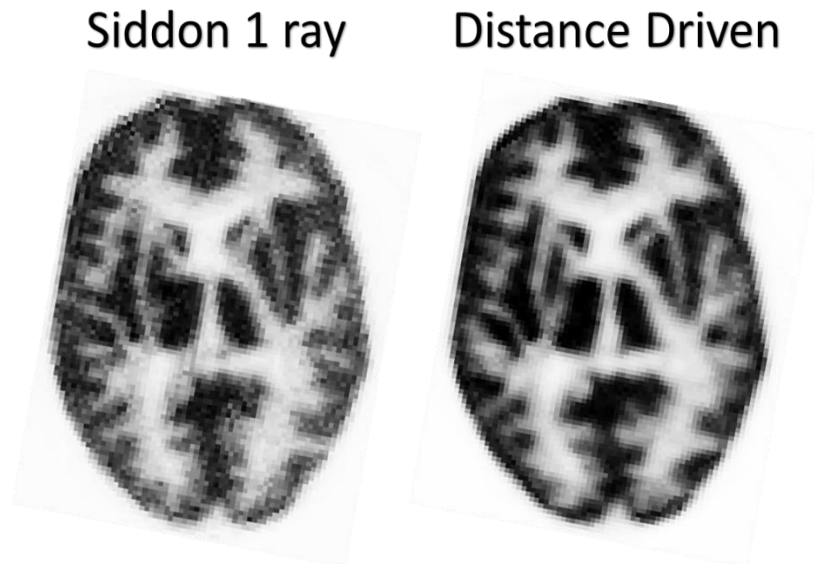


Figure 6.8 Comparison of the activation voxel grids between the Siddon 1ray (left) and the DD (right).



Regarding image reconstruction (Figure 6.9), with the same reconstruction parameters, the DD projector image yields visually improved images compared to a single ray Siddon in terms of noise and contrast.



*Figure 6.9 Hoffman phantom reconstructed with same parameters with Siddon 1 ray and distance driven.*

The distance-driven projector activates all the voxels inside the TOR uniformly. It scales in  $N \times n^2$ , with  $N$  the number of voxels in one direction and  $n$  the number of voxels intersected by a slice of the TOR projected in one direction. As a reminder, the Siddon 1-ray scales in  $3N$ , so the DD projector is inherently slower than the Siddon's projection. However, since we use a multi-ray approach with at least 20 rays per event in the context of SR, the DD approach becomes more practical. In fact, we can achieve a much faster projection for a comparable voxel sampling using DD. In our experiments, for 20 rays Siddon, the multi-ray is about 20 times slower than a single ray. In comparison, the DD projector only becomes about five times slower with a comparable sampling of voxels, making it more practical in this scenario.

#### **6.2.4 Evaluation of different projectors**

An evaluation of different projectors (ray- and distance-driven) on realistic phantoms has been carried out. We simulated a numerical 2D scanner where random lines of response were projected with the different projectors. Then, we compared the pixel overlap with the ideal analytical projector (ground truth), see Figure 6.10.

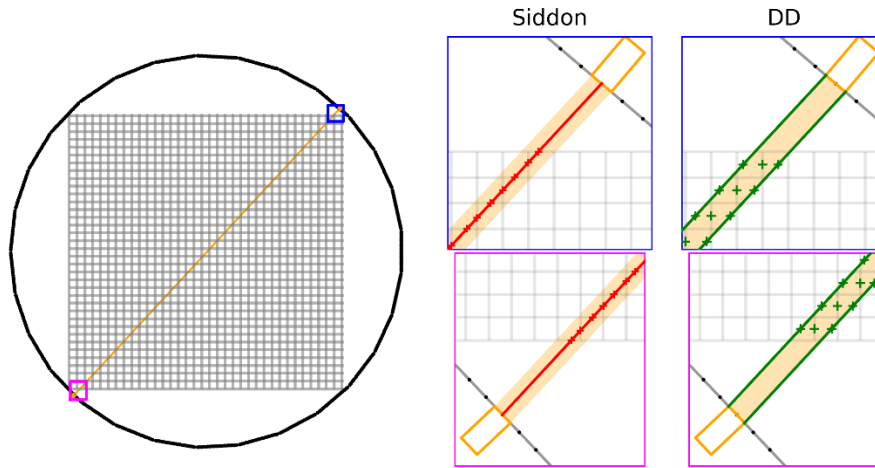


Figure 6.10 Schematic comparison of Siddon and distance-driven projectors.

The comparison of the different projectors, namely single-ray Siddon, multi-ray Siddon (20 rays), and DD projectors, was achieved by measuring the weight calculation error (compared to the ground truth projector) in terms of the normalized root mean squared error (NRMSE) for a large number of random events. The error distribution is summarized in histograms, shown in Figure 6.11.

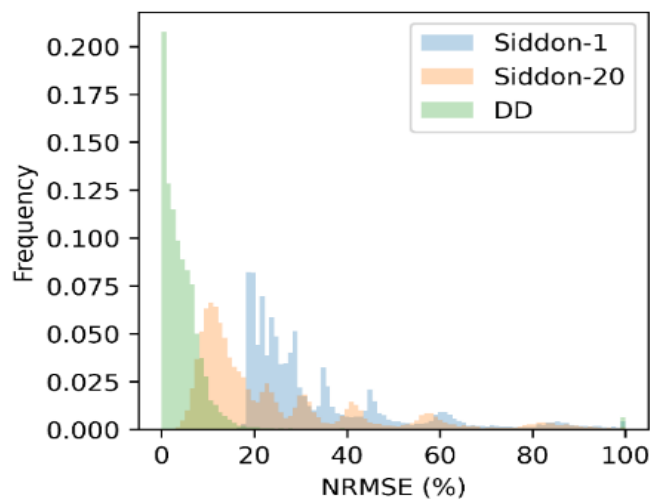


Figure 6.11 Histogram of overlap error of different projectors in terms of NRMSE.

We can observe that our implementation of the distance-driven projector seems to have the best performance, with an error being, on average, the smallest even compared to a multi-ray approach using 20 rays.

## 6.3 Kernel Method

### 6.3.1 Overview

We mentioned in Chapter 2 that one factor that can limit the quality and resolution of PET images is the presence of noise in the measurement data. We explained that noise could arise from various sources, such as photon counting statistics and detector non-uniformities, and can lead to degraded image contrast, reduced spatial resolution, and inaccurate quantification of tracer uptake. Therefore, reducing the impact of noise in PET images is an essential goal in the development of image reconstruction algorithms.

Maximum likelihood expectation maximization (MLEM) models the projection data as a set of Poisson random variables. However, MLEM is limited in reconstructing noise present in the data, particularly when applied to images with small voxel sizes. Various methods have been developed to address this issue that incorporate prior information about the structures being imaged into the reconstruction process. These methods can be broadly classified into two categories: penalized reconstruction methods and basis function-based methods.

Penalized reconstruction methods, such as maximum a posteriori expectation maximization (MAP-EM) (Zhou et al., 2007) and penalized maximum likelihood (PML) (Zhang et al., 2020), seeks to find the most probable image given the measurement data and a prior on the image. The prior can be formulated as a penalty term, which encourages the reconstructed image to have certain properties, such as smoothness or sparsity. The relative importance of the data fidelity term and the penalty term in the objective function is controlled by a hyperparameter, which can be adjusted to the tradeoff between variance and bias. Including prior information, such as anatomical information from co-registered magnetic resonance imaging (MRI) or computed tomography (CT), can be particularly useful in penalized reconstruction methods, as it can help guide the reconstruction process and improve the contrast and resolution of the reconstructed image. Bowsher's method (Bowsher et al., 2004), which utilized MRI information and was introduced in 2004, is a state-of-the-art anatomy-guided regularized PET image reconstruction technique. It uses a second-order smoothing prior, referred to as the "Bowsher prior," which encourages smoothing over an anatomy-dependent neighborhood, defined by selecting a set of most similar neighbors in the anatomical image. Variations of this method have also been proposed, but all aim to modify the weight of the potential function based on anatomical information rather than the PET image itself.

Basis function-based methods, such as dictionary learning (Cao et al., 2014) or, more recently, the kernel method (Wang and Qi, 2015), seek to reparametrize the emission image and the expectation maximization update equation using a set of spatial basis functions derived from the anatomical image. These basis functions can capture the structural features of the image and can be used to model the emission and attenuation distributions in the reconstruction process.

The kernel method is a mathematical approach that has been applied to the reconstruction of tomographic data, including PET. It is based on the non-local means filter, which is a denoising technique that uses a weighted average of the intensities of neighboring pixels to smooth an image and reduce noise. The kernel method extends this approach to the reconstruction of PET images by using a nearest neighbor search in a specified feature space to determine the voxels that contribute to a given basis function.

The feature space is defined by a set of features that describe the characteristics of the image, such as intensity, gradient, or texture. These features are typically extracted from an anatomical image, such as a magnetic resonance imaging (MRI) or computed tomography (CT) scan, which can provide valuable prior information about the structures being imaged. The distance between the features of a given voxel and its neighbors is used to determine the weights applied in the reconstruction process. These weights are typically defined by a kernel function, which determines the similarity between the features of the voxel and its neighbors.

### 6.3.2 Theory

#### Kernel MLEM

The kernel method can be mathematically formulated as follows (Wang and Qi, 2015): let  $\boldsymbol{\rho}$  be the PET image to be reconstructed (we recall that  $\boldsymbol{\rho} \in \mathbb{R}^J$  of size  $J \in \mathbb{N}$  which contains the radiotracer concentration  $\rho_j$  in each voxel  $j \in [1, \dots, J]$ ),  $\mathbf{f}$  the feature vectors of the image,  $\kappa$  be the kernel function. The basic idea is to represent the PET image  $\boldsymbol{\rho}$  by a linear function  $\Gamma$  of transformed anatomical features in a high-dimensional space.

$$\rho_j = \Gamma(f_j) \tag{6.3}$$

The idea is that  $\Gamma$  should be nonlinear to represent well a complex image in a low dimensional space spanned by  $\{f_j\}_{j=1}^N$ . A simple linear model  $\Gamma(f) = w^T f$  may not work because it assumes a linear relationship between the features and the image. But  $\Gamma$  can be described linearly in a transformed high dimensional space spanned by  $\{\varphi(f_j)\}_{j=1}^N$ .

We have then:

$$\Gamma(f_j) = \mathbf{w}^T \varphi(f_j) \quad (6.4)$$

Where:

- $\varphi$  is a mapping function from a low to very high dimensional space.
- $\mathbf{w}$  is a weight vector that also sits in the transformed space:

$$\mathbf{w} = \sum_{l=1}^N \alpha_l \varphi(f_l) \quad (6.5)$$

with  $\boldsymbol{\alpha}$  being a coefficient vector of size  $N$ .

The image is then represented by:

$$\rho_j = \Gamma(f_j) \quad (6.6)$$

$$= \mathbf{w}^T \varphi(f_j) \quad (6.7)$$

$$= \sum_{l=1}^N \alpha_l \varphi(f_l)^T \varphi(f_j) \quad (6.8)$$

$$= \sum_{l=1}^N \alpha_l \kappa(f_l, f_j) \quad (6.9)$$

Where  $\kappa$  is a kernel in which each column is a basis function.

The kernel function  $\kappa$  can be any function that satisfies Mercer's condition, which ensures that the kernel method has certain desirable properties, namely positiveness and semi-definiteness. Commonly used kernel functions that satisfy those conditions include the Gaussian kernel, the polynomial kernel, the Radial Basis Function (RBF), and the exponential kernel.

We can write Equation (6.9) in matrix form as:

$$\boldsymbol{\rho} = \mathbf{K}\boldsymbol{\alpha} \quad (6.10)$$

where  $\mathbf{K}$  is a  $J \times N$  matrix.

What we did is to represent an image  $\boldsymbol{\rho}$  by a linear combination of coefficients and basis functions where those lie in a very high dimensional space.

### Kernel-based MLEM formulation

In Chapter 1, we presented the following MLEM formulation, in sinogram and matrix form:

$$\boldsymbol{\rho}^{it+1} = \frac{\boldsymbol{\rho}^{it}}{\mathbf{P}^T \mathbf{1}} \mathbf{P}^T \frac{\mathbf{y}}{\mathbf{P}\boldsymbol{\rho}^{it} + \mathbf{R} + \mathbf{S}} \quad (6.11)$$

where we recall,  $\boldsymbol{\rho}$  is the PET image,  $\mathbf{P}$  is the system matrix,  $\mathbf{y}$  is the projection data,  $\mathbf{R}$  and  $\mathbf{S}$  are respectively the scatter and random contributions matrices.

Finally, (Wang and Qi, 2015) show that we can substitute  $\boldsymbol{\rho}$  by  $\mathbf{K}\boldsymbol{\alpha}$  in the MLEM algorithm which can be modified as follow:

$$\boldsymbol{\alpha}^{it+1} = \frac{\boldsymbol{\alpha}^{it}}{\mathbf{K}^T \mathbf{P}^T \mathbf{1}} \mathbf{K}^T \mathbf{P}^T \frac{\mathbf{y}}{\mathbf{P}\mathbf{K}\boldsymbol{\alpha}^{it} + \mathbf{R} + \mathbf{S}} \quad (6.12)$$

MLEM is calculated for  $\boldsymbol{\alpha}$  from which the PVE corrected image  $\boldsymbol{\rho}$  is calculated as  $\mathbf{K}\boldsymbol{\alpha}$ .

### Computation of the kernel matrix $\mathbf{K}$

In order to make it practical, only a subset of the full kernel matrix  $\mathbf{K}$  for an image is typically used, as a full kernel matrix  $\mathbf{K}$  of an image is usually too large to be computed in practice. To do this, k-nearest neighbors (k-NN) (Fix and Hodges, 1989) method is usually employed in machine learning. This method identifies in the feature space, the  $k$  most similar neighboring pixels for each pixel and uses this information to define the element at position  $(j, l)$  in the kernel matrix  $\mathbf{K}$ .

$$K_{jl} = \begin{cases} \kappa(f_j, f_l), & f_l \in kNN \text{ of } f_j, \\ 0, & \text{otherwise.} \end{cases} \quad (6.13)$$

where the k-NN is determined using the Euclidean distance between  $f_j$  and  $f_l$  in the prior image.

For our experiments, we chose  $\kappa$  to be a Gaussian kernel of the form:

$$\kappa(f_j, f_l) = \exp\left(\frac{-\|f_j - f_l\|^2}{\sigma^2}\right) \quad (6.14)$$

The process of extracting kernel features is illustrated in Figure 6.12.

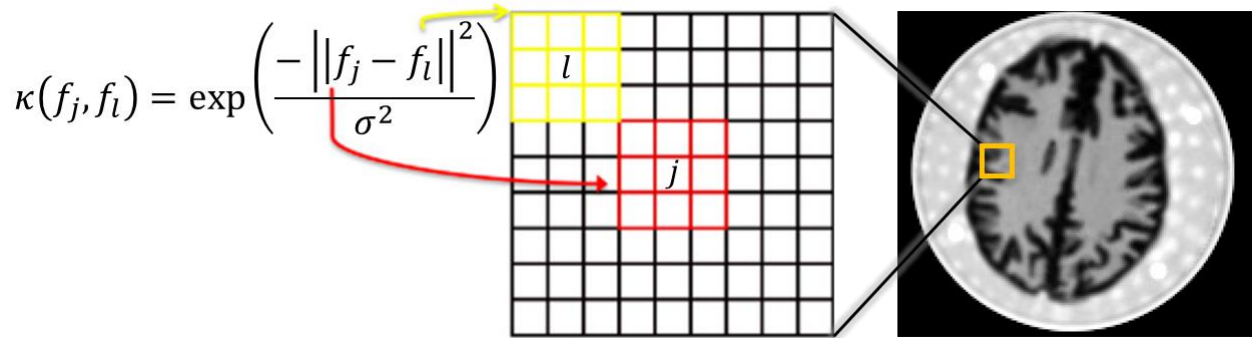


Figure 6.12 Kernel feature extraction. The radial Gaussian kernel function computes the patch-wise similarity between two voxels in the anatomical image. Adapted from (Hutchcroft et al., 2016).

## 6.4 Results

We performed a study on the Hoffman phantom from which we calculated a kernel matrix  $K$  using the co-registered CT image.

The reconstruction parameters were the following:

- 12 subsets, 3 iterations,
- 2 mm voxel size,
- one single ray Siddon,

and the parameters for the computation of  $K$  were:

- Number of neighbors  $k$ : 100,
- $\sigma = 10$ ,
- Search window: 10 pixels.

We obtained the reconstruction displayed in Figure 6.13.

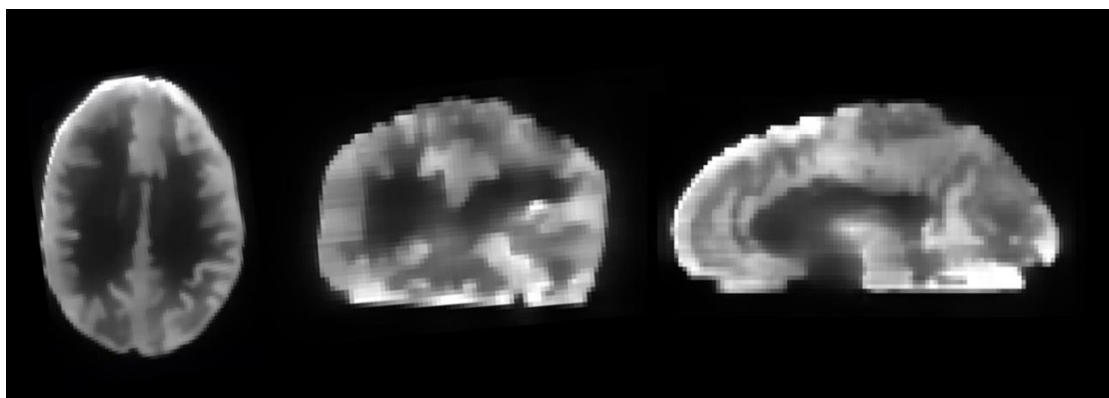
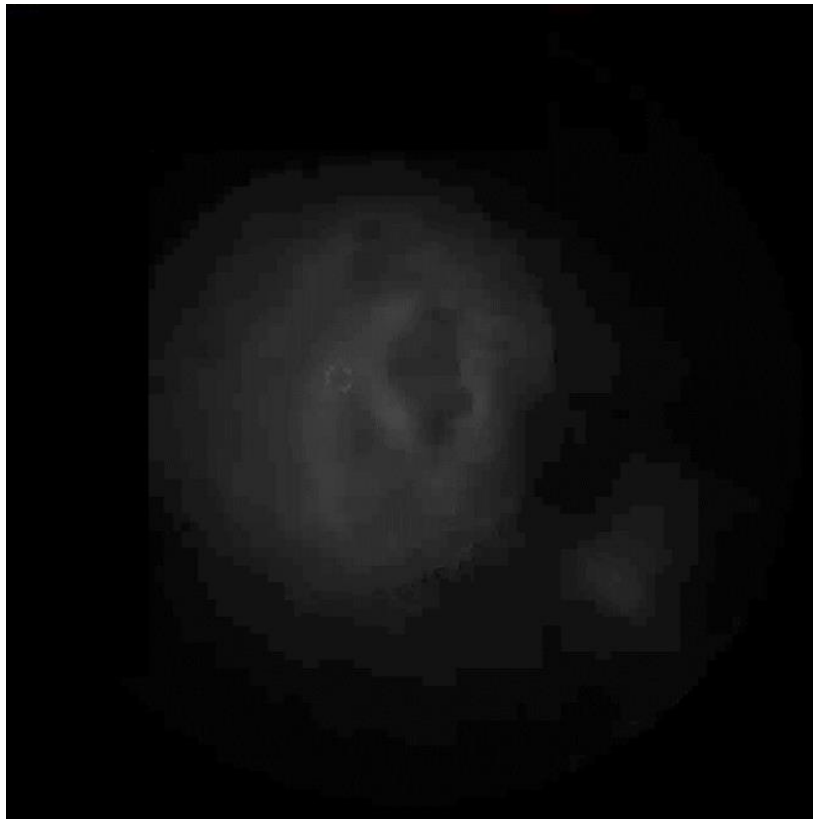


Figure 6.13 Kernel MLEM reconstruction on our Hoffman Phantom data a standard resolution.

We can observe a strong potential where we can notice reduced noise and artifacts, as well as better contrast and resolution compared to previous standard MLEM reconstructions (for example, in *Figure 6.9*). However, it is important to point out that the prior image registration to the PET must be very accurate, as any discrepancies will cause artifacts. In *Figure 6.13*, we can see that some parts of the brain jump in intensity due to a non-perfect registration.

Those are preliminary results that we obtained, and more efforts are continuing in improving, adapting, and quantifying the method.

In order to check that the influence of the anatomical prior using the kernel method does not introduce a strong bias, we reconstructed a random list-mode dataset using the same kernel matrix that was calculated using the Hoffman CT and the same reconstruction parameters. The result is presented in the axial view in *Figure 6.14*.



*Figure 6.14 Kernel MLEM reconstruction on a list-mode build with random events and with the same kernel matrix as in Figure 6.13.*

The signal, while mostly present at the location of the phantom, does not seem to display any relevant structure. This demonstrates that, at least, the kernel method does not introduce a strong bias.



While providing encouraging results, this work does not present a rigorous bias/variance study. This has been done in (Wang and Qi, 2015), where the authors used different reconstruction methods (maximum a posteriori method such as the Bowsher method, total variation, or expectation maximization with principal component analysis). They compared the results by looking at the quality of the images, as well as the trade-off between bias and variance. They used two different time frames, one with very low counts and one with high counts, and used the minimum mean squared error as a measure of image quality. They varied the parameters of the different methods (iteration number or regularization parameter) to see how they affect the bias and variance, concluding that the kernelized EM method (KEM) performed substantially better than the other methods in both low-count and high-count frames, and also achieved less bias at a fixed variance compared to any other method in the study.

## **6.5 Conclusion**

In this chapter, we explained that accurately modeling the PSF in PET imaging can significantly improve the resolution and overall quality of the reconstructed image. There are several methods for estimating and modeling the PSF, including analytical approaches, Monte Carlo simulations, and physical measurements. A hybrid approach, in which the PSF is corrected both in the image and projection spaces, has been found to have several benefits, including improved noise control, increased resolution, and increased robustness to high-frequency artifacts. Proper PSF modeling and projector selection are essential for achieving high-quality, clinically useful reconstructions in PET imaging.

In addition to PSF modeling, we studied how the choice of projector method can also significantly impact the accuracy and efficiency of the reconstruction process in PET imaging. The Siddon projector, which uses a ray-based approach, and the distance-driven projector, which uses a boundary-based approach to compute the boundaries of the "tube of response" and activates the voxels within it, are both commonly used in PET imaging. However, the distance-driven projector is considered a state-of-the-art method, as it accounts for the non-null width of the tube of response and can improve the accuracy of the reconstruction.

Finally, we explored the kernel method, a powerful technique that allows for the incorporation of anatomical priors in an MLEM reconstruction algorithm. One advantage of the kernel method is its simplicity of implementation compared to other basis function-based methods, such as dictionary learning. It has also been shown to have improved performance regarding region of interest quantification compared to other methods, such as Bowsher's method. The

kernel method has been applied to various types of tomographic data, including static PET, dynamic PET, reduced dose PET, diffuse optical tomography, and fluorescence molecular tomography. Its ability to reduce noise and preserve detail makes it a promising approach for improving the quality and resolution of reconstructed PET images. In further studies, we will try to combine all those optimizations with SR.

In the last contribution chapter, we attempt to correct for PVE in dynamic sequence using non-negative matrix factorization to improve quantification of hyperphosphorylated Tau protein using [ $^{18}\text{F}$ ]MK-6240 tracer.



# Chapter 7

## Disentangling tau-specific and off-target signals in [ $^{18}\text{F}$ ]MK-6240 PET using nonnegative matrix factorization

This chapter presents the theoretical foundations and practical applications of factor analysis and non-negative matrix factorization (NMF) in dynamic PET imaging (Section 7.2 and 7.3), with particular attention to the [ $^{18}\text{F}$ ]MK-6240 Tau PET tracer. We discuss the potential clinical limitations of this tracer, in particular its off-target binding, and how NMF can be used to overcome such limitations with a dynamic PET acquisition in Section 7.1. We first simulated a numerical phantom based on kinetics extracted from human data to test NMF, then we applied NMF to dynamic PET data acquired in human subjects, demonstrating the ability to accurately separate tau-specific, non-specific, and off-target signals in the acquired data. Finally, the results of the NMF analysis are presented in Section 7.6 and discussed in Section 7.7.

### 7.1 Introduction

As seen in Chapter 1, Section 1.4, Alzheimer's Disease represents the most common form of dementia accounting for 60 to 80% of dementia cases worldwide. Alzheimer's disease is characterized by the presence of hyper-phosphorylated tau proteins and amyloid beta ( $\text{A}\beta$ ) plaques in the brain. The progression of tau neurofibrillary tangles (NFTs) in the brain has been found to occur in a specific and predictable manner as the disease progresses, and it has been observed that the spread of NFTs is closely linked to the cognitive decline seen in AD patients (Arriagada et al., 1992; Braak and Braak, 1991; Villemagne et al., 2015).

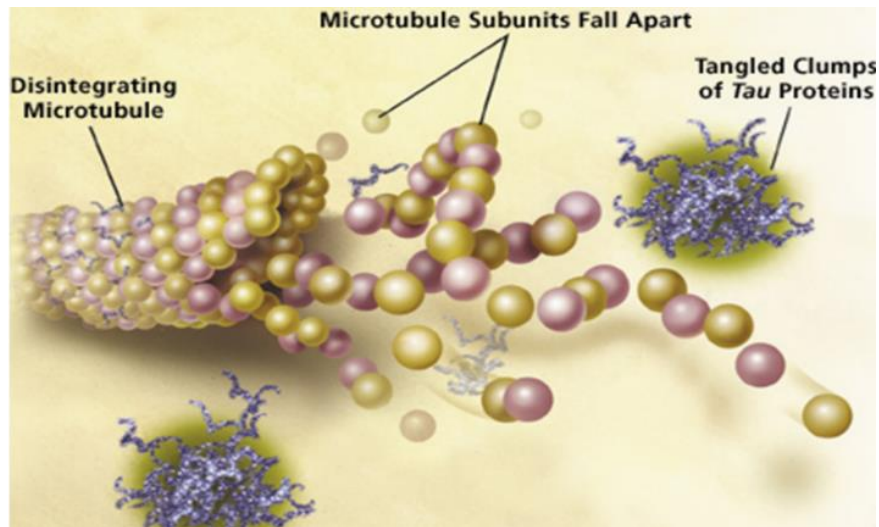


*Figure 7.1 Mechanism of tangled clumps of tau proteins. Adapted from (Alzheimer's Disease Education and Referral Center)*

Recently, there has been a significant effort to develop PET radiotracers for the in vivo measurement of NFT proteinopathy as biomarkers for AD and other types of dementia (Hall et al., 2017; Johnson et al., 2016; Schilling et al., 2016; Villemagne et al., 2015). These tracers are highly sought after as they would allow for the detection of small changes in NFT accumulation during the early stages of the disease and could be used in cross-sectional and longitudinal analyses and to evaluate the effectiveness of potential anti-tau therapeutics. However, despite the progress made by the first and second generations of tau radiotracers, there are still limitations with regard to off-target binding (Lemoine et al., 2018; Okamura et al., 2018). Importantly, even the most promising and widely used tau tracers, thus far, show some level of off-target signal, sometimes arising from structures located next to key brain regions, either directly implicated in the disease process or used as reference regions for signal quantification.

Although the second-generation tau tracer [ $^{18}\text{F}$ ]MK-6240 does not show significant binding in the choroid plexus or basal ganglia like previous tau tracers, several in vivo studies using PET, but also in vitro studies (mainly using autoradiographic techniques) have revealed off-target binding in the bone marrow, meninges, ethmoid sinus, and substantia nigra (Aguero et al., 2019; Betthausen et al., 2019; Guehl et al., 2019; Pascoal et al., 2018). Furthermore, it has been reported that in a significant number of cases, the specific [ $^{18}\text{F}$ ]MK-6240 signal measured in cortical areas may be contaminated by spill-in of off-target signals from adjacent regions, mostly extra-cerebral, such as the subarachnoid space and meninges (Betthausen et al., 2019). This extra-cerebral signal is also likely to contaminate the gray cerebellum, which is frequently

used as a reference region for quantifying PET signals in cross-sectional and longitudinal studies. Due to the limited spatial resolution of PET, the off-target signal spills into these key regions (Figure 7.2) and may greatly hinder the clinical and research utility of [ $^{18}\text{F}$ ]MK-6240.

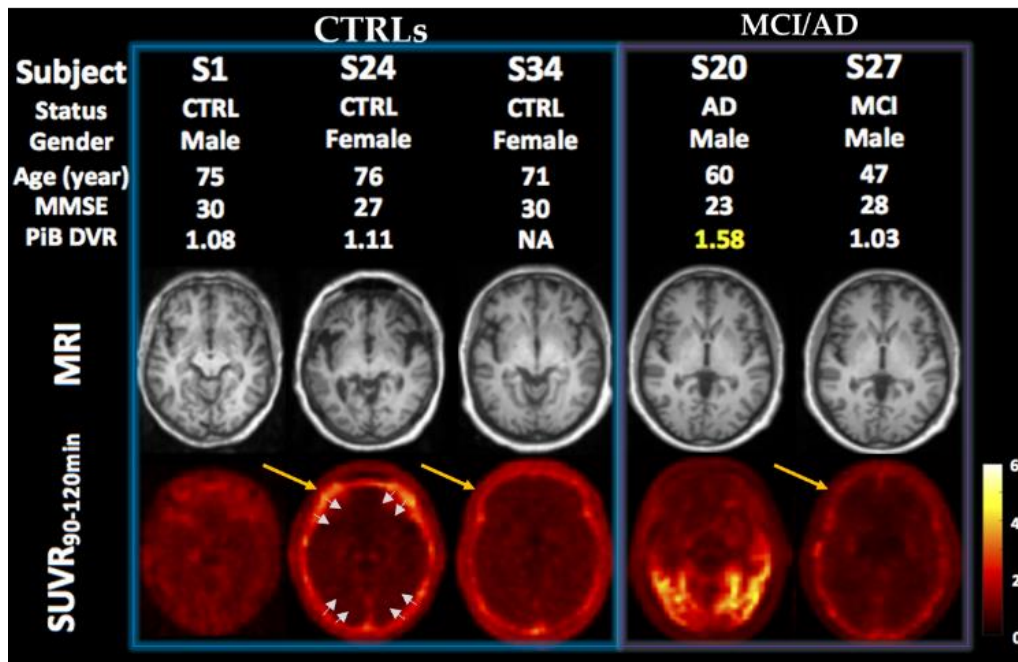


Figure 7.2 [ $^{18}\text{F}$ ]MK-6240 displays some off-target binding (yellow arrows) which was reported by several studies. This off-target binding is found mainly in extracerebral structures presumably coming from the meninges.

Interestingly, the kinetics in those extra-cerebral regions are quite different from those in the cortical regions (Figure 7.3).

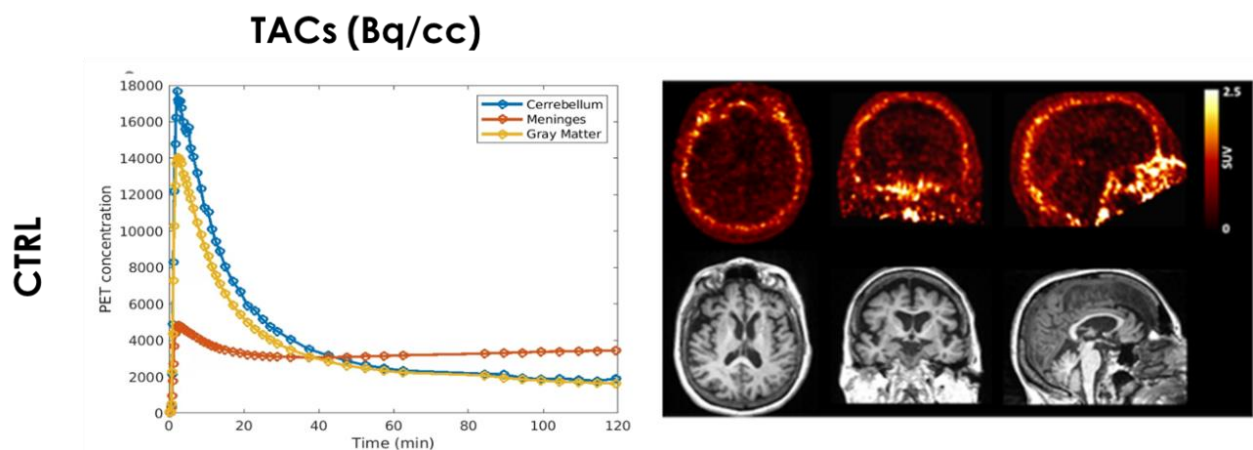


Figure 7.3 TACs manually extracted from different brain regions (cerebellum, meninges and gray matter) of a control patient on the left panel. The right panel displays different views of 90 to 120 minutes summed SUV PET, where we can see high off-target signal uptake in the meninges. The TAC extracted from the meninges has a specific dynamic, different from the other regions.

Knowing that, we may be able to exploit these spatiotemporal differences of signals in a dynamic sequence to extract automatically a target such as the off-target signal. In this work, we propose to address the off-target binding issue by factor analysis of the dynamic [ $^{18}\text{F}$ ]MK-6240 images using non-negative matrix factorization to disentangle the contribution of NFT-specific, non-specific and off-target components to the [ $^{18}\text{F}$ ]MK-6240 PET signal.

## 7.2 Literature review on factor analysis

While static imaging is often performed in clinical setups to obtain a map of the spatial distribution of the tracer concentration, dynamic PET has become increasingly popular, especially in research setups, due to its ability to provide both spatial and temporal information on the uptake of a tracer in vivo. PET images must first be quantified to understand their contents better. This is done using time-activity curves (TACs) which estimate the concentration of radiopharmaceuticals or radiotracers over time. The resulting data allows for calculating the kinetic parameters of the studied process. To ensure accurate quantification, reference TACs must be estimated for tissues, and an input function must be determined to describe blood flow.

Kinetic modeling techniques utilizing TACs are considered the gold standard method for quantifying physiological processes with PET. However, TAC extraction requires defining regions of interest, which can be done manually or through atlases. This manual process can be both time-consuming and inaccurate, and atlases may not always be available. To overcome these limitations, factor analysis, and related techniques have the potential to extract and separate kinetic information automatically, eliminating the need for manual ROI definition or reliance on atlases.

Factor analysis aims to uncover patterns in multivariate data by reducing the number of dimensions, which is done through various unsupervised learning techniques. It describes each voxel of the image as a combination of elementary temporal signatures, called factor curves, and a set of coefficients relating the tissue voxel with each factor curve (Barber, 1980). The method is hence based on the assumption that the observed data can be represented as a linear combination of a few factor curves, each representing the kinetic or spectral properties of the physiological compartments of interest. These factor curves are intrinsically associated with factor images, which provide a spatial representation of the physiological compartments (Figure 7.4).

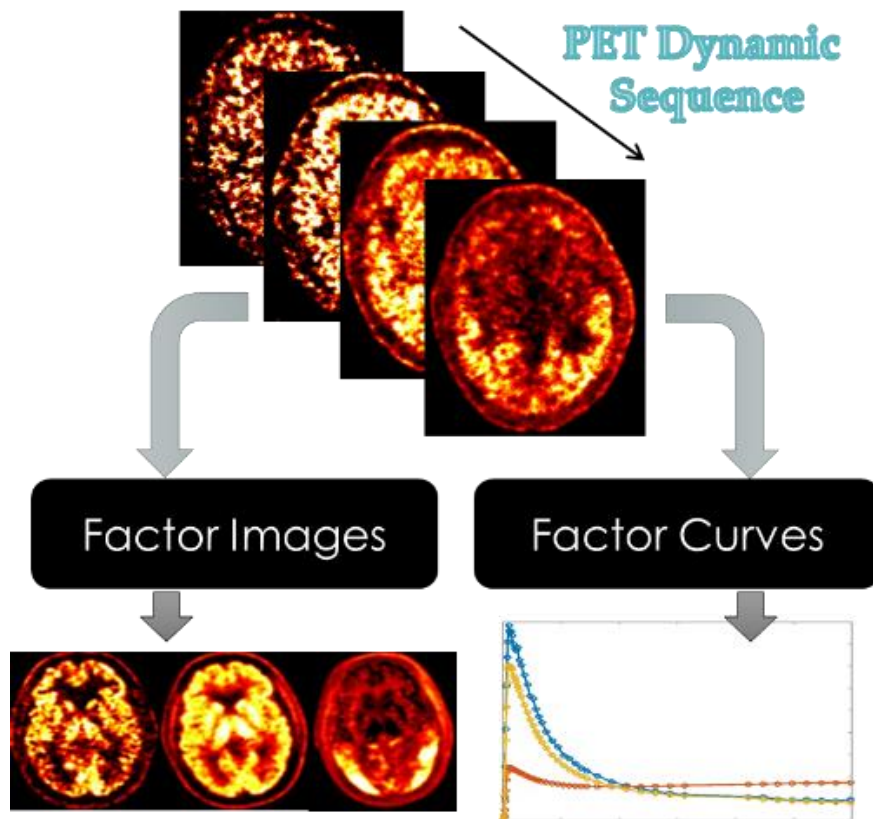


Figure 7.4 Factor analysis methods decompose a PET dynamic sequence into a combination of elementary signatures that can be interpreted as TACs associated with corresponding weight images.

One of the key challenges in using factor analysis for dynamic PET imaging is to accurately estimate the factors and factor images from the observed data. This is particularly challenging for dynamic images, which can be highly noisy and exhibit temporal variations. More importantly, accurately estimating factors with a physiological meaning and considering the non-uniqueness inherent to factor analysis are challenging tasks. To address those challenges, various techniques have been proposed to improve the estimation of the factors.

In the dynamic PET literature, two main approaches have stood out. The first one is based on singular value decomposition (SVD) or apex-seeking (Cavailloles et al., 1984; Di Paola et al., 1982), while the second one tries to directly estimate the factors and their respective fractions through optimization schemes (Sitek et al., 2000).

The first group of approaches is rooted in previous studies on principal component analysis for quantitative evaluation in medical imaging (Schmidlin, 1979). Barber (Barber, 1980) was the first author to propose this matrix factorization-based analysis technique for gamma camera imaging. This method is based on the assumption that tissues are spatially homogeneous with respect to a given tracer. Therefore, a single TAC is able to characterize the variation of tracer concentration over time for all points within an organ. This technique, referred to as factor



analysis of dynamic structures (FADS), was further developed by Di Paola et al. (Di Paola et al., 1982) and applied by Cavailloles (Cavailloles et al., 1984) for non-invasive gated cardiac studies under positivity constraints. Nijran and Barber (Nijran and Barber, 1986) highlighted the importance of providing physiological a priori information on at least one of the factors to reduce the number of possible solutions to the problem. Other researchers have also addressed the issue of identifying physiologically meaningful factors in FADS approaches using set theory and clustering (Houston, 1986) or rotation procedures (Sámal et al., 1987). In a later work, Sámal et al. investigated the ambiguous nature of general factor analysis problems applied to dynamic PET. The relevance of constraints on providing physically meaningful factors for FADS approaches was studied in (Nijran and Barber, 1988). Nakamura et al. (Nakamura et al., 1989) evaluated the performance of a factor analysis method based on the maximum entropy principle in dynamic radionuclide images. In (Van Daele et al., 1990), a background correction was implemented within factor analysis. Buvat et al. (Buvat et al., 1993) proposed a target apex-seeking method that identifies a factor when knowing part or the entirety of its shape. Benali et al. (Benali et al., 1993) summarized the step-by-step procedure applied in the domain until its publication as the following:

- first, a preprocessing step that often consists of clustering and selection of TACs is conducted on data to improve SNR,
- then, an orthogonal analysis (often SVD) is applied to the selected TACs to reduce dimensionality, producing basis vectors,
- an oblique rotation of the previously estimated basis vectors is then conducted to obtain non-orthogonal factor TACs, representative of tissues and blood,
- finally, an oblique projection of the image is used to produce factor coefficients.

In contrast to the previous SVD-based approaches, the second group of approaches in dynamic PET literature is based on optimization. A Monte-Carlo-simplex iterative method was first introduced by Bazin et al. (Bazin et al., 1979). Van Daele et al. (Van Daele et al., 1990) proposed a vertex-finding algorithm that is based on the minimization of a function of the vertices. Sitek et al. (Sitek et al., 2000) applied a conjugate gradient algorithm to conduct FADS on cardiac images by minimizing a least square function, such as in the optimization:

$$D(\mathbf{V}|\mathbf{WH}) = \|\mathbf{V} - \mathbf{WH}\|_F^2 \quad (7.1)$$

where  $\mathbf{V}$  represents the dynamic PET data,  $\mathbf{W}$  represents the factor images,  $\mathbf{H}$  represents the factor curves,  $\|\cdot\|_F$  is the Frobenius norm and is associated with a Gaussian assumption on the noise or the approximation residual. The article also proposed a post-processing step to

reduce the non-uniqueness encountered in factor analysis approaches. The works of Sitek et al. (Sitek et al., 2002) further improved nonnegative FADS with a penalization that promoted non-overlapping regions in each voxel, aiming at tackling the non-uniqueness problem inherent in factor analysis. El Fakhri et al. (El Fakhri et al., 2005) validated this approach by extracting left and right ventricle factor TACs in cardiac dynamic PET. In (El Fakhri et al., 2006), factor analysis was further generalized to a five-dimensional framework that includes three spatial dimensions, one temporal dimension, and a photon-energy dimension. In another study (El Fakhri et al., 2009), a factorization based on a Bayesian model was proposed to extract an interpretable and biologically meaningful factorization of dynamic PET data.

Overall, the first group of approaches in dynamic PET literature, based on SVD or apex-seeking methods, aims to extract principal components or factors through these methods and is rooted in earlier studies on principal component analysis in medical imaging. The second group of approaches, based on optimization methods, aims to minimize a function of the vertices to improve factor analysis and has been further enhanced by incorporating penalization to reduce non-uniqueness. These approaches have been continuously improved and refined over time to extract interpretable and biologically meaningful factorization of dynamic PET data.

In the second group of methods, there has recently been an increasing interest in the use of non-negative matrix factorization for the analysis of dynamic images in nuclear medicine. NMF is a powerful technique based on the assumption that the observed data can be represented as a non-negative linear combination of a few underlying basis images. Unlike traditional factor analysis, NMF does not require any assumptions about the data distribution.

## **7.3 Factor analysis using NMF for [<sup>18</sup>F]MK-6240**

### **7.3.1 Introduction to Non-Negative Matrix Factorization**

NMF exploits spatiotemporal differences of signals in a dynamic sequence to decompose this sequence into key temporal components. Dynamic [<sup>18</sup>F]MK-6240 PET data is represented by the matrix  $V$  of size  $N \times M$ , where  $N$  is the number of voxels in each 3D volume and  $M$  is the number of time frames. NMF assumes that the dynamic PET data can be represented by a linear combination of a small number of predefined  $k$  products, the factor images  $W$  of size  $N \times k$  and factor curves  $H$  of size  $k \times M$  such that  $V \approx WH$  (Figure 7.4).

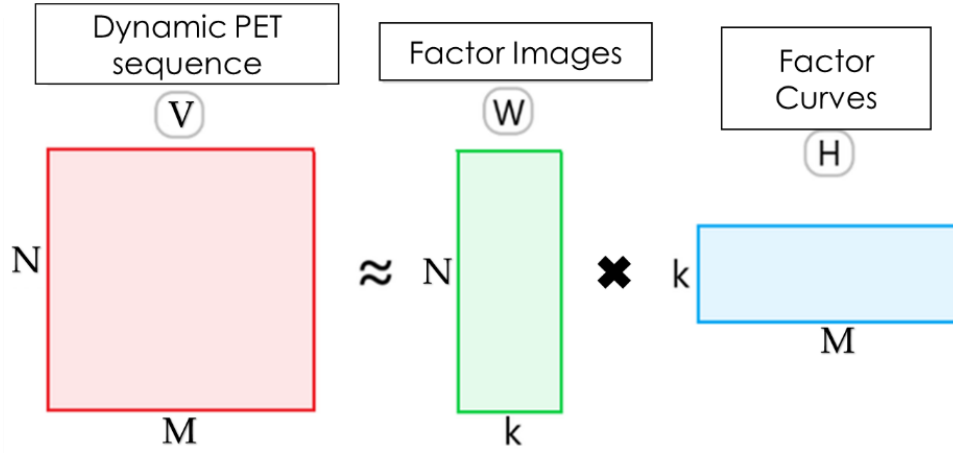


Figure 7.5 NMF compresses a matrix  $\mathbf{V}$  into the product of two low rank  $\mathbf{W}$  and  $\mathbf{H}$  matrices.  $\mathbf{V}$ ,  $\mathbf{W}$  and  $\mathbf{H}$  are positive matrices.

In the context of dynamic PET imaging,  $\mathbf{H}$  is the factor matrix containing the brain tissue TACs and  $\mathbf{W}$  is the factor image matrix containing their corresponding spatial representation.

However, NMF is NP-hard, there is no unique solution to the problem, and no analytic resolution exists in the general case (Vavasis, 2010). An approximation of the factorization is hence usually quantified by means of a dissimilarity in terms of distance or divergence between  $\mathbf{V}$  and  $\mathbf{WH}$ . An NMF algorithm is therefore an algorithm that minimizes  $\min_{\mathbf{W}, \mathbf{H} \geq 0} D(\mathbf{V} | \mathbf{W} \cdot \mathbf{H})$ , where  $D$  is the divergence.

Lee and Seung (Lee and Seung, 1999) proposed an algorithm with multiplicative update rules. They minimized the Euclidian distance to converge to a local minimum.

$$\min \frac{1}{2} \|\mathbf{V} - \mathbf{WH}\|_F^2 \text{ s. t. } \mathbf{V}, \mathbf{W}, \mathbf{H} \geq 0 \quad (7.2)$$

The matrices  $\mathbf{W}$  and  $\mathbf{H}$  are optimized successively. This algorithm is very commonly used because of its great simplicity of implementation and the speed of calculation of the iterations.

However, the Euclidian distance do not take into account the Poisson noise nature of PET data. The Kullback-Leibler divergence was used instead as it allows the uses of Poisson statistics as a noise model:

$$D(\mathbf{V} | \mathbf{WH}) = \sum_{m,n} V_{mn} \log \frac{V_{mn}}{(W \cdot H)_{mn}} - V_{mn} + (WH)_{mn} \quad (7.3)$$

where  $m = \{1, \dots, M\}$  and  $n = \{1, \dots, N\}$

From the divergence cost function, Lee and Seung (Lee and Seung, 1999) derived update rules that can be written as follows:

$$\mathbf{H} \leftarrow \mathbf{H} \circ \frac{\mathbf{W}^T \mathbf{V}}{\mathbf{W}^T \mathbf{J}} \quad (7.4)$$

$$\mathbf{W} \leftarrow \mathbf{W} \circ \frac{\mathbf{V}}{\mathbf{J} \mathbf{H}^T} \quad (7.5)$$

The operator  $\circ$  denotes the Hadamard product (point-by-point multiplication),  $\mathbf{J}$  denotes a unitary matrix, and the division is done point by point.

The classic NMF problem considers errors from all data to be the same. However, it frequently happens that data of a heterogeneous nature, resulting from an acquisition process, have different degrees of confidence. This stems in particular either from the conditions under which the measurements were obtained or from the different nature of the various sensors. For instance, in dynamic PET imaging, the frame durations are usually different. Short frames duration is used at the beginning of the acquisition to capture the fast-changing kinetics accurately (i.e. adequate temporal sampling), while longer frames duration are typically used later in the scan because the activity is not changing as rapidly and also to reduce statistical noise (especially for shorter lived isotopes.). Moreover, it happens that the data are partially missing at certain times, which is often the case for PET dynamic acquisitions. In our data, for instance, we can observe breaks in the TACs due to the subjects being allowed to take a bathroom break during the 120 minutes dynamic scan. Thus, the most reliable information should be considered more carefully and vice versa. This reliability is often encoded in the form of weights, in which a high weight represents a more reliable element. Thus, we can define the extension of Equation (7.2) by introducing a weight matrix  $\mathbf{P}$  of the same size as the data matrix. The update rules can be re-written as:

$$\mathbf{H} \leftarrow \frac{\mathbf{H}}{\mathbf{W}^T \mathbf{P}} \circ \frac{\mathbf{W}^T (\mathbf{V} \circ \mathbf{P})}{\mathbf{W} \mathbf{H}} \quad (7.6)$$

$$\mathbf{W} \leftarrow \frac{\mathbf{W}}{\mathbf{P} \mathbf{H}^T} \circ \frac{(\mathbf{V} \circ \mathbf{P}) \mathbf{H}^T}{\mathbf{W} \mathbf{H}} \quad (7.7)$$

$\mathbf{P}$  was built from the dynamic time frame information. In our case it makes sense to give more weight to later frames as the differences in tracer kinetics between off-target, NFT-specific and non-specific signals are exacerbated.

The overall optimization procedure is done as follows:

1. Initialize inputs  $\mathbf{W}$  and  $\mathbf{H}$  with random or arbitrary (positive) values,
2. Update  $\mathbf{W}$ ,
3. Update  $\mathbf{H}$ ,
4. Repeat steps 2 and 3 iteratively until stopping criterion.

It is important to note that this is not a convex problem in both  $\mathbf{W}$  and  $\mathbf{H}$  and that the solution is not unique. Hence, a good initialization of  $\mathbf{W}$  and  $\mathbf{H}$  is necessary to converge toward a physiologically plausible solution. One can also do multiple updates of  $\mathbf{W}$  and  $\mathbf{H}$  during one iteration to accelerate the convergence.

In addition, an  $l_1$  sparsity constraint is applied on the factor images by multiplying  $\mathbf{W}$  by a binary mask that is set to 1 for all elements of  $\mathbf{W}$  that are greater than a sparsity parameter and zero otherwise. This effectively sets all elements of  $\mathbf{W}$  that are below the sparsity parameter to zero. The  $l_1$  sparsity constraint can be helpful because it encourages the NMF algorithm to find a solution where the weights of the components are sparse, meaning that each component only has a small number of non-zero weights.

We applied this method to a simulation study as well as to real patient data.

## 7.4 Simulation and human studies

### 7.4.1 Simulation study

We generated realistic simulations of dynamic PET images in which we purposely mixed signals mimicking NFT-specific and off-target binding. We evaluated the performance of our method in situations where the ground truth is known to assess our ability to recover the “true” signals.

To build our simulation, we have segmented a clinical PET image using [ $^{18}\text{F}$ ]MK-6240 study of a subject into regions of interest using a corresponding MR image. Then we extracted and added noise on averaged time activity curves of each region that we associated with the voxels in the corresponding phantom region. By multiplying the overlapping masks by the noisy TACs, we obtained a dynamic sequence that we smoothed with a kernel of 4 mm matching a regular PET scanner resolution. The building blocks of the simulation are displayed in Figure 7.6.

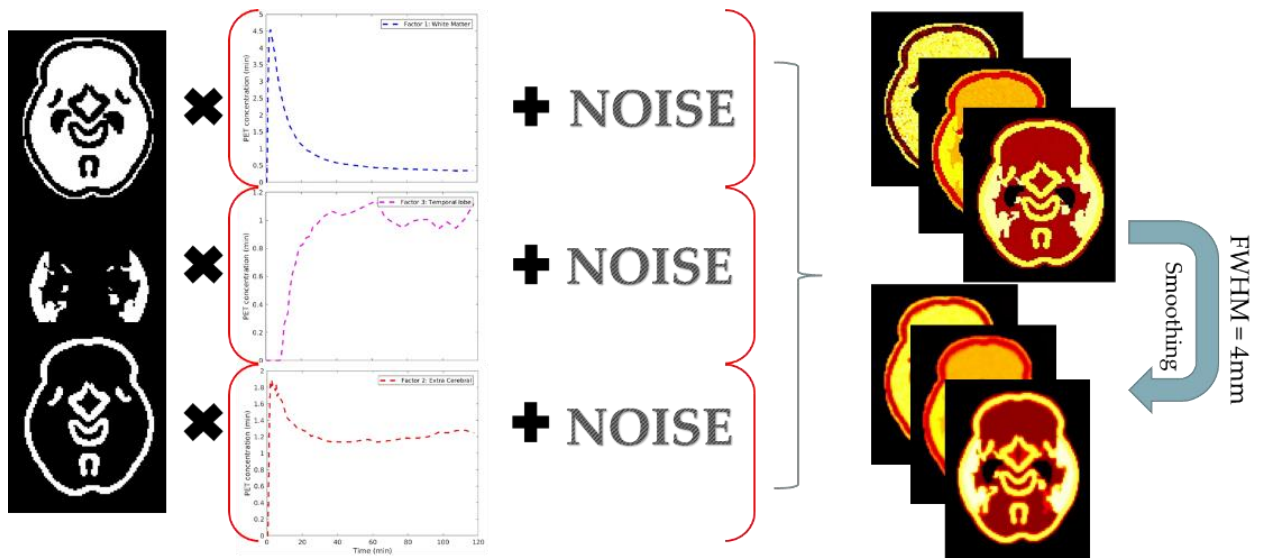


Figure 7.6 Simulation construction: masks from different regions are multiplied with noisy TACs, the result is then added to produce one volume that is then smoothed to correspond to a typical PET scanner resolution.

We applied NMF where the factor curves contained in matrix  $H$  were initialized using heavily noisy version of the original TACs (Figure 7.7).  $W$  the weight images were initialized using nonnegative double SVD (NNDSVD) (Boutsidis and Gallopoulos, 2008). This method is based on two SVD processes, one approximating the data matrix, the other approximating positive sections of the resulting partial SVD factors. We added an infinitesimal value to the factors to avoid the zero-locking property of multiplicative updates rule (which corresponds to having zero values that are never updated).

## Factor images Initialization



## Factor curves Initialization

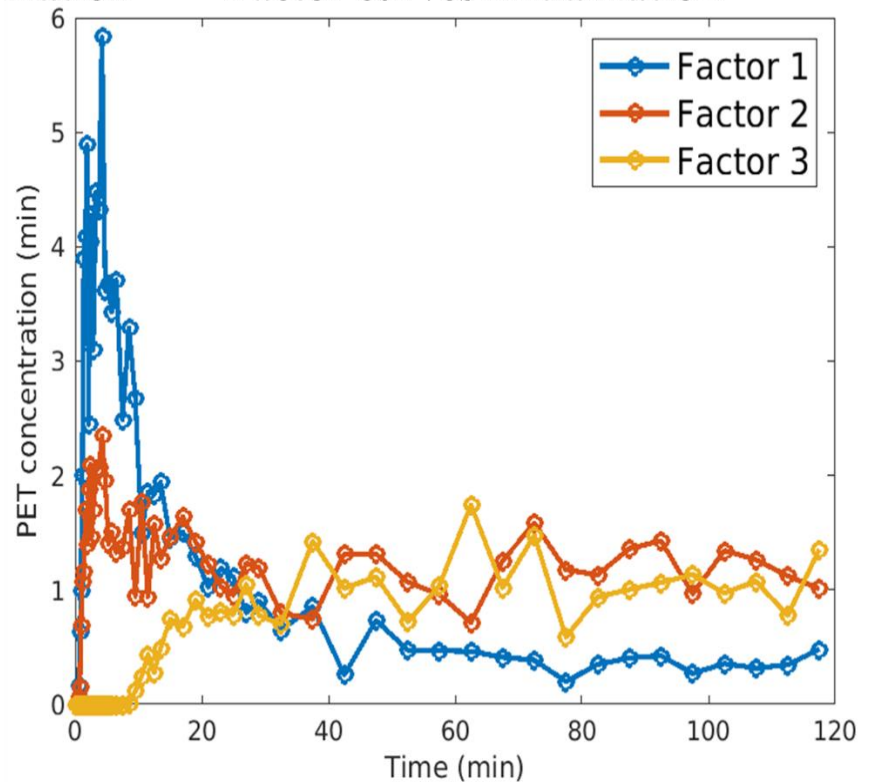


Figure 7.7 Initialization factors for the simulation. The factor images in  $\mathbf{W}$  were initialized using NNDSVD and the factor curves in  $\mathbf{H}$  were initialized using heavily noised version of the original TACs.

### 7.4.2 Human studies

#### $[^{18}\text{F}]\text{MK-6240}$ image acquisition and reconstruction

Cognitively normal (CN) subjects, mild cognitive impairment (MCI) subjects and subjects with Alzheimer's Disease underwent dynamic  $[^{18}\text{F}]\text{MK-6240}$  for at least 120 min. Each subject also had a 3-dimensional structural T1-weighted magnetization-prepared rapid gradient-echo (MPRAGE) for anatomical information. Regional brain time-activity curves were extracted in the native PET space using atlases derived from the Montreal Neurological Institute (MNI) template and also following FreeSurfer parcellation. The data collection was performed on our GE DMI PET/CT scanner. Each subject was imaged using the same protocol. The subject was placed in the camera with the head fixed in the middle of the camera field of view. The dynamic sequences were reconstructed using a validated fully 3D time-of-flight iterative reconstruction algorithm using 5 iterations and 16 subsets. Corrections for attenuation, scatter, random coincidences, normalization and deadtime were applied.  $[^{18}\text{F}]\text{MK-6240}$  was synthesized and PET data were acquired as described previously following bolus injection. Time bins used to frame the emission data were 6x10s, 8x15s, 6x30s, 8x60s, 8x120s, followed by 300s bins.

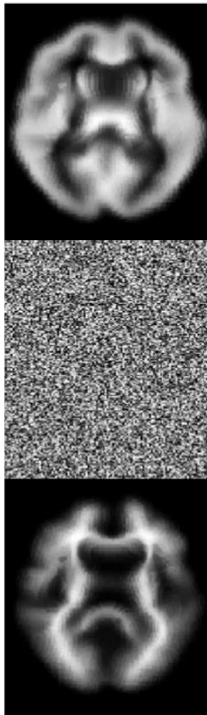
Injected PET tracer activities at the time of injection were  $184.1 \pm 10.3$  MBq (range: 153.2–200.9). The molar activity ( $A_m$ ) of [ $^{18}\text{F}$ ]MK-6240 at the time of injection was  $68.8 \pm 36.3$  GBq/ $\mu\text{mol}$  (range: 9.4–151.9). The total injected mass was  $1173.7 \pm 1119.8$  ng (range: 342.7–5676.0) corresponding to  $4.2 \pm 4.0$  nmol (range: 1.2–20.4).

### **NMF initialization process**

In order to address the non-uniqueness issue of NMF and help the optimization process converge toward a physiologically plausible solution, we use a priori information to initialize the factor curves in  $\mathbf{H}$  and the corresponding factor images in  $\mathbf{W}$ . To this end, the dynamic PET images were registered to the Montreal Neurological Institute (MNI) template space in which probabilistic masks of the gray and white matter are available. Additionally, we created a mask of extra-cerebral structures (skull/meningeal ROI) as described by (Smith et al., 2021) in the MNI template space. These masks were then transported to the native PET space after applying the inverse of transformations learned during the registration process. Time activity curves extracted using the white matter and gray matter probabilistic maps were used to provide an initial guess for non-specific binding and free (unbound) [ $^{18}\text{F}$ ]MK-6240 respectively (see results in 7.6 and discussion in 7.7). The TAC extracted using the extra-cerebral mask was used as an initial guess for the off-target signal. White-matter and grey matter probabilistic maps were also used as an initialization for the factor images. We purposely left a random initialization for the image corresponding to off target binding.



## Factor images Initialization



## Factor curves Initialization

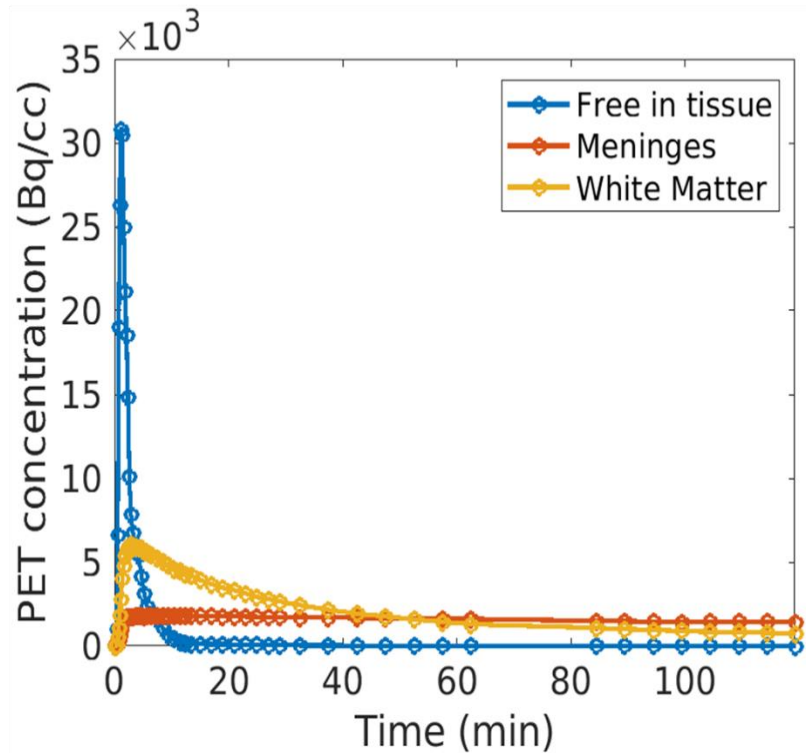


Figure 7.8 Example of initialization factors for a patient data. The factor images in  $\mathbf{W}$  were initialized using probabilistic masks extracted from the registration pipeline. Similarly, the factor curves in  $\mathbf{H}$  were initialized using extracted TACs from the dynamic sequence in specific regions.

## 7.5 Evaluation of image quality

We evaluate the quality of the NMF decomposition on our simulated dynamic PET sequence as we know the ground truth. The estimated weight images  $\mathbf{W}$  were assessed using the Sørensen–Dice coefficient (Dice, 1945; Sørensen, 1948). The estimated TACs in  $\mathbf{H}$  were assessed via two measures, namely the sum of squared differences (SSD) and the comparison of area under the curves (AUC) of real and estimated curves.

Dice coefficient or Sørensen–Dice coefficient is a spatial overlap index or similarity index used to quantify the similarity between two binary sets. The value of a DSC ranges from 0, indicating no spatial overlap between the sets of binary segmentation results, to 1, indicating complete overlap. It was computed as follows:

$$DSC(\mathbf{E}, \mathbf{R}) = \frac{2 |\mathbf{E} \cap \mathbf{R}|}{|\mathbf{E}| + |\mathbf{R}|}$$

where  $\mathbf{E}$  is the estimated factor images segmentation and  $\mathbf{R}$  is the ground truth segmentation.

The sum of squared differences (SSD) captures how dispersed two datasets are, by summing up the squared difference between an observation and the target value. Here, it was computed as:

$$SSD(TACs_{NMF}, TACs_{real}) = \sum_{f=1:Frames} (TACs_{real_f} - TACs_{NMF_f})^2$$

where  $TACs_{real}$  are the ground truth TACs and  $TACs_{NMF}$  are the estimated TACs by NMF.

For the real data, we qualitatively evaluated the factor curves computed from target and reference regions known to be contaminated by off-target signals and verified that the kinetics of the different components was consistent with uncontaminated signal and off-target binding as manually extracted in 7.4.2. Likewise, we evaluated the factor images to verify that the spatial representation of the factor curves corresponding to uncontaminated, and off-target binding signals was anatomically consistent with the known distribution of NFT and off-target binding as previously reported in the literature for [ $^{18}F$ ]MK-6240.

## 7.6 Results

### 7.6.1 Simulation

The factor images in  $\mathbf{W}$  correspond very well with the original masks and we can visually observe a good match between the ground truth factor curves and the estimated factor curves in  $\mathbf{H}$ .

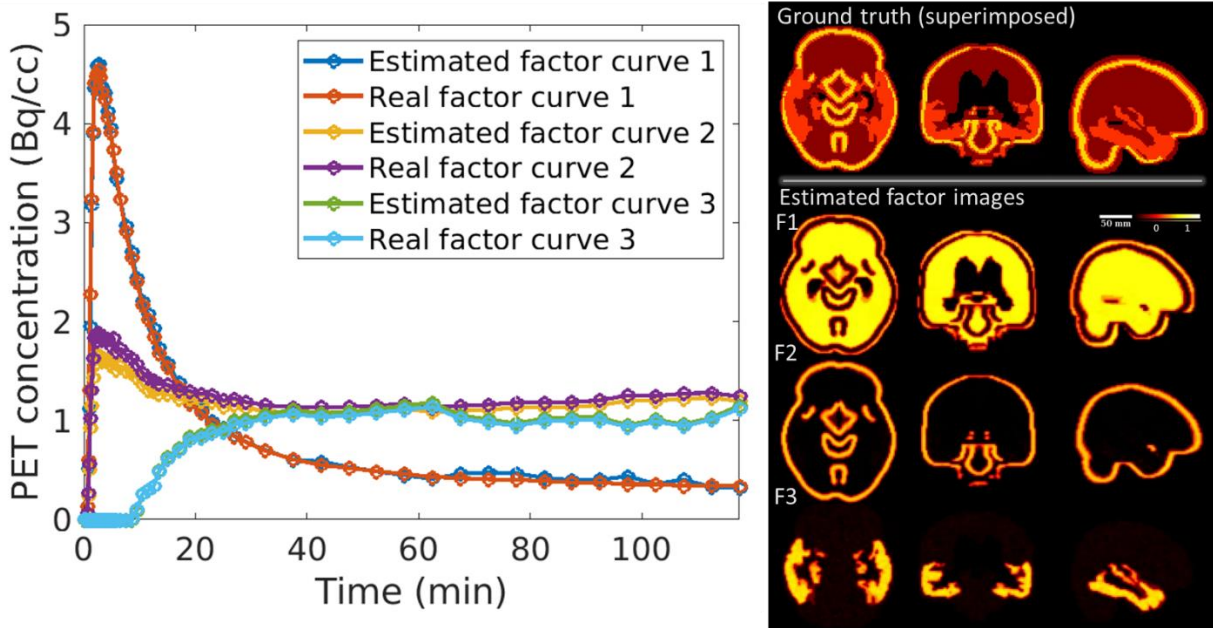


Figure 7.9 Results of the NMF decomposition for our simulation. Estimated factor curves and images visually correspond to the masks and original TACs.

However, recovery is not perfect, and we can observe that the estimated factor 2 undershoots the real curve. This is probably due to some loss of signal which can be attributed to the effect of the smoothing filter in the thin region F2.

Quantitative results (Table 7.1) in terms of area under the curve, sum of squared difference and Dice coefficient confirm our observations where we have very good recovery of each factor curve and factor images.

Table 7.1 Results in terms of area under the curve, sum of squared differences and Dice coefficient for the simulation.

	F1 (Non-Specific)	F2 (Off Target)	F3 (Specific)
<b>AUC (estimated)</b>	<b>93.29</b>	<b>62.58</b>	<b>26.78</b>
<b>AUC (real)</b>	<b>92.83</b>	<b>68.03</b>	<b>26.02</b>
<b>SSD (real, estimated TACs)</b>	<b>0.24</b>	<b>0.8</b>	<b>0.02</b>
<b>Dice (real, factor images)</b>	<b>95%</b>	<b>98%</b>	<b>92%</b>

## 7.6.2 Human studies

In this section, we present the results on two control patients exhibiting high and moderate off-target binding (as observed on the 90-120 standardized uptake value ratio (SUVR) images). We also present the results on one AD patient.

NMF produced meaningful TAC-like factors and the coefficient distributions.

### Control patient

#### High-off target binding

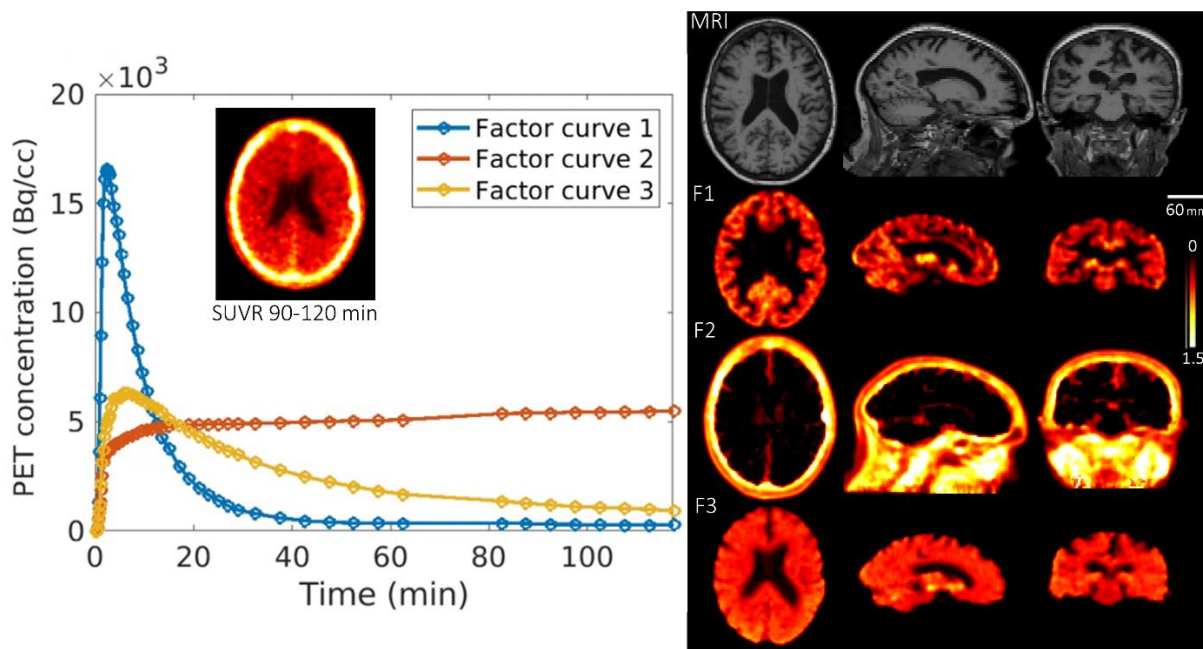


Figure 7.10 Unmixing results for a control patient presenting a high amount of off-target binding.

In this first human studies exhibiting high off-target binding (with mean SUVR in the meninges of 1.6), at the whole brain level, NMF was able to separate the [ $^{18}\text{F}$ ]MK-6240 dynamic PET measurements into three components (Figure 7.10, F1, F2, and F3 for the factor images and Factor curve 1 (FC1), Factor curve 2 (FC2), Factor curve 3 (FC3)). The first component (FC1), with a high peak and fast washout was identified as free concentration of [ $^{18}\text{F}$ ]MK-6240 in the brain tissue with the corresponding factor images (F1) resembling a map of cerebral perfusion. The second component (FC2), with a steady, specific-like dynamic, appeared to capture the off-target signal arising from the extra-cerebral areas visible in F2 and the third component (FC3) shows kinetics consistent with non-specific binding more relatively homogeneous across the brain as observed in the corresponding factor images F3.

### Moderate off-target binding

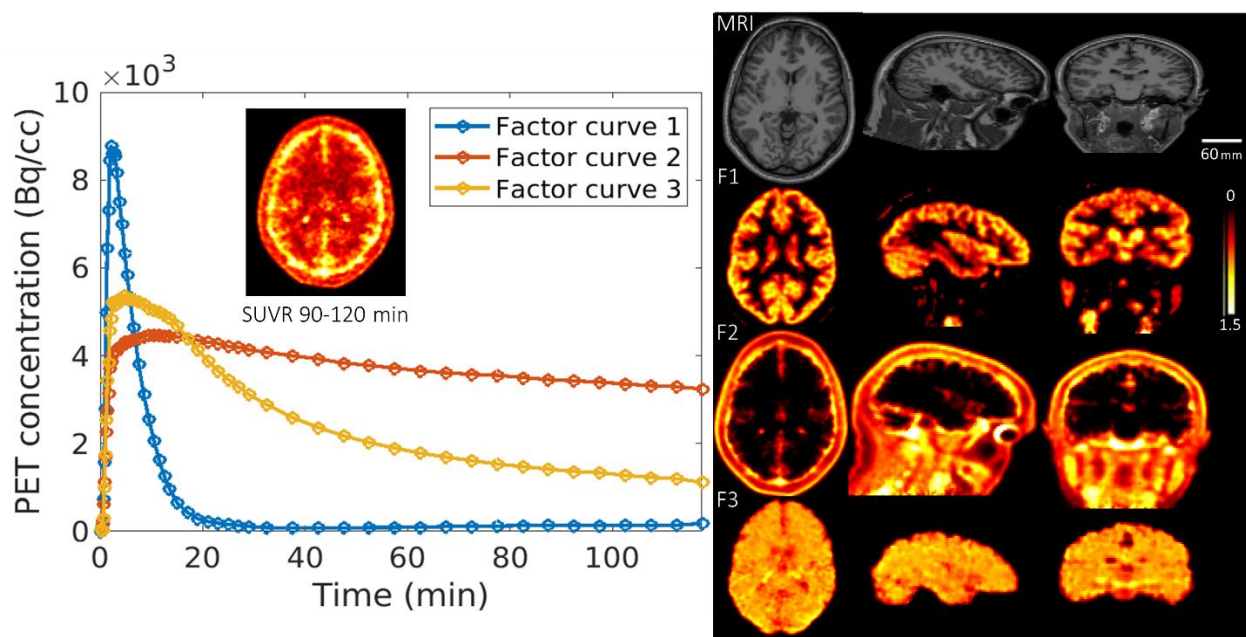


Figure 7.11 Unmixing results for a control patient presenting moderate amount of off-target binding.

NMF was still able to separate the PET signal into three components for a healthy control patient with lower off-target binding (Figure 7.11) (with mean SUVR in the meninges of 1.07). However, the second component (F2) capturing off-target binding has lower intensity, which was expected as this patient display lower off-target uptake.

Overall, this method was applied on eight healthy control patients from the cohort of 25 cognitive normals and the results showed that NMF could separate the tau tracer PET signal into three components: free tracer in brain tissue, non-specific and off-target.

### AD patient

We also applied the method to AD patients. In some the patients which results for one of them are presented in Figure 7.12, it was interesting to observe that the separation is not as good as what we saw in control patients but is nonetheless very encouraging.

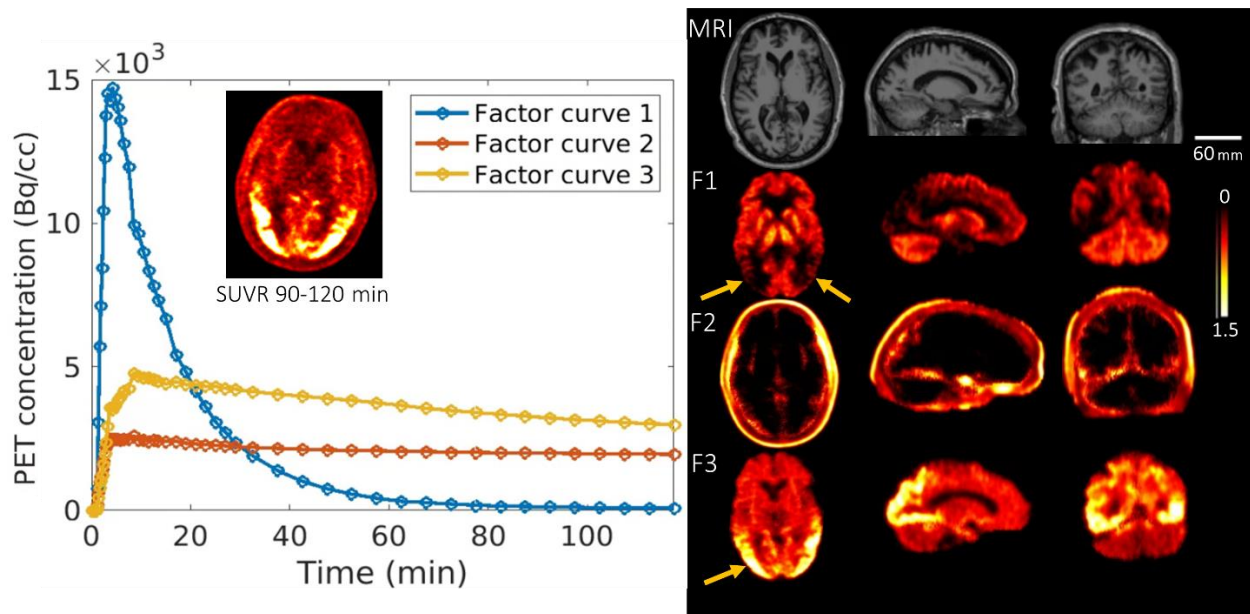


Figure 7.12 Unmixing results of an AD positive patient presenting some amount of off-target and specific binding.

The first factor image F1 still seems to reflect perfusion and even shows hypoperfusion in the temporal and parietal cortex, which has been reported in AD (Huang et al., 2018). This will obviously require further validation (for instance by comparing these maps to parametric maps obtained from standard kinetic modeling techniques.)

The second factor curve and factor image F2 seemed to extract the off-target signal even though the separation is not as clean as for the control patients.

Lastly, the third factor image F3 appears to effectively capture both the specific signal, as demonstrated by its correlation with areas of decreased perfusion seen in factor image F1, and the non-specific component of the signal which is homogeneously distributed across the brain. In other words, it appears to encompass both the specific and non-specific bindings.

### 7.6.3 Sanity check

In order to verify that the method does not excessively constrain the problem, we have applied it to patients who underwent both tau study using [<sup>18</sup>F]MK-6240 as well as a plaques study using <sup>11</sup>C-Pittsburgh Compound B or [<sup>11</sup>C]-PiB in which specific binding reflects the presence of  $\beta$ -amyloid. As [<sup>11</sup>C]-PiB does not usually present off target binding in the meninges, we verified that the method did force the NMF decomposition to produce signal in that region.

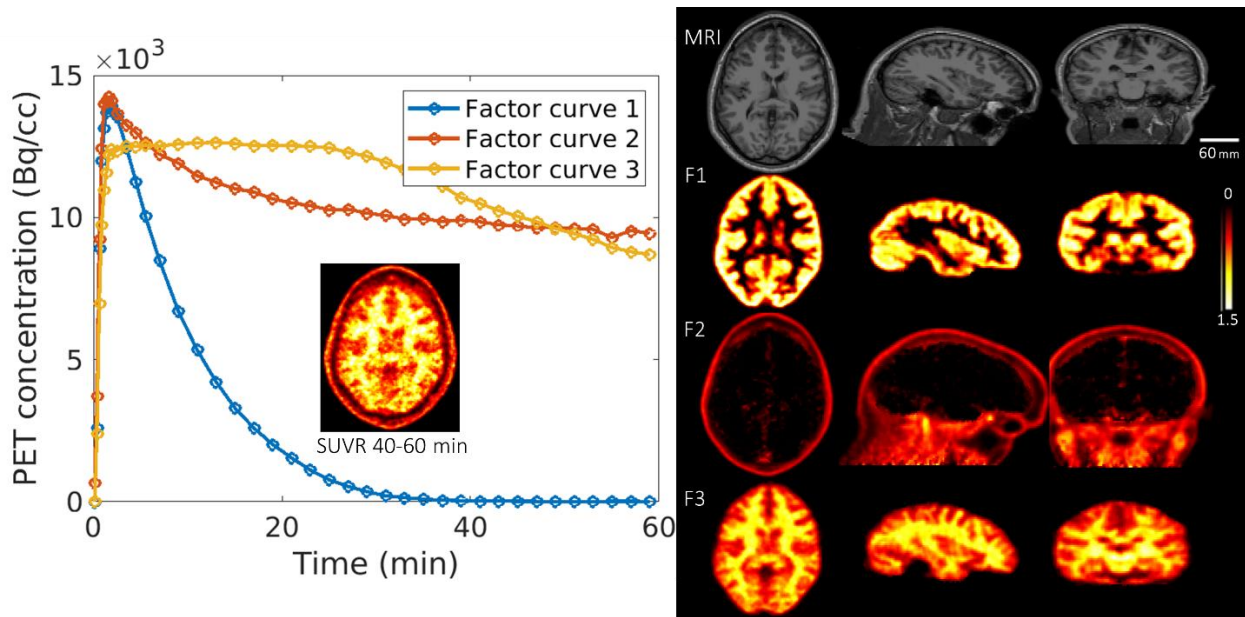


Figure 7.13 Unmixing results for the same control patient as in Figure 7.11, but scanned using  $[^{11}\text{C}]\text{-PiB}$  tracer. Factor image 2 does not present off-target binding in the meninges.

We applied NMF to the same patient that underwent a  $[^{18}\text{F}]\text{MK-6240}$  in Figure 7.11, using the same initialization extraction process. We can observe the results in Figure 7.13 that the Factor image F2 does not produce significant signal in the meninges, but also that the other factor images produce physiological meaningful results regarding  $[^{11}\text{C}]\text{-PiB}$  tracer bindings. That signifies the that our method is not forcing the optimization problem toward an overly constrained solution.

## 7.7 Discussion and Conclusion

To the best of our knowledge, this chapter presents the first systematic applications of NMF-based image analysis to  $[^{18}\text{F}]\text{MK-6240}$  tau dynamic brain PET. The NMF technique provides a tool for evaluating the amount of the unwanted off-target binding tissue in the brain to disentangle its contribution to other signals and that, without any participation of a human operator. The results of this study demonstrate the potential of using non-negative matrix factorization (NMF) to separate off-target, free concentration of  $[^{18}\text{F}]\text{MK-6240}$  and non-specific. In both simulations and clinical data, NMF was able to accurately disentangle the contributions from tau-specific, non-specific, and off-target components. The factor images generated by NMF could accurately be distinguished between the three tissue types.

However, the approach proposed in this study assumes that the combination of the factors is linear. While this might be a sufficiently adequate description in some cases, it may not be the best representation of the tracer dynamics in other cases.

Moreover, the NMF approach is limited to the number of components (three in this case) assumed. Disentangling the signal into more components without making further assumptions or introducing additional constraints is impossible.

Future work will focus on exploring ways to improve the separability of the PET signal using anatomical and temporal constraints to reliably separate [ $^{18}\text{F}$ ]MK-6240 dynamic signal into a greater number of components.

An alternative method to consider is to divide the brain into regions and analyze them separately, as this approach may lead to a more precise understanding of the tracer dynamics in different areas.

Additionally, it is important to remember that in clinical settings, the imaging sessions are usually limited to 90-120 minutes, which may limit the amount of data available for analysis using NMF. Therefore, testing the method using shorter imaging sequences to evaluate its performance may be beneficial.

The decomposition can also be affected by extrinsic effects such as the motion correction robustness of the dynamic PET data. Inter-image registration errors affect NMF decomposition of the dynamic PET data leading to inaccurate factor curves and factor images. This can be addressed by improving motion correction techniques, which can be difficult in practice. We are working on an ultra-fast inter-frame motion correction technique to improve the quality of the dynamic PET data and improve the robustness and accuracy of the NMF decomposition. The first results are promising and will be reported in future studies.

The decomposition can also be affected by extrinsic effects such as the motion correction robustness of the dynamic PET data. Inter-image registration errors affect NMF decomposition of the dynamic PET data leading to inaccurate factor curves and factor images. This can be addressed by improving motion correction techniques, which can be difficult in practice. We are working on an ultra-fast inter-frame motion correction technique to improve the quality of the dynamic PET data and improve the robustness and accuracy of the NMF decomposition. The first results are promising and will be reported in future studies.

Additionally, in Section 7.6.2, we applied MNF on an AD patient where we tried to separate off-target from specific binding. While the results were encouraging, the specific signal and non-specific were still mixed in together, and the off-target seemed not as well separated. More assumptions and constraints would be needed to separate specific binding and non-specific.



However, it is not the primary goal of the study, which ultimate goal is to remove off-target in the earliest stages of the disease. It is important to note that off-target binding is more prevalent in low tau-binders than AD patients and has a greater impact on quantifying early tau deposits as the signal is weaker. AD patients generally have a high tau burden (see Figure 7.2), which makes factor analysis irrelevant. Hence, the target population is individuals in the early stages of the disease.

Finally, the findings obtained from the study should be validated using larger clinical data that encompasses a variety of off-target binding sets to generalize the results and further evaluate the potential of NMF in separating tau-specific and off-target signals in [ $^{18}\text{F}$ ]MK-6240 PET imaging.

# Chapter 8

## Conclusions and Perspectives

In order to reach our goals, three main contributions, presented in Chapters 4, 5, 6, and 8, have been undertaken. Their outcome, limits, and potential perspectives are discussed in this chapter.

### 8.1 Conclusion

#### 8.1.1 Real-time motion correction

One of the scientific contributions of this work is developing and implementing techniques for real-time motion correction in brain PET imaging. In Chapter 3, we presented a motion correction method that integrates an optical tracking device to overcome motion artifacts. This method allowed for real-time monitoring of the subject's head position during the scan, and we incorporated that information into the image reconstruction process. To this end, we built a custom communication interface between the scanner and the optical tracking device. Since every PET scanner can have different inputs and protocols for communication, we opted for two different approaches. A hardware approach for the SAVANT scanner that we are currently building and for the LabPET-II scanner that we are using as a surrogate for the SAVANT, as well as a software approach for the existing GE DMI PET/CT scanner. The alignment of the optical tracking device and the PET coordinates grids leads to excellent motion recovery in the GE DMI experiments. However, in the LabPET-II experiments, blurring caused by the manual alignment of the coordinate grids affected the resolution of the phantom images. Hence, we anticipate that one of the main difficulties we will face when the SAVANT scanner is built is the accurate spatial alignment of the coordinate system of the scanner and the optical tracker. Any slight shift in the order of its exceptionally small crystal size (~1.2 mm axially and transaxial) will cause blurring artifacts. For the GE scanner, we manage to use its high-resolution CT, which shares the same image space as the PET. However, the SAVANT is a standalone PET system; hence, another spatial calibration strategy must be considered. Late discussions mentioned using physically known positions of bolts on the scanner's bore to

manually place reference markers, which relative positioning to the scanner's origin could be accurately known thanks to the bolts.

### **8.1.2 Super-resolution**

The main contribution of this work is the use of super-resolution techniques in brain PET imaging in Chapter 4 and Chapter 5. We saw that two key factors limit the spatial resolution of brain PET images: one relates to the intrinsic characteristics of the PET scanner, such as the size of its detectors, and the other to unwanted movements of the subject, which are in practice impossible to avoid during the time needed to acquire the PET data. Our research showed that it was possible to harness that usually undesired head motion to enhance the spatial resolution using SR.

We started by studying SR in a PET/MR setup where the idea was to scan an object at different positions in the field of view. The different positions were accurately determined using the simultaneous MR acquisitions done at each PET scan position. We integrated the motion information in an MLEM reconstruction scheme and were able to retrieve details that were not visible in the standard static acquisition. While interesting, the main limitation is that those results are clinically not convenient for brain imaging, especially for scanning awake animals or human subjects. In fact, a patient would have to stay still in multiple positions for an extended period, which can be, in many cases, impracticable. What we wanted to answer was hence: is it possible to allow patients to move freely during the acquisition and take advantage of the head movement to achieve SR using a PET/CT scanner? That was the subject of the principal contribution of this Ph.D. work, where we used our motion correction technique from Chapter 3, which relied on an optical tracking device. One of the main challenges was the generation of the sensitivity image that takes into account the motion. In fact, in a list-mode framework, it is not viable to generate a sensitivity matrix from every possible line of response in every recorded position as it would require doing one back-projection per motion step (this was possible for the PET/MR SR study because we dealt with 5 to ten positions). Our approach consisted of doing one back-projection and moving the image according to the motion. This approach is tricky, especially when we deal with a small voxel size. Depending on the projector used, artifacts appear and are propagated when the image is moved according to the motion information. Moreover, the reconstruction is very sensitive to mismatches between the list-mode data and the sensitivity image. To overcome that, we used a multi-ray Siddon approach where we used a relatively extensive number of rays per event, which made the reconstruction almost impracticable in terms of processing time (a few days/weeks, depending on the activity

and duration of a scan). PSF modeling, which helps smooth out some of the high-frequency artifacts present in the sensitivity image, helped, but the processing time is still in the order of a dozen hours.

We had to think of an accurate spatial calibration method to enable SR. As explained in the previous paragraph, accurate spatial calibration is fundamental for motion correction. This is even more true when we want to achieve SR. In fact, the spatial calibration was a limiting factor for SR, so we needed to ensure that it was as accurate as possible. We used paired position measurements of individual markers in both the scanner and Polaris tracker coordinate spaces. We used CT images for spatial calibration, which offers more accurate results than PET-based methods that use markers attached to a radioactive point source. However, our method relied on manually spotting the center of the marker in the CT images, which is probably not the most accurate way.

One of the main criticisms to be drawn from that contribution is the fact that the movements performed on the phantoms during the experiments were mainly back and forth (translation and rotation), resulting in a dominant motion direction for each SR acquisition. The applied movements may not have been optimal for oversampling, and the non-uniform movement could lead to non-uniform resolution recovery. For example, if an object only rotates around one axis, points on that axis will not move and, therefore, will not benefit from oversampling. Alternative motion patterns and amplitudes, such as wobbling, are under examination for potential improvement of SR. Finally, while preclinical tests on phantoms and on a non-human primate have been successful, we have not tried our method on humans. We expect good results; however, we must find a proper and robust way to attach the tracked marker to a patient's head.

### **8.1.3 Factor analysis using non-negative matrix factorization**

In another key contribution of this work in Chapter 7, we have explored a technique called non-negative matrix factorization, where we try to answer if it was possible to disentangle specific, non-specific, and off-target signals of [<sup>18</sup>F]MK-6240 in Tau dynamic sequences, which can help in the early diagnosis of AD. This method can be used to separate the signal of a specific tracer from other non-specific signals in the image, allowing for more accurate quantification of the tracer uptake in the brain. This research aimed to improve the diagnostic capabilities of brain PET imaging by providing more accurate quantification of tracer uptake in the brain, which can lead to more accurate diagnosis and monitoring of disease progression. However, the NMF approach has some limitations and challenges that should be considered. Firstly, the

approach assumes a linear combination of factors, which may not always be the best representation of the tracer dynamics. Some authors showed that it is possible to consider the non-linear aspect of the dynamic combination of bindings in a voxel (Cavalcanti et al., 2020). Secondly, the method is limited to the number of components assumed, and it is not possible to disentangle the signal into more components without making further assumptions or introducing additional constraints. We noticed that when we used more than three components, without additional constraints, NMF was mainly reconstructing noise starting from the fourth component. Additionally, the imaging sessions are usually limited to 90-120 minutes in clinical settings. In our study, we had access to data from 0-120 min, which is not common in practice. With less temporal information, the expected results may not be as robust as the ones we obtained. Another challenge is that extrinsic effects can affect the decomposition, such as the motion correction robustness of the dynamic PET data. Inter-image registration errors can result in inaccurate factor curves and factor images, which can be addressed by improving motion correction techniques. Further validation is also needed in more significant clinical data with different levels of off-target binding to generalize the findings and explore the potential of NMF for separating tau-specific and off-target signals in [ $^{18}\text{F}$ ]MK-6240 PET imaging. Despite these limitations and challenges, the NMF-based decomposition of [ $^{18}\text{F}$ ]MK-6240 tau tracer PET signals offers a promising tool for separating specific binding from non-specific and off-target binding.

## **8.2 Perspectives**

Looking at these limits and challenges, we aim to further improve image quality and reduce quantitative artifacts and bias when evaluating the radiotracer uptake in small anatomical regions by exploiting other algorithmic methods, such as penalized reconstructions, as well as available physical information from the GE PET/CT scanner, namely the time-of-flight information. We will also explore other spatial calibration techniques and movements to be applied to scanned objects in the context of super-resolution. In the context of factor analysis, we will explore nonlinear models as well as the use of a more robust motion correction technique.

### **8.2.1 Penalized reconstruction**

It is possible to get PET images by guiding the reconstruction using prior information. We want to regularize a reconstruction because of the unusually small reconstruction voxel size grid that is specific to SR. Moreover, one drawback of the OSEM algorithm is that it generally cannot be run to full convergence because the noise in the image grows with each iteration. To

compensate for this, the algorithm is generally stopped after a determined number of iterations, resulting in an under-converged image. To address the effects of convergence and provide more accuracy in PET quantitation, a regularized reconstruction iterative algorithm will be studied, incorporating prior knowledge about the image quality into the reconstruction. This prior knowledge can be incorporated as segmented anatomical information or as a term in the algorithm discouraging differences in neighboring image voxel values. By incorporating those factors into the reconstruction algorithm, the algorithm can be run to full convergence, provide more accurate quantitation levels, and improve SNR over OSEM. In Chapter 6, we studied a technique called the kernel method that allows the incorporation of such prior information; however, more investigation is required to validate the method, and a comparison is needed with more standard methods, such as the maximum a posteriori method.

### 8.2.2 A better calibration between the camera and scanner coordinate spaces

As previously explained, we calibrated our system (Polaris tracker and GE PET/CT scanner) using pair measurements in both respective spaces. Using the CT as the scanner's image space is believed to produce outstanding results compared to methods that use directly attached markers to a radioactive source to get measurements into the PET image space (no super-resolution is possible since the movement would be tracked at the scanner's resolution). However, it is not always easy to determine the position of the center of a marker using CT. Thus, to avoid the difficulty of accurately finding the center of a marker, the relative position calibration method was suggested. Instead of comparing the absolute positions of the object in PET and tracker coordinates, we can compare the relative motion between two static positions in both spaces. Relative motion in the two systems is independent of any offset between the object's position in the CT and tracker coordinates. Given two positions,  $\mathbf{P}_m$  and  $\mathbf{P}_n$ , as  $4 \times 4$  transformation matrices, the relative motion between them is:

$$\Delta \mathbf{P}_{mn} = \mathbf{P}_n \mathbf{P}_m^{-1} \quad (8.1)$$

Then the relation between the PET and tracker coordinates, via a calibration matrix  $\mathbf{M}_c$ , is:

$$\Delta \mathbf{P}_{mn}^{PET} = \mathbf{M}_c \Delta \mathbf{P}_{mn}^{POLARIS} \mathbf{M}_c^{-1} \quad (8.2)$$

Several static positions of a phantom with markers attached can be recorded in the CT simultaneously with the Polaris. The reconstructions of the phantom can be registered to each other to determine  $\Delta \mathbf{P}_{mn}^{PET}$ , and these can be compared to the corresponding  $\Delta \mathbf{P}_{mn}^{POLARIS}$  for the

tracker's measurements using a least squares optimization algorithm to determine an estimate of the calibration matrix  $M_c$ .

This method offers several advantages over the previous approach. First, it eliminates the need for precise measurements of the marker sphere's center in the CT space. Additionally, it enables more precise determination of relative position matrices for CT data, as it allows measurement of a complex phantom instead of just the absolute position of points.

### **8.2.3 Nature of movement applied to the scanned object**

The movements applied to the phantoms or NHP were mostly back and forth during our experiments. Hence, there we had a predominant motion direction for each SR acquisition is possible that this is not the optimal way of getting oversampling. Moreover, no real attention was given as to how this would be applied in clinical practice. For instance, we need to investigate if a patient's involuntary motion would be sufficient rather than introducing some mechanical motion. A simulation will be made to determine what motion magnitude and pattern of motion are necessary to achieve benefits in resolution. This work has started as part of our super-resolution paper revisions. Similarly, we will study how sufficient motion would be guaranteed in clinical practice.

### **8.2.4 Human studies**

While we only tested this super-resolution technique in preclinical studies, we are currently working on extending it to human subjects. The difficulty will be finding a way to rigidly attach markers to a patient's head. It is essential that no relative movement between the markers and the head occurs, as a relative movement of more than 0.7 mm (corresponding to the calibration using the CT that limits our resolution to 0.7 mm) would decrease the registration accuracy and, thus, the SR results. The attachment device must be comfortable for long scans and not interfere with CT and PET attenuation.

A protocol has been written to apply our method to humans, and a prototype of a marker fixation device has been built. It consists of a pair of swimming goggles where a rod is mounted, bringing markers on top of the head. We designed and printed a 3D model.

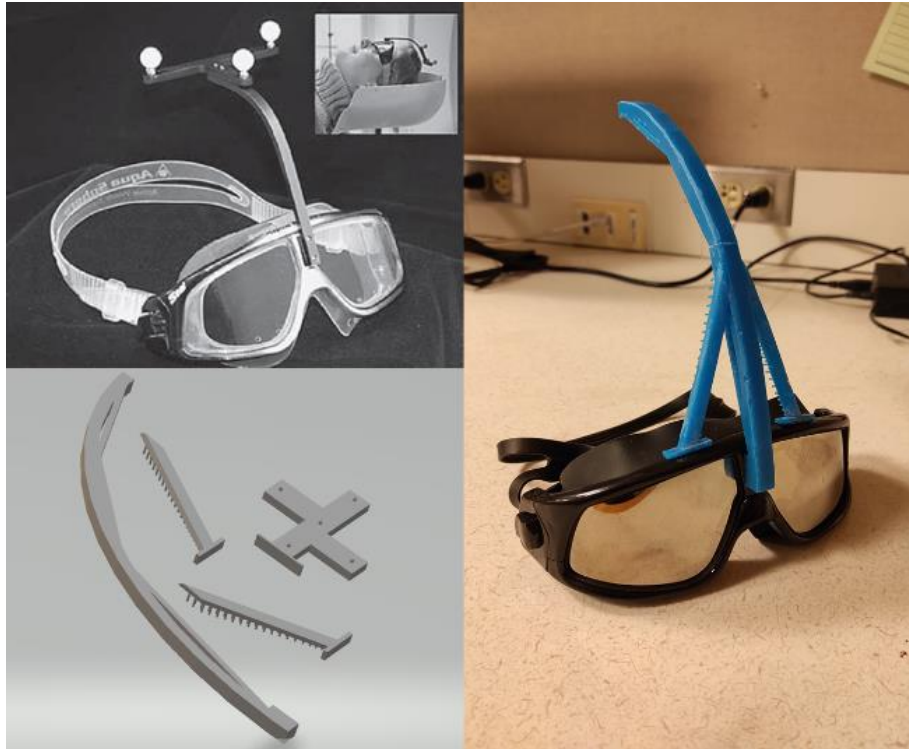


*Figure 8.1 Prototype of head marker fixation using swimming goggles. The top left panel is adapted from (Tellmann et al., 2006).*

The goggles attached to the head are relatively comfortable and hold well, thanks to the suction cup effect. However, facial muscles can introduce unwanted relative movement between the head and the goggles. A helmet or swimming cap will be considered if this issue occurs.

Another question to answer is how we are going to deal with a patient's head movement. We think that the camera will measure naturally occurring head movements, which always occur in the range of a few hundred microns. Another option is to impose a movement using a motorized neck pillow massage device. These types of devices can make the head move continuously in random directions, mostly in the plane. In addition, we can move the bed in the axial direction.

### **8.2.5 Perspectives on [ $^{18}\text{F}$ ]MK-6240 NMF unmixing**

To improve the accuracy of NMF decomposition in dynamic PET imaging, we need to better model the variability in tracer distribution between different tissues, especially in areas affected by specific binding. The current assumption of constant kinetic patterns may be appropriate for homogenous tissues like the perfusion compartment and non-specific binding tissues but not for the specific or off-target binding class. To address this issue, we plan to use nonlinear NMF (Chen et al., 2015) or other factor analysis techniques based on parametric nonlinear mixing



models (Cavalcanti et al., 2020), allowing for spatial variation in the TAC corresponding to specific binding. Additionally, we will divide the brain into regions and analyze each separately to gain a more physiologically relevant understanding of tracer dynamics.

Accurate motion correction is fundamental to get an accurate NMF estimation. We recently submitted an article on the impact of motion correction on [ $^{18}\text{F}$ ]MK-6240 tau PET imaging using ultra-fast interframe list mode motion correction for PET imaging (from the abstract (Tiss et al., 2022)). Individually, 26% of the scans exhibited notable motion quantified by the proposed motion metric, affecting 39% of the longitudinal datasets with two time points and 37% of all our [ $^{18}\text{F}$ ]MK-6240 subjects. The list-mode-based ultra-fast motion correction decreased the blurring in images from scans with notable motion and improved the accuracy in quantitative measures. This method has been applied to static data, and we will be applying it directly to our dynamic sequences, allowing for a robust inter-frame registration.

Finally, in coming [ $^{18}\text{F}$ ]MK-6240 dynamic studies, we also will attempt to integrate some of our contributions, such as our real-time motion correction technique, which has the advantage of achieving an intra-frame correction (meaning at a better resolution than a voxel size) or even SR. With SR, we hope to pre-correct the partial volume effect, giving a serious head start for NMF.

# Publications

## Journal papers:

Published articles:

Chemli, Y., Tétrault, M-A., Marin, T., Normandin, M. D., Bloch, I., El Fakhri, G., Ouyang, J., & Petibon, Y. (2023). Super-resolution in brain positron emission tomography using a real-time motion capture system. *NeuroImage*, 272, 120056..

Marin, T., Djebra, Y., Han, P. K., Chemli, Y., Bloch, I., El Fakhri, G., Ouyang, J., Petibon, Y., & Ma, C. (2020). Motion correction for PET data using subspace-based real-time MR imaging in simultaneous PET/MR. *Physics in Medicine & Biology*.

Petibon, Y., Fahey, F., Cao, X., Levin, Z., Falone, A., Zukotynski, K., Kwatra, N., Lim, R., Chemli, Y., Treves, S., El Fakhri, G., Ouyang, J., Hospital, M. G., Children, B., & Tikva, P. (2021). Detecting lumbar lesions in 99m Tc-MDP SPECT by deep learning: comparison with human observers. *Med Phys*. 2021 Aug;48(8):4249-4261.

Tiss, A., Marin, T., Chemli, Y., Gong, K., Lois, C., Petibon, Y., Landes, V., Grogg, K., Normandin, M., Spangler-Bickell, M., Becker, A., Thibault, E., Johnson, K. El Fakhri, G., Ouyang, J. (2023). Impact of motion correction on [18F]-MK6240 tau PET imaging. In *Physics in Medicine & Biology*.

Submitted Articles:

Tétrault, M.-A.\*, Chemli, Y.\*, Toussaint, M., Petibon, Y., Ouyang, J., Normandin, M., Thibaudeau, C., Najmaoui, Y., Lecomte, R., Fontaine, R., El Fakhri, G. (2023). Integration of a Network Motion Capture Camera into Positron Emission Tomography Data Acquisition Systems. In *IEEE Transactions on Nuclear Science*.

\*co-first authors

Anticipated submission:

Chemli, Y., Petibon, Y., Ouyang, J., Normandin, T., Bloch, I., El Fakhri, Guehl, N. (2023). Factor analysis for [18F]MK-6240 dynamic sequences using non-negative matrix factorization.

## Abstracts/Conferences:

Chemli, Y., Han, P., Ma, C., Fakhri, G. El, Ouyang, J., & Petibon, Y. (2019). Super-resolution 3-D PET reconstruction for simultaneous PET/MR. *Journal of Nuclear Medicine*, 60(supplement 1), 1367–1367.

Chemli, Y., Tétrault, M., Marin, T., Toussaint, M., Bloch, I., Fakhri, G. El, Normandin, M. D., Ouyang, J., & Petibon, Y. (2020). Motion Correction for brain PET using a Real Time Motion Capture System. 4–5. 2020 IEEE NSS MIC

- Tétrault, M., Chemli, Y., Toussaint, M., & Petitbon, Y. (2020). Integration of a Network Synchronized Motion Tracking Camera into a Real-Time Positron Emission Tomography Data Acquisition System. 2020 IEEE NPSS Real Time Conference.
- Chemli, Y., Tétrault, M., Normandin, M. D., Marin, T., Bloch, I., & Fakhri, G. El. (2021). Super-resolution in brain PET Using a Real Time Motion Capture System. *Journal of Nuclear Medicine*, 25(2), 1–2.
- Chemli, Y., Petitbon, Y., Normandin, Ouyang, J., Johnson K., Normandin, M., El Fakhri, G. & Guehl, N (2022). Disentangling tau-specific and off-target signals in [18F] MK-6240 PET using nonnegative matrix factorization. *Journal of Nuclear Medicine*, *Journal of Nuclear Medicine* June 2022, 63 (supplement 2) 2429.
- R. Lecomte, M. Normandin, C. Thibaudeau, L. Arpin, J.-D. Leroux, P.-Y. Lauzier-Trépanier, J. Bouchard, A. Samson, R. Espagnet, J.-F. Beaudoin, H. Bouziri, L.-M. Collin, É. Gaudin, M. Gaudreault, M.-A. Hachey, C. Pepin, M. Toussaint, Y. Chemli, T. Marin, Y. Petibon, J. Ouyang, Y. Najmaoui, M.-A. Tétrault, R. Fontaine, G. El Fakhri. Scanner Approaching in Vivo Autoradiographic Neuro Tomography (SAVANT): Progress Towards  $\mu$ L Resolution for Imaging the Human Brain, *Journal of Nuclear Medicine* June 2022, 63 (supplement 2) 2436.
- A. Tiss, T. Marin, K. Gong, C. Lois, Y Chemli, Y. Petibon, V. Landes, K. Grogg, M. Normandin, M. Spangler-Bickell, J. A. Becker, E. Thibault, K. Johnson, G. El Fakhri and J. Ouyang. Impact of motion correction on longitudinal [18F]-MK6240 tau PET imaging, *Journal of Nuclear Medicine* June 2022, 63 (supplement 2) 3277.
- Lecomte, R., Thibaudeau, C., Auger, É., Arpin, L., Leroux, J.-D., Beaudoin, J.-F., Croteau, É., Lavallée, É., Lauzier Trépanier, P.-Y., Gaudreault, M., Bouchard, J., Espagnet, R., Samson, A., Collin, L.-M., Hachey, M.-A., Dussault-Frenette, O., Dufour-Forget, D., Koua, K., Lemay, J., Viscogliosi, N., Bouziri, H., Pepin, C. M., Toussaint, M., Labrecque, V., Grève, M., Paulin, C., Chemli, Y., Marin, T., Normandin, M., Ouyang, J., Petibon, Y., Michaud, J.-B., Tétrault, M.-A., El Fakhri, G., & Fontaine, R. (2022). Initial Performance Characterization of the UHR Brain PET Scanner.
- Y. Zhuo, T. Marin, M. Orehar, R. Dolenc, Y. Chemli, J. Alamo, J. Barberá, J.M. Benlloch, G. Borghi, J. M. Fernández-Tenllado, D. Gascón, S. Gómez, A. Gola, K. Grogg, D. Guberman, S. Korpar, P. Križan, S. Majewski, R. Manera, A. Mariscal-Castilla, J. Mauricio, S. Merzi, C. Morera, G. Pavón, M. Penna, G. Razdevšek, H. Sabet, A. Seljak, A. Studen, R. Pestotnik, G. El Fakhri. Ultra-high spatial and time of flight resolution brain PET reconstruction, *Journal of Nuclear Medicine* June 2023

# Appendix

In Chapter 5 we have presented an extensive set of experimental studies to demonstrate the efficacy of the proposed super resolution technique. However, a key question about the desired motion pattern and amplitude that would lead to an optimized enhancement in spatial resolution remained unanswered.

To answer this question, we conducted a comprehensive set of simulations to determine the motion magnitude and pattern required to achieve super-resolution. For that, we generated a rasterized, high-resolution (0.1mm pixel size) 2D phantom image consisting of a circular background and nine hot spots of 2.4mm in size, which centers are spaced with 3 mm in an arbitrary pattern (Figure A.1).

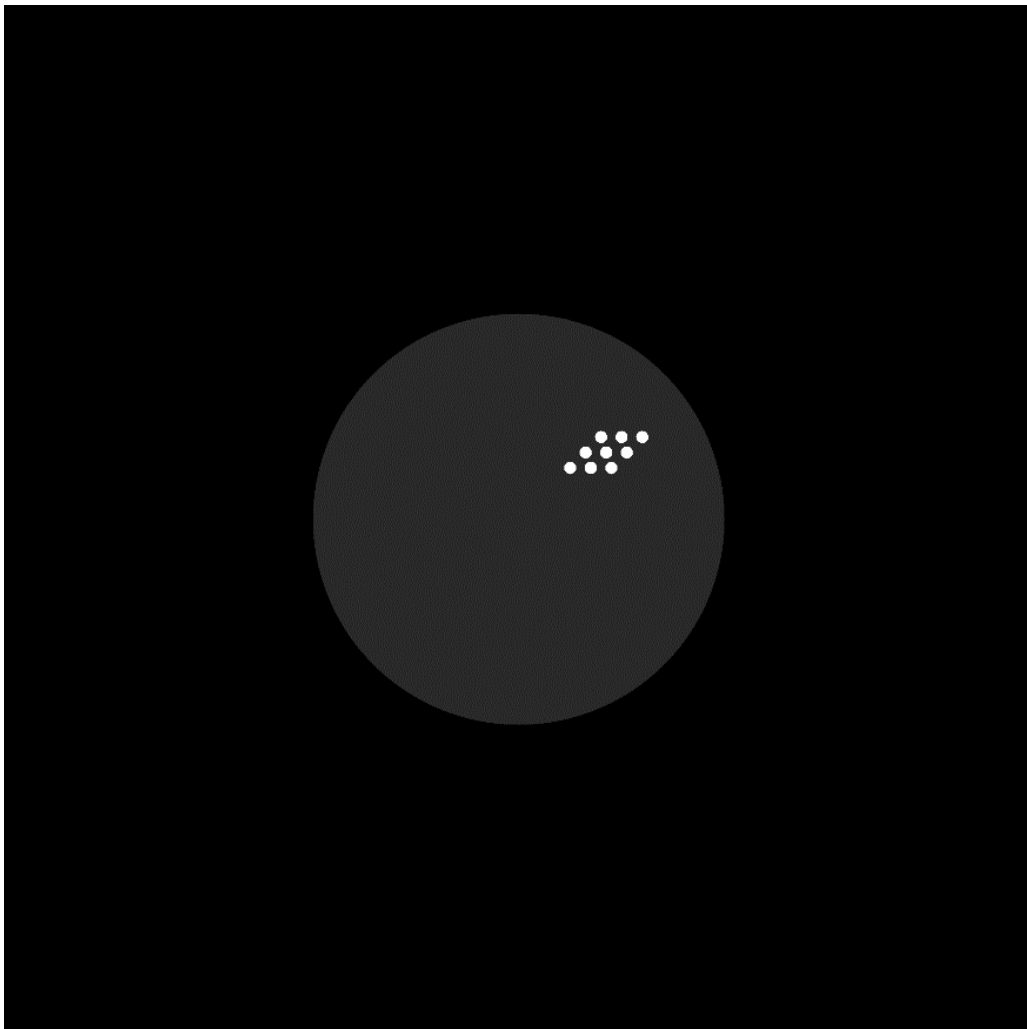


*Figure A.1 Digital phantom that we used for our simulation study. It is composed of nine hot spots of 2.4mm in size.*

We applied six specific patterns of motion to the object on a hundred frames, including linear, circular, a combination of linear and circular, Brownian-like, spiral, and random back and forth motions (Figure A.2). We varied the amplitude of motion for each pattern, generated and combined the corresponding list-mode data for each frame. For each pattern amplitude, we then applied our super-resolution reconstruction and compared the resulting images to a static reference. We reconstructed the images on a 1mm pixel grid with OSEM (15 iterations, 20 subsets).

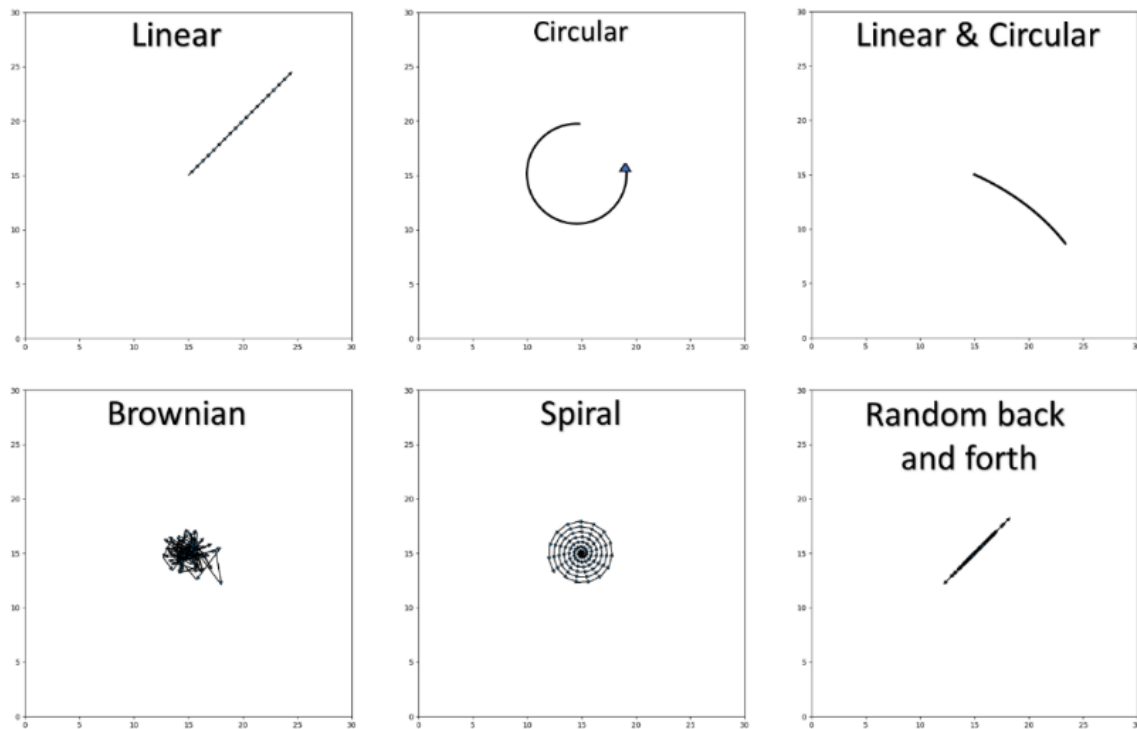


*Figure A.2 Illustration of the six patterns we defined for our simulations. For each pattern, we applied our SR reconstruction method with different amplitude steps. Those shapes were obtained by applying the motion on a point to have a sense of the path taken by the digital phantom for a given amplitude step.*

To quantify the benefits of super-resolution compared to the static reference, we calculated the mean peak-to-valley ratios (MPVR) of line profiles of the standard reconstruction and the super-resolution results across a set of increasing motion amplitudes. MPVR measures the ability of the imaging system to distinguish between adjacent points which makes it a well-suited metric for the phantom used in this evaluation.

Linear motion was defined as a translation along the X and Y axis, with the amplitude parameter defining the length between two frames. For this pattern, we observed that as the amplitude increased from 0mm to 10mm, the resolution initially increased, reaching a peak at

0.025 mm, before decreasing and stabilizing, but remaining better than the static reference (Figure A.3). Across all the different patterns and reconstructions, we found that it was the highest value we observed, with a MPVR of 10 compared to an average of 3.5 for the static reference (in the plots, we added in dashed blue lines one standard deviation corresponding varying MPVR on the static reference because it was recalculated at each amplitude step with a different Poisson noise realization). The high-resolution improvement for the linear pattern may be due to the additional linear sampling provided by the motion, which increases the number of independent samples taken along the line of motion.

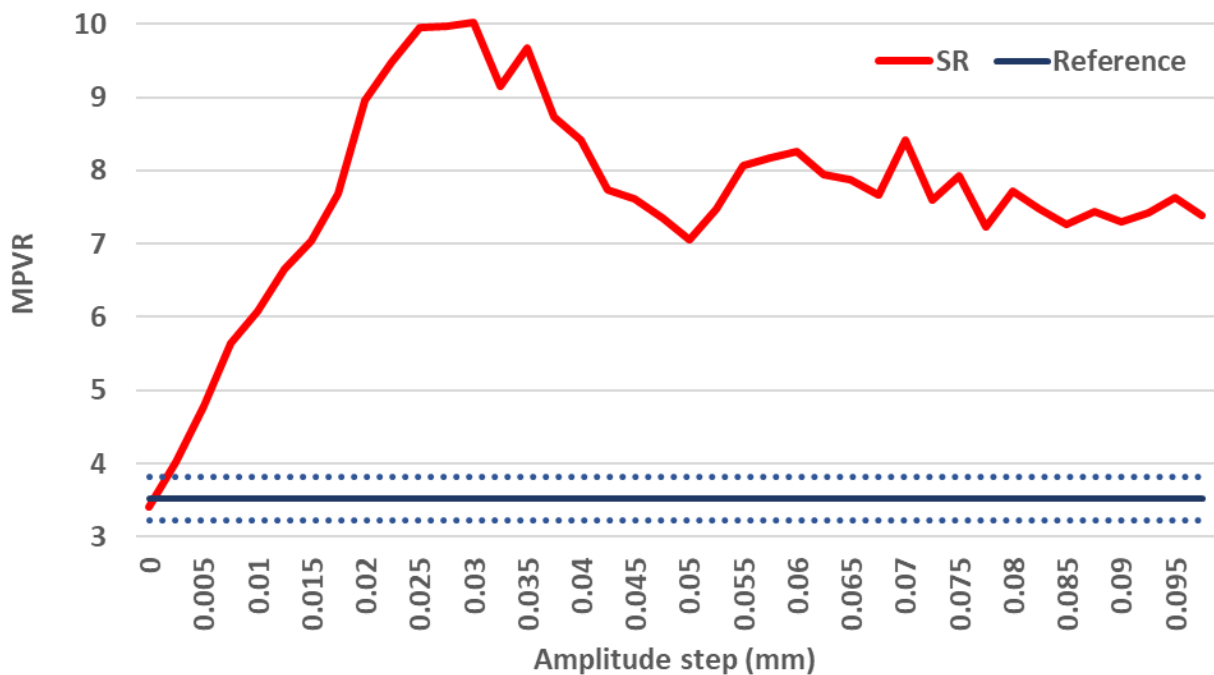


Figure A.3 Mean of peak to valley ratios values across different amplitudes for the “pure” linear pattern for SR in red and the static reference in blue. The dashed lines indicate one standard deviation around the mean reference MPVR.

For circular motion, while resolution improvement in terms of MPVR was noticeable, we observed (in Figure A.4) that it was lower than that of the linear pattern (Figure A.3). Circular motion involves rotation of the object around its center, which may not change the projection direction as significantly as linear motion. As a result, the extra information provided by a “pure” circular motion may not be as useful for super-resolution compared to linear motion. Those assumptions need to be validated in further studies.

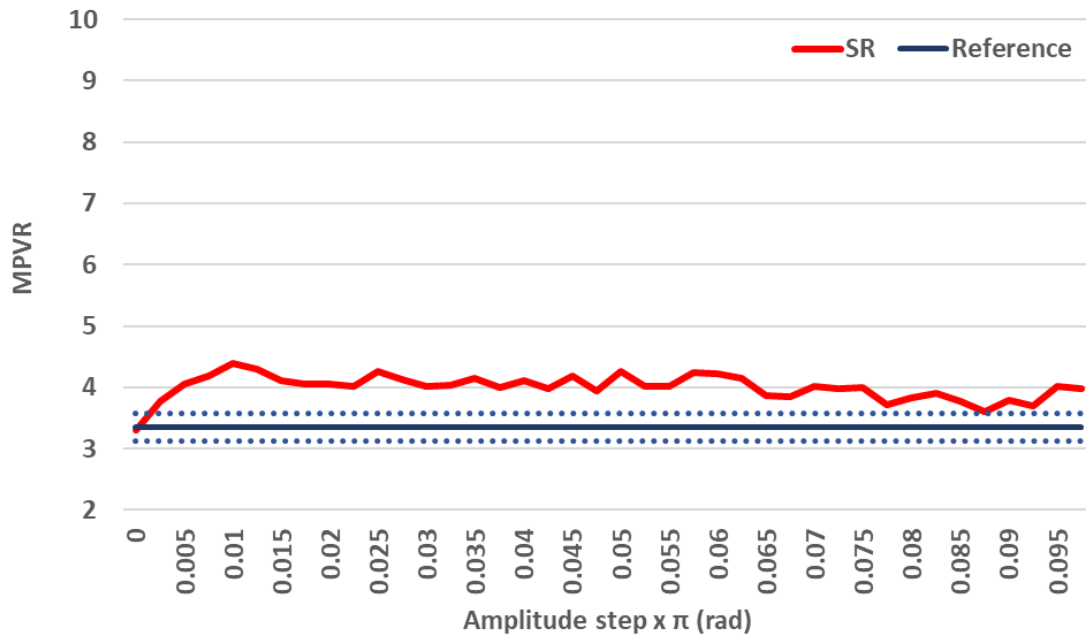


Figure A.4 Mean of peak to valley ratios values across different amplitudes for the “pure” circular pattern for SR in red and the static reference in blue. The dashed lines indicate one standard deviation around the mean reference MPVR.

The combination of linear and circular motion consisted of a combination of the two types of motion. We found that this pattern yielded a similar behavior to the “pure” linear pattern, with the resolution increased, reaching a peak at 0.025mm, before slightly decreasing and stabilizing (Figure A.5). In average, the results were slightly worse than the pure linear pattern, but still exhibited a MPVR twice higher than that of the static reconstruction.

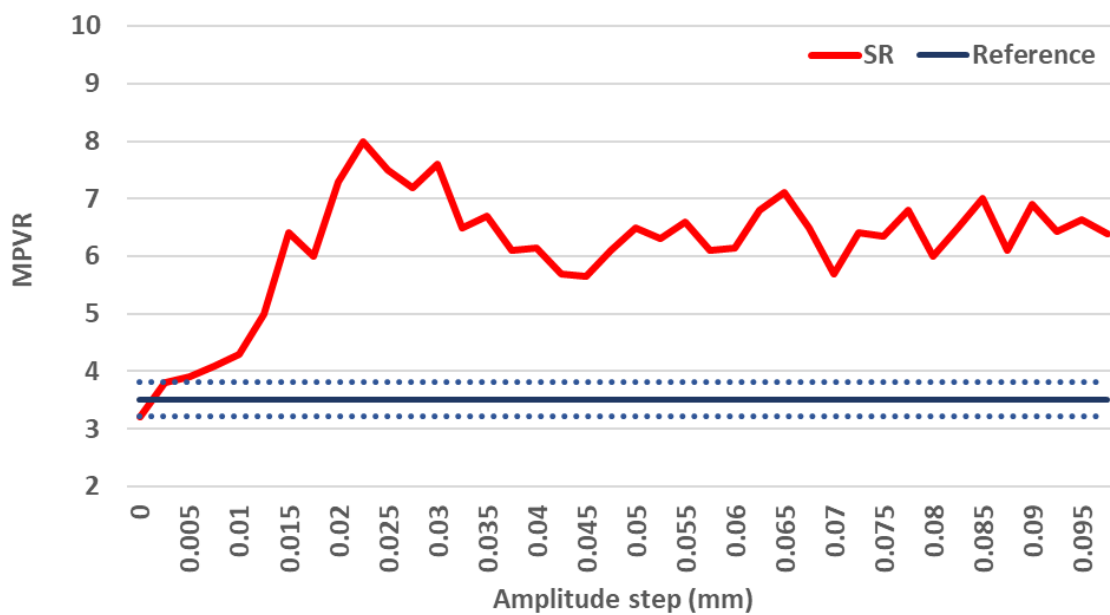


Figure A.5 Mean of peak to valley ratios values across different amplitudes for the combination of linear and circular pattern for SR in red and the static reference in blue. The dashed lines indicate one standard deviation around the mean reference MPVR.

Brownian-like motion, a random motion with a maximum displacement in a given time step, resulted in resolution improvement similar to that of the linear pattern for amplitude steps higher than 0.045mm. The Brownian-like pattern may provide a more isotropic increase in sampling due to its more random nature, which allows for more sampling in multiple directions as compared to linear motion. We believe that natural head motion during a scan could be approached by such a pattern, making it an effective pattern for achieving super-resolution benefits in clinical practice (Figure A.6).

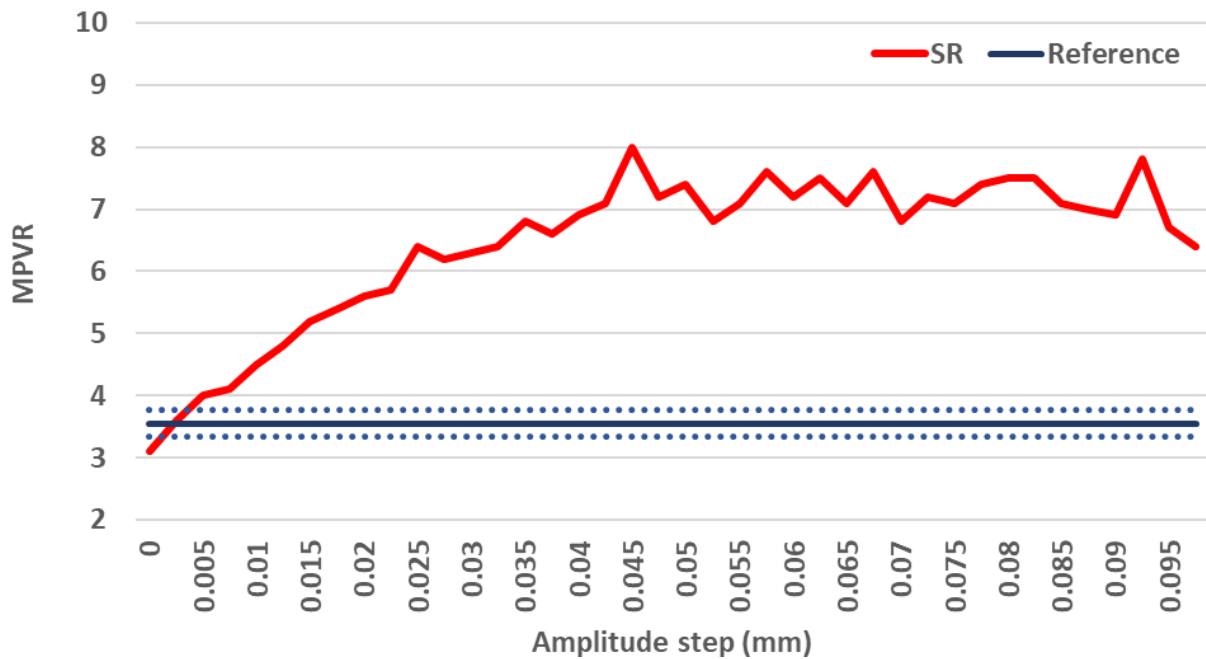


Figure A.6 Mean of peak to valley ratios values across different amplitudes for Brownian-like pattern for SR in red and the static reference in blue. The dashed lines indicate one standard deviation around the mean reference MPVR.

Spiral motion involved a spiral trajectory with a varying radius. While this spiral pattern is not applicable in clinical settings, it encompasses pseudo rotative type of patterns, which are in fact approachable using a motorized massage pillow. We observed in Figure A.7 that the resolution initially increased and reached a peak at 0.1mm before reaching a level comparable to the Brownian-like or linear patterns.



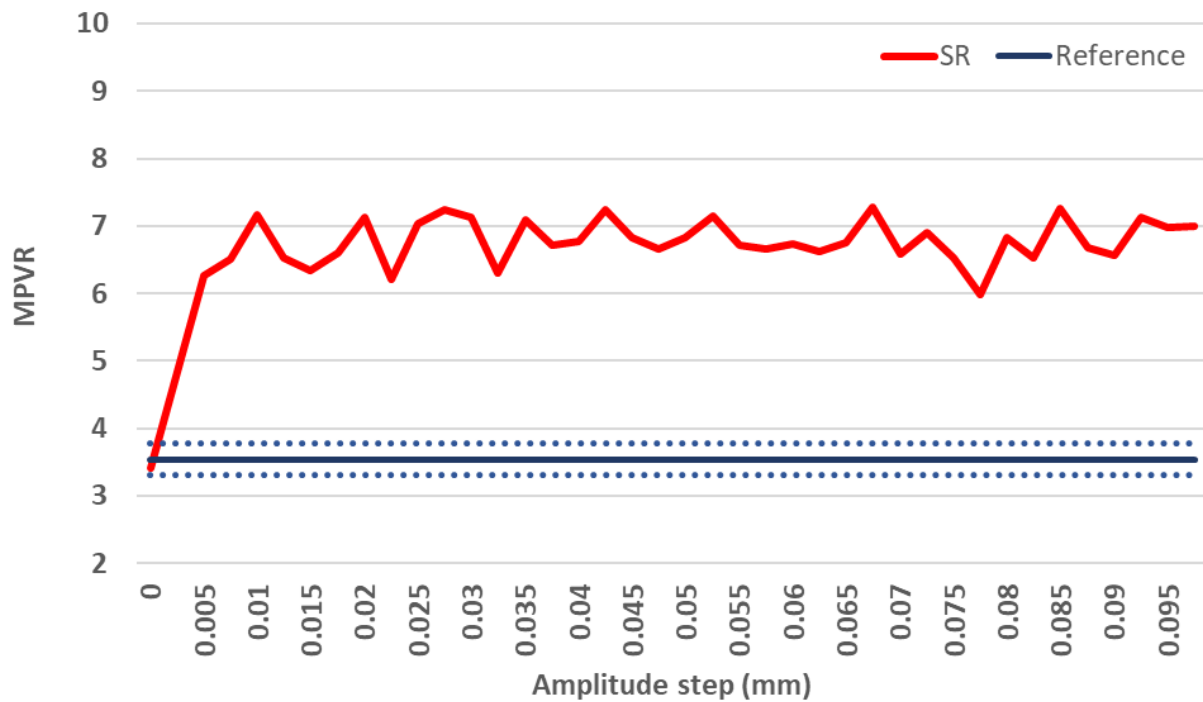


Figure A.7 Mean of peak to valley ratios values across different amplitudes for the spiral pattern for SR in red and the static reference in blue. The dashed lines indicate one standard deviation around the mean reference MPVR.

Finally, random back and forth pattern in the X and Y directions which involved a random translation in those directions, resulted in a significant but much slower increase in resolution, with a peak improvement at around 0.07mm amplitude step. Because the motion is less systematic, less predictable, and more importantly not as structured as in the linear pattern, it may lead to a less consistent increase in resolution as the amplitude increases. As a result, compared to the linear and Brownian-like patterns, the resolution improvement is less pronounced, and the peak improvement occurs starting at a larger amplitude step (around 0.07mm) (Figure A.8).

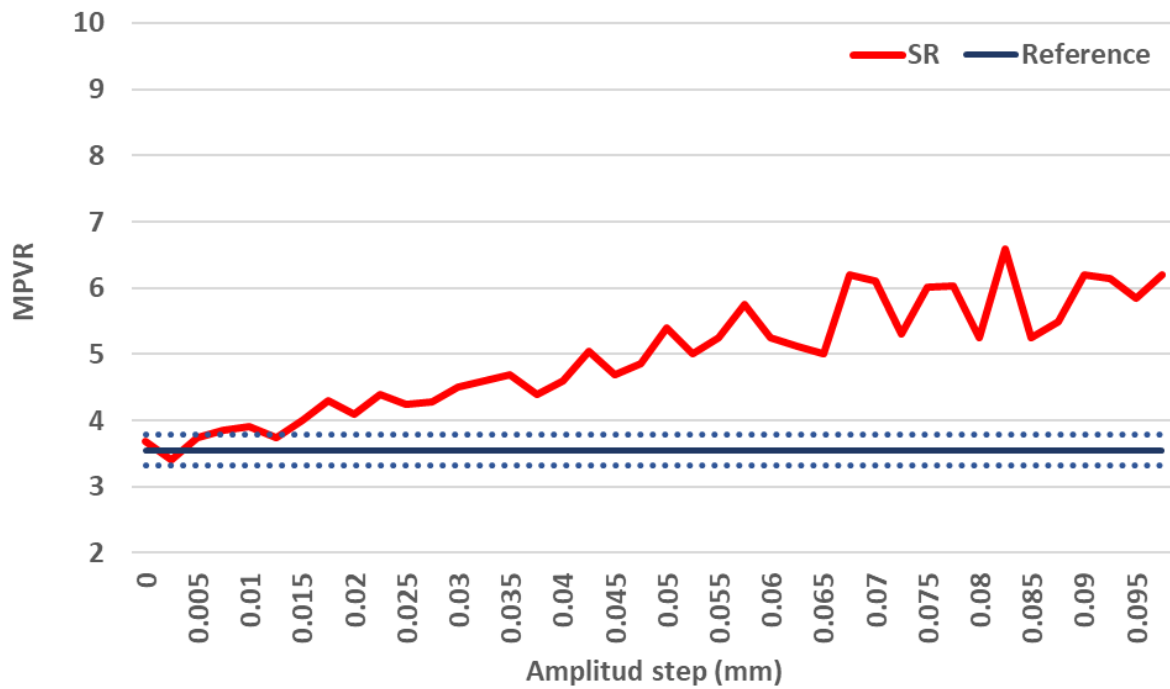


Figure A.8 Mean of peak to valley ratios values across different amplitudes for linear back-and-forth pattern for SR in red and the static reference in blue. The dashed lines indicate one standard deviation around the mean reference MPVR.

Similar behaviors were reproduced on different noise realizations. Our simulations showed that the linear, Brownian, combination of linear and circular, and spiral motion patterns yielded the highest super-resolution improvement, and that the specific motion amplitude required for optimal super-resolution benefits depends on the type of motion pattern used. However, any type of pattern will lead to an increase in resolution as long as the amplitude is sufficient. In a clinical setup, we believe that any of these patterns or their combination will result in an increase in resolution, as suggested by this study.

It is important to note that those quantitative results depend on several parameters that we chose to fix for this study, such as PSF modeling (we modeled it in the image space), projector choice (we used single ray Siddon), or even the phantom's shape, and may not be generalizable to other scenarios. Nonetheless, our findings provide valuable insights into the optimal motion patterns and amplitudes required for super-resolution, which can guide future clinical studies in this area.

In clinical practice, sufficient motion could be guaranteed using a defined mechanical motion. For example, motorized massage pillows could be used to impose a continuous pseudo-random motion in X and Y directions. Combined with the movement of the bed in Z direction, this could provide sampling in all three directions. However, we acknowledge that there may be

limitations to the extent of motion that can be safely applied to patients, and additional research is needed to determine the optimal approach for clinical implementation. While the carried study seems to provide a good indication that any type or composition of patterns implying continuous motion displacement bigger than a few microns will improve the native resolution of a scan, it is important to note that one of the main limitations in achieving super-resolution is the spatial calibration between the PET scanner and the tracking device.

# Bibliography

- Aguero, C., Dhaynaut, M., Normandin, M.D., Amaral, A.C., Guehl, N.J., Neelamegam, R., Marquie, M., Johnson, K.A., El Fakhri, G., Frosch, M.P., Gomez-Isla, T., 2019. Autoradiography validation of novel tau PET tracer [F-18]-MK-6240 on human postmortem brain tissue. *Acta Neuropathol. Commun.* 7, 37. <https://doi.org/10.1186/s40478-019-0686-6>
- Alessio, A.M., Kinahan, P.E., Lewellen, T.K., 2006. Modeling and incorporation of system response functions in 3-D whole body PET. *IEEE Trans. Med. Imaging* 25, 828–837. <https://doi.org/10.1109/TMI.2006.873222>
- Alessio, A.M., Stearns, C.W., Shan Tong, Ross, S.G., Kohlmyer, S., Ganin, A., Kinahan, P.E., 2010. Application and Evaluation of a Measured Spatially Variant System Model for PET Image Reconstruction. *IEEE Trans. Med. Imaging* 29, 938–949. <https://doi.org/10.1109/TMI.2010.2040188>
- Arpin, L., Koua, K., Panier, S., Bouziri, H., Abidi, M., Ben Attouch, M.W., Paulin, C., Maille, P., Geoffroy, C., Lecomte, R., Pratte, J.-F., Fontaine, R., 2011. Embedded real time digital signal processing unit for a 64-channel PET detector module, in: 2011 IEEE Nuclear Science Symposium Conference Record. IEEE, pp. 1545–1550. <https://doi.org/10.1109/NSSMIC.2011.6154367>
- Arriagada, P.V., Growdon, J.H., Hedley-Whyte, E.T., Hyman, B.T., 1992. Neurofibrillary tangles but not senile plaques parallel duration and severity of Alzheimer's disease. *Neurology* 9. <https://doi.org/10.1212/wnl.42.3.631>
- Arun, K.S., Huang, T.S., Blostein, S.D., 1987. Least-Squares Fitting of Two 3-D Point Sets. *IEEE Trans. Pattern Anal. Mach. Intell. PAMI-9*, 698–700. <https://doi.org/10.1109/TPAMI.1987.4767965>
- Badawi, R.D., Shi, H., Hu, P., Chen, S., Xu, T., Price, P.M., Ding, Y., Spencer, B.A., Nardo, L., Liu, W., Bao, J., Jones, T., Li, H., Cherry, S.R., 2019. First Human Imaging Studies with the EXPLORER Total-Body PET Scanner\*. *J. Nucl. Med.* 60, 299–303. <https://doi.org/10.2967/jnumed.119.226498>
- Baete, K., Nuyts, J., Laere, K.V., Van Paesschen, W., Ceyskens, S., De Ceuninck, L., Gheysens, O., Kelles, A., Van den Eynden, J., Suetens, P., Dupont, P., 2004. Evaluation of anatomy based reconstruction for partial volume correction in brain FDG-PET. *NeuroImage* 23, 305–317. <https://doi.org/10.1016/j.neuroimage.2004.04.041>
- Bai, B., Li, Q., Leahy, R.M., 2013. Magnetic resonance-guided positron emission tomography image reconstruction. *Semin. Nucl. Med.* 43, 30–44. <https://doi.org/10.1053/j.semnuclmed.2012.08.006>
- Bailey, D.L. (Ed.), 2005. Positron emission tomography: basic sciences. Springer, New York.

- Barber, D.C., 1980. The use of principal components in the quantitative analysis of gamma camera dynamic studies. *Phys. Med. Biol.* 25, 283–292. <https://doi.org/10.1088/0031-9155/25/2/008>
- Basu, S., Bresler, Y., 2000.  $O(N^2/\log^2 N)$  filtered backprojection reconstruction algorithm for tomography. *IEEE Trans. Image Process.* 9, 1760–1773. <https://doi.org/10.1109/83.869187>
- Bazin, J.P., Paola, R., Gibaud, B., Rougier, P., Tubiana, M., 1979. Factor analysis of dynamic scintigraphic data as a modelling method. An application to the detection of metastases. *Inf. Process. Med. Imaging* 345–366.
- Benali, H., Buvat, I., Frouin, F., Bazin, J.P., Di Paola, R., 1993. A statistical model for the determination of the optimal metric in factor analysis of medical image sequences (FAMIS). *Phys. Med. Biol.* 38, 1065–1080. <https://doi.org/10.1088/0031-9155/38/8/005>
- Bertero, M., Boccacci, P., 1998. Introduction to inverse problems in imaging. Institute of Physics Pub, Bristol, UK ; Philadelphia, Pa.
- Bethausser, T.J., Cody, K.A., Zammit, M.D., Murali, D., Converse, A.K., Barnhart, T.E., Stone, C.K., Rowley, H.A., Johnson, S.C., Christian, B.T., 2019. In Vivo Characterization and Quantification of Neurofibrillary Tau PET Radioligand  $^{18}\text{F}$ -MK-6240 in Humans from Alzheimer Disease Dementia to Young Controls. *J. Nucl. Med.* 60, 93–99. <https://doi.org/10.2967/jnumed.118.209650>
- Boussion, N., Hatt, M., Lamare, F., Bizais, Y., Turzo, A., Cheze-Le Rest, C., Visvikis, D., 2006. A multiresolution image based approach for correction of partial volume effects in emission tomography. *Phys. Med. Biol.* 51, 1857–1876. <https://doi.org/10.1088/0031-9155/51/7/016>
- Boutsidis, C., Gallopoulos, E., 2008. SVD based initialization: A head start for nonnegative matrix factorization. *Pattern Recognit.* 41, 1350–1362. <https://doi.org/10.1016/j.patcog.2007.09.010>
- Bowsher, J.E., Yuan, H., Hedlund, L.W., Turkington, T.G., Akabani, G., Badea, A., Kurylo, W.C., Wheeler, C.T., Cofer, G.P., Dewhurst, M.W., Johnson, G.A., 2004. Utilizing MRI information to estimate F18-FDG distributions in rat flank tumors, in: *IEEE Symposium Conference Record Nuclear Science 2004*. Presented at the IEEE Symposium Conference Record Nuclear Science 2004., pp. 2488-2492 Vol. 4. <https://doi.org/10.1109/NSSMIC.2004.1462760>
- Braak, H., Braak, E., 1991. Neuropathological staging of Alzheimer-related changes. *Acta Neuropathol. (Berl.)* 82, 239–259. <https://doi.org/10.1007/BF00308809>
- Brownell, S., 1953. Localization of brain tumors with positron emitters. *Nucleonics* 11, 40–45.
- Bruehlmeier, M., Roelcke, U., Schubiger, P.A., Ametamey, S.M., 2004. Assessment of hypoxia and perfusion in human brain tumors using PET with  $^{18}\text{F}$ -fluoromisonidazole and  $^{15}\text{O}$ -H $_2\text{O}$ . *J. Nucl. Med. Off. Publ. Soc. Nucl. Med.* 45, 1851–1859.

- Buck, A.K., Herrmann, K., Stargardt, T., Dechow, T., Krause, B.J., Schreyögg, J., 2010. Economic Evaluation of PET and PET/CT in Oncology: Evidence and Methodologic Approaches. *J. Nucl. Med.* 51, 401–412. <https://doi.org/10.2967/jnumed.108.059584>
- Burger, C., Goerres, G., Schoenes, S., Buck, A., Lonn, A.H.R., Von Schulthess, G.K., 2002. PET attenuation coefficients from CT images: experimental evaluation of the transformation of CT into PET 511-keV attenuation coefficients. *Eur. J. Nucl. Med. Mol. Imaging* 29, 922–927. <https://doi.org/10.1007/s00259-002-0796-3>
- Buvat, I., Benali, H., Frouin, F., Bazin, J.P., Di Paola, R., 1993. Target apex-seeking in factor analysis of medical image sequences. *Phys. Med. Biol.* 38, 123–138. <https://doi.org/10.1088/0031-9155/38/1/009>
- Cao, X., Xiao, P., Xie, Q., 2014. Dictionary learning based panel PET image reconstruction, in: 2014 IEEE Nuclear Science Symposium and Medical Imaging Conference (NSS/MIC). Presented at the 2014 IEEE Nuclear Science Symposium and Medical Imaging Conference (NSS/MIC), IEEE, Seattle, WA, USA, pp. 1–3. <https://doi.org/10.1109/NSSMIC.2014.7430797>
- Carson, R.E., Kuo, P.H., 2019. Brain-Dedicated Emission Tomography Systems: A Perspective on Requirements for Clinical Research and Clinical Needs in Brain Imaging. *IEEE Trans. Radiat. Plasma Med. Sci.* 3, 254–261. <https://doi.org/10.1109/TRPMS.2019.2912129>
- Catana, C., 2015. Motion correction options in pet/mri. *Semin. Nucl. Med.* 45, 212–223. <https://doi.org/10.1053/j.semnuclmed.2015.01.001>
- Cavaillolles, F., Bazin, J.P., Di Paola, R., 1984. Factor analysis in gated cardiac studies. *J. Nucl. Med. Off. Publ. Soc. Nucl. Med.* 25, 1067–1079.
- Cavalcanti, Y.C., Oberlin, T., Ferraris, V., Dobigeon, N., Ribeiro, M., Tauber, C., 2020. Compartment model-based nonlinear unmixing for kinetic analysis of dynamic PET images. <https://doi.org/10.48550/ARXIV.2011.10097>
- Chemli, Y., Tetrault, M.-A., Normandin, M., Marin, T., Bloch, I., Fakhri, G.E., Ouyang, J., Petibon, Y., 2021. Super-resolution in brain PET Using a Real Time Motion Capture System. *J. Nucl. Med.* 62, 34–34.
- Chen, W., Zhao, Y., Pan, B., Xu, C., 2015. Nonlinear Nonnegative Matrix Factorization Based on Discriminant Analysis with Application to Face Recognition, in: 2015 11th International Conference on Computational Intelligence and Security (CIS). Presented at the 2015 11th International Conference on Computational Intelligence and Security (CIS), IEEE, Shenzhen, China, pp. 191–194. <https://doi.org/10.1109/CIS.2015.54>
- Cherukupally, U., 2017. Zynq-7000 AP SoC - Precision Timing with IEEE1588 v2 Protocol Tech Tip. Xilinx Wiki Atlassian. URL <https://xilinx-wiki.atlassian.net/wiki/spaces/A/pages/18841712/Zynq-7000+AP+SoC+-+Precision+Timing+with+IEEE1588+v2+Protocol+Tech+Tip> (accessed 10.19.20).
- Christie, C., Martinez, D., Roca, M., O'Neill, S., Bustin, J., Richly, P., Manes, F., 2013. P4–130: Apraxia as initial presentation of Alzheimer's disease: A case series. *Alzheimers Dement.* 9, P751–P752. <https://doi.org/10.1016/j.jalz.2013.05.1520>

- Cloquet, C., Sureau, F.C., Defrise, M., Van Simaey, G., Trotta, N., Goldman, S., 2010. Non-Gaussian space-variant resolution modelling for list-mode reconstruction. *Phys. Med. Biol.* 55, 5045–5066. <https://doi.org/10.1088/0031-9155/55/17/011>
- Convert, L., Sarrhini, O., Paillé, M., Salem, N., Charette, P.G., Lecomte, R., 2022. The ultra high sensitivity blood counter: a compact, MRI-compatible, radioactivity counter for pharmacokinetic studies in  $\mu\text{l}$  volumes. *Biomed. Phys. Eng. Express* 8, 035022. <https://doi.org/10.1088/2057-1976/ac4c29>
- Cui, J., Pratz, G., Pevrhal, S., Levin, C.S., 2011. Fully 3D list-mode time-of-flight PET image reconstruction on GPUs using CUDA: Fully 3D list-mode time-of-flight PET on GPU-CUDA. *Med. Phys.* 38, 6775–6786. <https://doi.org/10.1118/1.3661998>
- Dagher, A., Thompson, C.J., 1985. Real-Time Data Rebinning in PET to Obtain Uniformly Sampled Projections. *IEEE Trans. Nucl. Sci.* 32, 811–817. <https://doi.org/10.1109/TNS.1985.4336946>
- Dahlbom, M., Hoffman, E.J., Hoh, C.K., Schiepers, C., Rosenqvist, G., Hawkins, R.A., Phelps, M.E., 1992. Whole-body positron emission tomography: Part I. Methods and performance characteristics. *J. Nucl. Med. Off. Publ. Soc. Nucl. Med.* 33, 1191–1199.
- Daou, D., 2008. Respiratory motion handling is mandatory to accomplish the high-resolution PET destiny. *Eur. J. Nucl. Med. Mol. Imaging* 35, 1961–1970. <https://doi.org/10.1007/s00259-008-0931-x>
- Dawood, M., Buther, F., Jiang, X., Schafers, K.P., 2008. Respiratory motion correction in 3-D PET data with advanced optical flow algorithms. *IEEE Trans. Med. Imaging* 27, 1164–1175. <https://doi.org/10.1109/TMI.2008.918321>
- Deller, T.W., Ahn, S., Jansen, F.P., Schramm, G., Wangerin, K.A., Spangler-Bickell, M.G., Stearns, C.W., Mehdi Khalighi, M., 2021. Implementation and Image Quality Benefit of a Hybrid-Space PET Point Spread Function, in: 2021 IEEE Nuclear Science Symposium and Medical Imaging Conference (NSS/MIC). Presented at the 2021 IEEE Nuclear Science Symposium and Medical Imaging Conference (NSS/MIC), IEEE, Piscataway, NJ, USA, pp. 1–5. <https://doi.org/10.1109/NSS/MIC44867.2021.9875877>
- Dempster, A.P., Laird, N.M., Rubin, D.B., 1977. Maximum Likelihood from Incomplete Data via the EM Algorithm. *J. R. Stat. Soc. Ser. B Methodol.* 39, 1–38.
- Di Paola, R., Bazin, J.P., Aubry, F., Aurengo, A., Cavailloles, F., Herry, J.Y., Kahn, E., 1982. Handling of Dynamic Sequences in Nuclear Medicine. *IEEE Trans. Nucl. Sci.* 29, 1310–1321. <https://doi.org/10.1109/TNS.1982.4332188>
- Dice, L.R., 1945. Measures of the Amount of Ecologic Association Between Species. *Ecology* 26, 297–302. <https://doi.org/10.2307/1932409>
- Drachman, D.A., 2006. Aging of the brain, entropy, and Alzheimer disease. *Neurology* 67, 1340–1352. <https://doi.org/10.1212/01.wnl.0000240127.89601.83>
- Eidson, J.C., 2006. Measurement, control, and communication using IEEE 1588, *Advances in industrial control*. Springer, London.

- El Fakhri, G., Kardan, A., Sitek, A., Dorbala, S., Abi-Hatem, N., Lahoud, Y., Fischman, A., Coughlan, M., Yasuda, T., Di Carli, M.F., 2009. Reproducibility and accuracy of quantitative myocardial blood flow assessment with (82)Rb PET: comparison with (13)N-ammonia PET. *J. Nucl. Med. Off. Publ. Soc. Nucl. Med.* 50, 1062–1071. <https://doi.org/10.2967/jnumed.104.007831>
- El Fakhri, G., Sitek, A., Guérin, B., Kijewski, M.F., Di Carli, M.F., Moore, S.C., 2005. Quantitative dynamic cardiac 82Rb PET using generalized factor and compartment analyses. *J. Nucl. Med. Off. Publ. Soc. Nucl. Med.* 46, 1264–1271.
- El Fakhri, G., Sitek, A., Zimmerman, R.E., Ouyang, J., 2006. Generalized five-dimensional dynamic and spectral factor analysis. *Med. Phys.* 33, 1016–1024. <https://doi.org/10.1118/1.2179168>
- Feng, L., Axel, L., Chandarana, H., Block, K.T., Sodickson, D.K., Otazo, R., 2016. XD-GRASP: Golden-angle radial MRI with reconstruction of extra motion-state dimensions using compressed sensing. *Magn. Reson. Med.* 75, 775–788. <https://doi.org/10.1002/mrm.25665>
- Fix, E., Hodges, J.L., 1989. Discriminatory Analysis. Nonparametric Discrimination: Consistency Properties. *Int. Stat. Rev. Rev. Int. Stat.* 57, 238–247. <https://doi.org/10.2307/1403797>
- Fulton, R.R., Meikle, S.R., Eberl, S., Pfeiffer, J., Constable, C.J., 2002a. Correction for head movements in positron emission tomography using an optical motion-tracking system. *IEEE Trans. Nucl. Sci.* 49, 116–123. <https://doi.org/10.1109/TNS.2002.998691>
- Fulton, R.R., Meikle, S.R., Eberl, S., Pfeiffer, J., Constable, C.J., 2002b. Correction for head movements in positron emission tomography using an optical motion-tracking system. *IEEE Trans. Nucl. Sci.* 49, 116–123. <https://doi.org/10.1109/TNS.2002.998691>
- Fulton, Roger R, Pfeiffer, J., Constable, C.J., Fulham, M.J., 2002. Correction for Head Movements in Positron Emission Tomography Using an Optical Motion-Tracking System. *IEEE Trans. Nucl. Sci.* 49, 8.
- Gaudin, E., Arpin, L., Bouchard, J., Paille, M., Bouziri, H., Bergeron, M., Pepin, C.M., Cadorette, J., Fontaine, R., Lecomte, R., 2015. Performance characterization of a dual-threshold time-over-threshold APD-based detector front-end module for PET imaging, in: 2015 IEEE Nuclear Science Symposium and Medical Imaging Conference (NSS/MIC). Presented at the 2015 IEEE Nuclear Science Symposium and Medical Imaging Conference (NSS/MIC), IEEE, San Diego, CA, USA, pp. 1–3. <https://doi.org/10.1109/NSSMIC.2015.7581828>
- Gaudin, É., Thibaudeau, C., Arpin, L., Leroux, J.-D., Toussaint, M., Beaudoin, J.-F., Cadorette, J., Paillé, M., Pepin, C.M., Koua, K., Bouchard, J., Viscogliosi, N., Paulin, C., Fontaine, R., Lecomte, R., 2021a. Performance evaluation of the mouse version of the LabPET II PET scanner. *Phys. Med. Biol.* 66, 065019. <https://doi.org/10.1088/1361-6560/abd952>
- Gaudin, É., Thibaudeau, C., Arpin, L., Leroux, J.D., Toussaint, M., Beaudoin, J.F., Cadorette, J., Paillé, M., Pepin, C.M., Koua, K., Bouchard, J., Viscogliosi, N., Paulin, C., Fontaine,



- R., Lecomte, R., 2021b. Remove: Performance evaluation of the mouse version of the LabPET II PET scanner. *Phys. Med. Biol.* 66. <https://doi.org/10.1088/1361-6560/abd952>
- Gaudin, E., Toussaint, M., Thibaudeau, C., Paille, M., Fontaine, R., Lecomte, R., 2019. Performance Simulation of an Ultrahigh Resolution Brain PET Scanner Using 1.2-mm Pixel Detectors. *IEEE Trans. Radiat. Plasma Med. Sci.* 3, 334–342. <https://doi.org/10.1109/TRPMS.2018.2877511>
- Gillman, A., Smith, J., Thomas, P., Rose, S., Dowson, N., 2017. PET motion correction in context of integrated PET/MR: Current techniques, limitations, and future projections. *Med. Phys.* 44, e430–e445. <https://doi.org/10.1002/mp.12577>
- Goldstein, S.R., Daube-Witherspoon, M.E., Green, M.V., Eidsath, A., 1997. A head motion measurement system suitable for emission computed tomography. *IEEE Trans. Med. Imaging* 16, 17–27. <https://doi.org/10.1109/42.552052>
- Golla, S.S.V., Lubberink, M., van Berckel, B.N.M., Lammertsma, A.A., Boellaard, R., 2017. Partial volume correction of brain PET studies using iterative deconvolution in combination with HYPR denoising. *EJNMMI Res.* 7, 36. <https://doi.org/10.1186/s13550-017-0284-1>
- Gould, K.L., Pan, T., Loghin, C., Johnson, N.P., Guha, A., Sdringola, S., 2007. Frequent diagnostic errors in cardiac PET/CT due to misregistration of CT attenuation and emission PET images: a definitive analysis of causes, consequences, and corrections. *J. Nucl. Med. Off. Publ. Soc. Nucl. Med.* 48, 1112–1121. <https://doi.org/10.2967/jnumed.107.039792>
- Green, M.V., Seidel, J., Stein, S.D., Tedder, T.E., Kempner, K.M., Kertzman, C., Zeffiro, T.A., 1994. Head movement in normal subjects during simulated PET brain imaging with and without head restraint. *J. Nucl. Med. Off. Publ. Soc. Nucl. Med.* 35, 1538–1546.
- Grimm, R., Fürst, S., Souvatzoglou, M., Forman, C., Hutter, J., Dregely, I., Ziegler, S.I., Kiefer, B., Hornegger, J., Block, K.T., Nekolla, S.G., 2015. Self-gated MRI motion modeling for respiratory motion compensation in integrated PET/MRI. *Med. Image Anal.* 19, 110–120. <https://doi.org/10.1016/j.media.2014.08.003>
- Guehl, N.J., Wooten, D.W., Yokell, D.L., Moon, S.-H., Dhaynaut, M., Katz, S., Moody, K.A., Gharagouzloo, C., Kas, A., Johnson, K.A., El Fakhri, G., Normandin, M.D., 2019. Evaluation of pharmacokinetic modeling strategies for in-vivo quantification of tau with the radiotracer [18F]MK6240 in human subjects. *Eur. J. Nucl. Med. Mol. Imaging* 46, 2099–2111. <https://doi.org/10.1007/s00259-019-04419-z>
- Gunn, R.N., Slifstein, M., Searle, G.E., Price, J.C., 2015. Quantitative imaging of protein targets in the human brain with PET. *Phys. Med. Biol.* 60, R363–R411. <https://doi.org/10.1088/0031-9155/60/22/R363>
- Hall, B., Mak, E., Cervenka, S., Aigbirhio, F.I., Rowe, J.B., O'Brien, J.T., 2017. In vivo tau PET imaging in dementia: Pathophysiology, radiotracer quantification, and a systematic review of clinical findings. *Ageing Res. Rev.* 36, 50–63. <https://doi.org/10.1016/j.arr.2017.03.002>

- Hammer, B.E., Christensen, N.L., Heil, B.G., 1994. Use of a magnetic field to increase the spatial resolution of positron emission tomography. *Med. Phys.* 21, 1917–1920. <https://doi.org/10.1118/1.597178>
- Harada, R., Furumoto, S., Tago, T., Furukawa, K., Ishiki, A., Tomita, N., Iwata, R., Tashiro, M., Arai, H., Yanai, K., Kudo, Y., Okamura, N., 2016. Characterization of the radiolabeled metabolite of tau PET tracer 18F-THK5351. *Eur. J. Nucl. Med. Mol. Imaging* 43, 2211–2218. <https://doi.org/10.1007/s00259-016-3453-y>
- Houston, A.S., 1986. The Use of Set Theory and Cluster Analysis to Investigate the Constraint Problem in Factor Analysis in Dynamic Structures (FADS), in: Bacharach, S.L. (Ed.), *Information Processing in Medical Imaging: Proceedings of the 9th Conference, Washington D.C., 10–14 June 1985*. Springer Netherlands, Dordrecht, pp. 177–192. [https://doi.org/10.1007/978-94-009-4261-5\\_13](https://doi.org/10.1007/978-94-009-4261-5_13)
- Huang, C., Ackerman, J.L., Petibon, Y., Normandin, M.D., Brady, T.J., El Fakhri, G., Ouyang, J., 2014. Motion compensation for brain PET imaging using wireless MR active markers in simultaneous PET-MR: phantom and non-human primate studies. *NeuroImage* 91, 129–137. <https://doi.org/10.1016/j.neuroimage.2013.12.061>
- Huang, C.-W., Hsu, S.-W., Chang, Y.-T., Huang, S.-H., Huang, Y.-C., Lee, C.-C., Chang, W.-N., Lui, C.-C., Chen, N.-C., Chang, C.-C., 2018. Cerebral Perfusion Insufficiency and Relationships with Cognitive Deficits in Alzheimer’s Disease: A Multiparametric Neuroimaging Study. *Sci. Rep.* 8, 1541. <https://doi.org/10.1038/s41598-018-19387-x>
- Huang, T.S., Tsai, R.Y., 1984. *Advances in Computer Vision and Image Processing*. JAI Press.
- Hudson, H.M., Larkin, R.S., 1994. Accelerated image reconstruction using ordered subsets of projection data. *IEEE Trans. Med. Imaging* 13, 601–609. <https://doi.org/10.1109/42.363108>
- Hutchcroft, W., Wang, G., Chen, K.T., Catana, C., Qi, J., 2016. Anatomically-aided PET reconstruction using the kernel method. *Phys. Med. Biol.* 61, 6668–6683. <https://doi.org/10.1088/0031-9155/61/18/6668>
- Hwang, S.I., Kim, J.H., Park, S.W., Han, M.H., Yu, I.K., Lee, S.H., Lee, D.S., Lee, S.K., Chung, C.K., Chang, K.H., 2001. Comparative analysis of MR imaging, positron emission tomography, and ictal single-photon emission CT in patients with neocortical epilepsy. *AJNR Am. J. Neuroradiol.* 22, 937–946.
- Jin, X., Chan, C., Mulnix, T., Panin, V., Casey, M.E., Liu, C., Carson, R.E., 2013. List-mode reconstruction for the Biograph mCT with physics modeling and event-by-event motion correction. *Phys. Med. Biol.* 58, 5567–5591. <https://doi.org/10.1088/0031-9155/58/16/5567>
- Jin, X., Mulnix, T., Sandiego, C.M., Carson, R.E., 2014. Evaluation of Frame-Based and Event-by-Event Motion-Correction Methods for Awake Monkey Brain PET Imaging. *J. Nucl. Med.* 55, 287–293. <https://doi.org/10.2967/jnumed.113.123299>
- Johnson, K.A., Schultz, A., Betensky, R.A., Becker, J.A., Sepulcre, J., Rentz, D., Mormino, E., Chhatwal, J., Amariglio, R., Papp, K., Marshall, G., Albers, M., Mauro, S., Pepin, L., Alverio, J., Judge, K., Philiossaint, M., Shoup, T., Yokell, D., Dickerson, B., Gomez-

- Isla, T., Hyman, B., Vasdev, N., Sperling, R., 2016. Tau positron emission tomographic imaging in aging and early Alzheimer disease: Tau PET in Aging and Early AD. *Ann. Neurol.* 79, 110–119. <https://doi.org/10.1002/ana.24546>
- Jones, T., Townsend, D., 2017. History and future technical innovation in positron emission tomography. *J. Med. Imaging Bellingham Wash* 4, 011013. <https://doi.org/10.1117/1.JMI.4.1.011013>
- Jucker, M., Walker, L.C., 2011. Pathogenic protein seeding in Alzheimer disease and other neurodegenerative disorders. *Ann. Neurol.* 70, 532–540. <https://doi.org/10.1002/ana.22615>
- Judenhofer, M.S., Wehrl, H.F., Newport, D.F., Catana, C., Siegel, S.B., Becker, M., Thielscher, A., Kneilling, M., Lichy, M.P., Eichner, M., Klingel, K., Reischl, G., Widmaier, S., Röcken, M., Nutt, R.E., Machulla, H.-J., Uludag, K., Cherry, S.R., Claussen, C.D., Pichler, B.J., 2008. Simultaneous PET-MRI: a new approach for functional and morphological imaging. *Nat. Med.* 14, 459–465. <https://doi.org/10.1038/nm1700>
- Kadrmas, D.J., 2004. LOR-OSEM: statistical PET reconstruction from raw line-of-response histograms. *Phys. Med. Biol.* 49, 4731. <https://doi.org/10.1088/0031-9155/49/20/005>
- Kennedy, J.A., Israel, O., Frenkel, A., Bar-Shalom, R., Haim Azhari, 2006. Super-resolution in PET imaging. *IEEE Trans. Med. Imaging* 25, 137–147. <https://doi.org/10.1109/TMI.2005.861705>
- Kesner, A.L., Bundschuh, R.A., Detorie, N.C., Dahlbom, M., Ziegler, S.I., Czernin, J., Silverman, D.H., 2009. Respiratory Gated PET Derived in a Fully Automated Manner From Raw PET Data. *IEEE Trans. Nucl. Sci.* 56, 677–686. <https://doi.org/10.1109/TNS.2009.2016341>
- Kinahan, P.E., Townsend, D.W., Beyer, T., Sashin, D., 1998. Attenuation correction for a combined 3D PET/CT scanner. *Med. Phys.* 25, 2046–2053. <https://doi.org/10.1118/1.598392>
- Klunk, W.E., Engler, H., Nordberg, A., Wang, Y., Blomqvist, G., Holt, D.P., Bergström, M., Savitcheva, I., Huang, G., Estrada, S., Ausén, B., Debnath, M.L., Barletta, J., Price, J.C., Sandell, J., Lopresti, B.J., Wall, A., Koivisto, P., Antoni, G., Mathis, C.A., Långström, B., 2004. Imaging brain amyloid in Alzheimer's disease with Pittsburgh Compound-B. *Ann. Neurol.* 55, 306–319. <https://doi.org/10.1002/ana.20009>
- Knoll, G.F., 2010. Radiation detection and measurement, 4th ed. ed. John Wiley, Hoboken, N.J.
- Krempser, A.R., Ichinose, R.M., Miranda de Sá, A.M.F.L., Velasques de Oliveira, S.M., Carneiro, M.P., 2013. Recovery coefficients determination for partial volume effect correction in oncological PET/CT images considering the effect of activity outside the field of view. *Ann. Nucl. Med.* 27, 924–930. <https://doi.org/10.1007/s12149-013-0773-x>
- Lecomte, R., Normandin, M., Thibaudeau, C., Arpin, L., Leroux, J.-D., Bouchard, J., Espagnet, R., Lauzier-Trépanier, P.-Y., Samson, A., Beaudoin, J.-F., Bouziri, H., Collin, L.-M., Gaudin, É., Gaudreault, M., Hachey, M.-A., Pepin, C., Toussaint, M., Chemli, Y.,

- Marin, T., Ouyang, J., Petibon, Y., Najmaoui, Y., Tétrault, M.-A., Fontaine, R., El Fakhri, G., 2022. Scanner Approaching in Vivo Autoradiographic Neuro Tomography (SAVANT): Progress Towards  $\mu$ L Resolution for Imaging the Human Brain. *Soc. Nucl. Med.* 63, 3.
- Lee, D.D., Seung, H.S., 1999. Learning the parts of objects by non-negative matrix factorization. *Nature* 401, 788–791. <https://doi.org/10.1038/44565>
- Lemoine, L., Leuzy, A., Chiotis, K., Rodriguez-Vieitez, E., Nordberg, A., 2018. Tau positron emission tomography imaging in tauopathies: The added hurdle of off-target binding. *Alzheimers Dement. Diagn. Assess. Dis. Monit.* 10, 232–236. <https://doi.org/10.1016/j.dadm.2018.01.007>
- Li, Y., Matej, S., Metzler, S.D., 2014. Image reconstructions from super-sampled data sets with resolution modeling in PET imaging: Image reconstructions from super-sampled data in PET imaging. *Med. Phys.* 41, 121912. <https://doi.org/10.1118/1.4901552>
- Liu, C., Pierce, L.A., Alessio, A.M., Kinahan, P.E., 2009. The impact of respiratory motion on tumor quantification and delineation in static PET/CT imaging. *Phys. Med. Biol.* 54, 7345–7362. <https://doi.org/10.1088/0031-9155/54/24/007>
- Lopresti, B.J., Russo, A., Jones, W.F., Fisher, T., Crouch, D.G., Altenburger, D.E., Townsend, D.W., 1999. Implementation and performance of an optical motion tracking system for high resolution brain PET imaging. *IEEE Trans. Nucl. Sci.* 46, 2059–2067. <https://doi.org/10.1109/23.819283>
- Lu, Y., Gallezot, J.-D., Naganawa, M., Ren, S., Fontaine, K., Wu, J., Onofrey, J.A., Toyonaga, T., Boutagy, N., Mulnix, T., Panin, V.Y., Casey, M.E., Carson, R.E., Liu, C., 2019. Data-driven voluntary body motion detection and non-rigid event-by-event correction for static and dynamic PET. *Phys. Med. Biol.* 64, 065002. <https://doi.org/10.1088/1361-6560/ab02c2>
- Manjeshwar, R.M., Ross, S.G., Iatrou, M., Deller, T.W., Stearns, C.W., 2006. Fully 3D PET Iterative Reconstruction Using Distance-Driven Projectors and Native Scanner Geometry, in: 2006 IEEE Nuclear Science Symposium Conference Record. Presented at the 2006 IEEE Nuclear Science Symposium Conference Record, IEEE, San Diego, CA, pp. 2804–2807. <https://doi.org/10.1109/NSSMIC.2006.356461>
- Marquié, M., Normandin, M.D., Meltzer, A.C., Siao Tick Chong, M., Andrea, N.V., Antón-Fernández, A., Klunk, W.E., Mathis, C.A., Ikonomic, M.D., Debnath, M., Bien, E.A., Vanderburg, C.R., Costantino, I., Makaretz, S., DeVos, S.L., Oakley, D.H., Gomperts, S.N., Growdon, J.H., Domoto-Reilly, K., Lucente, D., Dickerson, B.C., Frosch, M.P., Hyman, B.T., Johnson, K.A., Gómez-Isla, T., 2017. Pathological correlations of [F-18]-AV-1451 imaging in non-alzheimer tauopathies: Tau Imaging: Pathological Correlations. *Ann. Neurol.* 81, 117–128. <https://doi.org/10.1002/ana.24844>
- McKhann, G.M., Knopman, D.S., Chertkow, H., Hyman, B.T., Jack, C.R., Kawas, C.H., Klunk, W.E., Koroshetz, W.J., Manly, J.J., Mayeux, R., Mohs, R.C., Morris, J.C., Rossor, M.N., Scheltens, P., Carrillo, M.C., Thies, B., Weintraub, S., Phelps, C.H., 2011. The diagnosis of dementia due to Alzheimer’s disease: recommendations from

- the National Institute on Aging-Alzheimer's Association workgroups on diagnostic guidelines for Alzheimer's disease. *Alzheimers Dement. J. Alzheimers Assoc.* 7, 263–269. <https://doi.org/10.1016/j.jalz.2011.03.005>
- Mettivier, G., Salvati, R., Conti, M., Russo, P., 2011. The effect of count statistics on the convergence value in OSEM reconstruction in PET and TOF PET, in: 2011 IEEE Nuclear Science Symposium Conference Record. Presented at the 2011 IEEE Nuclear Science Symposium and Medical Imaging Conference (NSS/MIC 2011), IEEE, Valencia, pp. 2400–2406. <https://doi.org/10.1109/NSSMIC.2011.6152654>
- Michel, C., Sibomana, M., Boi, A., Bernard, X., Lonneux, M., Defrise, M., Comtat, C., Kinahan, P.E., Townsend, D.W., 1998. Preserving Poisson characteristics of PET data with weighted OSEM reconstruction, in: 1998 IEEE Nuclear Science Symposium Conference Record. 1998 IEEE Nuclear Science Symposium and Medical Imaging Conference (Cat. No.98CH36255). Presented at the 1998 IEEE Nuclear Science Symposium Conference Record. 1998 IEEE Nuclear Science Symposium and Medical Imaging Conference (Cat. No.98CH36255), pp. 1323–1329 vol.2. <https://doi.org/10.1109/NSSMIC.1998.774398>
- Mishra, S., Gordon, B.A., Su, Y., Christensen, J., Friedrichsen, K., Jackson, K., Hornbeck, R., Balota, D.A., Cairns, N.J., Morris, J.C., Ances, B.M., Benzinger, T.L.S., 2017. AV-1451 PET imaging of tau pathology in preclinical Alzheimer disease: Defining a summary measure. *NeuroImage* 161, 171–178. <https://doi.org/10.1016/j.neuroimage.2017.07.050>
- Moehrs, S., Defrise, M., Belcari, N., Guerra, A.D., Bartoli, A., Fabbri, S., Zanetti, G., 2008. Multi-ray-based system matrix generation for 3D PET reconstruction. *Phys. Med. Biol.* 53, 6925–6945. <https://doi.org/10.1088/0031-9155/53/23/018>
- Montandon, M.-L., Zaidi, H., 2005. Atlas-guided non-uniform attenuation correction in cerebral 3D PET imaging. *NeuroImage* 25, 278–286. <https://doi.org/10.1016/j.neuroimage.2004.11.021>
- Montgomery, A.J., Thielemans, K., Mehta, M.A., Turkheimer, F., Mustafovic, S., Grasby, P.M., 2006. Correction of Head Movement on PET Studies: Comparison of Methods. *J. Nucl. Med.* 47, 1936–1944.
- Moses, D., 1993. Empirical observation of resolution degradation in positron emission tomographs utilizing block detectors. *J. Nucl. Med.* 34, 101P-101P.
- Mullani, N.A., Markham, J., Ter-Pogossian, M.M., 1980. Feasibility of time-of-flight reconstruction in positron emission tomography. *J. Nucl. Med. Off. Publ. Soc. Nucl. Med.* 21, 1095–1097.
- Munoz, C., Neji, R., Cruz, G., Mallia, A., Jeljeli, S., Reader, A.J., Botnar, R.M., Prieto, C., 2018. Motion-corrected simultaneous cardiac positron emission tomography and coronary MR angiography with high acquisition efficiency. *Magn. Reson. Med.* 79, 339–350. <https://doi.org/10.1002/mrm.26690>
- Nakamura, M., Suzuki, Y., Kobayashi, S., 1989. A method for recovering physiological components from dynamic radionuclide images using the maximum entropy principle:

- a numerical investigation. *IEEE Trans. Biomed. Eng.* 36, 906–917. <https://doi.org/10.1109/10.35299>
- Nasreddine, Z.S., Phillips, N.A., Bédirian, V., Charbonneau, S., Whitehead, V., Collin, I., Cummings, J.L., Chertkow, H., 2005. The Montreal Cognitive Assessment, MoCA: a brief screening tool for mild cognitive impairment. *J. Am. Geriatr. Soc.* 53, 695–699. <https://doi.org/10.1111/j.1532-5415.2005.53221.x>
- Nijran, K.S., Barber, D.C., 1988. The Importance of Constraints in Factor Analysis of Dynamic Studies, in: de Graaf, C.N., Viergever, M.A. (Eds.), *Information Processing in Medical Imaging*. Springer US, Boston, MA, pp. 521–529. [https://doi.org/10.1007/978-1-4615-7263-3\\_34](https://doi.org/10.1007/978-1-4615-7263-3_34)
- Nijran, K.S., Barber, D.C., 1986. Factor analysis of dynamic function studies using a priori physiological information. *Phys. Med. Biol.* 31, 1107–1117. <https://doi.org/10.1088/0031-9155/31/10/004>
- Njejmiana, L., Arpin, L., Thibaudeau, C., Jurgensen, N., Bouziri, H., Tetrault, M.-A., Viscogliosi, N., Paulin, C., Lecomte, R., Fontaine, R., 2016. Firmware Architecture of the Data Acquisition System for the LabPET II Mouse Scanner, in: *IEEE Nuclear Science Symposium and Medical Imaging Conference Record*. IEEE, Strasbourg, pp. 1–3.
- Njejmiana, L., Tetrault, M.-A., Arpin, L., Burghgraeve, A., Maille, P., Lavoie, J.-C., Paulin, C., Koua, K.C., Bouziri, H., Panier, S., Ben Attouch, M.W., Abidi, M., Cadorette, J., Pratte, J.-F., Lecomte, R., Fontaine, R., 2013. Design of a Real-Time FPGA-Based Data Acquisition Architecture for the LabPET II: An APD-Based Scanner Dedicated to Small Animal PET Imaging. *IEEE Trans. Nucl. Sci.* 60, 3633–3638. <https://doi.org/10.1109/TNS.2013.2250307>
- Okamura, N., Harada, R., Ishiki, A., Kikuchi, A., Nakamura, T., Kudo, Y., 2018. The development and validation of tau PET tracers: current status and future directions. *Clin. Transl. Imaging* 6, 305–316. <https://doi.org/10.1007/s40336-018-0290-y>
- Ouyang, J., Li, Q., El Fakhri, G., 2013a. Magnetic resonance-based motion correction for positron emission tomography imaging. *Semin. Nucl. Med.* 43, 60–67. <https://doi.org/10.1053/j.semnuclmed.2012.08.007>
- Ouyang, J., Li, Q., El Fakhri, G., 2013b. Magnetic Resonance-Based Motion Correction for Positron Emission Tomography Imaging. *Semin. Nucl. Med., PET/MRI* 43, 60–67. <https://doi.org/10.1053/j.semnuclmed.2012.08.007>
- Padma, M.V., Said, S., Jacobs, M., Hwang, D.R., Dunigan, K., Satter, M., Christian, B., Ruppert, J., Bernstein, T., Kraus, G., Mantil, J.C., 2003. Prediction of pathology and survival by FDG PET in gliomas. *J. Neurooncol.* 64, 227–237. <https://doi.org/10.1023/a:1025665820001>
- Pan, T., Einstein, S.A., Kappadath, S.C., Grogg, K.S., Lois Gomez, C., Alessio, A.M., Hunter, W.C., El Fakhri, G., Kinahan, P.E., Mawlawi, O.R., 2019. Performance evaluation of the 5-Ring GE Discovery MI PET/CT system using the national electrical

- manufacturers association NU 2-2012 Standard. *Med. Phys.* 46, 3025–3033. <https://doi.org/10.1002/mp.13576>
- Panin, V.Y., Kehren, F., Michel, C., Casey, M., 2006. Fully 3-D PET reconstruction with system matrix derived from point source measurements. *IEEE Trans. Med. Imaging* 25, 907–921. <https://doi.org/10.1109/TMI.2006.876171>
- Pascoal, T.A., Shin, M., Kang, M.S., Chamoun, M., Chartrand, D., Mathotaarachchi, S., Bennacef, I., Therriault, J., Ng, K.P., Hopewell, R., Bouhachi, R., Hsiao, H.-H., Benedet, A.L., Soucy, J.-P., Massarweh, G., Gauthier, S., Rosa-Neto, P., 2018. In vivo quantification of neurofibrillary tangles with [18F]MK-6240. *Alzheimers Res. Ther.* 10, 74. <https://doi.org/10.1186/s13195-018-0402-y>
- Petibon, Y., Ouyang, J., Zhu, X., Huang, C., Reese, T.G., Chun, S.Y., Li, Q., Fakhri, G.E., 2013. Cardiac motion compensation and resolution modeling in simultaneous PET-MR: a cardiac lesion detection study. *Phys. Med. Biol.* 58, 2085. <https://doi.org/10.1088/0031-9155/58/7/2085>
- Petibon, Y., Sun, T., Han, P.K., Ma, C., Fakhri, G.E., Ouyang, J., 2019. MR-based cardiac and respiratory motion correction of PET: Application to static and dynamic cardiac 18F-FDG imaging. *Phys. Med. Biol.* 64, 195009. <https://doi.org/10.1088/1361-6560/ab39c2>
- Phelps, M.E., Hoffman, E.J., Mullani, N.A., Ter-Pogossian, M.M., 1975. Application of annihilation coincidence detection to transaxial reconstruction tomography. *J. Nucl. Med. Off. Publ. Soc. Nucl. Med.* 16, 210–224.
- Picard, Y., Thompson, C.J., 1997. Motion correction of PET images using multiple acquisition frames. *IEEE Trans. Med. Imaging* 16, 137–144. <https://doi.org/10.1109/42.563659>
- Picchio, M., Castellucci, P., 2012. Clinical Indications of 11C-Choline PET/CT in Prostate Cancer Patients with Biochemical Relapse. *Theranostics* 2, 313–317. <https://doi.org/10.7150/thno.4007>
- Qi, J., Leahy, R.M., Cherry, S.R., Chatziioannou, A., Farquhar, T.H., 1998. High-resolution 3D Bayesian image reconstruction using the microPET small-animal scanner. *Phys. Med. Biol.* 43, 1001–1013. <https://doi.org/10.1088/0031-9155/43/4/027>
- Radon, J., 1986. On the determination of functions from their integral values along certain manifolds. *IEEE Trans. Med. Imaging* 5, 170–176. <https://doi.org/10.1109/TMI.1986.4307775>
- Rahmim, A., Bloomfield, P., Houle, S., Lenox, M., Michel, C., Buckley, K.R., Ruth, T.J., Sossi, V., 2004. Motion compensation in histogram-mode and list-mode EM reconstructions: Beyond the event-driven approach. *IEEE Trans. Nucl. Sci.* 51, 2588–2596. <https://doi.org/10.1109/TNS.2004.835763>
- Rahmim, A., Dinelle, K., Cheng, J.-C., Shilov, M.A., Segars, W.P., Lidstone, S.C., Blinder, S., Rousset, O.G., Vajihollahi, H., Tsui, B., Wong, D.F., Sossi, V., 2008. Accurate Event-Driven Motion Compensation in High-Resolution PET Incorporating Scattered and Random Events. *IEEE Trans. Med. Imaging* 27, 1018–1033. <https://doi.org/10.1109/TMI.2008.917248>

- Rahmim, A., Rousset, O., Zaidi, H., 2007. Strategies for Motion Tracking and Correction in PET. *PET Clin.* 2, 251–266. <https://doi.org/10.1016/j.cpet.2007.08.002>
- Rahmim, A., Tang, J., Zaidi, H., 2013. Four-Dimensional Image Reconstruction Strategies in Cardiac-Gated and Respiratory-Gated PET Imaging. *PET Clin.* 8, 51–67. <https://doi.org/10.1016/j.cpet.2012.10.005>
- Rank, C.M., Heußer, T., Wetscherek, A., Freitag, M.T., Sedlaczek, O., Schlemmer, H.-P., Kachelrieß, M., 2016. Respiratory motion compensation for simultaneous PET/MR based on highly undersampled MR data. *Med. Phys.* 43, 6234. <https://doi.org/10.1118/1.4966128>
- Reader, A.J., Julyan, P.J., Williams, H., Hastings, D.L., Zweit, J., 2003. EM algorithm system modeling by image-space techniques for PET reconstruction. *IEEE Trans. Nucl. Sci.* 50, 1392–1397. <https://doi.org/10.1109/TNS.2003.817327>
- Robson, P.M., Trivieri, M., Karakatsanis, N.A., Padilla, M., Abgral, R., Dweck, M.R., Kovacic, J.C., Fayad, Z.A., 2018. Correction of respiratory and cardiac motion in cardiac PET/MR using MR-based motion modeling. *Phys. Med. Biol.* 63, 225011. <https://doi.org/10.1088/1361-6560/aaea97>
- Rousset, O.G., Ma, Y., Evans, A.C., 1998. Correction for partial volume effects in PET: principle and validation. *J. Nucl. Med. Off. Publ. Soc. Nucl. Med.* 39, 904–911.
- Salskov, A., Tammisetti, V.S., Grierson, J., Vesselle, H., 2007. FLT: measuring tumor cell proliferation in vivo with positron emission tomography and 3'-deoxy-3'-[18F]fluorothymidine. *Semin. Nucl. Med.* 37, 429–439. <https://doi.org/10.1053/j.semnuclmed.2007.08.001>
- Sámal, M., Kárný, M., Sůrová, H., Maríková, E., Dienstbier, Z., 1987. Rotation to simple structure in factor analysis of dynamic radionuclide studies. *Phys. Med. Biol.* 32, 371–382. <https://doi.org/10.1088/0031-9155/32/3/007>
- Santago, P., Gage, H.D., 1995. Statistical models of partial volume effect. *IEEE Trans. Image Process.* 4, 1531–1540. <https://doi.org/10.1109/83.469934>
- Schilling, L.P., Zimmer, E.R., Shin, M., Leuzy, A., Pascoal, T.A., Benedet, A.L., Borelli, W.V., Palmi, A., Gauthier, S., Rosa-Neto, P., 2016. Imaging Alzheimer's disease pathophysiology with PET. *Dement. Neuropsychol.* 10, 79–90. <https://doi.org/10.1590/S1980-5764-2016DN1002003>
- Schindler, T.H., Schelbert, H.R., Quercioli, A., Dilsizian, V., 2010. Cardiac PET Imaging for the Detection and Monitoring of Coronary Artery Disease and Microvascular Health. *JACC Cardiovasc. Imaging* 3, 623–640. <https://doi.org/10.1016/j.jcmg.2010.04.007>
- Schmidlin, P., 1979. Quantitative evaluation and imaging of functions using pattern recognition methods. *Phys. Med. Biol.* 24, 385. <https://doi.org/10.1088/0031-9155/24/2/014>
- Schöll, M., Lockhart, S.N., Schonhaut, D.R., O'Neil, J.P., Janabi, M., Ossenkoppele, R., Baker, S.L., Vogel, J.W., Faria, J., Schwimmer, H.D., Rabinovici, G.D., Jagust, W.J., 2016.



- PET Imaging of Tau Deposition in the Aging Human Brain. *Neuron* 89, 971–982. <https://doi.org/10.1016/j.neuron.2016.01.028>
- Selivanov, V.V., Picard, Y., Cadorette, J., Rodrigue, S., Lecomte, R., 2000. Detector response models for statistical iterative image reconstruction in high resolution PET. *IEEE Trans. Nucl. Sci.* 47, 1168–1175. <https://doi.org/10.1109/23.856565>
- Shepp, L.A., Vardi, Y., 1982. Maximum likelihood reconstruction for emission tomography. *IEEE Trans. Med. Imaging* 1, 113–122. <https://doi.org/10.1109/TMI.1982.4307558>
- Shivamurthy, V.K.N., Tahari, A.K., Marcus, C., Subramaniam, R.M., 2015. Brain FDG PET and the diagnosis of dementia. *AJR Am. J. Roentgenol.* 204, W76-85. <https://doi.org/10.2214/AJR.13.12363>
- Shreve, P.D., 2000. Adding Structure to Function. *J. Nucl. Med.* 41, 1380–1382.
- Siddon, R.L., 1985. Fast calculation of the exact radiological path for a three-dimensional CT array: Technical Reports: 3D CT array path calculation. *Med. Phys.* 12, 252–255. <https://doi.org/10.1118/1.595715>
- Sitek, A., Di Bella, E.V., Gullberg, G.T., 2000. Factor analysis with a priori knowledge--application in dynamic cardiac SPECT. *Phys. Med. Biol.* 45, 2619–2638. <https://doi.org/10.1088/0031-9155/45/9/314>
- Sitek, A., Gullberg, G.T., Huesman, R.H., 2002. Correction for ambiguous solutions in factor analysis using a penalized least squares objective. *IEEE Trans. Med. Imaging* 21, 216–225. <https://doi.org/10.1109/42.996340>
- Slart, R.H.J.A., Bax, J.J., van Veldhuisen, D.J., van der Wall, E.E., Irwan, R., Sluiter, W.J., Dierckx, R.A., de Boer, J., Jager, P.L., 2006. Prediction of functional recovery after revascularization in patients with chronic ischaemic left ventricular dysfunction: head-to-head comparison between Tc-99m-sestamibi/F-18-FDG DISA SPECT and N-13-ammonia/F-18-FDG PET. *Eur. J. Nucl. Med. Mol. Imaging* 33, 716–723. <https://doi.org/10.1007/s00259-005-0016-z>
- Smid, L.M., Kepe, V., Vinters, H.V., Bresjanac, M., Toyokuni, T., Satyamurthy, N., Wong, K.-P., Huang, S.-C., Silverman, D.H.S., Miller, K., Small, G.W., Barrio, J.R., 2013. Postmortem 3-D brain hemisphere cortical tau and amyloid- $\beta$  pathology mapping and quantification as a validation method of neuropathology imaging. *J. Alzheimers Dis. JAD* 36, 261–274. <https://doi.org/10.3233/JAD-122434>
- Smith, R., Strandberg, O., Leuzy, A., Betthausen, T.J., Johnson, S.C., Pereira, J.B., Hansson, O., 2021. Sex differences in off-target binding using tau positron emission tomography. *NeuroImage Clin.* 31, 102708. <https://doi.org/10.1016/j.nicl.2021.102708>
- Song, T.-A., Chowdhury, S.R., Yang, F., Dutta, J., 2020. Super-resolution PET imaging using convolutional neural networks. *IEEE Trans. Comput. Imaging* 6, 518–528. <https://doi.org/10.1109/TCI.2020.2964229>
- Sørensen, T., 1948. A Method of Establishing Groups of Equal Amplitude in Plant Sociology Based on Similarity of Species Content and Its Application to Analyses of the Vegetation on Danish Commons. I kommission hos E. Munksgaard.

- Soret, M., Bacharach, S.L., Buvat, I., 2007. Partial-Volume Effect in PET Tumor Imaging. *J. Nucl. Med.* 48, 932–945. <https://doi.org/10.2967/jnumed.106.035774>
- Spangler-Bickell, M.G., Zeineh, M., Jansen, F., Khalighi, M.M., Hoo, C., DiGiacomo, P.S., Maclaren, J., Aksoy, M., Rettmann, D., Bammer, R., Zaharchuk, G., 2019. Rigid Motion Correction for Brain PET/MR Imaging Using Optical Tracking. *IEEE Trans. Radiat. Plasma Med. Sci.* 3, 498–503. <https://doi.org/10.1109/TRPMS.2018.2878978>
- Spangler-Bickell, M.G., Zhou, L., Kyme, A.Z., De Laat, B., Fulton, R.R., Nuyts, J., 2016. Optimising rigid motion compensation for small animal brain PET imaging. *Phys. Med. Biol.* 61, 7074–7091. <https://doi.org/10.1088/0031-9155/61/19/7074>
- Sperling, R.A., Aisen, P.S., Beckett, L.A., Bennett, D.A., Craft, S., Fagan, A.M., Iwatsubo, T., Jack, C.R., Kaye, J., Montine, T.J., Park, D.C., Reiman, E.M., Rowe, C.C., Siemers, E., Stern, Y., Yaffe, K., Carrillo, M.C., Thies, B., Morrison-Bogorad, M., Wagster, M.V., Phelps, C.H., 2011. Toward defining the preclinical stages of Alzheimer’s disease: Recommendations from the National Institute on Aging-Alzheimer’s Association workgroups on diagnostic guidelines for Alzheimer’s disease. *Alzheimers Dement.* 7, 280–292. <https://doi.org/10.1016/j.jalz.2011.03.003>
- Strul, D., Slates, R.B., Dahlbom, M., Cherry, S.R., Marsden, P.K., 2003. An improved analytical detector response function model for multilayer small-diameter PET scanners. *Phys. Med. Biol.* 48, 979–994. <https://doi.org/10.1088/0031-9155/48/8/302>
- Sun, T., Petibon, Y., Han, P.K., Ma, C., Kim, S.J.W., Alpert, N.M., El Fakhri, G., Ouyang, J., 2019. Body motion detection and correction in cardiac PET: Phantom and human studies. *Med. Phys.* 46, 4898–4906. <https://doi.org/10.1002/mp.13815>
- Sureau, F.C., Reader, A.J., Comtat, C., Leroy, C., Ribeiro, M.-J., Buvat, I., Trébossen, R., 2008. Impact of Image-Space Resolution Modeling for Studies with the High-Resolution Research Tomograph. *J. Nucl. Med.* 49, 1000–1008. <https://doi.org/10.2967/jnumed.107.045351>
- Sweet, W.H., 1951. The Uses of Nuclear Disintegration in the Diagnosis and Treatment of Brain Tumor. *N. Engl. J. Med.* 245, 875–878. <https://doi.org/10.1056/NEJM195112062452301>
- Tellmann, L., Fulton, R., Pietrzyk, U., Nickel, I., Stangier, I., Winz, O., Herzog, H., 2006. Concepts of Registration and Correction of Head Motion in Positron Emission Tomography. *Z. Für Med. Phys.* 16, 67–74. <https://doi.org/10.1078/0939-3889-00293>
- Ter-Pogossian, M.M., Phelps, M.E., Hoffman, E.J., Mullani, N.A., 1975. A Positron-Emission Transaxial Tomograph for Nuclear Imaging (PETT). *Radiology* 114, 89–98. <https://doi.org/10.1148/114.1.89>
- Theofilas, P., Ehrenberg, A.J., Dunlop, S., Di Lorenzo Alho, A.T., Nguy, A., Leite, R.E.P., Rodriguez, R.D., Mejia, M.B., Suemoto, C.K., Ferretti-Rebustini, R.E.D.L., Polichiso, L., Nascimento, C.F., Seeley, W.W., Nitri, R., Pasqualucci, C.A., Jacob Filho, W., Rueb, U., Neuhaus, J., Heinsen, H., Grinberg, L.T., 2017. Locus coeruleus volume and cell population changes during Alzheimer’s disease progression: A stereological study in human postmortem brains with potential implication for early-stage biomarker

- discovery. *Alzheimers Dement.* 13, 236–246.  
<https://doi.org/10.1016/j.jalz.2016.06.2362>
- Tiss, A., Marin, T., Gong, K., Lois, C., Chemli, Y., Petibon, Y., Landes, V., Grogg, K., Normandin, M., Spangler-Bickell, M., Becker, J.A., Thibault, E., Johnson, K., Fakhri, G.E., Ouyang, J., 2022. Impact of motion correction on longitudinal [18F]-MK6240 tau PET imaging. *J. Nucl. Med.* 63, 3277–3277.
- Tombaugh, T.N., McIntyre, N.J., 1992. The mini-mental state examination: a comprehensive review. *J. Am. Geriatr. Soc.* 40, 922–935. <https://doi.org/10.1111/j.1532-5415.1992.tb01992.x>
- Townsend, D.W., 2008. Combined Positron Emission Tomography–Computed Tomography: The Historical Perspective. *Semin. Ultrasound CT MRI* 29, 232–235. <https://doi.org/10.1053/j.sult.2008.05.006>
- Townsend, D.W., Wensveen, M., Byars, L.G., Geissbuhler, A., Tochon-Danguy, H.J., Christin, A., Defrise, M., Bailey, D.L., Grootenck, S., Donath, A., 1993. A rotating PET scanner using BGO block detectors: design, performance and applications. *J. Nucl. Med. Off. Publ. Soc. Nucl. Med.* 34, 1367–1376.
- Tsuno, N., Homma, A., 2009. What is the association between depression and Alzheimer’s disease? *Expert Rev. Neurother.* 9, 1667–1676. <https://doi.org/10.1586/ern.09.106>
- Van Daele, M., Joosten, J., Devos, P., Vandecruys, A., Willems, J.L., De Roo, M., 1990. Background correction in factor analysis of dynamic scintigraphic studies: necessity and implementation. *Phys. Med. Biol.* 35, 1477–1485. <https://doi.org/10.1088/0031-9155/35/11/004>
- van Velden, F.H.P., Kloet, R.W., van Berckel, B.N.M., Buijs, F.L., Luurtsema, G., Lammertsma, A.A., Boellaard, R., 2009. HRRT Versus HR+ Human Brain PET Studies: An Interscanner Test–Retest Study. *J. Nucl. Med.* 50, 693–702. <https://doi.org/10.2967/jnumed.108.058628>
- Vavasis, S.A., 2010. On the Complexity of Nonnegative Matrix Factorization. *SIAM J. Optim.* 20, 1364–1377. <https://doi.org/10.1137/070709967>
- Verhaeghe, J., Reader, A.J., 2010. A PET superset data framework for exploitation of known motion in image reconstruction: PET superset data. *Med. Phys.* 37, 4709–4721. <https://doi.org/10.1118/1.3466832>
- Villemagne, V.L., Fodero-Tavoletti, M.T., Masters, C.L., Rowe, C.C., 2015. Tau imaging: early progress and future directions. *Lancet Neurol.* 14, 114–124. [https://doi.org/10.1016/S1474-4422\(14\)70252-2](https://doi.org/10.1016/S1474-4422(14)70252-2)
- Wang, G., Qi, J., 2015. PET Image Reconstruction Using Kernel Method. *IEEE Trans. Med. Imaging* 34, 61–71. <https://doi.org/10.1109/TMI.2014.2343916>
- Wang, Y., Balaji, V., Kaniyappan, S., Krüger, L., Irsen, S., Tepper, K., Chandupatla, R., Maetzler, W., Schneider, A., Mandelkow, E., Mandelkow, E.-M., 2017. The release and trans-synaptic transmission of Tau via exosomes. *Mol. Neurodegener.* 12, 5. <https://doi.org/10.1186/s13024-016-0143-y>

- Wang, Z., Bovik, A.C., Sheikh, H.R., Simoncelli, E.P., 2004. Image Quality Assessment: From Error Visibility to Structural Similarity. *IEEE Trans. Image Process.* 13, 600–612. <https://doi.org/10.1109/TIP.2003.819861>
- Watson, C.C., Newport, D., Casey, M.E., 1996. A Single Scatter Simulation Technique for Scatter Correction in 3D PET, in: Grangeat, P., Amans, J.-L. (Eds.), *Three-Dimensional Image Reconstruction in Radiology and Nuclear Medicine, Computational Imaging and Vision*. Springer Netherlands, Dordrecht, pp. 255–268. [https://doi.org/10.1007/978-94-015-8749-5\\_18](https://doi.org/10.1007/978-94-015-8749-5_18)
- Weber, W.A., 2006. Positron Emission Tomography As an Imaging Biomarker. *J. Clin. Oncol.* 24, 3282–3292. <https://doi.org/10.1200/JCO.2006.06.6068>
- Wernick, M.N., Chen, C.-T., 1992. Superresolved tomography by convex projections and detector motion. *J. Opt. Soc. Am. A* 9, 1547. <https://doi.org/10.1364/JOSAA.9.001547>
- Xia, C.-F., Arteaga, J., Chen, G., Gangadharmath, U., Gomez, L.F., Kasi, D., Lam, C., Liang, Q., Liu, C., Mocharla, V.P., Mu, F., Sinha, A., Su, H., Szardenings, A.K., Walsh, J.C., Wang, E., Yu, C., Zhang, W., Zhao, T., Kolb, H.C., 2013. [(18)F]T807, a novel tau positron emission tomography imaging agent for Alzheimer’s disease. *Alzheimers Dement. J. Alzheimers Assoc.* 9, 666–676. <https://doi.org/10.1016/j.jalz.2012.11.008>
- Yesavage, J.A., Brooks, J.O., Taylor, J., Tinklenberg, J., 1993. Development of aphasia, apraxia, and agnosia and decline in Alzheimer’s disease. *Am. J. Psychiatry* 150, 742–747. <https://doi.org/10.1176/ajp.150.5.742>
- Yu, Y., Chan, C., Ma, T., Liu, Y., Gallezot, J.-D., Naganawa, M., Kelada, O.J., Germino, M., Sinusas, A.J., Carson, R.E., Liu, C., 2016. Event-by-Event Continuous Respiratory Motion Correction for Dynamic PET Imaging. *J. Nucl. Med. Off. Publ. Soc. Nucl. Med.* 57, 1084–1090. <https://doi.org/10.2967/jnumed.115.167676>
- Zhang, H., Wang, Y., Qi, J., Abbaszadeh, S., 2020. Penalized Maximum-Likelihood Reconstruction for Improving Limited-Angle Artifacts in a Dedicated Head and Neck PET System. *Phys. Med. Biol.* 65, 165016. <https://doi.org/10.1088/1361-6560/ab8c92>
- Zhou, J., Coatrieux, J.-L., Bousse, A., Shu, H., Luo, L., 2007. A Bayesian MAP-EM Algorithm for PET Image Reconstruction Using Wavelet Transform. *IEEE Trans. Nucl. Sci.* 54, 1660–1669. <https://doi.org/10.1109/TNS.2007.901200>

## **Titre :** Méthodes pour l'amélioration de la quantification en imagerie TEP du cerveau à l'aide de Super-Résolution et Factorisation Matricielle Non-négative

**Mots clés :** Imagerie médicale, traitement de l'image, super-résolution, TEP, optimisation

**Résumé :** L'avènement de radiotraceurs se liant aux repliements de protéines telles que l'amyloïde et les enchevêtrements neurofibrillaires (tau) a inauguré une nouvelle ère d'imagerie en tomographie par émission de positrons (TEP) pour les maladies neurodégénératives, apportant de nouvelles exigences pour la quantification et le traitement des images. En particulier, l'imagerie de la pathologie tau, surtout dans les premiers stades de la maladie, alimente un besoin d'amélioration de la quantification TEP pour permettre une imagerie précise de la distribution des traceurs plus focalisés et des petites structures cérébrales, telles que le cortex entorhinal. Cependant, cette tâche est généralement affectée par la faible résolution spatiale inhérente à l'imagerie TEP ainsi que par le bruit et l'effet de volume partiel induit par l'effet de fraction tissulaire. Pour aborder ces problèmes, cette thèse explore différentes méthodes pour améliorer la quantification, telles que la super-résolution (SR) et la factorisation de matrices non négatives (NMF).

La super-résolution (SR) est une méthodologie qui cherche à améliorer la résolution d'image en exploitant les informations d'échantillonnage spatial accrues obtenues à partir de multiples acquisitions de la même cible avec des décalages connus avec une précision sub-pixellique. La première contribution de ce travail vise à étudier, développer et évaluer la SR pour la tomographie par émission de positrons du cerveau, en tirant parti d'une caméra de suivi infrarouge à haute résolution pour mesurer les décalages de manière précise et continue. Des expériences sur des fantômes mobiles et des primates non humains ont été réalisées sur un scanner GE Discovery MI PET/CT (GE Healthcare) en utilisant une NDI Polaris Vega (Northern Digital Inc), une caméra optique de suivi de mouvement. Pour permettre la SR, une

synchronisation temporelle et spatiale robuste des deux dispositifs a été développée ainsi qu'un algorithme de reconstruction de type « Ordered Subset Expectation Maximization » (OSEM) en mode liste, incorporant les données de suivi haute résolution de la Polaris Vega pour corriger le mouvement des lignes de réponse mesurées (LOR) événement par événement. Pour les études sur les fantômes et primates, la méthode de reconstruction SR a produit des images TEP avec une résolution spatiale visiblement accrue par rapport aux acquisitions statiques standard, permettant une meilleure visualisation des petites structures. Une analyse quantitative en termes de mesure d'indice de similarité (SSIM), de rapport contraste sur bruit (CNR) et de lignes de profils a été réalisée et a validé nos observations. Les résultats démontrent que la SR peut être réalisée en TEP cérébrale en mesurant le mouvement de la cible en temps réel à l'aide d'une caméra de suivi infrarouge à haute résolution. Le deuxième objectif de cette thèse était d'explorer l'utilisation de la factorisation de matrices non négatives en imagerie TEP dynamique, en particulier en relation avec le traceur TEP Tau [18F]MK6240. Ce traceur présente des limites cliniques potentielles, telles que la fixation hors cible (« off target binding »). La NMF est une méthode qui peut être utilisée pour séparer avec précision les signaux spécifiques au tau, les signaux non spécifiques et les signaux hors cible dans les données acquises. Dans cette thèse, les fondements théoriques de la NMF sont discutés et ses applications pratiques dans l'imagerie TEP dynamique sont examinées. Pour démontrer l'efficacité de la NMF, des simulations ont été appliquées sur un fantôme numérique et des études sur des images cliniques TEP dynamiques acquises auprès de sujets ont été réalisées. Les résultats de l'analyse NMF sont présentés et discutés, mettant en évidence le potentiel de cette méthode pour améliorer la quantification et l'interprétation des données d'imagerie TEP dynamique dans le contexte de la pathologie tau.

## **Title:** Methods for improved brain PET quantification using super-resolution and non-negative matrix factorization

**Keywords:** Medical imaging, Image processing, super-resolution, PET, optimization

**Abstract:** The advent of radiotracers binding to misfolded proteins such as amyloid and neurofibrillary tangles (tau), has ushered in a new era of PET imaging for neurodegenerative diseases, bringing new requirements for image quantification and processing. In particular, imaging of tau pathology, especially in early disease stages, is fueling a need for improved PET quantification to allow for accurate imaging of more focal tracer uptake patterns and small brain structures, such as the entorhinal cortex. However, this task is usually affected by the poor spatial resolution inherent to PET imaging as well as noise and the partial volume effect induced from tissue fraction effect. To address these issues, this thesis explores different methods for improving quantification, such as super-resolution (SR) and non-negative matrix factorization (NMF).

Super-resolution (SR) is a methodology that seeks to improve image resolution by exploiting the increased spatial sampling information obtained from multiple acquisitions of the same target with accurately known sub-resolution shifts. The first contribution of this work aims to study, develop and evaluate an SR estimation framework for brain positron emission tomography (PET), taking advantage of a high-resolution infra-red tracking camera to measure shifts precisely and continuously. Moving phantoms and non-human primate (NHP) experiments were performed on a GE Discovery MI PET/CT scanner (GE Healthcare) using an NDI Polaris Vega (Northern Digital Inc), an external optical motion tracking device.

To enable SR, a robust temporal and spatial calibration reconstruction algorithm, incorporating the high-resolution tracking data from the Polaris Vega to correct motion for measured line of responses (LORs) on an event-by-event basis. For both phantoms and NHP studies, the SR reconstruction method yielded PET images with visibly increased spatial resolution compared to standard static acquisitions, allowing improved visualization of small structures. Quantitative analysis in terms of SSIM, CNR and line profiles were conducted and validated our observations. The results demonstrate that SR can be achieved in brain PET by measuring target motion in real-time using a high-resolution infrared tracking camera.

The second objective of this thesis was to explore the use of non-negative matrix factorization (NMF) in dynamic PET imaging, specifically in relation to the [18F]MK6240 Tau PET tracer. This tracer has potential clinical limitations, such as off-target binding in dynamic imaging. NMF is a method that can be used to overcome these limitations by accurately separating tau-specific signals, non-specific signals, and off-target signals in the acquired data. In this thesis, the theoretical foundations of NMF are discussed and its practical applications in dynamic PET imaging are examined. To demonstrate the effectiveness of NMF, simulations were applied to a numerical phantom and real dynamic PET images acquired from cognitively normal subjects. The results of the NMF analysis are presented and discussed, highlighting the potential of this method to improve the quantification and interpretation of dynamic PET imaging data in the context of tau pathology.